marine drugs

Special Issue Reprint

# Application of Marine Chitin and Chitosan, 3rd Edition

Edited by
Jessica Amber Jennings and Tippabattini Jayaramudu

mdpi.com/journal/marinedrugs

MDPI

# Application of Marine Chitin and Chitosan, 3rd Edition

# Application of Marine Chitin and Chitosan, 3rd Edition

Guest Editors

**Jessica Amber Jennings**
**Tippabattini Jayaramudu**

Basel • Beijing • Wuhan • Barcelona • Belgrade • Novi Sad • Cluj • Manchester

*Guest Editors*

| | |
|---|---|
| Jessica Amber Jennings<br>Department of Biomedical Engineering<br>University of Memphis<br>Memphis<br>USA | Tippabattini Jayaramudu<br>Nanoscience and Biomedical Engineering Department<br>South Dakota School of Mines<br>Rapid City<br>USA |

*Editorial Office*
MDPI AG
Grosspeteranlage 5
4052 Basel, Switzerland

This is a reprint of the Special Issue, published open access by the journal *Marine Drugs* (ISSN 1660-3397), freely accessible at: https://www.mdpi.com/journal/marinedrugs/special_issues/V2705R8KY3.

For citation purposes, cite each article independently as indicated on the article page online and as indicated below:

Lastname, A.A.; Lastname, B.B. Article Title. *Journal Name* **Year**, *Volume Number*, Page Range.

**ISBN 978-3-7258-5373-1 (Hbk)**
**ISBN 978-3-7258-5374-8 (PDF)**
**https://doi.org/10.3390/books978-3-7258-5374-8**

# Contents

marine drugs

MDPI

Article

# Enhancing Electrospinnability of Chitosan Membranes in Low-Humidity Environments by Sodium Chloride Addition

**Hengjie Su [1], Xiaoqi Chen [2], Linna Mao [1] and Ting Li [1,*]**

[1] Institute of Biomedical Engineering, Chinese Academy of Medical Sciences & Peking Union Medical College, Tianjin 300192, China
[2] Department of Biomedical Engineering, Tiangong, Tianjin 300387, China
* Correspondence: liting@bme.pumc.edu.cn

**Abstract:** The electrospinning of pure chitosan nanofibers is highly sensitive to environmental humidity, which limits their production consistency and applicability. This study investigates the addition of sodium chloride (NaCl) to chitosan solutions to enhance spinnability and mitigate the effigurefects of low humidity. NaCl was incorporated into the electrospun chitosan solution, leading to increased conductivity and decreased viscosity. These modifications improved the electrospinning process. Comparative analyses between chitosan membranes (CM) and sodium-chloride-added chitosan membranes (SCM) revealed no significant differences in chemical structure, mechanical strength, or in vitro cell proliferation. This indicates that the addition of 1% (*w*/*v*) NaCl does not adversely affect the fundamental properties of the chitosan membranes. The findings demonstrate that NaCl addition is a viable strategy for producing electrospun chitosan nanofibers in low-humidity environments, maintaining their physicochemical properties while enhancing spinnability.

**Keywords:** chitosan; salt; electrospinning; environmental humidity; conductivity

## 1. Introduction

Electrospun chitosan membranes are being explored as biocompatible and biodegradable scaffolds for guided bone regeneration (GBR), with potential applications in periodontal treatment and craniofacial regeneration [1–3]. Chitosan, a nature polysaccharide derived from the shell of crustacean, offers advantages such as low cost, biocompatibility, biodegradability, and non-toxicity [4,5]. Consequently, it has been widely used in biomedical fields, including guided bone regeneration, vascular stents, and wound dressings [6,7]. Electrospinning is a method that uses an electrostatic field to create a jet from a polymer solution to form nanofibers [8]. Key factors for the successful spinning of nanofibers include viscosity, surface tension, and electrical conductivity of the solution [5]. These factors vary with changes in the solution concentration and solvent system.

Electrospinning pure chitosan nanofibers is challenging due to several inherent properties of chitosan. The solubility of chitosan in most common solvents is not ideal [9], and the solution viscosity, caused by strong intermolecular and intramolecular hydrogen bonds, makes it difficult to overcome the surface tension during electrospinning [10]. Acetic acid and trifluoroacetic acid (TFA) are widely used solvents for dissolving chitosan. Achieving suitable surface tension for electrospinning typically requires at least 30% acetic acid for chitosan with 56–65% deacetylation (DDA) [11]. TFA has been explored as a solvent because it can block the positive charges of amino groups on chitosan and decrease the electrostatic forces, enabling the production of homogeneous chitosan nanofibers [5]. When comparing the two solvents, TFA produces smoother and more continuous nanofibers than acetic acid [5]. Additionally, the addition of methylene chloride to TFA can result in more uniform fibers produced by electrospinning [12]. Although there have been concerns about the toxicity of TFA [13], studies have proved that electrospun chitosan membranes produced using TFA/DCM solvents are biocompatible both in vitro and in vivo [14,15]. Researchers continue to use TFA/DCM as the solvent for electrospinning chitosan due to its ability to produce a more controlled and stable electrospinning processes [16–20].

However, the success of electrospinning pure chitosan in TFA/DCM depends significantly on environmental moisture [13,21]. It has been observed that the ambient humidity suitable for chitosan electrospinning is between 40–60% [14,21]. The impact of environmental humidity on electrospinning is not fully understood, making pure chitosan electrospinning highly restricted to environmental humidity. It is suspected that lower humidity in the environment results in decreased electrostatic discharge on the spinning jet, as fewer water molecules are available for charge transfer [22]. Consequently, the charge density on the jet is higher at low humidity, causing fiber breakage. If the voltage applied to the electrostatic field is not high enough, or if the solution has low conductivity, the electrostatic force cannot overcome the surface tension, and fibers cannot be produced [23]. To address this, creating a humid atmosphere within the electrospinning apparatus has been explored. However, the dense water mist from the humidifier may cause short circuits in the high voltage electrostatic field, making it difficult to control the mist distribution and posing significant safety risks.

Another approach to improve spinnability is by enhancing the electrical conductivity of the electrospinning solution. In one study, adding tetraethylammonium bromide (TEAB) salt to a polyimides (PI) solution improved its conductivity, allowing successful spinning even at low PI concentrations [8]. Similarly, adding TEAB salt to a polymers of intrinsic microporosity (PIM-1) solution significantly increased its conductivity, enabling the formation of electrospun fibers at a low PIM-1 concentration (10% (*w*/*v*)) [24]. Salt ions act as charge carriers in the electric field and affect the motion of the spinning jet [25–27]. Although adding salt to electrospinning solutions to improve spinnability has been explored, no studies have focused on adding salt specifically to pure chitosan solutions for electrospinning. Additionally, the relationship between environmental humidity and the addition of salt to chitosan solutions has not been explored.

This study aims to address the issue of humidity constraints encountered during the electrospinning of chitosan using the TFA/DCM solvent combination. In this study, adding sodium chloride to the electrospun chitosan solution was explored to reduce the impact of environmental moisture. To further investigate the effect of salt on electrospun chitosan membranes, the physical and chemical properties of the electrospun chitosan solution and chitosan membrane (CM) were examined by comparing them with the electrospun chitosan solution with salt and chitosan membrane with salt (SCM).

## 2. Results and Discussion

### 2.1. Solution Conductivity and Viscosity

To prepare the chitosan solution with NaCl, 5.5% (*w*/*v*) chitosan was dissolved in 10 mL TFA/DCM (7:3 *v*/*v*) solution overnight [14,28]. Just before electrospinning, 100 mg of NaCl was dissolved in 300 μL of water and added to the chitosan solution. Given that the water solubility of NaCl is 360 g/L and NaCl is hardly soluble in TFA and DCM, the NaCl solution was added to the chitosan solution in this specified proportion. NaCl was selected to increase the solution's conductivity due to its biocompatibility as a natural component of the human body. Due to the immiscibility of water and DCM, the system separates into two phases after adding the NaCl solution to the electrospun chitosan solution: the TFA/water phase and the TFA/DCM phase. However, the TFA/water phase is very small and nearly invisible to the naked eye due to the tiny volume of water relative to the total volume. The NaCl dissolves in the TFA/water phase but not in the TFA/DCM phase. Given the small amount of water (300 μL) in a much larger volume of TFA/DCM (10 mL), the dissolution of NaCl is limited. This was confirmed in Figure 1a. After three days of deposition of the electrospun chitosan solutions with varying concentrations of NaCl, salt crystals were observed at the bottom of the solutions, indicating that the NaCl was relatively isolated from the electrospun solution (Figure 1a). Additionally, observations on the first day revealed that the mixed state of NaCl in the chitosan solution remained stable during the electrospinning process.

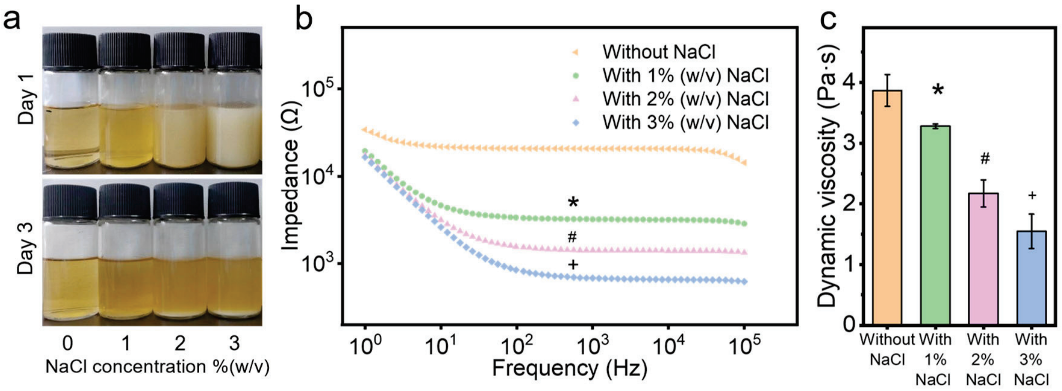

**Figure 1.** Properties of chitosan solutions with and without NaCl: (**a**) images of electrospun chitosan solutions on day 1 and day 3, (**b**) impedance, and (**c**) dynamic viscosity. *, #, and + denotes significant differences between groups.

An imperative step in electrospinning involves balancing the charge behavior and viscosity of the solution [28]. The charge behavior impacts the spinnability of the solution, as higher solution conductivity enables greater splaying ability to eject the solution into filaments from the Taylor cone [29,30]. Adding an NaCl water solution can enhance the conductivity of the solution, improving the electrospinning process by reducing the impedance and potentially increasing spinnability [31,32]. This is consistent with the results of this study, where the impedance of the chitosan solution significantly decreased ($p < 0.05$) after adding salt (Figure 1b). Chitosan solution with higher salt concentrations showed lower impedance, indicating higher conductivity and potentially greater spinnability.

The viscosity measures the resistance or internal friction of a fluid to flow, greatly influencing the electrospinning process and resulting fiber diameters [28,33]. After adding the NaCl solution, the dynamic viscosity of electrospun chitosan solutions decreased significantly ($p < 0.05$, Figure 1c). These results are consistent with Varnaitė-Žuravliova's research, which showed that conductivity increased and viscosity decreased after adding NaCl to the chitosan/PEO electrospun solution [25]. Previous studies demonstrated that adding NaCl to chitosan solution can lead to the breakdown of the hydrogen bond network of chitosan [25,31,34,35]. The hydroxyl group of chitosan is usually involved in the formation of intermolecular hydrogen bonds, and the destruction of these hydrogen bonds promotes the molecular motion of chitosan, increases the charge density, and decreases the solution viscosity, and thus, enhances spinnability [31,34]. The optimal viscosity range can vary depending on the specific polymer and solvent system used [11,36–40]. When the viscosity is lower than the optimal range, it is difficult to draw continuous nanofibers, resulting in the appearance of beads in the membrane [11]. The viscosity of 10 mL electrospun chitosan solution with 300 mg (3% (*w*/*v*)) NaCl decreased below 2 Pa·s (Figure 1c), making it challenging to perform the electrospinning at this viscosity. In lab experiments, it was demonstrated that adding 100 mg (1% (*w*/*v*)) and 200 mg (2% (*w*/*v*)) NaCl to 10 mL of electrospun chitosan solution allowed successful electrospinning under the environmental moisture levels of 25–35%. However, it was difficult to collect chitosan membranes with 2% (*w*/*v*) NaCl at the same volume solution, possibly because the increased amount of water melted the fibers during the process, thereby decreasing the final fiber volume. Hence, the most suitable concentration of NaCl to add in the chitosan solution is 1% (*w*/*v*).

### 2.2. Scanning Electron Microscopy (SEM)

After collecting the electrospun membranes, a post electrospinning treatment involving triethylamine (TEA) and di-tert-butyl dicarbonate (tBOC) was performed to neutralize the membranes, enhancing their aqueous stability and biocompatibility. SEM images showed that both SCM and CM maintained intact fiber structures before and after TEA/tBOC treatment, suggesting that the addition of the NaCl solution did not affect the uniformity of the spinning process, even with the formation of liquid phases (Figure 2). The diameter of SCM (with 2% (*w*/*v*) NaCl) fiber was significantly smaller ($p < 0.05$) than that of CM and SCM (with 1% (*w*/*v*) NaCl) before and after TEA/tBOC treatment (Figure 3a). The fiber diameter distribution showed that most fiber diameters of CM and SCM with 1% (*w*/*v*) NaCl were around 400 nm, whereas the majority of fiber diameters of SCM with 2% (*w*/*v*) NaCl were around 200 nm (Figure 2). Although there was no significant difference in fiber diameters between CM and SCM (with 1% (*w*/*v*) NaCl), a decreasing trend from CM to SCM (with 1% (*w*/*v*) NaCl) was observed. These results indicate that the addition of NaCl to the chitosan electrospinning solution reduces fiber diameter, but small amounts of salt do not significantly affect the fiber diameter. This aligns with findings that fiber diameter is influenced by the viscosity of the electrospun solution [40–42]. In this study, the addition of NaCl significantly decreased the viscosity of the electrospun chitosan solution, resulting in smaller diameters of electrospun chitosan nanofibers. Concurrently, the conductivity of the electrospun chitosan solution increased with the addition of NaCl, indicating an increase in charge density on the jet. This increased the extension level of the jet under the electric field [26]. Therefore, under the same applied voltage and spinning distance, higher solution conductivity enhances the jet's axial stretch, resulting in smaller electrospun fiber diameters [43], see more in Supplementary Materials.

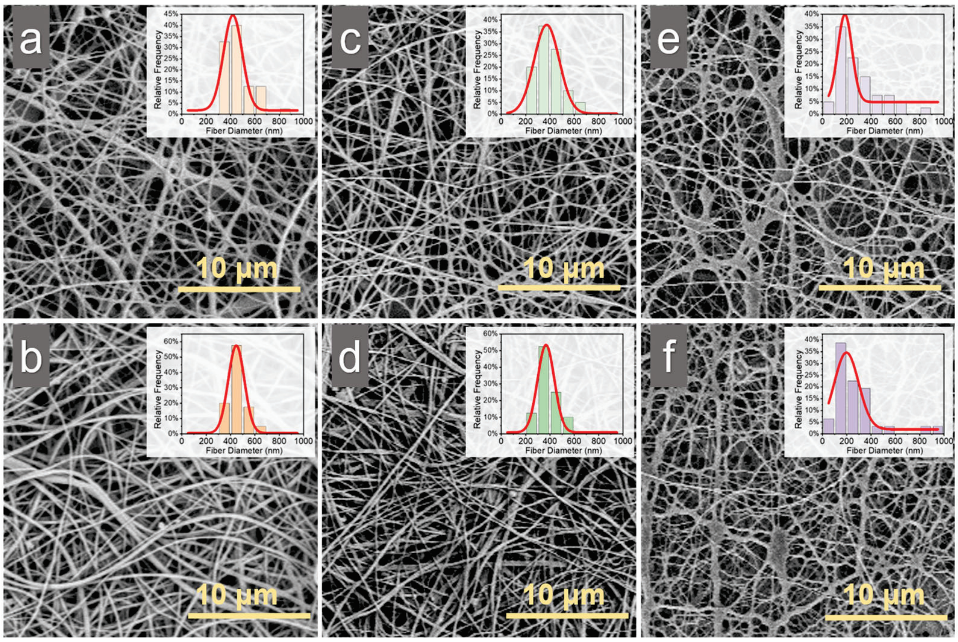

**Figure 2.** SEM images of electrospun chitosan membranes and the corresponding fiber diameter distribution: (**a**) CM without post-treatment, (**b**) CM with TEA/tBOC treatment, (**c**) SCM (1% NaCl) without post-treatment, (**d**) SCM (1% NaCl) with TEA/tBOC treatment, (**e**) SCM (2% NaCl) without post-treatment, and (**f**) SCM (2% NaCl) with TEA/tBOC treatment. "CM" denotes "chitosan membrane", while "SCM" denotes "chitosan membrane with salt".

After post-electrospinning treatment, there was no significant change ($p > 0.05$) in fiber diameter of both CM and SCM membranes. This is consistent with previous studies showing that post-electrospinning treatment with TEA/tBOC does not cause fiber expansion or structural loss [14].

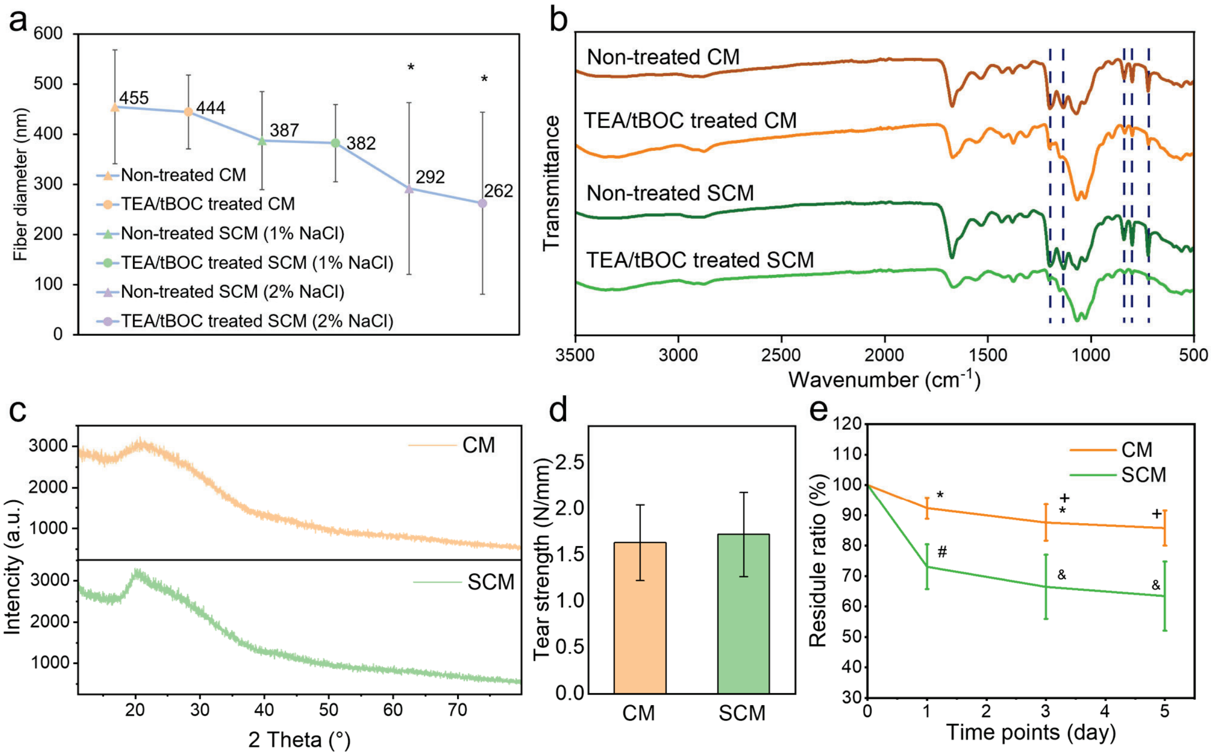

**Figure 3.** Physicochemical properties of electrospun chitosan membranes: (**a**) fiber diameter, (**b**) FTIR spectra, (**c**) XRD spectra, (**d**) tear strength, and (**e**) degradation ratio results. *, +, #, and & denote significant differences between groups.

### 2.3. Fourier Transform Infrared Spectroscopy (FTIR)

The FTIR spectra of CM and SCM (with 1% (*w*/*v*) NaCl) before and after TEA/tBOC treatment are compared in Figure 3b. The peaks associated with TFA salt at 723 $\text{cm}^{-1}$, 801 $\text{cm}^{-1}$, and 840 $\text{cm}^{-1}$ disappeared after the TEA/tBOC treatment of both CM and SCM membranes, which is consistent with the previous study [14]. Additionally, two peaks around 1100–1200 $\text{cm}^{-1}$ disappeared after the TEA/tBOC treatment, indicating the removal of trifluoromethyl groups.

The presence of NaCl in the FTIR spectrum was not clearly evident. There were hardly any characteristic bands related to NaCl salt near 1310 $\text{cm}^{-1}$, 1110 $\text{cm}^{-1}$, and 1640 $\text{cm}^{-1}$ in the SCM spectra, which is similar to the results of Varnaitė-Žuravliova's study [25]. The spectra of SCM showed the same peaks as those of CM, indicating that the addition of salt to the electrospinning solution of chitosan did not change the chemical composition of the electrospun chitosan film.

### 2.4. X-Ray Diffraction (XRD)

Figure 3c displays the XRD spectra of both CM and SCM (with 1% (*w*/*v*) NaCl). In both spectra, a broad peak was observed at $2\theta = 20°$, which is characteristic of partially crystalline forms of chitosan, including both anhydrous and hydrated crystalline structures [14]. When comparing with the XRD spectrum of sodium chloride crystals, no distinct characteristic peaks of NaCl are present in the SCM spectrum, indicating the absence of salt crystals in the SCM [44]. This result further supports the FTIR analysis, confirming that the addition of salt to the spinning solution did not alter the chemical composition of the chitosan nanofibers.

### 2.5. Water Retention

The water retention behavior of the membranes reflects their ability to absorb exudates from wounds. The abundant micropores within the membranes enhance water absorption by increasing surface contact with water, while also providing favorable conditions for cell adhesion and spreading [45]. As shown in the results, the water retention rate of SCM (736.81 ± 37.89%) was significantly higher than that of CM (372.97 ± 11.22%) after 0.5 h and remained stable thereafter (Table 1). Notably, both membranes exhibited minimal expansion in length, 102.79 ± 1.17% for CM and 97.24 ± 0.83% for SCM, indicating that the shape of both membranes remained largely unchanged after water absorption. SCM exhibited initial swelling and thickening during the early stages of water absorption, leading to a slight reduction in side length. FTIR and XRD analysis confirmed no significant differences in the chemical structures of the two membranes. Therefore, the observed variation in water retention may be attributed to differences in fiber diameter. As the fiber diameter decreases, the surface area-to-volume ratio increases, leading to a larger nanoporous space. This allows SCM to have more extensive contact with water, resulting in greater water absorption and swelling [46], see more in Supplementary Materials.

**Table 1.** CM and SCM membrane swelling extent and water retention content.

| Hours (h) | Membrane Swelling Length (%) | | Water Retention Content (%) | |
|---|---|---|---|---|
| | CM (Mean ± std) | SCM (Mean ± std) | CM (Mean ± std) | SCM (Mean ± std) |
| 0 | 100 ± 0 | 100 ± 0 | 100 ± 0 | 100 ± 0 |
| 0.5 | 102.79 ± 1.17 * | 97.24 ± 0.83 + | 372.97 ± 11.22 * | 736.81 ± 37.89 + |
| 2 | 102.2 ± 1.35 * | 97.61 ± 0.95 + | 383.91 ± 2 * | 743.39 ± 39.6 + |

* and + denote significant differences ($p < 0.05$).

### 2.6. Tear Strength

The suture pull-out test was used to evaluate the tear strength, indicating the handleability of the membrane in clinical operations. The results showed that the tear strength of CM and SCM (with 1% (*w*/*v*) NaCl) was 1.63 N/mm and 1.72 N/mm, respectively (Figure 3d). There was no significant difference ($p > 0.05$), indicating that adding NaCl solution before chitosan electrospinning did not affect the mechanical properties of the chitosan membrane, see more in Supplementary Materials.

### 2.7. Degradation

The degradation of the membranes was evaluated to assess their breakdown rate when implanted in the human body. In tissue engineering applications, the degradability of electrospun chitosan membranes is advantageous, as it eliminates the need for a second surgery and reduces unnecessary tissue damage. The results showed that both CM and SCM degraded significantly after 5 days, with substantial weight loss (Figure 3e). The degradation rate of CM was consistent with the previous study [47], while SCM exhibited a significantly faster degradation rate. This accelerated degradation could be attributed to the thinner fibers in SCM, which may be more susceptible to breakdown.

### 2.8. Cell Culture

The cell culture experiment was conducted to evaluate the biocompatibility of CM and SCM (with 1% (*w*/*v*) NaCl) after TEA/tBOC treatment. After 5 days of culture, both CM and SCM were proved to be biocompatible with fibroblasts (NIH3T3, Figure 4a) and osteoblasts (MC3T3E1, Figure 4b). Both cell types showed significant proliferation ($p < 0.05$) on CM and SCM from day 1 to day 5, similar to previous studies [14,17]. There was no significant difference ($p > 0.05$) between the two types of membranes at each time point in both the fibroblast and osteoblast cell culture experiments. Live and dead staining graphs showed no obvious dead cells on the 5th day for both CM and SCM, indicating a high cell survival rate. These results demonstrate that adding 1% (*w*/*v*) NaCl did not affect the biocompatibility of electrospun chitosan membranes, see more in Supplementary Materials.

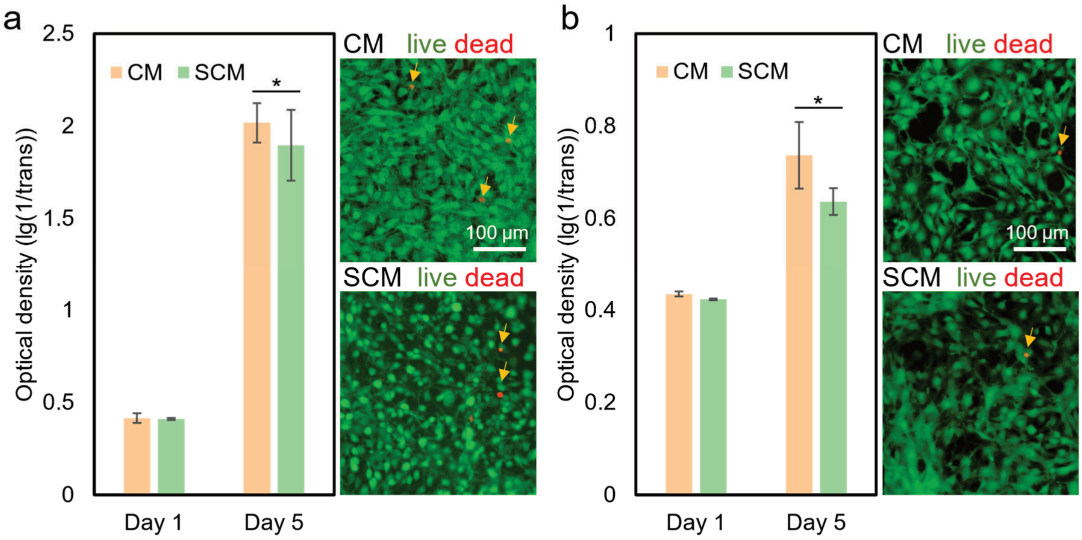

**Figure 4.** Cell culture results of CM and SCM (with 1% (*w*/*v*) NaCl). (**a**) Proliferation of fibroblasts (NIH3T3 cells) on CM and SCM (left), with live/dead staining images on the 5th day (right). (**b**) Proliferation of osteoblasts (MC3T3E1 cells) on CM and SCM (left), with live/dead staining images on the 5th day (right). * denotes a significant difference ($p < 0.05$). "CM" represents "chitosan membrane" and "SCM" represents "chitosan membrane with salt". Arrows indicate dead cells.

In previous studies, NaCl was also a commonly used additive in polymer electrospinning solutions and was proven to be biocompatible with cells [48,49]. MG63 cells proliferated significantly after 11 days on a chitosan/PEO scaffold that was electrospun with 0.2% NaCl. Additionally, smooth muscle cells showed significantly proliferation after 14 days on collagen/elastin membranes that were electrospun with 0.5% (*w*/*v*) PEO and 42.5 mM NaCl [45]. These studies demonstrate that the addition of a small amount of sodium chloride does not affect the biocompatibility of electrospun membranes.

## 3. Materials and Methods

### 3.1. Chitosan Solution and Membrane Preparation

The electrospun chitosan solution was prepared by dissolving 550 mg of chitosan (70% DDA, MW = 1,000,000, Meryer (Shanghai) chemical technology company, Shanghai, China) in 7 mL of TFA (Shanghai Macklin biochemical technology company, Shanghai, China) and 3 mL of dichloromethane (DCM, Shanghai Macklin biochemical technology company, China) overnight. The salt solution was prepared by dissolving 100 mg of sodium chloride (NaCl, 99% purity, Shanghai Aladdin biochemical technology company, Shanghai, China) in 300 µL of deionized (DI) water. The chitosan solution with NaCl was prepared just before the electrospinning by adding the required amount of salt solution to the prepared electrospun chitosan solution.

Electrospinning of the CM was based on a previously reported method [14,17]. After filling the electrospun solution into a 10 mL syringe, a high voltage of 26 kV was applied to the needle tip. An aluminum foil-covered round plate, rotating at a speed of 8.4 rpm, was placed 15 cm from the needle tip.

After collecting electrospun membranes, a post-electrospinning treatment involving TEA and tBOC, innovated in a previous study, was used to neutralize the membranes [15]. Membranes were immersed in a 10% (*w*/*v*) solution of TEA (Shanghai Macklin biochemical technology company, China)/tetrahydrofuran (THF, Shanghai Macklin biochemical technology company, China) for 24 h under mild magnetic stirring to remove the TFA salt. After rinsing the membranes with pure THF twice, the membranes were immersed in a 0.1 g/mL solution of tBOC (Shanghai Aladdin biochemical technology company, China)/THF for 24 h. After washing the membranes with pure THF three times, they were dried between two pieces of nylon mesh in the air to keep them flat.

### *3.2. Solution Conductivity*

The conductivity of 30 mL chitosan solutions (n = 3) was evaluated by electrochemical impedance spectroscopy (EIS) with the electrochemical workstation (CHI 660D, Chenhua, China). The testing electrodes (Wuhu keying new material corporation, Wuhu, China) were selected following the three-electrode system, which included a glassy carbon electrode for the working electrode, a platinum electrode for the counter electrode, and a mercurous sulphate electrode for the reference electrode. The frequency range of EIS measurements was set to 10 to $10^5$ Hz, with the voltage of 5 mV.

### *3.3. Solution Viscosity*

The viscosity of chitosan solutions (n = 3) was tested by a glass capillary viscometer (Shanghai Baoshan Qihang glass instrument factory, China) at room temperature. After recording the flowing time between the two markers ($t$), the dynamic viscosity of the tested solution was calculated using Equation (1):

$$\eta = C \times t \times \rho \tag{1}$$

where $\eta$ (mPa·s) represents the dynamic viscosity, $C$ ($\text{mm}^2/\text{S}^2$) denotes the viscosity number, and $\rho$ ($\text{g}/\text{cm}^3$) indicates the solution density.

### *3.4. Scanning Electron Microscopy (SEM)*

The nanostructure of the two types of membranes was examined using an SEM (MIRA LMS, TESCAN, Tempe, AZ, USA). The membranes were attached to an SEM stub and coated with an 8 nm layer of gold-palladium. They were then examined at 2500× magnification. In each sample, more than 20 fiber diameters were measured.

### *3.5. Fourier Transform Infrared Spectroscopy (FTIR)*

FTIR spectra were collected to evaluate the chemical structure of SCM and CM using a Nicolet$^{\text{TM}}$ iS20 FTIR spectrometer (Thermo Fisher Scientific, Lenexa, KS, USA). Spectra were collected by scanning samples from 500 $\text{cm}^{-1}$ to 4000 $\text{cm}^{-1}$ for 32 scans each.

### *3.6. X-Ray Diffraction (XRD)*

XRD analysis was conducted to assess the crystallinity of the chitosan membranes. Both CM and SCM were first immersed in liquid nitrogen and then ground into fine powders using a mortar and pestle. The samples were subsequently analyzed using an automated multipurpose X-ray diffractometer (Ultima IV, Rigaku, Tokyo, Japan) operating in grazing incidence mode with a wavelength of 1.54 Å. Data collection was performed over a 2θ range of 10° to 80°.

### *3.7. Water Retention*

Water absorption was evaluated to determine the swelling extent and water retention capacity of the membranes. Both CM and SCM were cut into 3 cm × 2 cm rectangle. The samples were then immersed in DI water, and the edge length and weight were measured at specific time intervals. The initial edge length and weight were recorded as "$l_0$" and "$w_0$", respectively. At each time point, the samples were taken out and the excess water was removed using filter paper. The edge length of samples was recorded as "$l_t$" and the weight as "$w_t$". The membrane swelling length was calculated using Equation (2), and the water retention content was calculated using Equation (3):

$$membrane\ swelling\ length\ (\%) = \frac{l_t}{l_0}, \tag{2}$$

$$water\ retention\ content\ (\%) = \frac{m_t}{m_0} \tag{3}$$

### *3.8. Tear Strength*

The tear strength of CM and SCM (n = 3/membrane type) treated with TEA/tBOC was evaluated using an electronic universal testing machine (STS20K, Xiamen Yishite Instruments, Xiamen, China) as an indicator of clinical operability.

Each sample was cut into a 10 × 40 $\mathrm{mm}^2$ rectangle, and surgical sutures were passed through one end at a point 5 mm from the wide edge of the sample and 5 mm from the long edge. The upper clamp of the tension testing machine was used to secure the surgical sutures, while the lower clamp was used to secure the other end of the sample. The load cell used was 50 N, and the extension rate was 10 mm/min. The maximum load was recorded in Newtons (N) and then normalized to film thickness. Three samples of each membrane were tested.

### *3.9. Degradation*

The degradation of the membranes was assessed by measuring mass loss over time. Membranes were cut into 3 cm × 2 cm rectangle and immersed in phosphate-buffered saline (PBS) solution (Beijing Solarbio Science & Technology Co., Beijing, China) containing 100 μg/mL lysozyme (Beijing Solarbio Science & Technology Co., China), and a 5% penicillin–streptomycin–gentamicin solution (Beijing Solarbio Science & Technology Co., China). At each time point, the membranes were removed from the solution, rinsed with DI water, dried overnight at 60 °C, and weighed to determine the change in mass. After weighing, the membranes were returned to the solution to continue the incubation period. A higher concentration of lysozyme was used in this experiment compared to the physiological levels found in human plasma (3–8 μg/mL) to accelerate the degradation process.

### *3.10. Cell Culture*

After high-pressure steam sterilization, round CM and SCM samples ($n$ = 3/membrane type, diameter = 1 cm) were placed into the 48-well plate. Fibroblasts (NIH3T3 cells) and osteoblasts (MC3T3E1 cells) were seeded on the membrane, respectively. The CM and SCM samples were rinsed in culture media and then seeded with cells at $2 \times 10^4$ cells/well. Cells were grown in DMEM media supplemented with 10% FBS and 1% penicillin/streptomycin. At the required time point, the media was removed, and each well was cleaned with PBS three times. Subsequently, 500 μL of media containing 10% CCK-8 were added to each well, and the plate was cultured in a constant temperature incubator at 37 °C with 5% $CO_2$ for 2 h. Afterward, 100 μL of the media was transferred into a new 96-well plate, and the absorbance at 450 nm was measured with a microplate reader (SPARK 10M, TECAN, Tempe, AZ, USA). The absorbance value is proportional to the number of cells. The survival rate and morphology of the cells on the fifth day were observed by inverted fluorescence microscopy and staining with Calcein acetoxymethyl ester (Calcein-AM)/propidium iodide (PI).

### *3.11. Statistical Analysis*

A single factor analysis of variance (ANOVA) was used to analyze the results of solution viscosity and fiber diameter. An independent sample *t*-test was used to analyze the results of mechanical strength, while a two-way ANOVA was employed for analyzing solution conductivity, water retention, degradation, and cell proliferation.

## **4. Conclusions**

In this study, the addition of NaCl to chitosan solutions during electrospinning significantly improved spinnability and reduced the limitations posed by environmental humidity. The incorporation of NaCl led to an increase in solution conductivity and a decrease in viscosity, facilitating the electrospinning process. Comparative analysis of the physicochemical properties of CM and SCM revealed that the addition of 1% (*w*/*v*) NaCl did not alter the chemical groups, mechanical strength, or in vitro cell proliferation characteristics of the membranes. However, the reduced fiber diameter in SCM may contribute to its higher water retention capacity and faster degradation rate. These results suggest that 1% (*w*/*v*) NaCl serves as an effective additive to enhance the electrospinning of chitosan in low-humidity environments, optimizing fiber formation while maintaining key physicochemical properties. This study addresses the challenge of humidity limitations in electrospinning chitosan using the TFA/DCM solvent system, bridging the gap in current advancements within the field.

**Supplementary Materials:** The following supporting information can be downloaded at: https://www.mdpi.com/article/10.3390/md22100443/s1.

**Author Contributions:** H.S. conceived and designed the study, analyzed the data, and contributed to writing and revising the paper. X.C. carried out significant laboratory work, analyzed the data, and contributed to partial writing. L.M. contributed to paper revision. T.L. supervised the laboratory work and provided funding. All authors have read and agreed to the published version of the manuscript.

**Funding:** This work was supported by the Chinese Academy of Medical Science Health Innovation project, grant number 2021-I2M-1-058 and 2021-I2M-1-042, Tianjin Outstanding Youth Fund Project, grant number 20JCJQIC00230, and Fundamental Research Funds for the Central Universities, grant number 3332023070.

**Data Availability Statement:** The data presented in this study are available on request from the corresponding author.

**Conflicts of Interest:** The authors declare no conflicts of interest.

## References

1. Qasim, S.B.; Najeeb, S.; Delaine-Smith, R.M.; Rawlinson, A.; Ur Rehman, I. Potential of Electrospun Chitosan Fibers as a Surface Layer in Functionally Graded GTR Membrane for Periodontal Regeneration. *Dent. Mater.* **2017**, *33*, 71–83. [CrossRef] [PubMed]
2. Zhang, Y.; Wang, T.; Li, J.; Cui, X.; Jiang, M.; Zhang, M.; Wang, X.; Zhang, W.; Liu, Z. Bilayer Membrane Composed of Mineralized Collagen and Chitosan Cast Film Coated with Berberine-Loaded PCL/PVP Electrospun Nanofiber Promotes Bone Regeneration. *Front. Bioeng. Biotechnol.* **2021**, *9*, 684335. [CrossRef]
3. Rodríguez-Méndez, I.; Fernández-Gutiérrez, M.; Rodríguez-Navarrete, A.; Rosales-Ibáñez, R.; Benito-Garzón, L.; Vázquez-Lasa, B.; San Román, J. Bioactive Sr(II)/Chitosan/Poly(ε-Caprolactone) Scaffolds for Craniofacial Tissue Regeneration. In Vitro and In Vivo Behavior. *Polymers* **2018**, *10*, 279. [CrossRef] [PubMed]
4. Toskas, G.; Cherif, C.; Hund, R.-D.; Laourine, E.; Mahltig, B.; Fahmi, A.; Heinemann, C.; Hanke, T. Chitosan(PEO)/Silica Hybrid Nanofibers as a Potential Biomaterial for Bone Regeneration. *Carbohydr. Polym.* **2013**, *94*, 713–722. [CrossRef]
5. Ohkawa, K.; Cha, D.; Kim, H.; Nishida, A.; Yamamoto, H. Electrospinning of Chitosan. *Macromol. Rapid Commun.* **2004**, *25*, 1600–1605. [CrossRef]
6. Yang, W.; Fu, J.; Wang, D.; Wang, T.; Wang, H.; Jin, S.; He, N. Study on Chitosan/Polycaprolactone Blending Vascular Scaffolds by Electrospinning. *J. Biomed. Nanotechnol.* **2010**, *6*, 254–259. [CrossRef]
7. Valachová, K.; El Meligy, M.A.; Šoltés, L. Hyaluronic Acid and Chitosan-Based Electrospun Wound Dressings: Problems and Solutions. *Int. J. Biol. Macromol.* **2022**, *206*, 74–91. [CrossRef]
8. Topuz, F.; Abdulhamid, M.A.; Holtzl, T.; Szekely, G. Nanofiber Engineering of Microporous Polyimides through Electrospinning: Influence of Electrospinning Parameters and Salt Addition. *Mater. Des.* **2021**, *198*, 109280. [CrossRef]
9. Pérez-Nava, A.; Reyes-Mercado, E.; González-Campos, J.B. Production of Chitosan Nanofibers Using the HFIP/Acetic Acid Mixture as Electrospinning Solvent. *Chem. Eng. Process. Process Intensif.* **2022**, *173*, 108849. [CrossRef]
10. Alam, M.R.; Alimuzzaman, S.; Shahid, M.A.; Fahmida-E-Karim; Hoque, M.E. Collagen/Nigella Sativa/Chitosan Inscribed Electrospun Hybrid Bio-Nanocomposites for Skin Tissue Engineering. *J. Biomater. Sci. Polym. Ed.* **2023**, *34*, 1517–1538. [CrossRef]
11. Geng, X.; Kwon, O.-H.; Jang, J. Electrospinning of Chitosan Dissolved in Concentrated Acetic Acid Solution. *Biomaterials* **2005**, *26*, 5427–5432. [CrossRef] [PubMed]
12. Sohofi, N.; Tavanai, H.; Morshed, M.; Abdolmaleki, A. Electrospinning of 100% Carboxymethyl Chitosan Nanofibers. *J. Eng. Fibers Fabr.* **2014**, *9*, 155892501400900110. [CrossRef]
13. Anisiei, A.; Oancea, F.; Marin, L. Electrospinning of Chitosan-Based Nanofibers: From Design to Prospective Applications. *Rev. Chem. Eng.* **2023**, *39*, 31–70. [CrossRef]
14. Su, H.; Liu, K.-Y.; Karydis, A.; Abebe, D.G.; Wu, C.; Anderson, K.M.; Ghadri, N.; Adatrow, P.; Fujiwara, T.; Bumgardner, J.D. In Vitro and in Vivo Evaluations of a Novel Post-Electrospinning Treatment to Improve the Fibrous Structure of Chitosan Membranes for Guided Bone Regeneration. *Biomed. Mater.* **2016**, *12*, 015003. [CrossRef]
15. Su, H.; Fujiwara, T.; Anderson, K.M.; Karydis, A.; Ghadri, M.N.; Bumgardner, J.D. A Comparison of Two Types of Electrospun Chitosan Membranes and a Collagen Membrane in Vivo. *Dent. Mater.* **2021**, *37*, 60–70. [CrossRef]

16. Totito, T.C.; Laatikainen, K.; Bode-Aluko, C.; Pereao, O.; Petrik, L. Fabrication and Characterization of Electrospun Waste Polyethylene Terephthalate Blended with Chitosan: A Potential Single-Use Material. *Polymers* **2023**, *15*, 442. [CrossRef]
17. Su, H.; Fujiwara, T.; Skalli, O.; Selders, G.S.; Li, T.; Mao, L.; Bumgardner, J.D. Porous Nano-Fiber Structure of Modified Electrospun Chitosan GBR Membranes Improve Osteoblast Calcium Phosphate Deposition in Osteoblast-Fibroblast Co-Cultures. *Mar. Drugs* **2024**, *22*, 160. [CrossRef]
18. Korniienko, V.; Husak, Y.; Radwan-Pragłowska, J.; Holubnycha, V.; Samokhin, Y.; Yanovska, A.; Varava, J.; Diedkova, K.; Janus, Ł.; Pogorielov, M. Impact of Electrospinning Parameters and Post-Treatment Method on Antibacterial and Antibiofilm Activity of Chitosan Nanofibers. *Molecules* **2022**, *27*, 3343. [CrossRef]
19. Korniienko, V.; Husak, Y.; Yanovska, A.; Banasiuk, R.; Yusupova, A.; Savchenko, A.; Holubnycha, V.; Pogorielov, M. Functional and Biological Characterization of Chitosan Electrospun Nanofibrous Membrane Nucleated with Silver Nanoparticles. *Appl. Nanosci.* **2022**, *12*, 1061–1070. [CrossRef]
20. Varava, Y.; Samokhin, Y.; Savchenko, A.; Diedkova, K.; Kyrylenko, S.; Korniienko, V. Antimicrobial Electrospun Chitosan Nanofibrous Membranes Functionalized with Silver Nanoparticles. In Proceedings of the 2021 IEEE 11th International Conference Nanomaterials: Applications & Properties (NAP), Odessa, Ukraine, 5–11 September 2021; pp. 1–4.
21. Schiffman, J.D.; Schauer, C.L. Cross-Linking Chitosan Nanofibers. *Biomacromolecules* **2007**, *8*, 594–601. [CrossRef]
22. Nezarati, R.M.; Eifert, M.B.; Cosgriff-Hernandez, E. Effects of Humidity and Solution Viscosity on Electrospun Fiber Morphology. *Tissue Eng. Part C Methods* **2013**, *19*, 810–819. [CrossRef] [PubMed]
23. Qin, X.-H.; Yang, E.-L.; Li, N.; Wang, S.-Y. Effect of Different Salts on Electrospinning of Polyacrylonitrile (PAN) Polymer Solution. *J. Appl. Polym. Sci.* **2007**, *103*, 3865–3870. [CrossRef]
24. Topuz, F.; Satilmis, B.; Uyar, T. Electrospinning of Uniform Nanofibers of Polymers of Intrinsic Microporosity (PIM-1): The Influence of Solution Conductivity and Relative Humidity. *Polymer* **2019**, *178*, 121610. [CrossRef]
25. Varnaitė-Žuravliova, S.; Savest, N.; Baltušnikaitė-Guzaitienė, J.; Abraitienė, A.; Krumme, A. The Investigation of the Production of Salt-Added Polyethylene Oxide/Chitosan Nanofibers. *Materials* **2024**, *17*, 132. [CrossRef]
26. Angammana, C.J.; Jayaram, S.H. Analysis of the Effects of Solution Conductivity on Electrospinning Process and Fiber Morphology. *IEEE Trans. Ind. Appl.* **2011**, *47*, 1109–1117. [CrossRef]
27. Fong, H.; Chun, I.; Reneker, D.H. Beaded Nanofibers Formed during Electrospinning. *Polymer* **1999**, *40*, 4585–4592. [CrossRef]
28. Drew, C.; Wang, X.; Samuelson, L.A.; Kumar, J. The Effect of Viscosity and Filler on Electrospun Fiber Morphology. *J. Macromol. Sci. Part A* **2003**, *40*, 1415–1422. [CrossRef]
29. Choudhury, R.R.; Gohil, J.M.; Dutta, K. Poly(Vinyl Alcohol)-Based Membranes for Fuel Cell and Water Treatment Applications: A Review on Recent Advancements. *Polym. Adv. Technol.* **2021**, *32*, 4175–4203. [CrossRef]
30. Shin, Y.M.; Hohman, M.M.; Brenner, M.P.; Rutledge, G.C. Experimental Characterization of Electrospinning: The Electrically Forced Jet and Instabilities. *Polymer* **2001**, *42*, 09955–09967. [CrossRef]
31. Zahra, F.T.; Zhang, Y.; Ajayi, A.O.; Quick, Q.; Mu, R. Optimization of Electrospinning Parameters for Lower Molecular Weight Polymers: A Case Study on Polyvinylpyrrolidone. *Polymers* **2024**, *16*, 1217. [CrossRef]
32. Ahmadi Bonakdar, M.; Rodrigue, D. Electrospinning: Processes, Structures, and Materials. *Macromol* **2024**, *4*, 58–103. [CrossRef]
33. Nada, A.A.; James, R.; Shelke, N.B.; Harmon, M.D.; Awad, H.M.; Nagarale, R.K.; Kumbar, S.G. A Smart Methodology to Fabricate Electrospun Chitosan Nanofiber Matrices for Regenerative Engineering Applications. *Polym. Adv. Technol.* **2014**, *25*, 507–515. [CrossRef]
34. Su, P.; Wang, C.; Yang, X.; Chen, X.; Gao, C.; Feng, X.-X.; Chen, J.-Y.; Ye, J.; Gou, Z. Electrospinning of Chitosan Nanofibers: The Favorable Effect of Metal Ions. *Carbohydr. Polym.* **2011**, *84*, 239–246. [CrossRef]
35. Bizarria, M.T.M.; d'Ávila, M.A.; Mei, L.H.I. Non-Woven Nanofiber Chitosan/Peo Membranes Obtained by Electrospinning. *Braz. J. Chem. Eng.* **2014**, *31*, 57–68. [CrossRef]
36. Cheng, T.; Hund, R.-D.; Aibibu, D.; Horakova, J.; Cherif, C. Pure Chitosan and Chitsoan/Chitosan Lactate Blended Nanofibres Made by Single Step Electrospinning. *Autex Res. J.* **2013**, *13*, 128–133. [CrossRef]
37. Rieger, K.A.; Birch, N.P.; Schiffman, J.D. Electrospinning Chitosan/Poly(Ethylene Oxide) Solutions with Essential Oils: Correlating Solution Rheology to Nanofiber Formation. *Carbohydr. Polym.* **2016**, *139*, 131–138. [CrossRef]
38. Padmini Tamilarasi, G.; Sabarees, G.; Manikandan, K.; Gouthaman, S.; Alagarsamy, V.; Raja Solomon, V. Advances in Electrospun Chitosan Nanofiber Biomaterials for Biomedical Applications. *Mater. Adv.* **2023**, *4*, 3114–3139. [CrossRef]
39. Mohammad Ali Zadeh, M.; Keyanpour-Rad, M.; Ebadzadeh, T. Effect of Viscosity of Polyvinyl Alcohol Solution on Morphology of the Electrospun Mullite Nanofibres. *Ceram. Int.* **2014**, *40*, 5461–5466. [CrossRef]
40. Geltmeyer, J.; Van der Schueren, L.; Goethals, F.; De Buysser, K.; De Clerck, K. Optimum Sol Viscosity for Stable Electrospinning of Silica Nanofibres. *J. Sol-Gel Sci. Technol.* **2013**, *67*, 188–195. [CrossRef]
41. Fridrikh, S.V.; Yu, J.H.; Brenner, M.P.; Rutledge, G.C. Controlling the Fiber Diameter during Electrospinning. *Phys. Rev. Lett.* **2003**, *90*, 144502. [CrossRef]
42. Kim, B.; Park, H.; Lee, S.-H.; Sigmund, W.M. Poly(Acrylic Acid) Nanofibers by Electrospinning. *Mater. Lett.* **2005**, *59*, 829–832. [CrossRef]
43. Tan, S.-H.; Inai, R.; Kotaki, M.; Ramakrishna, S. Systematic Parameter Study for Ultra-Fine Fiber Fabrication via Electrospinning Process. *Polymer* **2005**, *46*, 6128–6134. [CrossRef]

44. Piyasin, P.; Yensano, R.; Pinitsoontorn, S. Size-Controllable Melt-Electrospun Polycaprolactone (PCL) Fibers with a Sodium Chloride Additive. *Polymers* **2019**, *11*, 1768. [CrossRef]
45. Park, Y.R.; Ju, H.W.; Lee, J.M.; Kim, D.-K.; Lee, O.J.; Moon, B.M.; Park, H.J.; Jeong, J.Y.; Yeon, Y.K.; Park, C.H. Three-Dimensional Electrospun Silk-Fibroin Nanofiber for Skin Tissue Engineering. *Int. J. Biol. Macromol.* **2016**, *93*, 1567–1574. [CrossRef]
46. Sazegar, M.; Bazgir, S.; Katbab, A.A. Preparation and Characterization of Water-Absorbing Gas-Assisted Electrospun Nanofibers Based on Poly(Vinyl Alcohol)/Chitosan. *Mater. Today Commun.* **2020**, *25*, 101489. [CrossRef]
47. Su, H.; Fujiwara, T.; Bumgardner, J.D. A Study of Combining Elastin in the Chitosan Electrospinning to Increase the Mechanical Strength and Bioactivity. *Mar. Drugs* **2021**, *19*, 169. [CrossRef]
48. Singh, Y.P.; Dasgupta, S.; Nayar, S.; Bhaskar, R. Optimization of Electrospinning Process & Parameters for Producing Defect-Free Chitosan/Polyethylene Oxide Nanofibers for Bone Tissue Engineering. *J. Biomater. Sci. Polym. Ed.* **2020**, *31*, 781–803. [CrossRef]
49. Buttafoco, L.; Kolkman, N.G.; Engbers-Buijtenhuijs, P.; Poot, A.A.; Dijkstra, P.J.; Vermes, I.; Feijen, J. Electrospinning of Collagen and Elastin for Tissue Engineering Applications. *Biomaterials* **2006**, *27*, 724–734. [CrossRef]

marine drugs

Article

# Synthesis and Characterization of a Novel Chitosan-Based Nanoparticle–Hydrogel Composite System Promising for Skin Wound Drug Delivery

**Yueying Huang [1], Shuting Hao [1], Jiayu Chen [1], Mengyuan Wang [1], Ziheng Lin [1] and Yanan Liu [1,2,3,*]**

[1] Department of Food Science and Engineering, Ningbo University, Ningbo 315800, China; huangyueyingnbu@163.com (Y.H.); 17857395807@163.com (S.H.); 18857475416@163.com (J.C.); w17858875621@163.com (M.W.); anrimoce@outlook.com (Z.L.)
[2] Ningbo Key Laboratory of Detection, Control and Early Warning of Key Hazardous Materials in Food, Ningbo Academy of Product and Food Quality Inspection, Ningbo Fibre Inspection Institute, Ningbo 315048, China
[3] College of Food Science and Technology, Nanjing Agricultural University, Nanjing 210095, China
* Correspondence: yliu98@126.com

**Abstract:** As a natural preservative, nisin is widely used in the food industry, while its application in biomedicine is limited due to its susceptibility to interference from external conditions. In this study, a nanoparticle–hydrogel composite system was designed to encapsulate and release nisin. Nisin nanoparticles were identified with a smooth, spherical visual morphology, particle size of 122.72 ± 4.88 nm, polydispersity coefficient of 0.473 ± 0.063, and zeta potential of 23.89 ± 0.37 mV. Based on the sample state and critical properties, three temperature-sensitive hydrogels based on chitosan were ultimately chosen with a rapid gelation time of 112 s, outstanding reticular structure, and optimal swelling ratio of 239.05 ± 7.15%. The composite system exhibited the same antibacterial properties as nisin, demonstrated by the composite system's inhibition zone diameter of 17.06 ± 0.83 mm, compared to 20.20 ± 0.58 mm for nisin, which was attributed to the prolonged release effect of the hydrogel at the appropriate temperature. The composite system also demonstrated good biocompatibility and safety, making it suitable for application as short-term wound dressings in biomedicine due to its low hemolysis rate of less than 2%. In summary, our nanoparticle-based hydrogel composite system offers a novel application form of nisin while ensuring its stability, thereby deepening and broadening the employment of nisin.

**Keywords:** nisin; nanoparticles; thermo-sensitive hydrogels; composite drug delivery system; bacteriostasis

## 1. Introduction

Nisin is the only bacteriocin in the world that is permitted as a food additive, owing to its GRAS (Generally Regarded as Safe) status approved by the WHO and FDA [1,2]. Nisin, one of the metabolites of *Lactococcus lactis*, is a natural antimicrobial with broad-spectrum antibacterial activity, which is commonly employed in food preservation [3]. In the process of its extensive application, some characteristics of nisin that hinder its effectiveness have gradually emerged, including susceptibility to external environment interference leading to loss of antibacterial activity, susceptibility to hydrolysis by proteolytic enzymes, and poor stability under certain pH conditions [4,5]. Furthermore, nisin has been reported to play a role in immunological modulation, but due to the aforementioned characteristics, little information is available regarding its application in biomedicine [6,7]. Many efforts have been made to ensure the stability of nisin and extend its application. Many methods have been developed to modify and encapsulate it, such as hybridization with active substances or grafting of active groups [8,9], conjugation with polymers [1,10], preparation of encapsulated sustained-release systems [6,11,12], etc.

Nisin is often utilized in the food sector as films or nanofibers for incorporation into food packaging [13,14]. Although nisin currently has fewer biomedical applications than food applications, existing data show that it is mostly utilized in biological dressings and drug delivery systems [15]. At present, there is significant interest in the encapsulation and delivery system of active substances as a research topic, primarily due to its advantages of local drug delivery, ensuring the activity of substances, and high safety [16,17]. The inhibitory mechanism of nisin in destroying the bacterial cell wall demonstrates that moderate contact with the bacteria is essential to suppress its activity, which means that a delivery system capable of stabilizing and releasing it as needed is required [6]. In addition, biomedical applications necessitate delivery mechanisms with high safety and biocompatibility. The application of nanotechnology has achieved remarkable success in enhancing the antibacterial property and stability of nisin as well as the ability to achieve prolonged release, which has been widely used in the food industry [18,19]. However, its use in biomedicine is currently limited due to a scarcity of closed carriers that can make contact with humans. Another typical application is the direct use of nisin to produce hydrogels, which has stringent criteria for the many components involved [20,21]. All elements that influence the activity of nisin must be considered while designing the product. Thus, the nanoparticle–hydrogel composite system is an appropriate form of nisin for biomedical purposes. To date, many studies have been carried out on nanoparticle–hydrogel composite systems, but the encapsulation of nisin in this system has not been documented [22–24].

Chitosan (CS), a product derived from the deacetylation of chitin from marine arthropods, is a natural cationic polymer with good degradability and biocompatibility and is widely used in delivery systems such as hydrogels and nanoparticles [25]. $\gamma$-Polyglutamic acid ($\gamma$-PGA) is a natural polymer with excellent hydrophilicity, biocompatibility and safety. Due to the presence of carboxyl groups, the negatively charged $\gamma$-PGA is able to provide multiple cation-binding sites in aqueous solution, a phenomenon that has been used in nanoencapsulation, self-assembled hydrogels, and other applications [26,27]. There are many cases of synthesizing nanoparticle drug delivery systems using ionic interactions between polymer CS and $\gamma$-PGA, mainly relying on the interaction between $-NH4^+$ in CS and $-COO^-$ in $\gamma$-PGA, which leads to spontaneous cross-linking to form nanoparticles [28,29]. In addition to this, CS is able to cross-link with other substances to form hydrogel encapsulation systems. Nisin Z, one of the variants of nisin, is an amphiphilic small molecule peptide with strong inhibitory effects on Gram-positive bacteria, and has also been reported to inhibit certain Gram-negative bacteria [30–32]. It has been reported that nisin Z can be extracted from a wide range of lactic acid bacteria strains, e.g., wild strains, strains isolated from marine organisms, etc. [33,34]. Nisin Z also has a wide range of applications, and is capable of assisting aquatic organisms in resisting pathogenic bacteria, in addition to food preservation and preservation [35,36]. Nisin Z is positively charged in aqueous solution and thus is able to bind to negatively charged $\gamma$-PGA via electrostatic interactions, while $-COO^-$ on the surface of the $\gamma$-PGA is able to further cross-link with CS to form nanoparticles [37]. The nanoparticles are positively charged by chitosan encapsulation, and can be loaded onto supportive hydrogels in order to realize multi-environmental applications. Nanoparticles synthesized using nisin Z and pectin, as reported previously, exhibited a low PDI and high potential value, indicating a strong interaction [38]. However, CS can only be solubilized in an acidic environment, which have been reported to also promote the dissolution and encapsulation of nisin Z [18,39,40]. Therefore, we selected CS as the main constituent of the composite material.

In this study, we used a thermo-sensitive hydrogel based on CS to encapsulate nanoparticles (NPs) made of CS, $\gamma$-PGA, and nisin Z. Following this approach, we created an encapsulating, sustained-release, and biocompatible nanoparticle–hydrogel composite system. The surface properties of the nanoparticles are important factors in the formation of composite systems [41]. Particle characteristic parameters, such as the particle size, potential, and polydispersity coefficient, reflected the appropriate particle volume and agglomeration degree of nanoparticles. SEM was used to examine the appearance and conditions of the particles, corresponding to the particle properties. Accordingly, a series of characterizations were performed to assess the properties of the NPs. In addition, the composition of the hydrogel was also optimized to make the hydrogel more compatible with the NPs. The groups with better performance were comprehensively selected as carriers according to a series of characterization results, particularly microstructure, sustained release effect, and swelling performance. This study focused on the antimicrobial properties and biocompatibility of the composite system, which will be evaluated and predicted for applications in biomedicine and other fields.

## 2. Results and Discussion

### *2.1. Characterization of Nanoparticles*

### 2.1.1. Properties of Particles

NPs with concentrations of 3, 4, and 5 mg/mL of nisin Z in the final NPs solution were prepared to determine the particle characteristics. As seen in Figure 1a, the nanoparticle sizes at the three concentrations of nisin Z were concentrated between 100 and 200 nm, with nanoparticles with concentrations of 3 and 4 mg/mL of nisin Z showing a small amount of concentrated distribution between 10 and 100 nm. As shown in Table S1, the distribution of nanoparticles with nisin Z concentrations of 5 mg/mL was more uniform for minimum PDI; therefore, it was selected as the loaded particles for the composite system. The average hydrodynamic diameter of nanoparticles with nisin Z concentrations of 5 mg/mL was 122.72 ± 4.88 nm (mean ± SD) and the PDI was 0.473 ± 0.063, demonstrating a minor state of aggregation. The obtained zeta potential of 23.89 ± 0.37 mV indicates that the surface of the nanoparticles was positively charged and had a certain level of stability. The surface conditions of the NPs were observed and photographed using SEM. Figure 1b shows the smooth surface and spherical shape of the NPs. As shown in Figure 1c, the shape of the NPs changed slightly after being loaded into the hydrogel, showing signs of extrusion or entanglement. In summary, our NPs have good surface properties and particle properties, providing an excellent basis for the formation of composites, though further design and optimization are still needed for both NPs and hydrogels to maintain the same excellent properties.

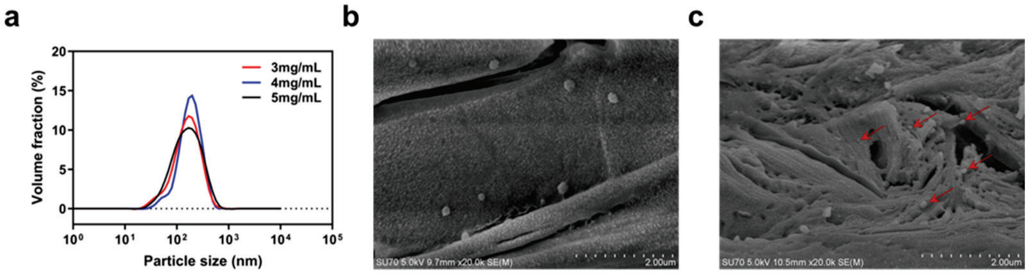

**Figure 1.** Properties of particles. (**a**) the particle size of nanoparticles with nisin Z concentration of 3, 4, and 5 mg/mL in the final solution, (**b**) SEM of NPs, (**c**) SEM of NPs in freeze-dried nanoparticle–hydrogel composite system. The NPs that were loaded on the hydrogel are indicated by the red arrows in the figure. Scale bar: 2 µm.

### 2.1.2. Entrapment Efficiency of Nisin Z

Previous reports have shown that the encapsulation efficiency of nisin Z in nanoparticles gradually decreases with an increasing nisin Z concentration. The measured encapsulation efficiency of nanoparticles with nisin Z concentrations of 3, 4, and 5 mg/mL was approximately 80%, and it increased with the increase of nisin Z concentration in our experiment. The encapsulation efficiency of the nanoparticles containing 5 mg/mL nisin Z was 86.18%, indicating a good encapsulation effect. The reason for this phenomenon in this experiment is related to the acidic environment to which nisin Z is exposed. It has been reported that the solubility of nisin Z is related to the pH [39]. Studies have shown that the solubility of nisin Z is higher under acidic conditions, and the corresponding encapsulation efficiency is also higher [18,40]. In the preparation of nanoparticles, the solution is acidic due to the presence of acetic acid, with a pH of approximately 3.40, thus providing suitable environmental conditions for the maximum encapsulation of nisin Z. The encapsulation efficiency of a previously reported nisin Z nanoparticle for beef preservation was 86.6%, demonstrating an excellent preservation effect [42]. In terms of the encapsulation effect, our nanoparticles remain at the same gradient as those in previous studies, which is critical for subsequent activation. The loading capacity of NPs with 5 mg/mL of nisin Z in the final solution was 59.35%, and the loading capacity of NPs with 3 mg/mL and 4 mg/mL of nisin Z in the final solution was 37.16% and 44.08%, respectively. The degree of superiority in the loading capacity results for each NP sample is consistent with the encapsulation rate. Accordingly, the weight percentage of other substances in each NPs can be analyzed. The mass percentage of CS and $\gamma$-PGA in the NPs with a concentration of 5 mg/mL of nisin Z in the final solution was 40.65%. In the NPs with 3 mg/mL and 4 mg/mL of nisin Z in the final solution, it was 62.84% and 55.92%, respectively.

## *2.2. Characterization of Hydrogel and Composite*

### 2.2.1. Choosing the Best Formula

In this study, the effects of time, temperature, and raw material ratio were investigated to select better hydrogels. We also compared the effects of two groups of CS with different molecular weights. Figure 2 shows the state change and final state diagram of each group of samples as the temperature rises from 5 °C to 55 °C. The color (from gray to black) represents the gradual weakening of the fluidity of the samples; that is, gray represents the solution state, and black represents the gel state without fluidity. The two types of CS with different molecular weights showed similarities in terms of the influence of the raw material ratio. When the content of β-Glycerol phosphate disodium salt (β-GP) was low, the fluidity did not change with the increase in temperature. When the β-GP content was high, the fluidity of the sample decreased slightly with an increase in temperature and then remained stable, but no gel change occurred. When the ratios of CS with molecular weight of 100 kDa ($CS_{100}$) to β-GP were 8:2 and 7:3, the temperature-sensitive gel phenomenon occurred; the same occurred when the ratio of CS with molecular weight of 500 kDa ($CS_{500}$) to β-GP was 8:2. According to the data on the time required for gelation at 37 °C, the above three groups completed gelation within 5 min; additionally, the time required for gelation gradually decreased with the increase in temperature. Similarly, studies have investigated the effect of CS and β-GP concentrations on gelation, with the results showing that when the concentration of β-GP was 3% (*w*/*v*), the gelation phenomenon occurred within 0.5–1% (*w*/*v*) of CS concentrations. This result is consistent with our study, and gelation of CS and β-GP can only occur within the appropriate dosage range [43]. Three groups of samples ($Gel_{100\text{-}73}$, $Gel_{100\text{-}82}$, and $Gel_{500\text{-}82}$) capable of temperature-sensitive gelation were preliminarily investigated, and subsequent studies were conducted on the basis of these samples to further compare the performance differences.

### 2.2.2. Rheological Characterization

The time and temperature of gelation were redetermined through time and temperature scanning using rheology. The storage modulus and loss modulus exhibited variations with the passage of time or increase in temperature, while the point of intersection between these two curves indicated the respective gelation time and gelation temperature (Figure 3). In the time-scanning process, $Gel_{500\text{-}82}$ first underwent gelation for approximately 1 min and 52 s, and its storage modulus reached a high, stable value within 5 min of gelation, relating to the gel strength. The gelation times of $Gel_{100\text{-}73}$ and $Gel_{100\text{-}82}$ were relatively close, as can be seen from the temporal scan detail map; $Gel_{100\text{-}73}$ gelation occurred at approximately 4 min and 5 s, and $Gel_{100\text{-}82}$ gelation occurred at approximately 3 min and 42 s (Figure 3b). Similar to the results of previous experiments, all of our gel samples were able to undergo gelation within a short time [44]. $Gel_{500\text{-}82}$ was also the first to undergo gelation transition at approximately 28.24 °C in the temperature scanning process. The gelation temperature point of $Gel_{100\text{-}82}$ was 31.56 °C, while that of $Gel_{100\text{-}73}$ was 38.56 °C

(Figure 3d). Under the influence of temperature change, the modulus change curve of the sample shows a small fluctuation, likely associated with the environment or equipment, especially for Gel$_{100\text{-}73}$. Small fluctuations had little effect on the measurement of the experimental results, but they were sufficient to reflect the significant influence of temperature change on the sample state, further verifying the temperature responsiveness of the hydrogel. The results obtained from the rheological experiments were consistent with those obtained when the gel effect was investigated. Additionally, our samples exhibited a more sensitive temperature response with the same gelation time as previous hydrogels of the same type [44,45]. The rapid gelation of the above samples at approximately the physiological temperature of the human body (37 °C) provides a prerequisite for their wide application in biomedicine. The time scans of each composite (Figure 3e,f) showed that the addition of NPs did not have significant effect on the gelation time, and each sample was still able to gel within 5 min. However, due to the more complex composition, the gel temperature of the composites in Figure 3g,h showed an increase, and the temperature scanning curves showed small fluctuations. The gel temperature of Gel$_{100}$-$_{73}$/NPs even exceeded 40 °C, which is still considered to be suitable for biological excipients.

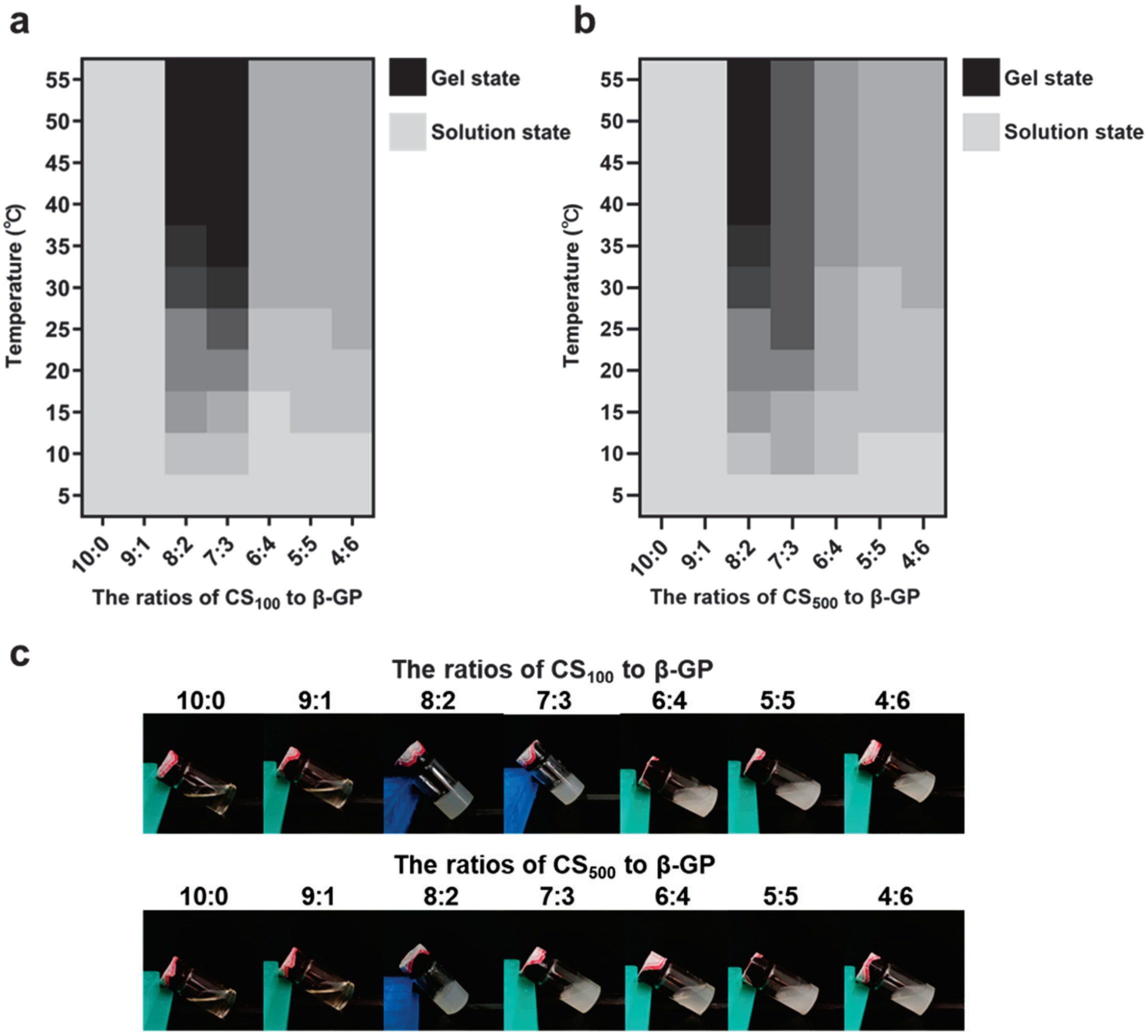

**Figure 2.** Schematic of optimal formulation selection. (**a**) gel condition of each sample of CS$_{100}$ as a function of temperature, (**b**) gel condition of each sample of CS$_{500}$ as a function of temperature, (**c**) schematic representation of the gel state of each sample.

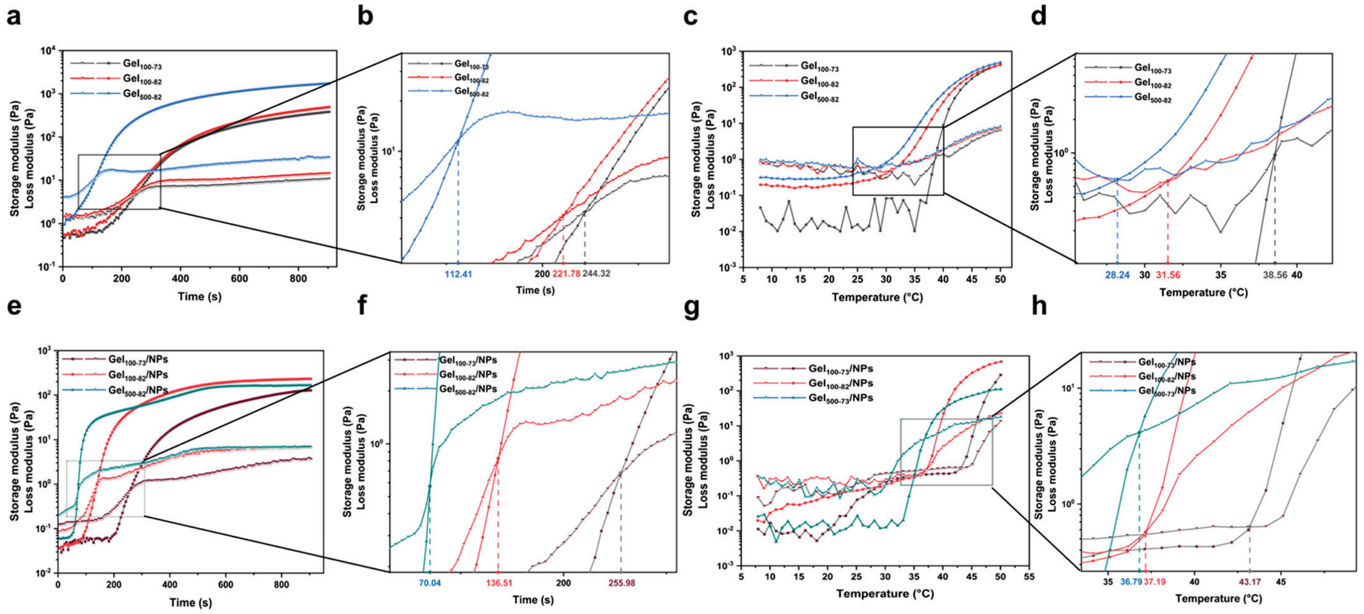

**Figure 3.** Storage modulus (G′) and loss modulus (G″) of the samples. (**a**) time scanning of gel samples, (**b**) detail map of time scanning of gel samples, (**c**) temperature scanning of gel samples, (**d**) detail map of temperature scanning of gel samples, (**e**) time scanning of composite samples, (**f**) detail map of time scanning of composite samples, (**g**) temperature scanning of composite samples, (**h**) detail map of temperature scanning of composite samples.

### 2.2.3. FTIR Characterization

The gel formation mechanism can be clearly observed in the FTIR characteristic curve. The FTIR results obtained were identical to those obtained in previous hydrogel experiments [44,46]. The stretching of -OH and -NH corresponded to the strong and wide overlapping peak at 3450 cm$^{-1}$ in the infrared spectrum of CS$_{100}$, and the band at 1657 cm$^{-1}$ was attributed to the bending vibration of -C=O (Figure 4a). The peak of the infrared spectral line of CS$_{500}$ was similar to that of CS$_{100}$ (Figure 4b). For β-GP, the peak of stretching -OH was found at 3273 cm$^{-1}$. The asymmetric stretching vibration of -PO$_4^{3-}$ appeared at 1095 cm$^{-1}$, and the symmetrical stretching vibration peak of -PO$_4^{3-}$ was observed at 977 cm$^{-1}$. The overlapping peaks of stretching -OH and -NH can also be seen on the bands of gel samples. However, the electrostatic interaction between -PO$_4^{3-}$ and -NH caused the peak shape and corresponding wavelength of the peak tip to change slightly. The characteristic peaks of -PO$_4^{3-}$ on the bands of the gel samples coincided with those of β-GP. Moreover, the small magnitude of the shift exhibited by the peak of -C=O may be caused by the formation of hydrogen bonds during gelation.

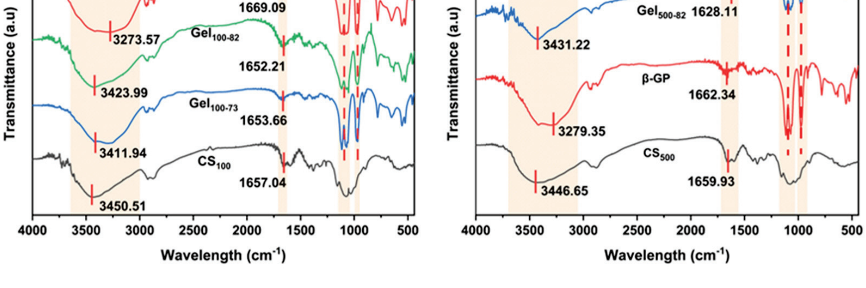

**Figure 4.** FTIR spectrogram of samples of the CS$_{100}$ progenitor (**a**) and the CS$_{500}$ progenitor (**b**).

### 2.2.4. Microstructure

The morphology and microstructure of each cryogel and freeze-dried composite can be seen in the SEM images. Cryogels and freeze-dried composites were obtained from original samples by freeze-drying, and the structures were related to the expected structure of the hydrogels and composites. As shown in Figure 5, each sample has a network structure distinguished by the size and degree of porosity, which is in agreement with published results [46]. Gel$_{100\text{-}73}$ had large and loose pores with an overall elongated appearance (Figure 5a). The network structures of Gel$_{100\text{-}82}$ and Gel$_{500\text{-}82}$ were relatively dense, and their pores were small and nearly circular (Figure 5b,c). In contrast, the pores of Gel$_{500\text{-}82}$ were slightly smaller than those of Gel$_{100\text{-}82}$, which may be related to the larger molecular weight of CS$_{500}$. The large molecular weight determines the relatively long molecular chain of CS$_{500}$, leading to enhanced intermolecular interaction forces (hydrogen bonding and hydrophobic interactions). This is the same principle as that in a study in which the introduction of titanium (Ti) assisted in the enhancement of gel strength [47]. The SEM images of each composite (Figure 5d–f) presented similar results to the SEM images of the corresponding hydrogels, with little variation in the grid size of the gel organization; however, the grid structure of Gel$_{100\text{-}73}$/NPs and Gel$_{100\text{-}82}$/NPs was not as pronounced as that of the corresponding hydrogel samples due to the influence of the surface charge of the NPs. The microstructure of the group without gelation showed neatly arranged fibers, without obvious reticular structures or complex winding structures (Figure 6). This indicated that, in the group without gelation, the addition of β-GP formed a hydration layer around the CS molecules; thus, the molecular chains originally in the entangled state were extended and arranged in order, but no cross-linking occurred under the effect of temperature or no network structure was formed after cross-linking.

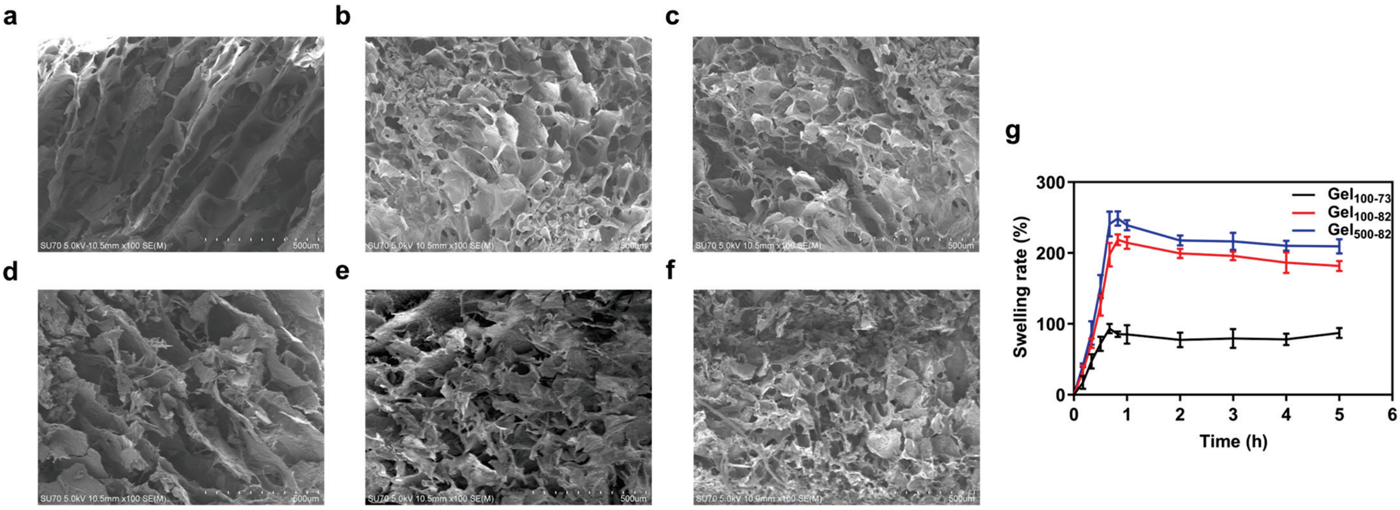

**Figure 5.** SEM of Gel$_{100\text{-}73}$ (**a**), Gel$_{100\text{-}82}$ (**b**), and Gel$_{500\text{-}82}$ (**c**) SEM of Gel$_{100\text{-}73}$/NPs (**d**) Gel$_{100\text{-}82}$/NPs (**e**) and Gel$_{500\text{-}82}$/NPs (**f**) and swelling rate of gel samples (**g**). Scale bar: 500 μm.

### 2.2.5. Swelling Ratios

The swelling rate is commonly used to measure the degree of water absorption and swelling of hydrogels which, to a certain extent, determines the application field and specific use of hydrogels [48,49]. Gel$_{100\text{-}73}$ and Gel$_{100\text{-}82}$ reached the maximum swelling rate at around 50 min. Gel$_{500\text{-}82}$ reached the maximum swelling rate at around 40 min. The swelling rate of the gel samples rapidly reached the maximum value within 1 h and then gradually stabilized (Figure 5g). Both Gel$_{100\text{-}82}$ and Gel$_{500\text{-}82}$ had a maximum swelling of more than twice the original mass, at 220.54 ± 6.20% and 248.55 ± 10.02%, respectively, indicating excellent swelling efficiency. The swelling rate of Gel$_{100\text{-}73}$ was relatively small but also close to 100%. An excellent swelling effect indicates that the hydrogel has a strong water-holding capacity (WHC), which enables the hydrogel to provide a moist environment for the surrounding contacts. At the same time, correlating with the SEM images of the samples, it can be inferred that the WHC of the loosely structured reticular structure is not as good as that of the tightly structured reticular structure [45]. Similar to the previous results of Bhuiyan et al., the change in the CS ratio is also one of the factors affecting the swelling rate [43]. The increase in the CS ratio contributes to an increased swelling ratio, likely because the introduction of the polar groups generates a more hydrophilic chemical structure.

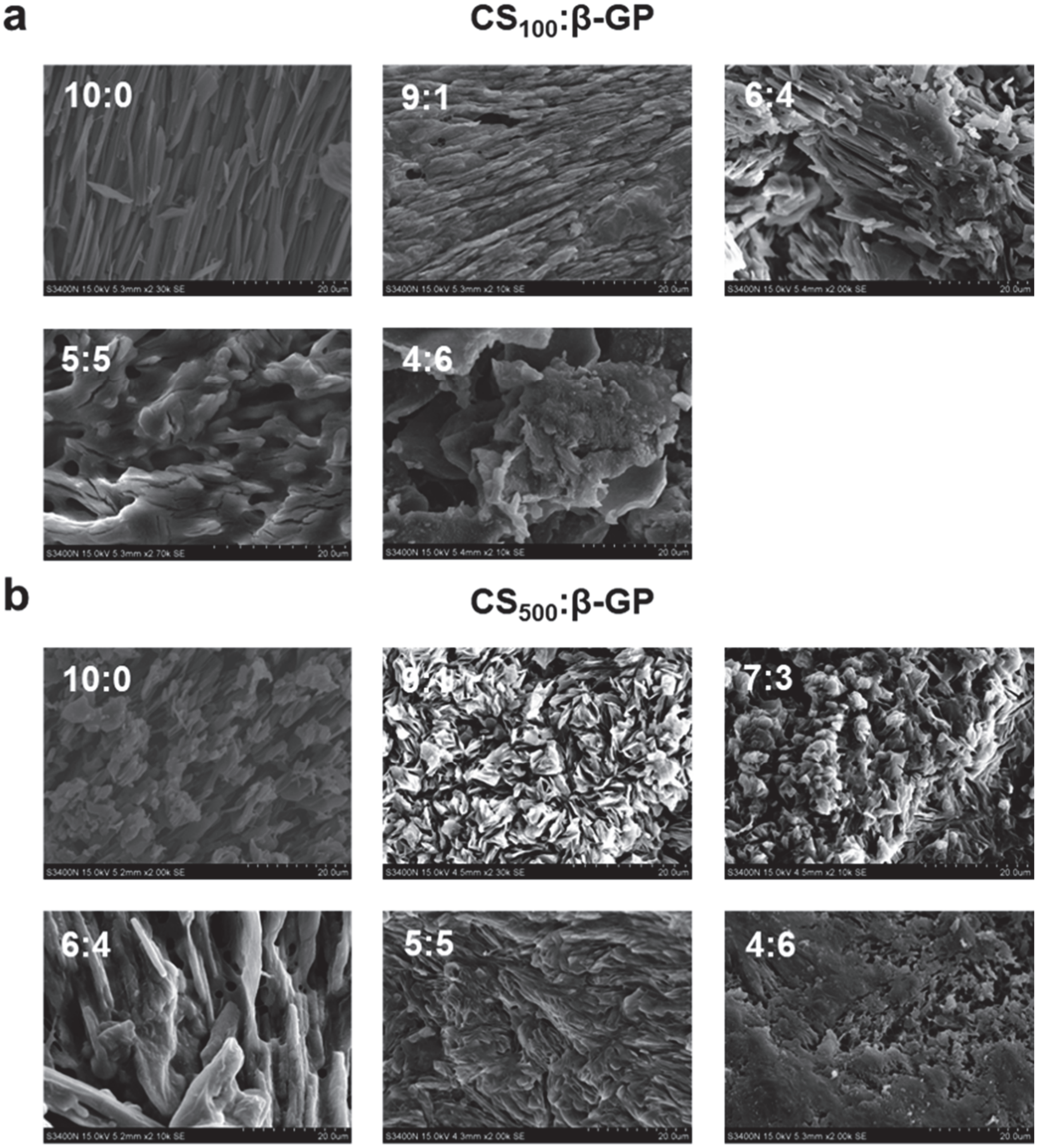

**Figure 6.** SEM of the non-gel group of $CS_{100}$ (**a**) and $CS_{500}$ (**b**). Scale bar: 20 μm.

### 2.2.6. In Vitro Release Assays

The composite system released nisin Z into the PBS solution it was in contact with, and the release efficiency was determined using the BCA method. The experimental results show that the nisin Z release rate of the sample reached the maximum within

24 h, after which the nisin Z was released steadily (Figure 7a). It is worth noting that the release rate of $Gel_{100\text{-}82}$ was always higher than that of $Gel_{100\text{-}73}$ and $Gel_{500\text{-}82}$, finally reaching 20.09 ± 1.68%. The release rates of $Gel_{100\text{-}73}$ and $Gel_{500\text{-}82}$ ultimately stabilized at 18.43 ± 0.47% and 19.16 ± 0.57%, respectively. Compared with complexes reported in the literature, the release rates of our samples were low [50,51]. The method used in the release rate calculation was based on the entrapment efficiency of nanoparticles. However, some nisin Z may remain on the surface of the NPs and be bound by intermolecular forces, resulting in a high encapsulation efficiency. This part of nisin Z is also unable to be subsequently released from the gel tissue, thus resulting in a low overall release rate from the sample. The low level and sustained drug release efficiency are more suitable for use in situations where tight control of the drug concentration is required. The ophthalmic drug delivery system developed by Hsu et al. exploited this property [52].

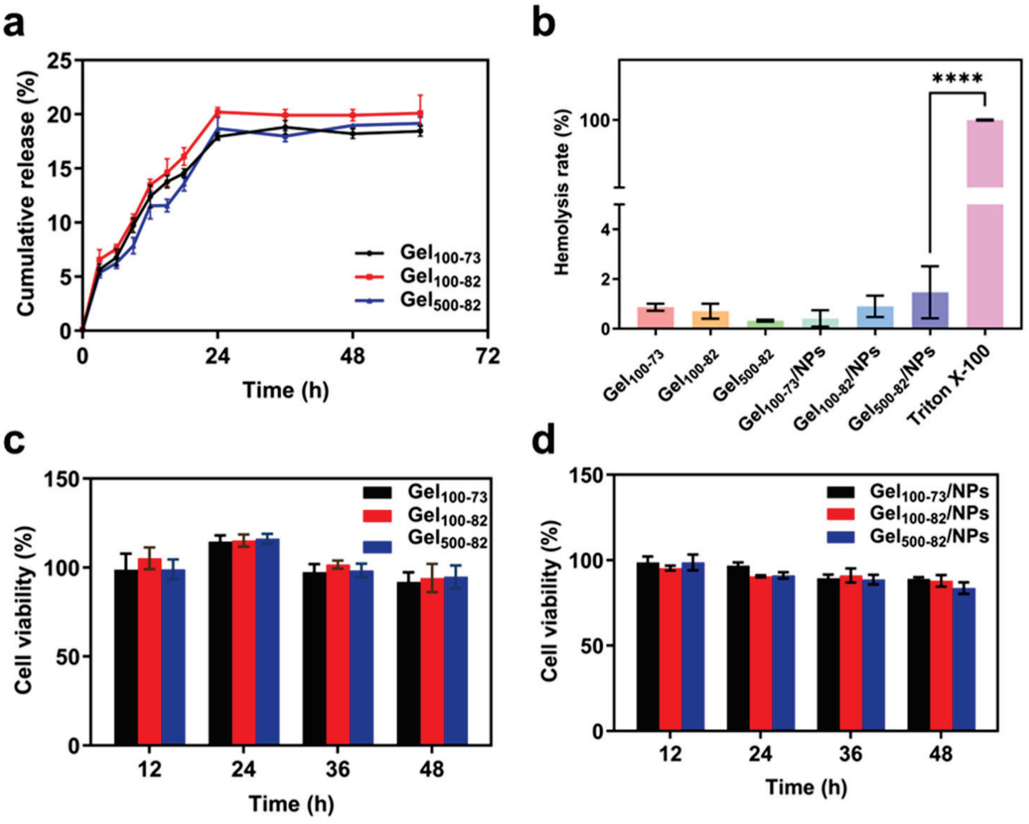

**Figure 7.** Characterization of nanoparticle–hydrogel composite system. (**a**) efficiency of nisin Z release from $Gel_{100\text{-}73}$, $Gel_{100\text{-}82}$, and $Gel_{500\text{-}82}$, (**b**) hemolysis rate of samples, (**c**) in vitro toxicity of gel samples, (**d**) in vitro toxicity of gel composite system. **** $p < 0.0001$ indicates significant differences between samples and Triton X-100 control group.

### 2.2.7. In Vitro Toxicity Assays

For the toxicity experiment, the CCK-8 method was used to explore the cytotoxicity of the samples. The cytotoxicity levels of materials are generally classified into four grades: grade 0 (no cytotoxicity, cell viability ≥ 100%), grade 1 (mild cytotoxicity, cell viability ranging from 75% to 99%), grade 2 (moderate cytotoxicity, cell viability ranging from 50% to 74%), and grade 3 (severe cytotoxicity, cell viability ranging from 25% to 49%) [50,51]. The cell viability of the hydrogel samples was more than 100% when they were in contact with the cells for 24 h (Figure 7c). With the extension of time, the cell survival rate decreased, but it was still grade 2 with a level of mild cytotoxicity. The cell viability of the composite systems showed a decreasing trend with the extension of time, which may be related to the introduction of antimicrobial peptides (Figure 7d). However, the overall level was still maintained at grade 2, showing great biocompatibility. Compared to the complex encapsulated with inorganic nanoparticles, our material presents lower cytotoxicity, correlated with the safety of nisin Z [53]. The cytotoxicity of previously developed composites utilized in wound dressings is equivalent to that of this product, which is a decisive factor of the material as a wound dressing [54,55].

### 2.2.8. Hemolysis Evaluation

The hemolysis rate is an important factor in evaluating the biocompatibility of materials, which represents the degree of damage to erythrocytes. To a certain extent, the lower the hemolysis rate, the safer the material, as hemolysis will not occur when the blood is in contact with the material [56]. It can be seen from Figure 7b that the hemolysis rate of each gel sample and composite system was lower than 2%, and there was no significant difference between the samples. Previous materials typically used 5% as a critical point for the hemolysis rate; from this point of view, our materials have the safety and biocompatibility required for biological dressings [51]. In practical application, the effects of endogenous and exogenous factors on the hemolysis rate should be comprehensively considered. The ability of our material to provide a low hemolysis rate at the point of use enhances the tolerance to hemolysis caused by internal factors.

### 2.2.9. In Vitro Antibacterial Characterization

The antibacterial activity of the samples was evaluated using the inhibition zone and colony counting method. As shown in Figure 8b, neither the hydrogel nor the complex exhibited antibacterial properties against *E. coli*. According to previous studies, nisin Z is able to inhibit Gram-positive bacteria by forming membrane channels with them, leading to the efflux of cellular contents. However, nisin Z is usually unable to form membrane channels on the surface of Gram-negative bacteria and needs to disrupt the cellular membranes with the help of other active substances before exerting an inhibitory effect through the outer membranes [57–59]. $\text{Gel}_{100\text{-}73}$ and each complex exhibited significant inhibitory effects against *S. aureus*, with the diameter of the zone of inhibition for each complex against *S. aureus* provided in Table S2. The results of the colony counting method also showed the same antibacterial effect (Figure 8a). There was no significant difference in the number of *E. coli* colonies on the serial dilution plates, but the inhibitory effect on *S. aureus* was more obvious at a $10^3$-fold dilution. In Figure 8c, the antibacterial effect of the nisin Z solution and NPs is also shown, and it can be observed that the antibacterial effect of the above complex mainly comes from nisin Z. The antibacterial properties of $\text{Gel}_{100\text{-}73}$ may be related to those of the CS [60–62]. Furthermore, $\text{Gel}_{100\text{-}82}$ and $\text{Gel}_{500\text{-}82}$ showed similar dense reticulation structures in SEM results. Combined with this, we envisioned that the failure of both $\text{Gel}_{100\text{-}82}$ and $\text{Gel}_{500\text{-}82}$ to inhibit *S. aureus* could also be due to their overly dense structures, which blocked the inhibitory sites of chitosan in the hydrogels. *S. aureus* is a common foodborne pathogen that also poses a great risk in human wounds and disease infection. The complex shows an excellent inhibitory effect against *S. aureus*, and the loaded antimicrobial peptides can also avoid drug resistance, which has great application prospects in biology [63]. A recently reported nisin nanoparticle pre-formulation, with improved antibacterial effects encapsulated with a special material, has a similar effect to our material [64]. The nano-encapsulation technology significantly enhances the antibacterial efficacy of active substances, thereby ensuring their effectiveness and potentially even improving it. Another experiment utilizing nisin as a gel coating further substantiated its antibacterial efficacy [65]. This investigation not only validated the functionality of NPs but also provided evidence for the encapsulation and subsequent release of NPs via hydrogel.

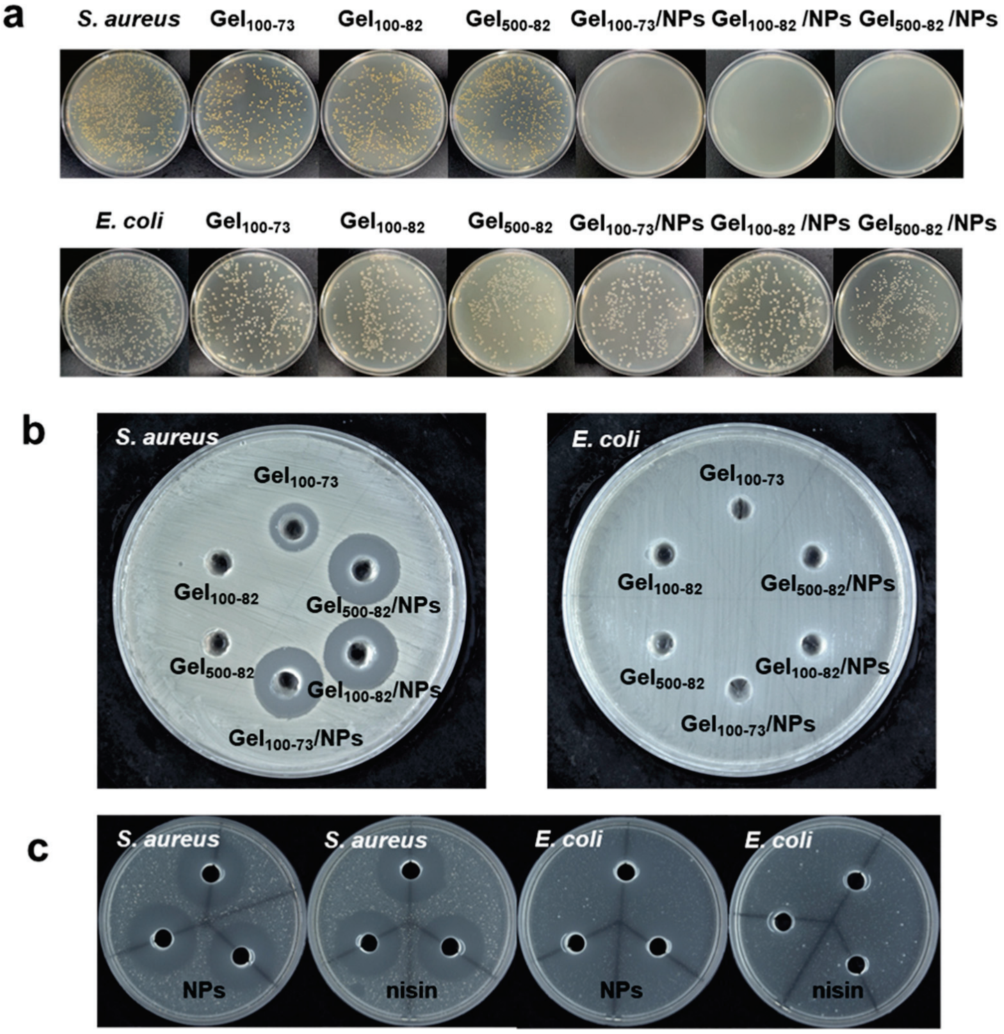

**Figure 8.** Antibacterial properties of the material. (**a**) results of plate count assay for the inhibition of samples against *S. aureus* and *E. coli*, (**b**) results of inhibition zone test of samples against *S. aureus* and *E. coli*, (**c**) Inhibition zone results of NPs and nisin Z against *S. aureus* and *E. coli*.

## 3. Materials and Methods

### 3.1. Materials

For this study, the supplier of nisin (3%) was CHIHONBIO Co., Ltd. (Luoyang, China), and its specific species was nisin Z. $\gamma$-Polyglutamic acid (MW > 700 kDa) was provided by Shanghai Yongchuan Biotechnology Co., Ltd. (Shanghai, China). Chitosan and $\beta$-Glycerol phosphate disodium salt ($\beta$-GP, purity > 95%) were purchased from Shanghai Yongchuan Biotechnology Co., Ltd. (Shanghai, China). The molecular weights of CS were 100 (degree of deacetylation 85%) and 500 (degree of deacetylation 80%) kDa, denoted as $CS_{100}$ and $CS_{500}$, respectively. The hydrochloric acid (37%) used in the experiment was provided by the Hazardous Chemicals Management Department of Ningbo University, and substances, such as acetic acid glacial (99.5%), PBS buffer, and paraffin oil (99%) were also provided by Shanghai Yongchuan Biotechnology Co., Ltd. (Shanghai, China).

### 3.2. Synthesis of Nanoparticles

The synthesis of nanoparticles employed a modified approach based on previous methods [66]. After being dialyzed and freeze-dried for 24 h using a SCIENTZ-18N freeze-dryer, purchased from Ningbo Scientz Biotechnology Co., Ltd. (Ningbo, China), the purchased nisin Z samples were stored in a refrigerator at 4 °C for future use. For the synthesis of nanoparticles, the nisin Z aqueous solution was filtered through a disposable

0.22 μm membrane and then progressively added to the equivalent volume of a γ-PGA solution (4 mg/mL) and stirred for 30 min. $CS_{100}$ was added to an acetic acid solution (1%, *v*/*v*) to form a 2 mg/mL chitosan acetate solution and agitated at room temperature until completely dissolved. The specific proportions of the various substances are detailed in Table S3. The mixed solution with nisin Z and γ-PGA was added dropwise to the acetic acid solution of $CS_{100}$ and stirred overnight. It was then briefly homogenized using a handheld homogenizer and filtered through a disposable 0.22 μm membrane to obtain the NPs solution.

### 3.3. Zetasizer Particle Characterization

A Malvern Zetasizer Advance Series Lab (Malvern Panalytical, Malvern, UK) was used to measure the nanoparticle size, zeta potential, and polydispersity index (PDI). The nanoparticle size and polydispersity index were determined at 25 °C and a 173° scattering angle in a disposable cell (DTS0012) [67]. Similarly, potential measurements were also conducted in a specific sample dish (DTS1070). To ensure that the resultant values were within the confidence interval, the nanoparticle solution was diluted 5-fold using ultrapure water before measurement. The measurements were repeated three times for each sample.

### 3.4. Entrapment Efficiency of Nisin Z

Inspired by the prior approach of testing the encapsulation efficiency of gel beads, in this experiment, we permitted the unencapsulated nisin Z to enter the dialysate from the nanoparticle solution via dialysis and then utilized an Enhanced BCA Protein Assay Kit (Beyotime Biotechnology, Shanghai, China) to quantify the concentration of nisin Z in the dialysate [68]. The encapsulation rate of nisin Z was estimated using the following Equation (1). Dialysate of *n* times the volume of the nanoparticle solution was added to the dialysis vessel to facilitate calculation of the results. At the same time, we dried and weighed the NPs and calculated the loading capacity of each NPs sample for nisin Z according to the following Formula (2). The experiment was repeated to obtain three readings.

$$Entrapment\ efficiency\ (\%) = \frac{Total\ nisin\ Z\ concentration - Unencapsulated\ nisin\ Z\ concentration}{Total\ nisin\ Z\ concentration} \times 100 \quad (1)$$

$$Loading\ capacity(\%) = \frac{Total\ mass\ of\ nisin\ Z - Unencapsulated\ nisin\ Z\ mass}{Total\ mass\ of\ NPs} \times 100 \quad (2)$$

### 3.5. Preparation of Hydrogel and Nanoparticle–Hydrogel Composite System

We drew on previous ice bath methods for hydrogel fabrication [69] to identify the optimal ratios for achieving a temperature response hydrogel in subsequent experiments. A quantity of CS was weighed and added to a 0.1 mol/L hydrochloric acid solution with simultaneous magnetic stirring to prepare a hydrochloric acid solution with a CS concentration of 2% (*m*/*v*). It was mixed at room temperature until completely dissolved, then sterilized and stored in a refrigerator at 4 °C. An appropriate amount of β-GP was dissolved in sterile water to obtain a 45% (*m*/*v*) aqueous solution of β-GP, followed by its filtration through a 0.22 μm disposable sterile needle filter membrane. To create a clear and uniform CS/β-GP combination, the 45% aqueous β-GP solution was added dropwise to the 2% CS solution and stirred continuously in an ice bath for 30 min. The mixture was then incubated in a water bath for a set amount of time at a suitable temperature to form a hydrogel.

In preparing the composites, the CS/β-GP mixture was first stirred in an ice bath for 30 min according to the above steps. Next, the NPs solution was added drop by drop to the CS/β-GP mixture under ice bath conditions. To ensure uniform distribution of NPs, the mixture was again stirred in an ice bath for 30 min. Then, the nanoparticle–hydrogel composite system can be generated following further water bath incubation [70].

### 3.6. Determination of the Optimal Ratio of Gel Components

Two molecular weights ($CS_{100}$ and $CS_{500}$) of CS were selected, and the ratio of CS to β-GP was adjusted to investigate the optimal gel composition. Provided that the total volume was the same, the volume ratios chosen for the experiment were 10:0, 9:1, 8:2, 7:3, 6:4, 5:5, and 4:6. Preliminarily, the gel environment temperature was set at 37 °C, with a total testing duration of 15 min [71]. The group with the best gelation was selected visually using the inversion method, which involved inverting the container every 30 s for 15 min to observe the fluidity of each sample, determine whether gelation occurred, and document the time it took for gelation. In addition, the gelation state of the sieved groups at various temperatures was recorded to observe the transition from solution to gel, and temperature gradients were set up between 5 °C and 55 °C. The whole experiment was repeated three times.

### 3.7. Rheological Characterization

The dynamic oscillation tests were performed using a DHR-2 rheometer (Discovery Hybrid Rheometer, TA Instrument, Newcastle, DE, USA), including time scanning and oscillatory temperature change [72]. For the experiments, we equipped a parallel disk of 40 mm and lowered it to a gap of 1 mm. To prevent moisture loss, a ring of paraffin oil was dripped around the sample to seal it after the disc was lowered. Time scans were performed at 37 °C to record the dynamic modulus versus time over 1000 s, enabling the time required for gelation to be analyzed. Oscillatory temperature changes were performed to record the temperature at which the sol–gel transition behavior occurred, and the temperature was programmed to rise from 5 °C to 55 °C. A constant frequency of 1 Hz was set for all these measurements. The measurements were repeated three times for each sample.

### 3.8. Fourier Transform Infrared Spectroscopy (FTIR)

The hydrogel was freeze-dried for FTIR spectral analysis using a Nicolet iS50 FTIR spectrometer (Thermo Fisher Scientific Inc., Waltham, MA, USA). The freeze-dried samples were evenly mixed with KBr at a ratio of 1:100 and finely ground using a clean and dry agate mortar. The powder was placed in a tablet press and scanned in the energy range of 400 to 4000 $cm^{-1}$, provided that the tablet was uniform and crack-free [73]. The measurements were repeated three times for each sample.

### 3.9. Scanning Electron Microscopy (SEM)

The morphological structures of the samples were observed using a Hitachi S-3400 scanning electron microscope (Hitachi High-Technologies Corporation, Tokyo, Japan). In order to photograph the internal structure of the hydrogel, the freeze-dried sample was cut into cubes of the same size to photograph the cutting section. The sample was loaded on a cylindrical stage with conductive tape and scanned at an accelerating voltage of 15 kV after spraying a layer of gold [74]. The experiment was performed three times in parallel.

### 3.10. Swelling Ratios

The swelling rate of the sample was determined using the weighing method; that is, the proportion of mass increase in the freeze-dried sample after water absorption over a certain period of time was determined. After weighing, the freeze-dried samples were soaked in distilled water at room temperature and subsequently taken out and weighed every hour (recording measurements every ten minutes for the first hour) after drying the surface moisture with filter paper [75]. The experiment was performed three times in parallel.

### 3.11. In Vitro Release Assays

The release efficiency of nisin Z in the composite system was monitored for 60 h at 37 °C. The sustained-release test was carried out in a glass bottle using 2 mL gel complex and 18 mL PBS solution. A certain amount of PBS solution was taken out regularly, and the content of nisin Z was determined using the BCA method. The corresponding volume of PBS was supplemented for subsequent measurements [52]. The measurements were repeated three times for each sample.

### *3.12. In Vitro Toxicity Assays*

RAW264.7 macrophages were used for the CCK-8 (2-(2-methoxy-4-nitrophenyl)-3-(4-nitrophenyl)-5-(2,4-disulfophenyl)-2H-tetrazolium monosodium salt) method to evaluate the cytotoxicity of the materials [76]. The RAW264.7 cell line was stored at the Department of Food Science and Engineering, Ningbo University. After activation and passage of RAW cells, a batch of cells with good growth and a differentiation of less than 20% was selected for the experiment. The sample was co-cultured with the cell complete medium (the same volume) in a 6-well plate for 12 h to obtain the hydrogel extract. Cells were seeded into 96-well plates at a density of $5 \times 10^4$ cells/well and incubated at 37 °C and 5% $CO_2$ for 12 h. Subsequently, the medium was discarded, 100 µL of the extract was added to each well, and a control group with complete medium was set. After co-incubation for 12 h, 24 h, 36 h and 48 h, the original culture was discarded and 100 µL of complete culture medium containing 10% CCK-8 was added. Simultaneously, a control group with only CCK-8 and complete culture medium without cells was established. The culture plate was incubated for 1.5 h, and the absorbance at 450 nm was measured using a microplate reader. The experiment involved the conduction of three parallel tests. The cytotoxicity was calculated using the following formula:

$$Cell\ viability\ (\%) = \frac{A_s - A_b}{A_c - A_b} \times 100 \tag{3}$$

where $A_s$ represents the absorbance of the experimental wells (containing cells, medium, CCK-8 and extract), $A_b$ represents the absorbance of the blank wells (containing medium and CCK-8), and $A_c$ refers to the absorbance of the control wells (containing cells, medium and CCK-8). The measurements were repeated three times for each sample.

### *3.13. Assay for Erythrocyte Hemolysis*

The hemolysis assay was determined using the induction method, following a previous protocol with minor modifications [77]. Anticoagulated fresh sheep blood for testing was centrifuged at 2000 rpm and 4 °C for 10 min, and the supernatant was removed. Erythrocytes were resuspended in PBS and washed three times with centrifugation at 2000 rpm and 4 °C for 10 min. The concentration of the washed cells was adjusted to $1 \times 10^8$ cells/mL (200 µL of erythrocyte precipitate was added to 10 mL of PBS via suction). Blood cell suspension (100 µL) was mixed with 100 µL of each sample extract in a centrifuge tube; sterile PBS and Triton were used as controls for 0% and 100% hemolysis, respectively. After exposing the mixture for 30 min in an incubator at 37 °C, the mixture was centrifuged at 2000 rpm and 4 °C for 3 min. The absorbance of the supernatant was measured at 540 nm, and the hemolysis rate was calculated using the following formula:

$$Hemolysis\ rate\ (\%) = \frac{A_x - A_{0\%}}{A_{100\%} - A_{0\%}} \times 100 \tag{4}$$

where $A_x$ refers to the absorbance of experimental wells (extract group), $A_{0\%}$ denotes the absorbance of blank wells (PBS group), and $A_{100\%}$ denotes the absorbance of control wells (Triton group). The measurements were repeated three times for each sample.

### *3.14. In Vitro Antibacterial Assays*

The inhibition circle and colony counting methods were used to investigate the antimicrobial properties of materials. Gram-positive bacteria (*S. aureus* ATCC 6538) and Gram-negative bacteria (*E. coli* ATCC 25922) were selected for antibacterial experiments. The specific operation of the inhibition zone method was as follows: first, 100 µL of the bacterial solution (*S. aureus* or *E. coli*, $OD_{600\ nm} = 0.4$) was poured into the agar solid medium and mixed well. The plate was then poured and punched, and 200 μL of the sample was added to each hole, one by one. Finally, it was cultured in an incubator at 37 °C for 24 h, and then the diameter of the inhibition zone was measured [78].

The colony plate counting method is divided into three steps: co-culture, dilution coating, and colony counting [79]. Equal amounts of bacterial solution and samples were co-cultured in an incubator for 18 h, and the group with only bacterial solution was used as a control. After culturing, the bacteria on the surface of the sample were removed using ultrasonic treatment. The bacterial solution from each group was diluted and coated with a gradient dilution. Three dilution factors—$10^2$, $10^3$, and $10^4$—were selected. After 24 h of continuous culturing, colony counting was performed. The samples used for bacteriostatic experiments were prepared under sterile conditions, and the sterility of the raw materials and instruments was ensured. The measurements were repeated three times for each sample.

### 3.15. Statistical Analysis

The statistical analysis was carried out in triplicate. All data were expressed as the mean values and standard deviations (SDs) ($n = 3$). The images were generated using GraphPad Prism 10 (GraphPad Software, San Diego, CA, USA) or Origin 2021 software (OriginLab Corporation, Northampton, MA, USA). Significant differences were defined as $p < 0.05$.

## 4. Conclusions

We embedded nisin Z in nanoparticles and then used temperature-sensitive hydrogel as a carrier to obtain an effective sustained-release nanoparticle–hydrogel composite system. To achieve efficient encapsulation and release, we optimized the design of both the NPs and hydrogel. Within the experimental range, the NPs with a nisin Z content of 5 mg/mL were ultimately designated for the highest encapsulation effectiveness (86.18%) and optimal particle properties. The thermosensitive hydrogel was fabricated via the electrostatic interaction between CS and β-GP, and the three optimal gel groups ($Gel_{100\text{-}73}$, $Gel_{100\text{-}82}$, and $Gel_{500\text{-}82}$) were determined using the inverted tube method. The thermosensitive gel phenomenon is observed only when the interaction force between CS and β-GP is relatively balanced; otherwise, they will remain in a solution or sol state. The NPs–hydrogel composite system had a strong antibacterial effect on *S. aureus* and great biocompatibility, attributed to the efficient encapsulation and sustained release (20.09 ± 1.68%) of nisin Z. In this study, we attempted to incorporate nisin Z into a nanoparticle–hydrogel composite system, resulting in a novel encapsulation form for nisin Z in the biomedical field, particularly for trauma dressings.

**Supplementary Materials:** The following supporting information can be downloaded at: https://www.mdpi.com/article/10.3390/md22090428/s1, Table S1: Characterization results of all nanoparticles; Table S2: Circle of inhibition diameters of nisin Z, NPs and composites on *S. aureus*; Table S3: Specific compositions of hydrogels, NPs and composites.

**Author Contributions:** Conceptualization, Y.L.; methodology, Y.L. and Y.H.; software, Y.H. and S.H.; validation, Y.H., S.H. and J.C.; formal analysis, Y.L., Y.H., S.H., J.C., M.W. and Z.L.; investigation, Y.H., S.H., J.C., M.W. and Z.L.; resources, Y.L.; data curation, Y.H., S.H., J.C. and M.W.; writing—original draft preparation, Y.H. and S.H.; writing—review and editing, Y.L. and Y.H.; project administration, Y.L.; funding acquisition, Y.L.; supervision, Y.L. All authors have read and agreed to the published version of the manuscript.

**Funding:** This research was funded by the National Training Program of Innovation and Entrepreneurship for Undergraduates, grant number 202211646012.

**Institutional Review Board Statement:** Not applicable.

**Data Availability Statement:** The data presented in this study are available on request from the corresponding author.

**Acknowledgments:** We are grateful for the equipment-sharing service provided by the Ningbo University Large Instrument Sharing Management Platform.

**Conflicts of Interest:** The authors declare no conflicts of interest. The funders had no role in the design of this study, the collection, analyses, or interpretation of data, in the writing of the manuscript, or in the decision to publish the results.

## References

1. Yu, X.; Lu, N.; Wang, J.; Chen, Z.; Chen, C.; Mac Regenstein, J.; Zhou, P. Effect of N-terminal modification on the antimicrobial activity of nisin. *Food Control* **2020**, *114*, 107227. [CrossRef]
2. Chandrasekar, V.; Coupland, J.N.; Anantheswaran, R.C. Characterization of nisin containing chitosan-alginate microparticles. *Food Hydrocoll.* **2017**, *69*, 301–307. [CrossRef]
3. Flynn, J.; Mallen, S.; Durack, E.; O'Connor, P.M.; Hudson, S.P. Mesoporous matrices for the delivery of the broad spectrum bacteriocin, nisin A. *J. Colloid Interface Sci.* **2019**, *537*, 396–406. [CrossRef]
4. Ibarra-Sanchez, L.A.; El-Haddad, N.; Mahmoud, D.; Miller, M.J.; Karam, L. *Invited review*: Advances in nisin use for preservation of dairy products. *J. Dairy Sci.* **2020**, *103*, 2041–2052. [CrossRef]
5. Duchateau, A.L.L.; van Scheppingen, W.B. Stability study of a nisin/natamycin blend by LC-MS. *Food Chem.* **2018**, *266*, 240–244. [CrossRef]
6. Khan, F.; Singh, P.; Joshi, A.S.; Tabassum, N.; Jeong, G.-J.; Bamunuarachchi, N.I.; Mijakovic, I.; Kim, Y.-M. Multiple potential strategies for the application of nisin and derivatives. *Crit. Rev. Microbiol.* **2023**, *49*, 628–657. [CrossRef] [PubMed]
7. LeBel, G.; Piche, F.; Frenette, M.; Gottschalk, M.; Grenier, D. Antimicrobial activity of nisin against the swine pathogen *Streptococcus suis* and its synergistic interaction with antibiotics. *Peptides* **2013**, *50*, 19–23. [CrossRef]
8. Zhao, X.; Kuipers, O.P. Synthesis of silver-nisin nanoparticles with low cytotoxicity as antimicrobials against biofilm-forming pathogens. *Colloids Surf. B-Biointerfaces* **2021**, *206*, 111965. [CrossRef] [PubMed]
9. Zhu, C.; Zou, S.; Rao, Z.; Min, L.; Liu, M.; Liu, L.; Fan, L. Preparation and characterization of hydroxypropyl chitosan modified with nisin. *Int. J. Biol. Macromol.* **2017**, *105*, 1017–1024. [CrossRef]
10. Gedarawatte, S.T.G.; Ravensdale, J.T.; Al-Salami, H.; Dykes, G.A.; Coorey, R. Antimicrobial efficacy of nisin-loaded bacterial cellulose nanocrystals against selected meat spoilage lactic acid bacteria. *Carbohydr. Polym.* **2021**, *251*, 117096. [CrossRef]
11. Luo, L.; Wu, Y.; Liu, C.; Zou, Y.; Huang, L.; Liang, Y.; Ren, J.; Liu, Y.; Lin, Q. Elaboration and characterization of curcumin-loaded soy soluble polysaccharide (SSPS)-based nanocarriers mediated by antimicrobial peptide nisin. *Food Chem.* **2021**, *336*, 127669. [CrossRef]
12. Niaz, T.; Shabbir, S.; Noor, T.; Rahman, A.; Bokhari, H.; Imran, M. Potential of polymer stabilized nano-liposomes to enhance antimicrobial activity of nisin Z against foodborne pathogens. *Lwt-Food Sci. Technol.* **2018**, *96*, 98–110. [CrossRef]
13. Monfared, Y.K.; Mahmoudian, M.; Hoti, G.; Caldera, F.; Lopez Nicolas, J.M.; Zakeri-Milani, P.; Matencio, A.; Trotta, F. Cyclodextrin-Based Nanosponges as Perse Antimicrobial Agents Increase the Activity of Natural Antimicrobial Peptide Nisin. *Pharmaceutics* **2022**, *14*, 685. [CrossRef]
14. Niaz, T.; Shabbir, S.; Noor, T.; Imran, M. Active Composite Packaging Reinforced with Nisin-Loaded Nano-Vesicles for Extended Shelf Life of Chicken Breast Filets and Cheese Slices. *Food Bioprocess Technol.* **2022**, *15*, 1284–1298. [CrossRef]
15. Reczynska-Kolman, K.; Hartman, K.; Kwiecien, K.; Brzychczy-Wloch, M.; Pamula, E. Composites Based on Gellan Gum, Alginate and Nisin-Enriched Lipid Nanoparticles for the Treatment of Infected Wounds. *Int. J. Mol. Sci.* **2022**, *23*, 321. [CrossRef]
16. Zakaria, F.; Ashari, S.E.; Azmi, I.D.M.; Rahman, M.B.A. Recent advances in encapsulation of drug delivery (active substance) in cubosomes for skin diseases. *J. Drug Deliv. Sci. Technol.* **2022**, *68*, 103097. [CrossRef]
17. Li, S.; Zhang, Y.-X. Sensitive delivery systems and novel encapsulation technologies for live biotherapeutic products and probiotics. *Crit. Rev. Microbiol.* **2023**, *50*, 371–384. [CrossRef]
18. Celen, T.; Anumudu, C.; Miri, T.; Onyeaka, H.; Fernandez-Trillo, P. Nisin:Carboxymethylcellulose polyion complex (PIC) nanoparticles. *Prep. Antimicrob. Activity. Carbohydr. Polym.* **2023**, *317*, 121032.
19. Pachaleva, J.; Gruskiene, R.; Bockuviene, A.; Sereikaite, J. The application of pectin and chitooligosaccharides for the preparation of nisin-loaded nanoparticles with different surface charges. *Cellulose* **2023**, *30*, 8985–8996. [CrossRef]
20. Flynn, J.; Culebras, M.; Collins, M.N.; Hudson, S.P. The impact of varying dextran oxidation levels on the inhibitory activity of a bacteriocin loaded injectable hydrogel. *Drug Deliv. Transl. Res.* **2023**, *13*, 308–319. [CrossRef] [PubMed]
21. Soares, R.S.; Santos, R.; Cunha, E.; Tavares, L.; Trindade, A.; Oliveira, M. Influence of Storage on the Antimicrobial and Cytotoxic Activities of a Nisin-biogel with Potential to be Applied to Diabetic Foot Infections Treatment. *Antibiotics* **2020**, *9*, 781. [CrossRef] [PubMed]
22. Cui, G.; Guo, X.; Su, P.; Zhang, T.; Guan, J.; Wang, C. Mussel-inspired nanoparticle composite hydrogels for hemostasis and wound healing. *Front. Chem.* **2023**, *11*, 1154788. [CrossRef] [PubMed]

23. Jing, Y.; Ruan, L.; Jiang, G.; Nie, L.; Shavandi, A.; Sun, Y.; Xu, J.; Shao, X.; Zhu, J. Regenerated silk fibroin and alginate composite hydrogel dressings loaded with curcumin nanoparticles for bacterial-infected wound closure. *Biomater. Adv.* **2023**, *149*, 213405. [CrossRef] [PubMed]
24. Rojas, M.A.; Amalraj, J.; Santos, L.S. Biopolymer-Based Composite Hydrogels Embedding Small Silver Nanoparticles for Advanced Antimicrobial Applications: Experimental and Theoretical Insights. *Polymers* **2023**, *15*, 3370. [CrossRef]
25. Saadh, M.J.; Hsu, C.-Y.; Mustafa, M.A.; Mutee, A.F.; Kaur, I.; Ghildiyal, P.; Ali, A.-J.A.; Adil, M.; Ali, M.S.; Alsaikhan, F.; et al. Advances in chitosan-based blends as potential drug delivery systems: A review. *Int. J. Biol. Macromol.* **2024**, *273*, 132916. [CrossRef]
26. Balogun-Agbaje, O.A.; Odeniyi, O.A.; Odeniyi, M.A. Drug delivery applications of poly-γ-glutamic acid. *Future J. Pharm. Sci.* **2021**, *7*, 125. [CrossRef]
27. Hu, Z.; Liu, D.; Wang, M.; Yu, C.; Han, Z.; Xu, M.; Yue, W.; Nie, G. β-Alanine enhancing the crosslink of chitosan/poly-(γ-glutamic acid) hydrogel for a potential alkaline-adapted wound dressing. *Int. J. Biol. Macromol.* **2023**, *231*, 123157. [CrossRef]
28. Liu, K.; Chen, Y.; Yang, Z.; Jin, J. Preparation and characterization of CS/γ-PGA/PC complex nanoparticles for insulin oral delivery. *Colloid Polym. Sci.* **2023**, *301*, 481–490. [CrossRef]
29. Chen, H.; Zhuang, J.; Wu, X.; Shen, X.; Zhang, Q.; Zhang, W. Preparation of the Chitosan/Poly-γ-Glutamic Acid/Glabrid in Hybrid Nanoparticles and Study on its Releasing Property. *Curr. Drug Deliv.* **2023**, *20*, 1195–1205. [CrossRef]
30. Serrano, I.; Alhinho, B.; Cunha, E.; Tavares, L.; Trindade, A.; Oliveira, M. Bacteriostatic and Antibiofilm Efficacy of a Nisin Z Solution against Co-Cultures of *Staphylococcus aureus* and *Pseudomonas aeruginosa* from Diabetic Foot Infections. *Life* **2023**, *13*, 504. [CrossRef]
31. Shin, J.M.; Gwak, J.W.; Kamarajan, P.; Fenno, J.C.; Rickard, A.H.; Kapila, Y.L. Biomedical applications of nisin. *J. Appl. Microbiol.* **2016**, *120*, 1449–1465. [CrossRef] [PubMed]
32. Oliveira, W.d.S.; Teixeira, C.R.V.; Mantovani, H.C.; Dolabella, S.S.; Jain, S.; Barbosa, A.A.T. Nisin variants: What makes them different and unique? *Peptides* **2024**, *177*, 171220.
33. Murat, D.; Hakki, T.I. Food stabilizing potential of nisin Z produced by wild *Lactococcus lactis* subsp. lactis from raw milk and some fermented products. *Lwt-Food Sci. Technol.* **2021**, *150*, 112065. [CrossRef]
34. Heo, W.-S.; Kim, E.-Y.; Kim, Y.-R.; Hossain, M.T.; Kong, I.-S. Salt effect of nisin Z isolated from a marine fish on the growth inhibition of *Streptococcus iniae*, a pathogen of streptococcosis. *Biotechnol. Lett.* **2012**, *34*, 315–320. [CrossRef]
35. Araujo, C.; Munoz-Atienza, E.; Perez-Sanchez, T.; Poeta, P.; Igrejas, G.; Hernandez, P.E.; Herranz, C.; Ruiz-Zarzuela, I.; Cintas, L.M. Nisin Z Production by *Lactococcus lactis* subsp *cremoris* WA2-67 of Aquatic Origin as a Defense Mechanism to Protect Rainbow Trout (*Oncorhynchus mykiss*, Walbaum) Against *Lactococcus garvieae*. *Mar. Biotechnol.* **2015**, *17*, 820–830. [CrossRef]
36. Araujo, M.K.; Gumiela, A.M.; Bordin, K.; Luciano, F.B.; Freitas de Macedo, R.E. Combination of garlic essential oil, allyl isothiocyanate, and nisin Z as bio-preservatives in fresh sausage. *Meat Sci.* **2018**, *143*, 177–183. [CrossRef]
37. Cohen-Erez, I.; Rapaport, H. Coassemblies of the Anionic Polypeptide γ-PGA and Cationic β-Sheet Peptides for Drug Delivery to Mitochondria. *Biomacromolecules* **2015**, *16*, 3827–3835. [CrossRef]
38. Zhang, L.; Chen, D.; Yu, D.; Regenstein, J.M.; Jiang, Q.; Dong, J.; Chen, W.; Xia, W. Modulating physicochemical, antimicrobial and release properties of chitosan/zein bilayer films with curcumin/nisin-loaded pectin nanoparticles. *Food Hydrocoll.* **2022**, *133*, 107955. [CrossRef]
39. Pandey, P.; Hansmann, U.H.E.; Wang, F. Altering the Solubility of the Antibiotic Candidate Nisin-A Computational Study. *Acs Omega* **2020**, *5*, 24854–24863. [CrossRef]
40. Luo, L.; Wu, Y.; Liu, C.; Huang, L.; Zou, Y.; Shen, Y.; Lin, Q. Designing soluble soybean polysaccharides-based nanoparticles to improve sustained antimicrobial activity of nisin. *Carbohydr. Polym.* **2019**, *225*, 115251. [CrossRef]
41. Dannert, C.; Stokke, B.T.; Dias, R.S. Nanoparticle-Hydrogel Composites: From Molecular Interactions to Macroscopic Behavior. *Polymers* **2019**, *11*, 275. [CrossRef] [PubMed]
42. Lin, L.; Luo, C.; Li, C.; Chen, X.; Cui, H. A Novel Biocompatible Ternary Nanoparticle with High Antibacterial Activity: Synthesis, Characterization, and Its Application in Beef Preservation. *Foods* **2022**, *11*, 438. [CrossRef] [PubMed]
43. Bhuiyan, M.H.; Clarkson, A.N.; Ali, M.A. Optimization of thermoresponsive chitosan/B-glycerophosphate hydrogels for injectable neural tissue engineering application. *Colloids Surf. B-Biointerfaces* **2023**, *224*, 113193. [CrossRef] [PubMed]
44. Tan, W.; Sijie, C.; Xu, Y.; Chen, M.; Liao, H.; Niu, C. Temperature-Sensitive Nanocarbon Hydrogel for Photothermal Therapy of Tumors. *Int. J. Nanomed.* **2023**, *18*, 6137–6151. [CrossRef]
45. Moradi, L.; Witek, L.; Nayak, V.V.; Pereira, A.C.; Kim, E.; Good, J.; Liu, C.-J. Injectable hydrogel for sustained delivery of progranulin derivative Atsttrin in treating diabetic fracture healing. *Biomaterials* **2023**, *301*, 122289. [CrossRef]
46. Dehghan-Baniani, D.; Chen, Y.; Wang, D.; Bagheri, R.; Solouk, A.; Wu, H. Injectable in situ forming kartogenin-loaded chitosan hydrogel with tunable rheological properties for cartilage tissue engineering. *Colloids Surf. B-Biointerfaces* **2020**, *192*, 111059. [CrossRef]
47. Liu, C.; Yang, P.; Li, J.; Cao, S.; Shi, J. NIR/pH-responsive chitosan hydrogels containing $Ti_3C_2$/AuNRs with NIR-triggered photothermal effect. *Carbohydr. Polym.* **2022**, *295*, 119853. [CrossRef]
48. Uysal, Y.; Dogaroglu, Z.G.; Caylali, Z.; Makas, M.N. Evaluation of swelling properties of different biochar-doped hydrogels. *J. Soils Sediments* **2023**, *23*, 3787–3805. [CrossRef]

49. Wang, H.; Lu, Z.; Wang, F.; Li, Y.; Ou, Z.; Jiang, J. A novel strategy to reinforce double network hydrogels with enhanced mechanical strength and swelling ratio by nano cement hydrates. *Polymer* **2023**, *269*, 125725. [CrossRef]
50. Zang, S.; Mu, R.; Chen, F.; Wei, X.; Zhu, L.; Han, B.; Yu, H.; Bi, B.; Chen, B.; Wang, Q.; et al. Injectable chitosan/β-glycerophosphate hydrogels with sustained release of BMP-7 and ornidazole in periodontal wound healing of class III furcation defects. *Mater. Sci. Eng. C-Mater. Biol. Appl.* **2019**, *99*, 919–928. [CrossRef]
51. Zhang, D.; Ouyang, Q.; Hu, Z.; Lu, S.; Quan, W.; Li, P.; Chen, Y.; Li, S. Catechol functionalized chitosan/active peptide microsphere hydrogel for skin wound healing. *Int. J. Biol. Macromol.* **2021**, *173*, 591–606. [CrossRef] [PubMed]
52. Hsu, X.-L.; Wu, L.-C.; Hsieh, J.-Y.; Huang, Y.-Y. Nanoparticle-Hydrogel Composite Drug Delivery System for Potential Ocular Applications. *Polymers* **2021**, *13*, 642. [CrossRef] [PubMed]
53. Yu, Y.-C.; Hu, M.-H.; Zhuang, H.-Z.; Phan, T.H.M.; Jiang, Y.-S.; Jan, J.-S. Antibacterial Gelatin Composite Hydrogels Comprised of In Situ Formed Zinc Oxide Nanoparticles. *Polymers* **2023**, *15*, 3978. [CrossRef] [PubMed]
54. Hu, J.; Liu, X.; Gao, Q.; Ouyang, C.; Zheng, K.; Shan, X. Thermosensitive PNIPAM-Based Hydrogel Crosslinked by Composite Nanoparticles as Rapid Wound-Healing Dressings. *Biomacromolecules* **2023**, *24*, 1345–1354. [CrossRef]
55. Yuan, Q.; Yin, J.; Li, L.; Bao, B.; Zhang, X.; Li, M.; Tang, Y. Conjugated Polymer Composite Nanoparticles Augmenting Photosynthesis-Based Light-Triggered Hydrogel Promotes Chronic Wound Healing. *Adv. Sci.* **2024**, *11*, 2304048. [CrossRef]
56. Lv, X.; Liu, Y.; Song, S.; Tong, C.; Shi, X.; Zhao, Y.; Zhang, J.; Hou, M. Influence of chitosan oligosaccharide on the gelling and wound healing properties of injectable hydrogels based on carboxymethyl chitosan/alginate polyelectrolyte complexes. *Carbohydr. Polym.* **2019**, *205*, 312–321. [CrossRef]
57. Pattanayaiying, R.; H-Kittikun, A.; Cutter, C.N. Effect of lauric arginate, nisin Z, and a combination against several food-related bacteria. *Int. J. Food Microbiol.* **2014**, *188*, 135–146. [CrossRef]
58. Yoon, J.-H.; Jeong, D.Y.; Lee, S.B.; Kim, S.R. Control of Listeria monocytogenes and *Escherichia coli* O157:H7 in enoki mushrooms (*Flammulina velutipes*) by combined treatments with organic acids, nisin, and ultrasound. *Food Control* **2021**, *129*, 108204. [CrossRef]
59. Costello, K.M.; Velliou, E.; Gutierrez-Merino, J.; Smet, C.; El Kadri, H.; Van Impe, J.F.; Bussemaker, M. The effect of ultrasound treatment in combination with nisin on the inactivation of *Listeria innocua* and *Escherichia coli*. *Ultrason. Sonochem.* **2021**, *79*, 105776. [CrossRef]
60. Liu, X.; Liao, W.; Xia, W. Recent advances in chitosan based bioactive materials for food preservation. *Food Hydrocoll.* **2023**, *140*, 108612. [CrossRef]
61. Huang, P.; Su, W.; Han, R.; Lin, H.; Yang, J.; Xu, L.; Ma, L. Physicochemical, Antibacterial Properties, and Compatibility of ZnO-NP/Chitosan/11-Glycerophosphate Composite Hydrogels. *J. Microbiol. Biotechnol.* **2022**, *32*, 522–530. [CrossRef] [PubMed]
62. Costa, E.M.; Silva, S.; Tavaria, F.K.; Pintado, M.M. Insights into chitosan antibiofilm activity against methicillin-resistant *Staphylococcus aureus*. *J. Appl. Microbiol.* **2017**, *122*, 1547–1557. [CrossRef] [PubMed]
63. Haidari, H.; Bright, R.; Strudwick, X.L.; Garg, S.; Vasilev, K.; Cowin, A.J.; Kopecki, Z. Multifunctional ultrasmall AgNP hydrogel accelerates healing of *S. aureus* infected wounds. *Acta Biomaterialia* **2021**, *128*, 420–434. [CrossRef]
64. Naranjo, M.F.; Kumar, A.; Ratrey, P.; Hudson, S.P. Pre-formulation of an additive combination of two antimicrobial agents, clofazimine and nisin A, to boost antimicrobial activity. *J. Mater. Chem. B* **2024**, *12*, 1558–1568. [CrossRef]
65. Lu, P.; Zhao, H.; Zheng, L.; Duan, Y.; Wu, M.; Yu, X.; Yang, Y. Nanocellulose/Nisin Hydrogel Microparticles as Sustained Antimicrobial Coatings for Paper Packaging. *Acs Appl. Polym. Mater.* **2022**, *4*, 2664–2673. [CrossRef]
66. Sullivan, D.J.; Cruz-Romero, M.; Collins, T.; Cummins, E.; Kerry, J.P.; Morris, M.A. Synthesis of monodisperse chitosan nanoparticles. *Food Hydrocoll.* **2018**, *83*, 355–364. [CrossRef]
67. Ji, S.; Sun, R.; Wang, W.; Xia, Q. Preparation, characterization, and evaluation of tamarind seed polysaccharide-carboxymethylcellulose buccal films loaded with soybean peptides-chitosan nanoparticles. *Food Hydrocoll.* **2023**, *141*, 108684. [CrossRef]
68. Savic Gajic, I.M.; Savic, I.M.; Gajic, D.G.; Dosic, A. Ultrasound-Assisted Extraction of Carotenoids from Orange Peel Using Olive Oil and Its Encapsulation in Ca-Alginate Beads. *Biomolecules* **2021**, *11*, 225. [CrossRef]
69. Tucker, L.J.; Grant, C.S.; Gautreaux, M.A.; Amarasekara, D.L.; Fitzkee, N.C.; Janorkar, A.V.; Varadarajan, A.; Kundu, S.; Priddy, L.B. Physicochemical and Antimicrobial Properties of Thermosensitive Chitosan Hydrogel Loaded with Fosfomycin. *Mar. Drugs* **2021**, *19*, 144. [CrossRef]
70. Li, Y.; Li, G.; Sha, X.; Li, L.; Zhang, K.; Liu, D.; Hao, Y.; Cui, X.; Wang, L.; Wang, H. An intelligent vancomycin release system for preventing surgical site infections of bone tissues. *Biomater. Sci.* **2020**, *8*, 3202–3211. [CrossRef]
71. Liu, Y.; Lang, C.; Ding, Y.; Sun, S.; Sun, G. Chitosan with enhanced deprotonation for accelerated thermosensitive gelation with β-glycerophosphate. *Eur. Polym. J.* **2023**, *196*, 112229. [CrossRef]
72. Khoobbakht, F.; Khorshidi, S.; Bahmanyar, F.; Hosseini, S.M.; Aminikhah, N.; Farhoodi, M.; Mirmoghtadaie, L. Modification of mechanical, rheological and structural properties of agar hydrogel using xanthan and locust bean gum. *Food Hydrocoll.* **2024**, *147*, 109411. [CrossRef]
73. Li, D.; Cui, H.; Hayat, K.; Zhang, X.; Ho, C.-T. Superior environmental stability of gelatin/CMC complex coacervated microcapsules via chitosan electrostatic modification. *Food Hydrocoll.* **2022**, *124*, 107341. [CrossRef]
74. Shu, X.; Liu, J.; Mao, L.; Yuan, F.; Gao, Y. Composite hydrogels filled with rhamnolipid-based nanoemulsion, nanostructured lipid carrier, or solid lipid nanoparticle: A comparative study on gel properties and the delivery of lutein. *Food Hydrocoll.* **2024**, *146*, 109264. [CrossRef]

75. Moradi, S.; Barati, A.; Tonelli, A.E.; Hamedi, H. Chitosan-based hydrogels loading with thyme oil cyclodextrin inclusion compounds: From preparation to characterization. *Eur. Polym. J.* **2020**, *122*, 109303. [CrossRef]
76. Zhang, A.; Fan, X.; Zeng, X.; Xu, J.; Zhou, C.; Xia, Q.; Sun, Y.; Wu, Z.; Pan, D. Enhancing physicochemical, antimicrobial, and release properties of fish skin gelatin films using dual-layer nanoparticles loaded with tea polyphenols/kojic acid for air-dried chicken preservation. *Food Hydrocoll.* **2024**, *149*, 109580. [CrossRef]
77. He, J.-R.; Zhu, J.-J.; Yin, S.-W.; Yang, X.-Q. Bioaccessibility and intracellular antioxidant activity of phloretin embodied by gliadin/sodium carboxymethyl cellulose nanoparticles. *Food Hydrocoll.* **2022**, *122*, 107076. [CrossRef]
78. Tian, B.; Cheng, J.; Zhang, T.; Liu, Y.; Chen, D. Multifunctional chitosan-based film loaded with hops β-acids: Preparation, characterization, controlled release and antibacterial mechanism. *Food Hydrocoll.* **2022**, *124*, 107337. [CrossRef]
79. Dong, Z.; Ma, F.; Wei, X.; Zhang, L.; Ding, Y.; Shi, L.; Chen, C.; Ma, Y.; Ma, Y. Injectable, thermo-sensitive and self-adhesive supramolecular hydrogels built from binary herbal small molecules towards reusable antibacterial coatings. *Rsc Adv.* **2024**, *14*, 2027–2035. [CrossRef]

marine drugs

Article

# High Degree of Polymerization of Chitin Oligosaccharides Produced from Shrimp Shell Waste by Enrichment Microbiota Using Two-Stage Temperature-Controlled Technique of Inducing Enzyme Production and Metagenomic Analysis of Microbiota Succession

**Delong Pan, Peiyao Xiao, Fuyi Li, Jinze Liu, Tengfei Zhang, Xiuling Zhou * and Yang Zhang ***

School of Life Science, Liaocheng University, Liaocheng 252059, China; 2210150302@stu.lcu.edu.cn (D.P.); m19861908982@163.com (P.X.); 15653129517@163.com (F.L.); 13176629777@163.com (J.L.); lcubiozy@163.com (T.Z.)
* Correspondence: xiulingzhou@lcu.edu.cn (X.Z.); zhy@lcu.edu.cn (Y.Z.)

**Abstract:** The direct enzymatic conversion of untreated waste shrimp and crab shells has been a key problem that plagues the large-scale utilization of chitin biological resources. The microorganisms in soil samples were enriched in two stages with powdered chitin (CP) and shrimp shell powder (SSP) as substrates. The enrichment microbiota XHQ10 with SSP degradation ability was obtained. The activities of chitinase and lytic polysaccharide monooxygenase of XHQ10 were 1.46 and 54.62 U/mL. Metagenomic analysis showed that *Chitinolyticbacter meiyuanensis*, *Chitiniphilus shinanonensis*, and *Chitinimonas koreensis*, with excellent chitin degradation performance, were highly enriched in XHQ10. Chitin oligosaccharides (CHOSs) are produced by XHQ10 through enzyme induction and two-stage temperature control technology, which contains CHOSs with a degree of polymerization (DP) more significant than ten and has excellent antioxidant activity. This work is the first study on the direct enzymatic preparation of CHOSs from SSP using enrichment microbiota, which provides a new path for the large-scale utilization of chitin bioresources.

**Keywords:** directional domestication; enrichment microbiota; metagenomics; high degree of polymerization; chitin oligosaccharides

## 1. Introduction

Chitin polymerized from N-acetylglucosamine (GlcNAc) is widely found in the exoskeletons of crustaceans (e.g., shrimps and crabs), insects, and the cell walls of fungi. Chitin is the most abundant nitrogen-containing natural biopolymer on earth [1]. Although about $10^{11}$ tons of chitin are produced globally each year, large accumulation in nature is not a problem, mainly due to the degradation of chitin by microorganisms. The formation and degradation of chitin play an important role in the carbon and nitrogen cycle of the earth. With the booming of the global fishing industry, about 6–8 million tons of crab, shrimp, and lobster shell waste are generated every year [2]. These seafood wastes have not been properly treated, which not only causes a waste of resources but also creates challenges related to environmental protection. Chitin and its deacetylated product, chitosan, extracted from shrimp and crab shell residues, are biocompatible, biodegradable, nontoxic, and antibacterial. Chitin and chitosan have been used in agriculture, medicine, food, cosmetics, and the textile industry [3,4]. However, the water insolubility of chitin and chitosan limits their wide application [5]. Chitin oligosaccharides (CHOSs) are a high value-added degradation product of chitin. They have antibacterial, anti-inflammatory, and immune protective activities, intestinal regulation activity, and other biological activities. In particular, their excellent solubility gives them a broad application prospect [6–8]. As a positively charged basic amino oligosaccharide, the efficient preparation and application of CHOSs can provide a green method for the high value-added utilization of seafood waste. Currently, CHOSs are obtained through two main methods: chitin degradation and biosynthesis [9,10]. Chitin degradation uses chitin as raw material to prepare CHOSs by physical, chemical, and biological degradation methods. Biodegradation can overcome the disadvantages of physical and chemical methods, such as non-environmental protection and poor quality. It is the trend for CHOS production and preparation in the future [11]. However, CHOSs have not yet been fully industrialized due to the poor activity of the single enzyme, low production efficiency, and the limitation of separation methods, thus hindering its biological activity research and application promotion [12].

So far, much experimental data on the enzymatic preparation of CHOSs has been accumulated [13]. The research results on the structure and mechanism of action of chitin-degrading enzymes significantly increased the possibility of controlling the depolymerization process of chitin. Theoretically, various forms of oligosaccharides can be prepared by selecting different substrates and hydrolases [14]. However, most of the existing preparation theories and production methods of CHOSs are based on chitin and its non-crystalline chitin as substrates, and most of the products obtained are low-molecular-weight CHOSs with a degree of polymerization (DP) below 10 [15]. How to realize the direct enzymatic utilization of crystalline chitin and even natural chitin materials, such as shrimp and crab shells, has become a hot issue in the green and efficient preparation of CHOSs.

Shrimp and crab shells can be completely degraded by chitin-degrading enzymes produced by microorganisms in the natural environment, such as chitin, chitosanase, and lytic polysaccharide monooxygenase (LPMO), through synergistic action [1]. Under the action of a specific multi-enzyme system, high-efficiency CHOS preparation from shrimp and crab shells can be realized. Currently, the cognition of the synergistic action mode of chitin-degrading enzymes mainly depends on the summary of the enzymatic properties and mechanism of action of a single enzyme. However, this type of study is relatively scarce. It has become a major bottleneck in resolving the synergistic mechanism of chitin-degrading enzymes due to the complexity of the multi-enzymatic degradation process of chitin and the lack of samples. Obtaining microbial communities that degrade biomass efficiently from nature has become a new idea and scheme to solve the problems of the degradation and biotransformation of complex substances [16,17]. Enrichment, domestication, and other technologies are effective methods to obtain microbial communities, which play an important role in the culture of extreme microorganisms and special microbiota [18–20]. With the rapid development of high-throughput sequencing technology and modern mass spectrometry (MS) technology, metagenome and metaproteome have been applied to the analysis of microbial community functions and mechanisms. Existing metagenomic studies have shown that although the diversity of microbial communities tends to decline during the enrichment process [21,22], it is conducive to the recovery and enrichment of functional strains, especially dormant cells [23]. Therefore, the combined application of enrichment, domestication and metagenomic technologies has great potential in improving the performance of functional microbiota and analyzing potential mechanisms.

In this study, the soil sample (named LNM) was enriched with chitin powder (CP) and shrimp shell powder (SSP) as substrates by using directional enrichment technology to obtain the acclimated bacteria with the ability to degrade SSP to produce CHOSs with a high DP. With the help of metagenomics technology, the community composition and succession rules of the original samples and the enrichment microbiota were systematically compared. The results provide new insights for the enrichment and domestication in improving the performance of functional microbiota and laid the foundation for studying the synergistic mechanism between chitin-degrading enzymes and the large-scale production of CHOSs.

## 2. Results and Discussions

### 2.1. Domestication of SSP-Degrading Microbiota

The previously established enrichment and acclimation technology was used to conduct a two-stage directional culture of LNM in soil samples [24]. After 20 experimental cycles of enrichment with CP as the substrate, a microbial community (LNM20) with high CP degradation ability was obtained. During the enrichment process, the activities of chitinase and LPMO gradually increased with the increase in enriched experimental cycles (Figure 1a), and the chitinase and LPMO enzyme activities of LNM20 were 0.76 and 34.98 U/mL, respectively. LNM20 was inoculated onto agar plates with CP as the substrate. After culturing, the CP around the colony dissolved and disappeared, forming a visible dissolution circle (Figure 1b), indicating that LNM20 has good CP degradation ability. LNM20 was further acclimated with SSP as the substrate to obtain a high-efficiency degradation bacteria group with SSP degradation performance. After ten experimental acclimation cycles, an enrichment microbiota (XHQ10) that can directly degrade SSP was obtained. The activities of chitinase and LPMO increased during acclimation, but the upward trend gradually slowed. The highest enzyme activities were 1.46 and 54.62 U/mL, which were 1.92 and 1.56 times that of LNM20. Under the condition of liquid fermentation, XHQ10 could degrade most of the powdery SSP in 3 days (Figure 1c,d). Therefore, XHQ10 has a good SSP degradation ability.

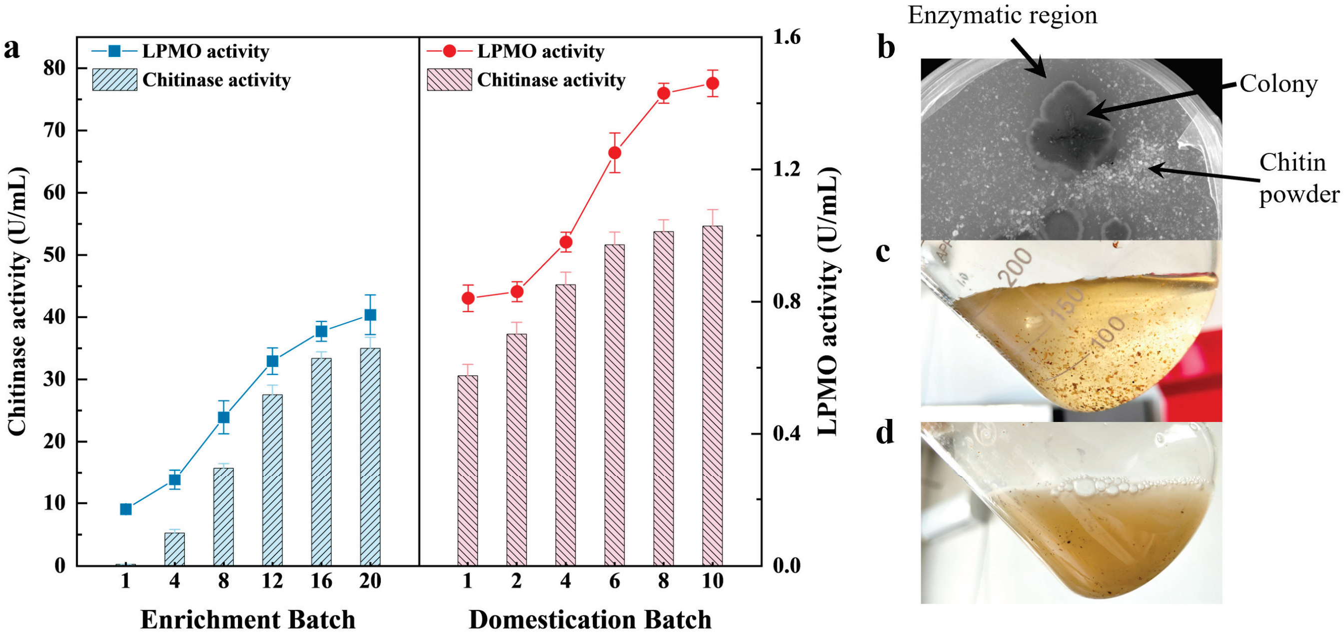

**Figure 1.** Enrichment effect and degradation performance of different experimental cycles of enrichment microbiota. (**a**) Chitin-degrading enzyme activity of enrichment microbiota in different experimental cycles. (**b**) Enzymatic region degrading CP and producing clear transparent circles on agar plates. (**c**,**d**) State of SSP in the fermentation broth before inoculation with XHQ10 and three days after fermentation.

### 2.2. Comparison of Chitin Degradation Enzyme Activities of Enrichment Microbiota

Shrimp and crab shells can be completely degraded by microorganisms in the natural environment, and this process is completed by chitin-degrading enzymes produced by microorganisms. The synergistic mechanism of chitin degradation by LPMO and chitinase has opened up a new strategy for the efficient production of CHOSs [25]. The activities of the chitin enzyme and LPMO were determined at different fermentation time points to compare the ability of LNM, LNM20, and XHQ10 to produce the chitin enzyme and LPMO. The results are shown in Figure 2a. The fermentation enzyme production processes of LNM, LNM20, and XHQ10 showed significant differences. The activities of chitinase and LPMO in the whole fermentation process of LNM were close to 0. The chitinase and LPMO activities of LNM20 and XHQ10 were low at the initial stage of fermentation (0–24 h), and then the activity of LPMO showed an obvious upward trend. In contrast, the chitinase activity increased at a greater rate at 60 h. When the fermentation time was 84 h, the two enzyme activities of LNM20 and XHQ10 reached the maximum value, and then the enzyme activities showed a slow downward trend. XHQ10 and LNM20 had the highest chitinase activity of 1.41 and 0.70 U/mL, respectively, and the highest LPMO activity of 55.58 and 34.31 U/mL, respectively. XHQ10 had a higher chitin-degrading enzyme activity than LNM20. The proteins contained in the supernatants of LNM20 and XHQ10 after 84 h of fermentation were analyzed by SDS-PAGE. Figure 2b shows that the proteins secreted by LNM20 and XHQ10 differed greatly in type and concentration, and the number of proteins secreted by XHQ10 that accounted for a higher content was significantly higher. Therefore, enrichment can effectively improve the activities of chitinase and LPMO, and the substrate transition from CP to SSP significantly changes the species and concentration of proteins secreted by the microbiota.

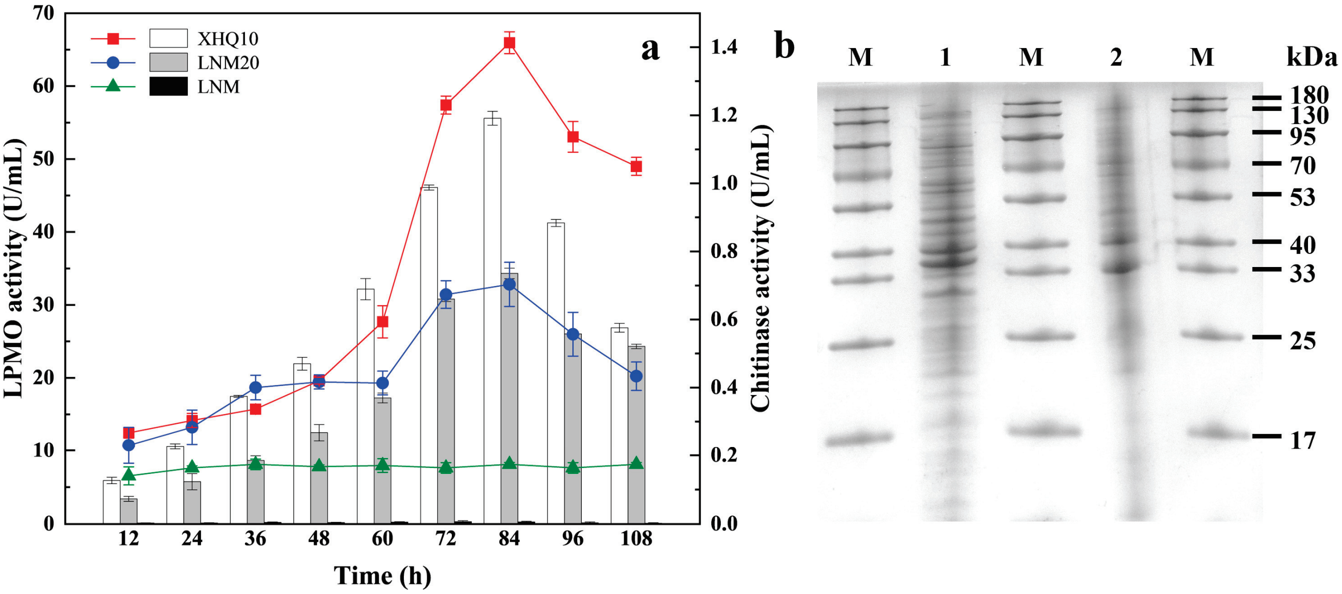

**Figure 2.** Enzyme production of different bacterial groups during domestication. (**a**) Changes in enzyme activity during different microbial fermentation processes. (**b**) SDS-PAGE analysis of LNM20 and XHQ10 fermentation supernatants. M, molecular mass markers; lane 1, protein contained in XHQ10 supernatant after 84h of fermentation; and lane 2, protein contained in LNM20 supernatant after 84h of fermentation.

### *2.3. Comparison of Fermentation Products of Enrichment Microbiota*

The products obtained by fermentation of LNM20 and XHQ10 after 84 h were analyzed by HPLC, and the results are shown in Figure 3a. With reference to the peak times of DP1-6 in the CHOS standard, the LNM20 and XHQ10 products contained CHOSs at different DPs [26]. The LNM20 product contained DP1-DP6 CHOSs, and the XHQ10 product contained DP3-6 CHOSs. The LNM20 and XHQ10 products still had multiple response peaks after the DP6 standard, and the products were presumed to contain CHOSs with higher DPs. MALDI-TOF MS was used based on HPLC analysis to understand the difference between LNM20 and XHQ10 hydrolysates. As shown in Figure 3b,c, the main peak in the MALDI TOF MS spectrum in positive mode, was attributed to CHOSs with different DPs. The results proved that LNM20 and XHQ10 could degrade SSP effectively and produce CHOSs. The MALDI-TOF MS spectrum of LNM20 showed that CHOSs with a DP of 2–6, determined by HPLC, and CHOSs with a DP of 7–10 were captured. Similarly, CHOSs with DPs of 7–13 were detected in the MALDI-TOF MS spectra of XHQ10. The hydrolysate of XHQ10 contained more CHOSs with high DPs than that of LNM20.

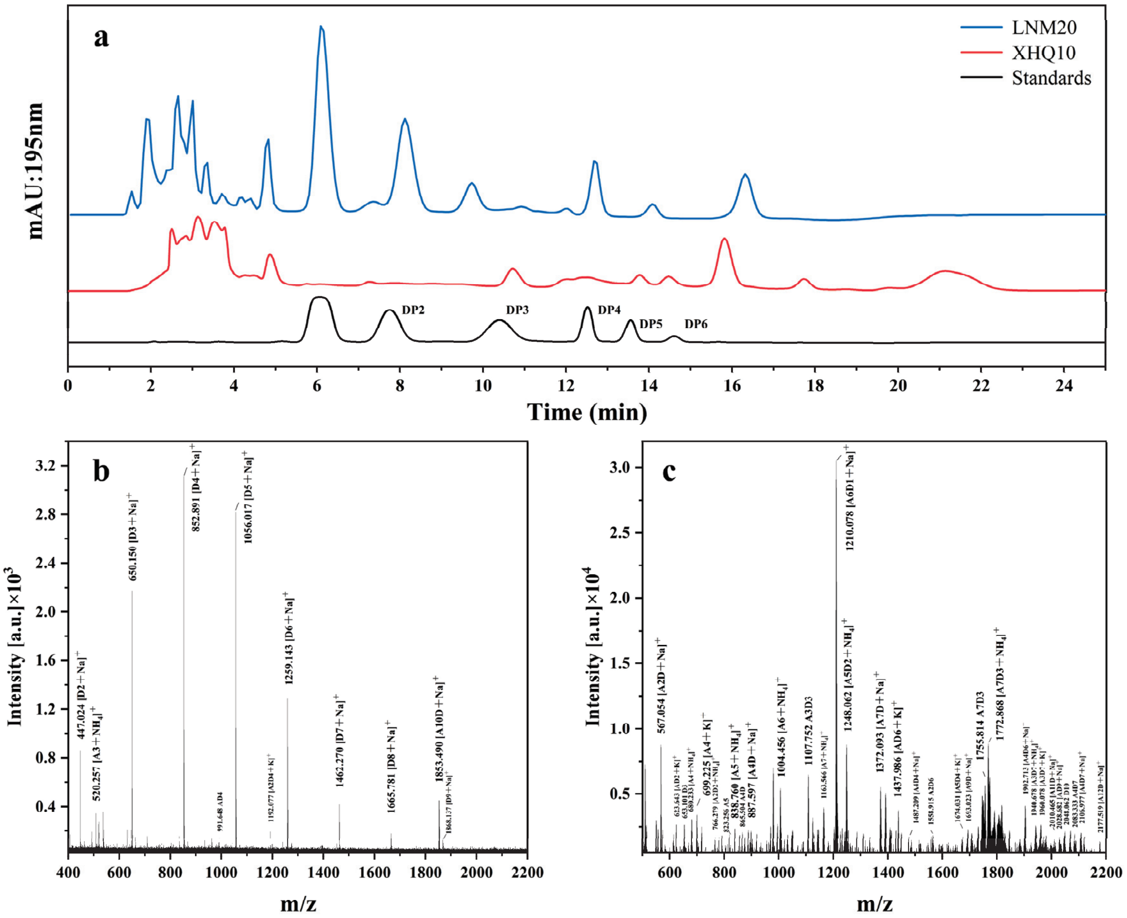

**Figure 3.** Hydrolysis of CP-, SSP-, and CHOS-generating capacity of LNM20 and XHQ10. (**a**) HPLC profiles of fermentation products of LNM20 and XHQ10. MALDI-TOF MS analysis of LNM20 (**b**) and XHQ10 (**c**) fermentation products.

Chitin degradation by chitinase (endochitinase and exochitinase) is an important way to produce CHOSs [27]. However, the DP of CHOSs obtained by chitin enzymes is mostly below 10 [2]. Studies have shown that the biological activity of CHOSs is closely related to their physical and chemical parameters, such as DP, acetylation degree, and charge distribution [28,29]. CHOSs with slightly higher DPs (DP 5–10) have higher activity in anti-tumor activity, superoxide anion scavenging activity, and immune activation than CHOSs with low DPs (DP 2–4) [13]. High DP CHOSs prepared by XHQ10 are of great significance in promoting CHOS application research.

### *2.4. Community Composition and Succession Analysis during Acclimation*

#### 2.4.1. Dataset Overview

Three parallel metagenomic sequences were performed for each of LNM, LNM20, and XHQ10 to reveal the changes in the composition of microbial communities during the enrichment and acclimation of chitin-degrading bacteria. A total of 74,926,897 (22.48 GB) RawReads were obtained for three samples of LNM, with an average of 6.10 GB RawReads per sample; a total of 70,840,368 (21.25 GB) RawReads were obtained for three samples of LNM20, with an average of 7.08 GB RawReads per sample; and XHQ10 received a total of 61,019,577 (18.31 GB) RawReads for three samples, with an average of 7.49 GB RawReads per sample. After low-quality data were removed and host contamination was filtered out, 71,610,263, 67,902,878, and 58,569,366 clean reads were obtained for samples of LNM, LNM20, and XHQ10, respectively, (Table 1).

**Table 1.** Overview of the quality of metagenomic sequencing data.

| Sample ID | Grouping | RawReads | Raw Base (GB) | Clean Reads | Cleaned (%) |
|---|---|---|---|---|---|
| LNM | SS11 | 19784882 | 5.94 | 18925514 | 95.66 |
| | SS12 | 26947750 | 8.08 | 25736535 | 95.51 |
| | SS13 | 28194265 | 8.46 | 26948214 | 95.58 |
| LNM20 | FS21 | 22424308 | 6.73 | 21512100 | 95.93 |
| | FS22 | 26312463 | 7.89 | 25221987 | 95.86 |
| | FS23 | 22103597 | 6.63 | 21168791 | 95.77 |
| XHQ10 | FS11 | 20613776 | 6.18 | 19727621 | 95.7 |
| | FS12 | 20716845 | 6.22 | 19935093 | 96.23 |
| | FS13 | 19688956 | 5.91 | 18906652 | 96.03 |

### 2.4.2. Community Composition and Taxonomic Changes

The similarity and uniqueness of species composition among sample groups can be intuitively expressed by comparing the number of common and unique species among LNM, LNM20, and XHQ10. As shown in Figure 4a, 68 species were common in the domestication process. In addition, 279 of the 555 species obtained from the 2811 species included in LNM after 20 enrichments were absent from the species composition before domestication. Among the 208 species obtained by XHQ10, 45 species reappeared after the disappearance of LNM20, and 63 species were specific to XHQ10 (Supplementary Table S1). The results showed that enrichment and domestication significantly changed the number and species composition of OTUs. The microbial community structure of three sample phylum and genus levels were analyzed. At the phylum level, Pseudomonadota and Actinomycetota were the most abundant taxonomic groups in LNM, accounting for 33.78% and 26.34%, respectively, whereas LNM20 and XHQ10 were dominated by Pseudomonadota, accounting for 98.51% and 99.95%, respectively (Figure 4b,c, Table S2). At the genus level, *Chitinolyticbacter*, *Laribacter*, *Sinorhizobium*, *Chitiniphilus*, *Streptomyces*, *Herbaspirillum*, *Chitinimonas*, *Microvirga*, and *Stenotrophomonas* were the dominant types in the three samples (Figure 4b,d, Table S2). Significant differences between the samples at all levels are shown in Figure 4b–d. These results suggest significant changes in the community during enrichment and acclimation.

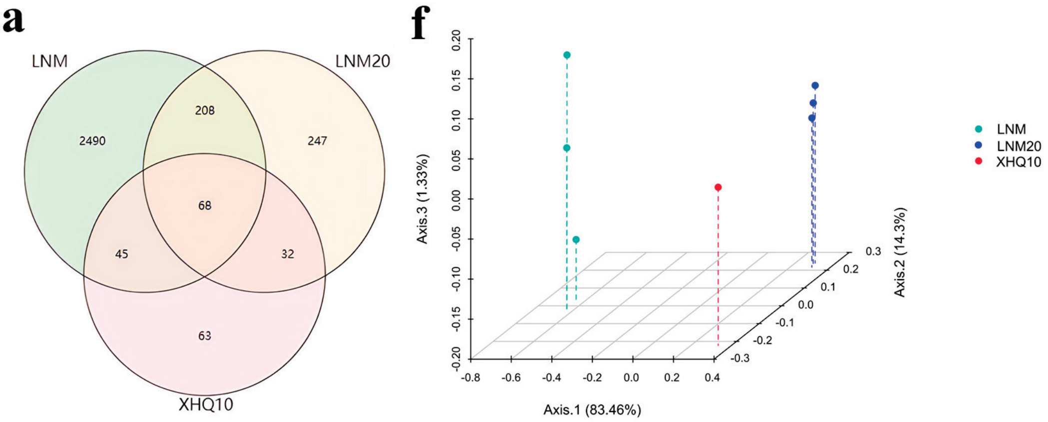

**Figure 4.** *Cont.*

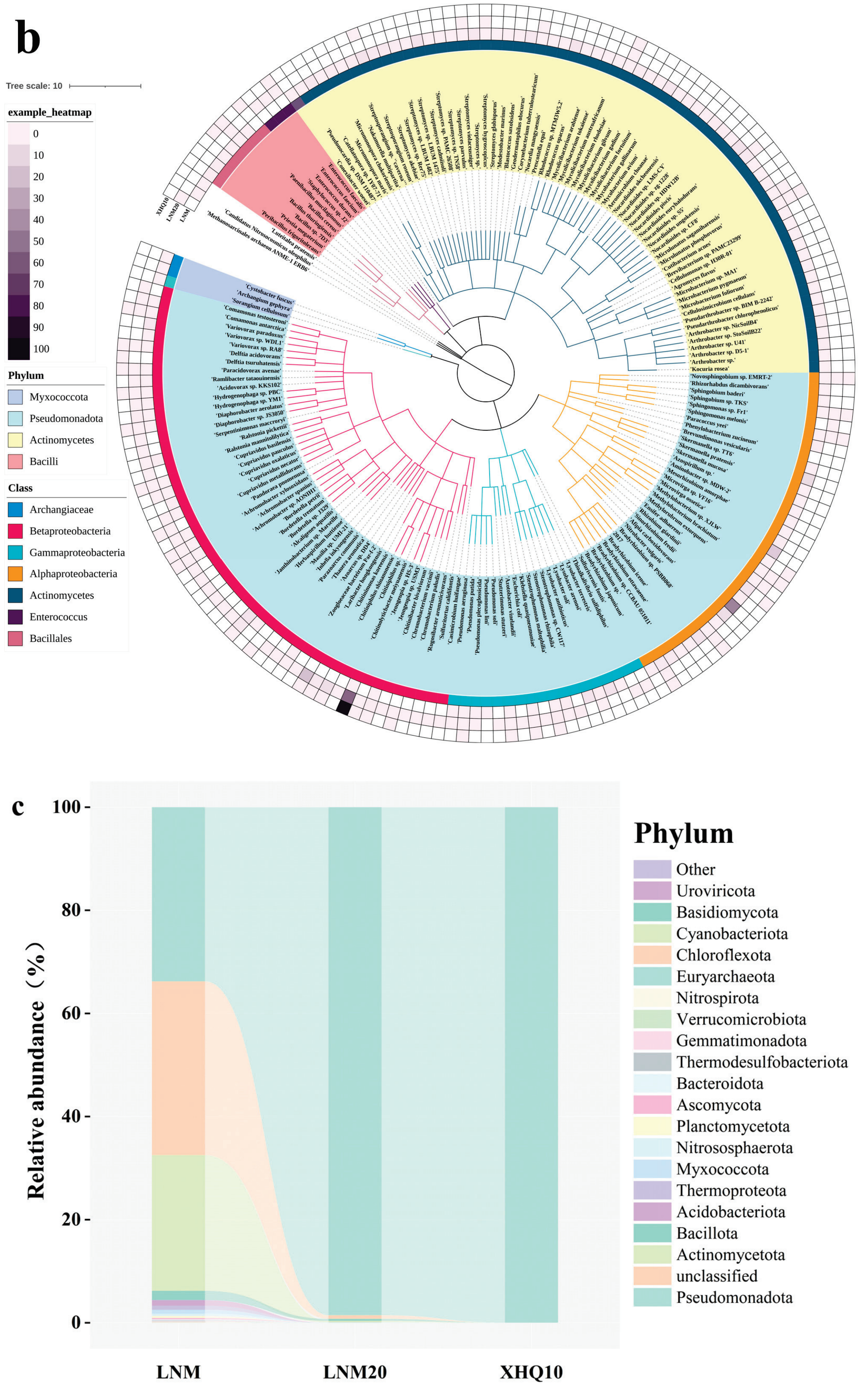

**Figure 4.** *Cont.*

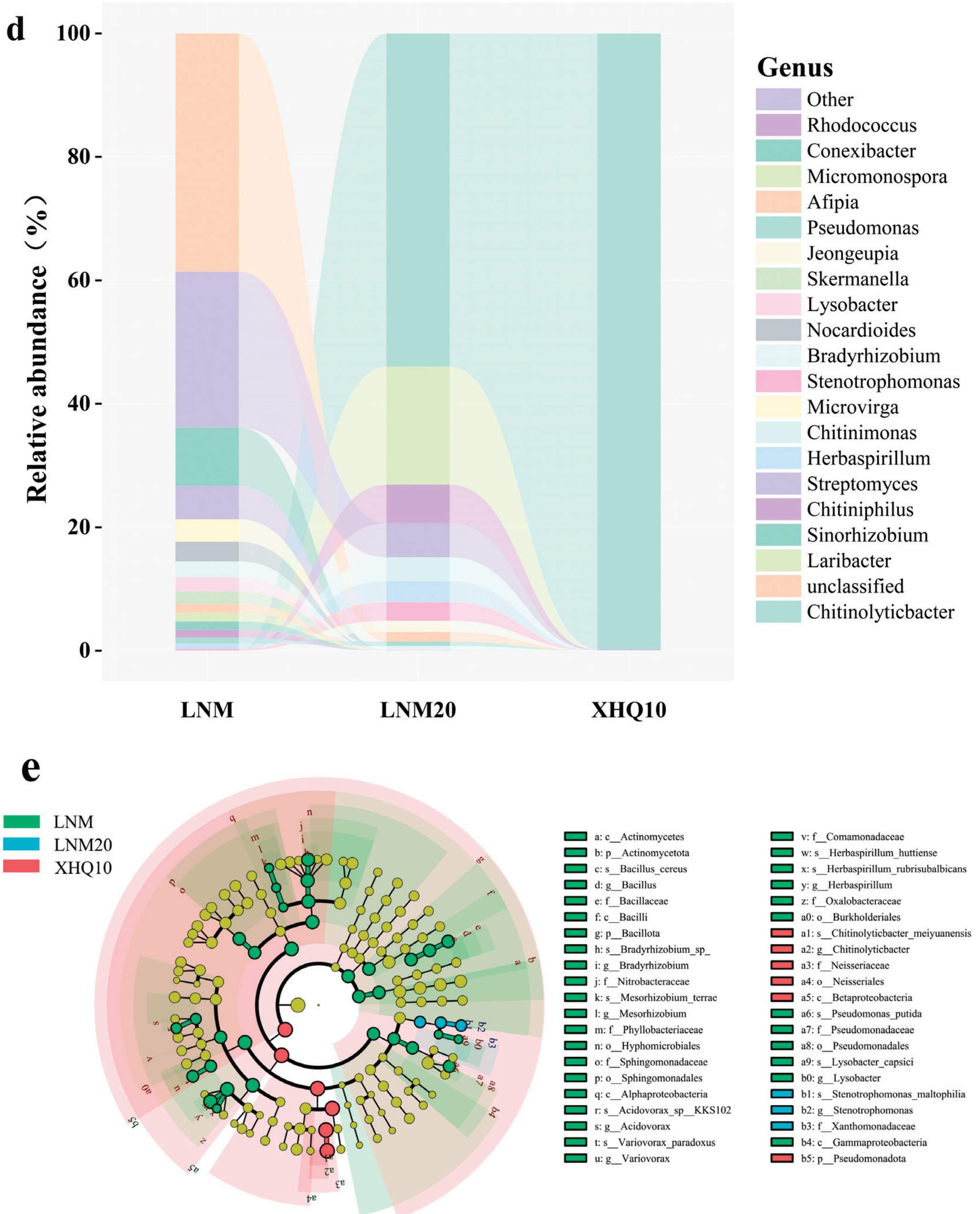

**Figure 4.** Metagenomic analysis of the microbiota during domestication. (**a**) Venn diagram of OTUs for three samples. (**b**) Three sample species-level phylogenetic trees. The color of the heatmap represents the number of strains contained by each species in the three samples. (**c**) Relative abundance at the phylum level. (**d**) Relative abundance at the genus level. (**e**) Dynamic branching diagram of microbial phylogeny of three samples. Nodes with different colors represent microorganisms that play a key role in the grouping indicated by the color, and yellow nodes indicate that they are not significant. Microbial markers with LDA score ≥ 4 in the three samples are listed. Volcano plot of the differences between LNM and LNM20. (**f**) Between-group analysis of PCoA based on the Bray-Curtis distance. Different colors represent different groups.

### 2.4.3. Excavation of Key Microbiota

The species level and abundance of each macrogenomic sample were analyzed using the linear discriminant analysis effect size method [30] to identify further the microbiota in which the domestication process plays a role. The branching diagram contains six levels from phylum to species, revealing iconic microbiota, with three bacterial taxa enriched in LNM20, six bacterial taxa enriched in XHQ10, and thirty-three bacterial taxa enriched in LNM (Figure 4e). The specifications *Stenotropionas maltohilia*, genus *Stenotropionas*, and family Xanthomonadaceae may play important roles in LNM20, whereas the specifications *Chitolyticbacter meiyuanensis*, genus chitolytic bacteria, family Neisseriaceae, order Neisseriales, class Betaprotecteria, and phylum Pseudomonas may play important roles in XHQ10. A species-level volcano plot (Figures S1 and S2) showed that compared with LNM, *Laribacter hongkongensis*, *Chitinolyticbacter meiyuanensis*, *Chitiniphilus shinanonensis*, *Chitinimonas koreensis,* and *Jeongeupia* sp. USM3 were significantly upregulated in LNM20. The top three bacterial groups significantly upregulated in XHQ10 were *Chitinolyticbacter meiyuanensis*, *Chitiniphilus shinanonensis*, and *Chitinimonas koreensis*. *Stenotrophomonas maltophilia* contains nine genes related to chitin turnover [31]. The *Jeongeupia* species has a complete chitin degradation system and shows good chitin degradation performance [32,33]. Although no detailed report on chitin degradation by *Jeongeupia* sp. USM3 is available, 11 potential chitinase genomes were found in its genes [34]. *Laribacter hongkongensis* has chitinase and chitin deacetylase activities, but its chitin degradation ability is relatively weak [35]. *Chitinolyticbacterium meiyuanensis*, *Chitiniphilus shinanonensis*, and *Chitinimonas koreensis* have good chitin degradation ability [36–38]. In summary, the proportion of genera related to chitin degradation gradually increased during the enrichment process, with an increase in the enrichment of chitin-degrading bacteria in LNM20 and ultimately, the species in XHQ10 were dominated by chitin-degrading bacteria.

### 2.4.4. Analysis of Microbiota Diversity

PCoA analysis was performed based on Bray–Curtis distance to determine the diversity and community structure differences of the whole dataset [39]. Figure 4f shows that three parallel datasets from three samples were clustered, with some overlap and dispersion within each cluster. LNM showed considerable dispersion, LNM20 was relatively concentrated, and XHQ10 completely overlapped. The differences in microbial diversity among LNM, LNM20, and XHQ10 samples were revealed. The LNM20 had low abundance and diversity, and the XHQ10 had even lower abundance and diversity.

### 2.4.5. Functional Annotation Analysis

During acclimation, the microbiota can encode various complex Carbohydrate-Active enZYmes (CAZymes), and these CAZymes contain many enzymes involved in chitin degradation. The relative abundance changes of Glycoside Hydrolase (GHS), Glycosyl-Transferases (GTs), Polysaccharide Lyases (PLs), Carbohydrate Esterases (CEs), Auxiliary Activities (AAs), and Carbohydrate-Binding Modules (CBMs) in the three samples are summarized in Figure 5a to understand the differences at the gene level in the domestication process. In previous studies, GH, CBM, and AA have been identified as the main CAZymes involved in chitin degradation [40,41]. The GH family is the main component of CAZyme involved in chitin degradation. They can directly hydrolyze the glycosidic bonds of carbohydrate CBMs, which are not directly involved in catalysis, but they help relax the crystal structure of the substrate, improving the overall catalytic efficiency of chitin degradation [40]. The AA family is a newly introduced CAZyme class in recent years, and the multi-enzyme synergism with GHs has an important potential for application in biorefineries. It has become a new direction for developing chitin resources [25]. The relative abundance of GHs was maintained at a high level in the three samples, and no obvious change was found in the relative abundance during domestication (Figure 5a and Supplementary Table S3). The relative abundance of CBMs significantly increased at LNM20 and further increased at XHQ10, indicating that the domestication process increased the relative abundance of CBMs (Figure 5a and Table S3). A notable detail is that the relative abundance of AAs in XHQ10 increased to some extent compared with that of LNM and LNM20 (Figure 5a and Table S3).

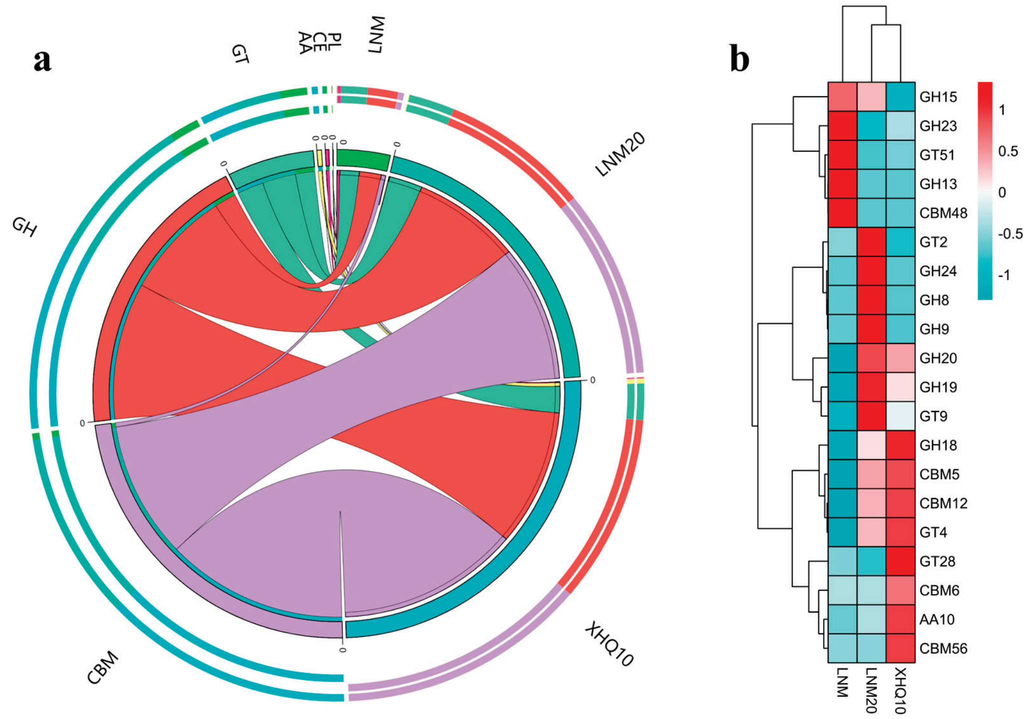

**Figure 5.** Analysis of CAZyme composition. (**a**) Dynamic changes in CAZyme class-level composition of three samples. (**b**) Heatmap of the top 20 CAZymes' relative abundance at the family-level of three samples.

Figure 5b shows the CAZyme heatmap of the top 20 relative abundances. Significant differences were observed in the CAZyme family with the change in the enrichment process. Among these CAZyme families, the GH18 family has chitinase, exo-β-1,4-n-acetylglucosaminidase, and β-n-acetylhexosaminidase activities; the GH19 family has chitinase and exochitinase activities; and the GH20 family has β-1,6-n-acetylglucosaminidase and β-n-acetylhexosaminidase activities. The chitin-degrading enzymes of the three GH families, especially the GH18 family of chitinases, play an important role in degrading chitin [42]. Its relative abundance increased significantly during acclimation (Figure 5b and Table S4). CBM5 and CBM12 are distantly related, and both have chitin-binding functions that promote the hydrolysis of chitin, whose relative abundance increased significantly during acclimation (Figure 5b and Table S4). The AA10 family has lytic chitin monooxygenase activity, which plays an important role in synergizing other chitin-degrading enzymes to crystallize chitin [25]. AA10s were significantly enriched in LNM20 and more abundant in XHQ10.

In general, the enrichment of the CAZymes family related to chitin degradation indicates that the hydrolysis ability is improved, which also shows that the domestication enrichment effect is significant. *Chitinolyticbacter meiyuanensis*, *Chitiniphilus shinanonensis*, and *Chitinimonas koreensis* are the main contributors of CAZymes in chitin degradation. Therefore, changes in microbial communities during domestication cause changes in the enzyme family, further improving the chitin degradation ability of enrichment microbiota.

### *2.5. Optimization of Enzyme Production and Degradation Conditions of SSP by XHQ10 and Characterization of Products*

#### 2.5.1. Induction of Enzyme Production and Construction of Two-Stage Temperature Control Technology

Except for a few strains, chitinase expression is constitutive and inducible, and most microbial chitinases belong to inducible enzymes. The expression of the microbial chitinase gene significantly increased when it was induced by chitin and its degradation products (such as CHOSs, Nacetylglucosamine, and D-glucosamine) [43,44]. XHQ10 fermentation broth contains chitin and its degradation products, so XHQ10 (XFP) fermentation products were tried as inducers. After XHQ10 was cultured for 12 h, CP, CC, SSP, and XFP (calculated as CHOSs) were added at a final concentration of 1g/L to evaluate their effect on the induction of the enzyme production of XHQ10. By evaluating the induction results, CC and XFP were selected as inducers of XHQ10. The two-stage temperature-controlled fermentation process curve of XHQ10 with XFP and CC as inducers is shown in Figure 6a. The chitinase activity was lower in the early stage of XFP induction than in the control, but the chitinase activity increased significantly after 24 h. The chitinase activity of XFP as an inducer reached a maximum value of 1.61 U/mL at 60 h, which was 1.34 and 2.78 times higher than that of CC as an inducer and control, respectively. After the temperature was adjusted to 50 °C, the chitinase activity of XFP as an inducer showed a slight downward trend. Although the chitinase activity induced by control and CC as inducer still increased, it was consistently lower than that of XFP as an inducer.

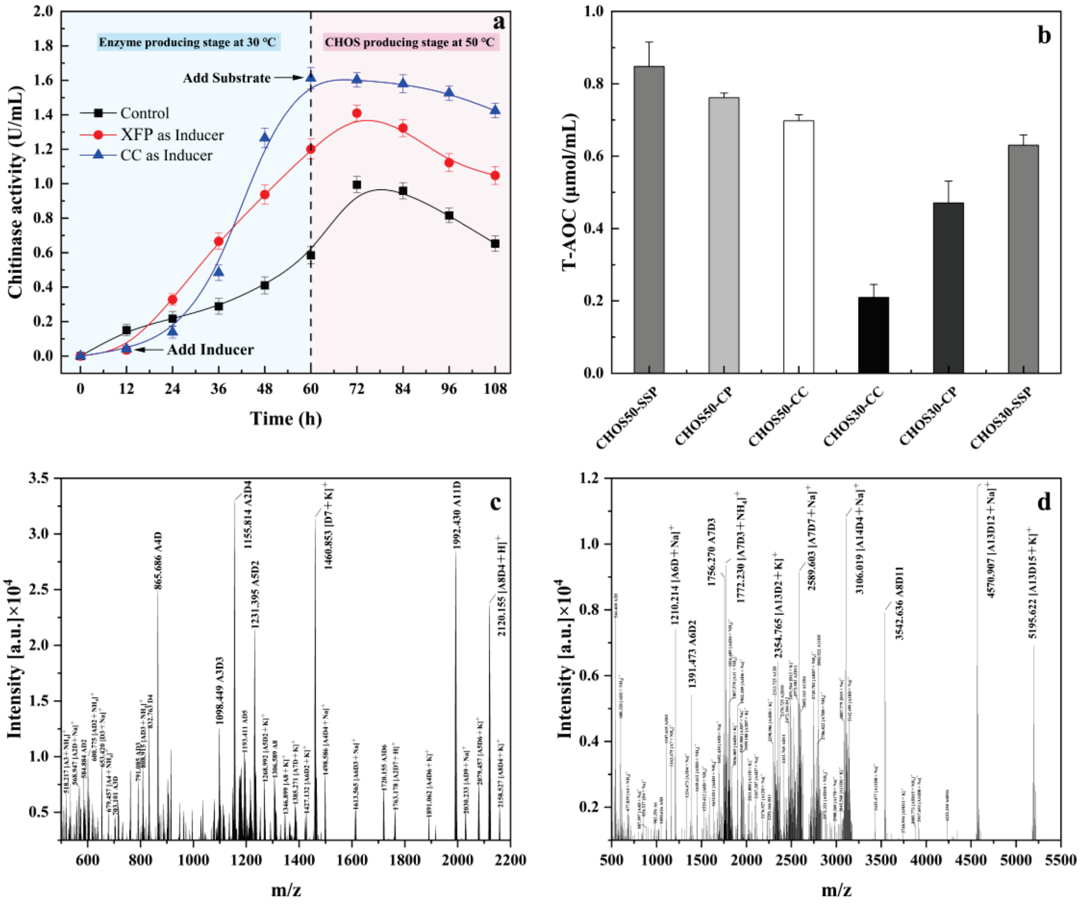

**Figure 6.** Changes in chitinase enzyme activity under enzyme-producing induction and two-stage temperature control techniques. (**a**) Changes in enzyme activity of different substrates under a two-step mechanism. (**b**) Antioxidant capacity. (**c**) CHOS30-SSP MALDI-TOF MS analysis. (**d**) CHOS50-SSP MALDI-TOF MS analysis.

### 2.5.2. Antioxidant Activity of XHQ10 Hydrolysates

CP, CC, and SSP were selected as substrates for enzymatic hydrolysis at 30 °C and 50 °C to investigate the degradation effect of XFP-induced XHQ10 on different substrates at different temperatures. The lyophilized hydrolysates of the three substrates were named CHOS30-CP, CHOS30-CC, and CHOS30-SSP at 30 °C, and the lyophilized hydrolysates at 50 °C were named CHOS50-CP, CHOS50-CC, and CHOS50-SSP. Reactive oxygen species (ROS) are oxygen-active molecules formed during metabolism. Excess ROS and its oxidative stress can cause damage to the body, inducing cancer, cardiovascular disease, and inflammatory diseases [45]. Antioxidants can delay or block the oxidation process to reduce the damage caused by oxidative stress. Existing studies have shown that CHOSs have a certain antioxidant activity [8,46,47]. Therefore, antioxidant capacity is an important indicator of CHOSs. A total antioxidant capacity (T-AOC) assay was performed on lyophilized enzymatic hydrolysates obtained at 30 °C and 50 °C. As shown in Figure 6b, all enzymatic hydrolysates had a certain antioxidant capacity. The order of T-AOC was CHOS50-SSP > CHOS50-CP > CHOS50-CC. The changing trend of T-AOC of the hydrolysates obtained by the enzymatic hydrolysis of the three substrates at 30 °C was the same as that obtained at 50 °C, but the T-AOC of the three hydrolysates was lower than that of CHOS50-CC.

#### 2.5.3. MALDI-TOF/TOF MS Analysis of XHQ10 Enzymatic Hydrolysates

The CHOS50-SSP obtained after 8 h of enzymatic hydrolysis at 50 °C was analyzed by MALDI-TOF/TOF MS and compared with CHOS30-SSP. Figure 6b,c show that CHOS30-SSP and CHOS50-SSP were composed of multiple types of CHOSs. The CHOS30-SSP had a higher percentage of CHOSs, with DPs of 5, 6, 7, and 12, whereas the CHOSs comprising CHOS50-SSP had a higher degree of aggregation, and most of these were CHOSs with DPs > 10. The highest degree of aggregation that could be detected was 28, which is a rarity in studies of enzymatically dissociated gibberellic acid materials.

XFP was selected as the inducer of XHQ10, and a two-stage process technology was constructed, which induced enzyme production culture at 30 °C and the enzymatic hydrolysis of SSP at 50 °C. This technology can effectively improve the enzyme production level of XHQ10 and effectively degrade SSP to obtain CHOSs with good antioxidant activity and a high DP, which has significant potential in the high-value utilization of discarded shrimp and crab shells.

## 3. Materials and Methods

### *3.1. Chemical Reagents and Enrichment Microbiota*

CP was purchased from Shanghai Yuanye Biotechnology Co., Ltd. (Shanghai, China). Shrimp (*Litopenaeus vannamei*) was purchased from local seafood markets. Soil samples were collected in Liaocheng, Shandong, China (36°43′36″ N, 116°01′67″ E). The shells were obtained, thoroughly washed with running water to remove residual shrimp meat and dried in a 60 °C vacuum oven for 24 h. The dried material was crushed in a pulverizer, and then SSP was prepared through a 40-mesh sieve. Colloidal chitin (CC) was prepared using the previous method [48]. Briefly, dissolve 10 g chitin powder in 200 mL pre-cooled concentrated HCl, stir at 4 °C for 2 h, add 2.5 L pre-cooled deionized water, and continue stirring for 10 min. The suspension was centrifuged at 10,000 rpm at 4 °C for 10 min, and the precipitate was repeatedly washed with deionized water to neutral pH and stored at 4 °C for future use. The remaining reagents were analytical grade reagents, and they can be used without additional purification. In accordance with previous research methods [24], 20 experimental cycles of microbiota (LNM20) were enriched and cultured on CP as the initial enrichment microbiota, and LNM20 was acclimated by SSP. The acclimation medium consisted of 2 g/L peptone, 1 g/L glucose, 0.7 g/L $K_2HPO_4$, 0.3 g/L $KH_2PO_4$, 0.5 g/L $MgSO_4$, and 4 g/L SSP. After ten experimental cycles of enrichment, the XHQ10 with the ability to degrade SSP was obtained. Soil samples (LNM), LNM20, and XHQ10 were selected for comparison with the fermentation experiment and metagenomic sequencing analysis.

### *3.2. Comparison of Fermentation Performance of LNM, LNM20, and XHQ10*

LNM, LNM20, and XHQ10 were individually fermented for 108 h. The fermentation medium consisted of 1 g/L glucose, 2 g/L peptone, 2 g/L yeast extract, 0.7 g/L $K_2HPO_4$, 0.3 g/L $KH_2PO_4$, 0.5 g/L $MgSO_4$, and 4 g/L SSP. The culture conditions were as follows: a 250 mL Erlenmeyer flask was filled with 50 mL of fermentation medium, the inoculation volume was 4% (*v*/*v*), the temperature was 30 °C, the pH was 7.0, and the rotating speed was 200 rpm. The fermentation experiment was set up three times in parallel. During the culture process, 1 mL of fermentation broth was sampled every 12 h to determine chitinase and LPMO activities, and the products were analyzed.

### *3.3. Chitin Enzyme and LPMO Activity Analysis*

Fixed-point fermentation broth (1 mL) was centrifuged at 4 °C for 10 min at 12,000× *g*, and the supernatant was used for chitin enzyme and LPMO activity assays. Using the method described by Rojas-Avelizapa [49], the chitinase activity was determined by the DNS method under the condition of the chitinase enzymatic hydrolysis of colloidal chitin to release N-acetyl-D-glucosamine (GlcNAc). The absorbance was recorded at 540 nm. The readings were compared with the GlcNAc standard curve. The linear regression equation for the GlcNAc standard curve was $Y = 1.2075X - 0.0887$ ($R^2 = 0.9994$). The unit chitin enzyme activity (U) was defined as the amount of enzyme required to produce 1 mmol of GlcNAc during 1 min at 37 °C. The activity of LPMO was determined in accordance with a previous method [24]. The secreted proteins of LNM20 and XHQ10 after 84 h of fermentation were analyzed by SDS-PAGE with 5% stacked gel and 12.5% resolved gel in Tris-glycine buffer (pH 8.3).

### *3.4. Analysis of Fermentation and Enzymatic Hydrolysis Products*

When sampling at a specific time or after reaching the enzyme reaction time, an equal amount of acetonitrile was added to the fermentation broth or enzyme reaction system to terminate the fermentation or enzyme reaction and centrifuged at 4 °C at 12,000× *g* for 10 min through membrane treatment. Samples were separated on a Prevail Carbohydrate ES column (4.6 × 250 mm) at a column temperature of 30 °C, a flow rate of 1.0 mL/min, and a detection wavelength of 195 nm. The mobile phase was acetonitrile and water, and the detection method was as follows: 0 min, acetonitrile: water (75:25, *v*/*v*); 7 min, acetonitrile: water (75:25, *v*/*v*); 8 min, acetonitrile: water (65:35, *v*/*v*); 15 min, acetonitrile: water (65:35, *v*/*v*); 16 min, acetonitrile: water (75:25, *v*/*v*); and 22 min, acetonitrile: water (75:25, *v*/*v*). The detection time was 30 min.

An appropriate amount of freeze-dried enzymatic hydrolysate was obtained, dissolved in ultrapure water with 2,5-DHB as a substrate, and analyzed using UltrafleXtreme MALDI-TOF/TOF (Bruker Daltonics GmbH, Bremen, Germany) forward collection mode. The collection adopted the reflective type, the acceleration voltage was 20 kV, the reflective layer voltage was 21.1 kV, and the collection range was *m*/*z* 400–6000.

### *3.5. Metagenomic Sequencing*

The total DNA of LNM, LNM20, and XHQ10 was extracted using the E.Z.N.A. Soil DNA Kit (Omega Bio-Tek, Norcross, GA, USA). The metagenomic library was prepared and sequenced by Shenzhen Microecology Technology Co., Ltd. (Shenzhen, China) using the HiSeq2000 platform (Illumina PE150, San Diego, CA, USA).

### *3.6. Bioinformatics and Data Analysis*

Kraken2 was used to compare with the self-built microbial nucleic acid database (screening the sequences belonging to bacteria, fungi, archaea, and viruses in the NCBI NT nucleic acid database and RefSeq whole genome database) to calculate the sequence number of species contained in the sample. Bracken was then used to estimate the actual abundance of species in the sample. Read-based metagenomic species annotation is more comprehensive and accurate than assembly-based species annotation. Starting from quality control and removing the reads of host genes, the reads of each sample were compared to the database (UniRef90) by using HUMAnN 3 3.6 software (based on DIAMOND, and the annotation information and relative abundance table of the CAZY database were obtained in accordance with the corresponding relationship between UniRef90 ID and the CAZY database.

### 3.7. Two-Stage Temperature-Controlled Degradation of SSP by XHQ10 to Prepare CHOSs

XHQ10 was cultured in a culture medium without SSP at 30 °C and 200 rpm. After 12 h, CC and XFP were added and continued to be induced to culture for 60 h. After the temperature was increased to 50 °C, SSP with a final concentration of 8 g/L was added. After eight hours of incubation, it was centrifuged at 4 °C at 12,000× *g* for 10 min. The supernatant was lyophilized, and the CHOS product was obtained.

### 3.8. Analysis of the Antioxidant Activity of CHOSs

The modified FRAP method [50] was used to detect the total antioxidant capacity (T-AOC) of different CHOS samples. The specific operation and analysis steps were carried out in accordance with the specification of the T-AOC Assay Kit (BIOBOX, AKAO012C, Beijing, China).

## 4. Conclusions

In this study, LNM from soil samples was enrichment cultured with CP as a substrate to obtain chitin-degrading microbiota LNM20, and LNM20 was acclimated with SSP to obtain the enrichment microbiota XHQ10 with high-efficiency SSP degradation. The community composition and succession rules of the original samples and enrichment microbiota were systematically compared using metagenomics technology. The high antioxidant activity of CHOSs was obtained by optimizing the conditions of XHQ10 enzymatic hydrolysis and constructing the enzyme induction and two-stage temperature control technology. The results provide new insights for enrichment and acclimation in improving the performance of functional microbiota. They lay the foundation for studying the synergistic mechanism between degrading enzymes in chitin and the large-scale production of CHOSs.

**Supplementary Materials:** The following supporting information can be downloaded at: https://www.mdpi.com/article/10.3390/md22080346/s1. Volcano plot of the differences between LNM and LNM20 (Figure S1) and LNM and XHQ10 (Figure S2) at the species level. The X coordinate was $|\log2\ (\text{fold change})|$ and the Y coordinate was $-\log 10$ (P adj), $p < 0.05$, log2 (fold change) >2. Each point represented a species. Table S1: All OTU classification information table; Table S2: Table of relative abundance of each sample at each taxonomic level; Table S3: Cazy database class level abundance table; Table S4: Cazy database abundance table.

**Author Contributions:** Conceptualization, X.Z. and Y.Z.; methodology, D.P. and Y.Z.; software, D.P. and Y.Z.; validation, P.X. and F.L.; formal analysis, D.P. and P.X.; investigation, D.P., P.X., F.L., J.L., T.Z. and X.Z.; resources, X.Z. and Y.Z.; data curation, D.P.; writing—original draft preparation, D.P., P.X. and Y.Z.; writing—review and editing, X.Z. and Y.Z.; visualization, D.P. and Y.Z.; supervision, X.Z.; project administration, Y.Z.; funding acquisition, Y.Z. and X.Z. All authors have read and agreed to the published version of the manuscript.

**Funding:** This research was funded by the National Natural Science Foundation of China (32100065 and 32300031), Shandong Province Youth Entrepreneurship Technology Support Program for Higher Education Institutions (2023KJ207), and the Natural Science Foundation of Shandong Province of China (ZR2023MB095).

**Institutional Review Board Statement:** Not applicable.

**Data Availability Statement:** The data from the present study are available in the article; further inquiries can be directed to the corresponding author.

**Conflicts of Interest:** The authors declare no conflicts of interest.

## References

1. Jiang, W.-X.; Li, P.-Y.; Chen, X.-L.; Zhang, Y.-S.; Wang, J.-P.; Wang, Y.-J.; Sheng, Q.; Sun, Z.-Z.; Qin, Q.-L.; Ren, X.-B.; et al. A Pathway for Chitin Oxidation in Marine Bacteria. *Nat. Commun.* **2022**, *13*, 5899. [CrossRef]
2. Zhang, R.; Zhao, Q.; Yi, Z.; Zhang, K.; Shi, J.; Zhu, L.; Chen, Y.; Jin, J.; Zhao, L. Chitin Oligosaccharides for the Food Industry: Production and Applications. *Syst. Microbiol. Biomanuf.* **2022**, *3*, 49–74. [CrossRef]

3. Roy, V.C.; Islam, M.R.; Sadia, S.; Yeasmin, M.; Park, J.-S.; Lee, H.-J.; Chun, B.-S. Trash to Treasure: An Up-to-Date Understanding of the Valorization of Seafood By-Products, Targeting the Major Bioactive Compounds. *Mar. Drugs* **2023**, *21*, 485. [CrossRef]
4. Yadav, M.; Goswami, P.; Paritosh, K.; Kumar, M.; Pareek, N.; Vivekanand, V. Seafood Waste: A Source for Preparation of Commercially Employable Chitin/Chitosan Materials. *Bioresour. Bioprocess.* **2019**, *6*, 8. [CrossRef]
5. Aranaz, I.; Alcántara, A.R.; Civera, M.C.; Arias, C.; Elorza, B.; Heras Caballero, A.; Acosta, N. Chitosan: An Overview of Its Properties and Applications. *Polymers* **2021**, *13*, 3256. [CrossRef]
6. Sun, Y.; Cui, J.; Tian, L.; Mi, Y.; Guo, Z. Phenolic Acid Functional Quaternized Chitooligosaccharide Derivatives: Preparation, Characterization, Antioxidant, Antibacterial, and Antifungal Activity. *Mar. Drugs* **2023**, *21*, 535. [CrossRef]
7. Benchamas, G.; Huang, G.; Huang, S.; Huang, H. Preparation and Biological Activities of Chitosan Oligosaccharides. *Trends Food Sci. Technol.* **2021**, *107*, 38–44. [CrossRef]
8. Li, B.; Cui, J.; Xu, T.; Xu, Y.; Long, M.; Li, J.; Liu, M.; Yang, T.; Du, Y.; Xu, Q. Advances in the Preparation, Characterization, and Biological Functions of Chitosan Oligosaccharide Derivatives: A Review. *Carbohydr. Polym.* **2024**, *332*, 121914. [CrossRef]
9. Shi, J.; Deng, C.; Zhang, C.; Quan, S.; Fan, L.; Zhao, L. Combinatorial Metabolic Engineering of Escherichia Coli for de Novo Production of Structurally Defined and Homogeneous Amino Oligosaccharides. *Synth. Syst. Biotechnol.* **2024**, *9*, 713–722. [CrossRef]
10. Yamabhai, M.; Khamphio, M.; Min, T.T.; Soem, C.N.; Cuong, N.C.; Aprilia, W.R.; Luesukprasert, K.; Teeranitayatarn, K.; Maneedaeng, A.; Tuveng, T.R.; et al. Valorization of Shrimp Processing Waste-Derived Chitosan into Anti-Inflammatory Chitosan-Oligosaccharides (CHOS). *Carbohydr. Polym.* **2024**, *324*, 121546. [CrossRef]
11. Subramanian, K.; Balaraman, D.; Panangal, M.; Nageswara Rao, T.; Perumal, E.; Kumarappan, A.; Sampath Renuga, P.; Arumugam, S.; Thirunavukkarasu, R.; Aruni, W.; et al. Bioconversion of Chitin Waste through *Stenotrophomonas maltophilia* for Production of Chitin Derivatives as a Seabass Enrichment Diet. *Sci. Rep.* **2022**, *12*, 4792. [CrossRef] [PubMed]
12. Kumar, M.; Madhuprakash, J.; Balan, V.; Kumar Singh, A.; Vivekanand, V.; Pareek, N. Chemoenzymatic Production of Chitooligosaccharides Employing Ionic Liquids and *Thermomyces lanuginosus* Chitinase. *Bioresour. Technol.* **2021**, *337*, 125399. [CrossRef]
13. Zhou, J.; Wen, B.; Xie, H.; Zhang, C.; Bai, Y.; Cao, H.; Che, Q.; Guo, J.; Su, Z. Advances in the Preparation and Assessment of the Biological Activities of Chitosan Oligosaccharides with Different Characteristics. *Food Funct.* **2021**, *12*, 926–951. [CrossRef] [PubMed]
14. Aktuganov, G.E.; Melent'ev, A.I. Specific Features of Chitosan Depolymerization by Chitinases, Chitosanases, and Nonspecific Enzymes in the Production of Bioactive Chitooligosaccharides (Review). *Appl. Biochem. Microbiol.* **2017**, *53*, 611–627. [CrossRef]
15. Liu, Y.; Qin, Z.; Wang, C.; Jiang, Z. N-Acetyl-d-Glucosamine-Based Oligosaccharides from Chitin: Enzymatic Production, Characterization and Biological Activities. *Carbohydr. Polym.* **2023**, *315*, 121019. [CrossRef]
16. Dai, Y.; Yang, F.; Liu, X.; Wang, H. The Discovery and Characterization of a Novel Chitinase with Dual Catalytic Domains from a Qinghai-Tibetan Plateau Wetland Soil Metagenome. *Int. J. Biol. Macromol.* **2021**, *188*, 482–490. [CrossRef]
17. Sethupathy, S.; Morales, G.M.; Li, Y.; Wang, Y.; Jiang, J.; Sun, J.; Zhu, D. Harnessing Microbial Wealth for Lignocellulose Biomass Valorization through Secretomics: A Review. *Biotechnol. Biofuels* **2021**, *14*, 154. [CrossRef] [PubMed]
18. Wang, J.; Cao, L.; Liu, Y.; Zhang, Q.; Ruan, R.; Luo, X. Effect of Acclimatized Paddy Soil Microorganisms Using Swine Wastewater on Degradation of Rice Straw. *Bioresour. Technol.* **2021**, *332*, 125039. [CrossRef]
19. Barbosa, R.G.; van Veelen, H.P.J.; Pinheiro, V.; Sleutels, T.; Verstraete, W.; Boon, N. Enrichment of Hydrogen-Oxidizing Bacteria from High-Temperature and High-Salinity Environments. *Appl. Environ. Microbiol.* **2021**, *87*, e02439-20–20. [CrossRef]
20. Ibáñez, A.; Barreiro, C.; Diez-Galán, A.; Cobos, R.; Calvo-Peña, C.; Coque, J.J.R. Molecular Identification and Acid Stress Response of an *Acidithiobacillus thiooxidans* Strain Isolated from Rio Tinto (Spain). *IJMS* **2023**, *24*, 13391. [CrossRef]
21. Niu, L.; Chen, Y.; Li, Y.; Wang, Y.; Shen, J.; Wang, L.; Zhang, W.; Zhang, H.; Zhao, B. Diversity, Abundance and Distribution Characteristics of Potential Polyethylene and Polypropylene Microplastic Degradation Bacterial Communities in the Urban River. *Water Res.* **2023**, *232*, 119704. [CrossRef] [PubMed]
22. Mendes, I.V.; Garcia, M.B.; Bitencourt, A.C.A.; Santana, R.H.; de Castro Lins, P.; Silveira, R.; Simmons, B.A.; Gladden, J.M.; Kruger, R.H.; Quirino, B.F. Bacterial Diversity Dynamics in Microbial Consortia Selected for Lignin Utilization. *PLoS ONE* **2021**, *16*, e0255083. [CrossRef] [PubMed]
23. Mu, D.-S.; Liang, Q.-Y.; Wang, X.-M.; Lu, D.-C.; Shi, M.-J.; Chen, G.-J.; Du, Z.-J. Metatranscriptomic and Comparative Genomic Insights into Resuscitation Mechanisms during Enrichment Culturing. *Microbiome* **2018**, *6*, 230. [CrossRef] [PubMed]
24. Zhang, Y.; Pan, D.; Xiao, P.; Xu, Q.; Geng, F.; Zhang, X.; Zhou, X.; Xu, H. A Novel Lytic Polysaccharide Monooxygenase from Enrichment Microbiota and Its Application for Shrimp Shell Powder Biodegradation. *Front. Microbiol.* **2023**, *14*, 1097492. [CrossRef] [PubMed]
25. Pan, D.; Liu, J.; Xiao, P.; Xie, Y.; Zhou, X.; Zhang, Y. Research Progress of Lytic Chitin Monooxygenase and Its Utilization in Chitin Resource Fermentation Transformation. *Fermentation* **2023**, *9*, 754. [CrossRef]
26. Chen, Y.; Zhou, N.; Chen, X.; Wei, G.; Zhang, A.; Chen, K.; Ouyang, P. Characterization of a New Multifunctional GH20 β-N-Acetylglucosaminidase From *Chitinibacter* sp. GC72 and Its Application in Converting Chitin Into N-Acetyl Glucosamine. *Front. Microbiol.* **2022**, *13*, 874908. [CrossRef] [PubMed]
27. Wang, J.; Zhu, M.; Wang, P.; Chen, W. Biochemical Properties of a Cold-Active Chitinase from Marine Trichoderma Gamsii R1 and Its Application to Preparation of Chitin Oligosaccharides. *Mar. Drugs* **2023**, *21*, 332. [CrossRef] [PubMed]

28. Aam, B.B.; Heggset, E.B.; Norberg, A.L.; Sørlie, M.; Vårum, K.M.; Eijsink, V.G.H. Production of Chitooligosaccharides and Their Potential Applications in Medicine. *Mar. Drugs* **2010**, *8*, 1482–1517. [CrossRef] [PubMed]
29. Kumar, M.; Brar, A.; Vivekanand, V.; Pareek, N. Bioconversion of Chitin to Bioactive Chitooligosaccharides: Amelioration and Coastal Pollution Reduction by Microbial Resources. *Mar. Biotechnol.* **2018**, *20*, 269–281. [CrossRef]
30. Segata, N.; Izard, J.; Waldron, L.; Gevers, D.; Miropolsky, L.; Garrett, W.S.; Huttenhower, C. Metagenomic Biomarker Discovery and Explanation. *Genome Biol.* **2011**, *12*, R60. [CrossRef]
31. Suma, K.; Podile, A.R. Chitinase A from Stenotrophomonas Maltophilia Shows Transglycosylation and Antifungal Activities. *Bioresour. Technol.* **2013**, *133*, 213–220. [CrossRef] [PubMed]
32. Arnold, N.D.; Garbe, D.; Brück, T.B. Isolation, Biochemical Characterization, and Genome Sequencing of Two High-quality Genomes of a Novel Chitinolytic *Jeongeupia* Species. *Microbiologyopen* **2023**, *12*, e1372. [CrossRef] [PubMed]
33. Arnold, N.D.; Garbe, D.; Brück, T.B. Proteomic and Transcriptomic Analyses to Decipher the Chitinolytic Response of *Jeongeupia* spp. *Mar. Drugs* **2023**, *21*, 448. [CrossRef] [PubMed]
34. Zain, N.-A.A.; Ng, L.-M.; Foong, C.P.; Tai, Y.T.; Nanthini, J.; Sudesh, K. Complete Genome Sequence of a Novel Polyhydroxyalkanoate (PHA) Producer, *Jeongeupia* sp. USM3 (JCM 19920) and Characterization of Its PHA Synthases. *Curr. Microbiol.* **2020**, *77*, 500–508. [CrossRef] [PubMed]
35. Yuan, P.-B.; Zhan, Y.; Zhu, J.-H.; Ling, J.-H.; Chen, E.-Z.; Liu, W.-T.; Wang, L.-J.; Zhong, Y.-X.; Chen, D.-Q. Pan-Genome Analysis of *Laribacter hongkongensis*: Virulence Gene Profiles, Carbohydrate-Active Enzyme Prediction, and Antimicrobial Resistance Characterization. *Front. Microbiol.* **2022**, *13*, 862776. [CrossRef] [PubMed]
36. Kim, B.-Y.; Weon, H.-Y.; Yoo, S.-H.; Chen, W.-M.; Kwon, S.-W.; Go, S.-J.; Stackebrandt, E. *Chitinimonas Koreensis* sp. Nov., Isolated from Greenhouse Soil in Korea. *Int. J. Syst. Evol. Microbiol.* **2006**, *56*, 1761–1764. [CrossRef] [PubMed]
37. Zhang, A.; Mo, X.; Zhou, N.; Wang, Y.; Wei, G.; Hao, Z.; Chen, K. Identification of Chitinolytic Enzymes in *Chitinolyticbacter meiyuanensis* and Mechanism of Efficiently Hydrolyzing Chitin to N-Acetyl Glucosamine. *Front. Microbiol.* **2020**, *11*, 572053. [CrossRef]
38. Rani, T.S.; Madhuprakash, J.; Podile, A.R. Chitinase-E from *Chitiniphilus shinanonensis* Generates Chitobiose from Chitin Flakes. *Int. J. Biol. Macromol.* **2020**, *163*, 1037–1043. [CrossRef] [PubMed]
39. Roesch, L.F.W.; Fulthorpe, R.R.; Riva, A.; Casella, G.; Hadwin, A.K.M.; Kent, A.D.; Daroub, S.H.; Camargo, F.A.O.; Farmerie, W.G.; Triplett, E.W. Pyrosequencing Enumerates and Contrasts Soil Microbial Diversity. *ISME J.* **2007**, *1*, 283–290. [CrossRef]
40. Nguyen, S.T.C.; Freund, H.L.; Kasanjian, J.; Berlemont, R. Function, Distribution, and Annotation of Characterized Cellulases, Xylanases, and Chitinases from CAZy. *Appl. Microbiol. Biotechnol.* **2018**, *102*, 1629–1637. [CrossRef]
41. Moon, M.; Lee, J.-P.; Park, G.W.; Lee, J.-S.; Park, H.J.; Min, K. Lytic Polysaccharide Monooxygenase (LPMO)-Derived Saccharification of Lignocellulosic Biomass. *Bioresour. Technol.* **2022**, *359*, 127501. [CrossRef] [PubMed]
42. Ren, X.-B.; Dang, Y.-R.; Liu, S.-S.; Huang, K.-X.; Qin, Q.-L.; Chen, X.-L.; Zhang, Y.-Z.; Wang, Y.-J.; Li, P.-Y. Identification and Characterization of Three Chitinases with Potential in Direct Conversion of Crystalline Chitin into N, N′-Diacetylchitobiose. *Mar. Drug* **2022**, *20*, 165. [CrossRef] [PubMed]
43. Colson, S.; van Wezel, G.P.; Craig, M.; Noens, E.E.E.; Nothaft, H.; Mommaas, A.M.; Titgemeyer, F.; Joris, B.; Rigali, S. The Chitobiose-Binding Protein, DasA, Acts as a Link between Chitin Utilization and Morphogenesis in Streptomyces Coelicolor. *Microbiology* **2008**, *154*, 373–382. [CrossRef] [PubMed]
44. López-García, C.L.; Guerra-Sánchez, G.; Santoyo-Tepole, F.; Olicón-Hernández, D.R. Chitinase Induction in *Trichoderma harzianum*: A Solid-State Fermentation Approach Using Shrimp Waste and Wheat Bran/Commercial Chitin for Chitooligosaccharides Synthesis. *Prep. Biochem. Biotechnol.* **2024**, *12*, 1–11. [CrossRef] [PubMed]
45. Zhang, J.; Wang, L.; Tan, W.; Li, Q.; Dong, F.; Guo, Z. Preparation of Chitosan-Rosmarinic Acid Derivatives with Enhanced Antioxidant and Anti-Inflammatory Activities. *Carbohydr. Polym.* **2022**, *296*, 119943. [CrossRef] [PubMed]
46. Wang, K.; Yu, D.; Bai, Y.; Cao, H.; Guo, J.; Su, Z. Isolation and Purification of Chitosan Oligosaccharides (Mw $\leq$ 1000) and Their Protective Effect on Acute Liver Injury Caused by CCl4. *Mar. Drugs* **2024**, *22*, 128. [CrossRef] [PubMed]
47. Xia, W.; Wei, X.Y.; Xie, Y.Y.; Zhou, T. A Novel Chitosan Oligosaccharide Derivative: Synthesis, Antioxidant and Antibacterial Properties. *Carbohydr. Polym.* **2022**, *291*, 119608. [CrossRef]
48. Zhang, Y.; Zhou, X.; Ji, L.; Du, X.; Sang, Q.; Chen, F. Enzymatic Single-Step Preparation and Antioxidant Activity of Hetero-Chitooligosaccharides Using Non-Pretreated Housefly Larvae Powder. *Carbohydr. Polym.* **2017**, *172*, 113–119. [CrossRef]
49. Rojas-Avelizapa, L.I.; Cruz-Camarillo, R.; Guerrero, M.I.; Rodríguez-Vázquez, R.; Ibarra, J. Selection and Characterization of a Proteo-Chitinolytic Strain of Bacillus Thuringiensis, Able to Grow in Shrimp Waste Media. *World J. Microbiol. Biotechnol.* **1999**, *15*, 299–308. [CrossRef]
50. Benzie, I.F.F.; Strain, J.J. The Ferric Reducing Ability of Plasma (FRAP) as a Measure of "Antioxidant Power": The FRAP Assay. *Anal. Biochem.* **1996**, *239*, 70–76. [CrossRef]

marine drugs

Article

# Tunable Oxidized-Chitin Hydrogels with Customizable Mechanical Properties by Metal or Hydrogen Ion Exposure

**Angelica Mucaria, Demetra Giuri, Claudia Tomasini, Giuseppe Falini and Devis Montroni ***

Department of Chemistry "Giacomo Ciamician", University of Bologna, Via F. Selmi 2, 40126 Bologna, Italy; angelica.mucaria2@unibo.it (A.M.); demetra.giuri2@unibo.it (D.G.); claudia.tomasini@unibo.it (C.T.); giuseppe.falini@unibo.it (G.F.)
* Correspondence: devis.montroni@unibo.it

**Abstract:** This study focuses on the optimization of chitin oxidation in C6 to carboxylic acid and its use to obtain a hydrogel with tunable resistance. After the optimization, water-soluble crystalline β-chitin fibrils (β-chitOx) with a degree of functionalization of 10% were obtained. Diverse reaction conditions were also tested for α-chitin, which showed a lower reactivity and a slower reaction kinetic. After that, a set of hydrogels was synthesized from β-chitOx 1 wt.% at pH 9, inducing the gelation by sonication. These hydrogels were exposed to different environments, such as different amounts of $Ca^{2+}$, $Na^{+}$ or $Mg^{2+}$ solutions, buffered environments such as pH 9, PBS, pH 5, and pH 1, and pure water. These hydrogels were characterized using rheology, XRPD, SEM, and FT-IR. The notable feature of these hydrogels is their ability to be strengthened through cation chelation, being metal cations or hydrogen ions, with a five- to tenfold increase in their storage modulus (G′). The ions were theorized to alter the hydrogen-bonding network of the polymer and intercalate in chitin's crystal structure along the a-axis. On the other hand, the hydrogel dissolved at pH 9 and pure water. These bio-based tunable hydrogels represent an intriguing material suitable for biomedical applications.

**Keywords:** chitin; gel; oxidation; calcium; pH

## 1. Introduction

Hydrogels are materials characterized by a crosslinked 3D network of polymeric molecules, fibers, or particles, in which the aqueous phase acts as a dispersing medium. Due to their nature, these materials have the ability to absorb and retain large quantities of water without dissolving or undergoing significant changes in shape [1,2].

Hydrogels can be classified based on their framework molecules, method of synthesis, and the type of interactions (i.e., chemical or physical) that define them. However, a relevant distinction is made between synthetic and natural hydrogels, depending on the source of the constituent molecule or molecules [3]. The latter are frequently preferred over their synthetic counterparts due to their reproducibility, biodegradability, non-toxicity, and biocompatibility. Currently, a variety of natural biopolymers are used to prepare hydrogels including cellulose, hemicellulose, chitin, chitosan, gelatin, agarose, starch, hyaluronic acid, alginate, collagen, and DNA [2,4]. Among these biopolymers, chitin has attracted great interest due to its huge reserves in nature, being the second most abundant biopolymer on Earth [5,6], high hydration, and strong network of hydrogen bonds [7]. All these properties make it a promising candidate for the preparation of highly swelling hydrogel systems [8,9]. Chitin exists in nature as three polymorphs, α-chitin, β-chitin, and ɣ-chitin, which differ in their arrangements of polymeric chains: anti-parallel, parallel, and alternating, respectively [10]. The α-chitin is the most abundant polymorph and can be found in arthropods cuticles, fungi cell walls, or the cysts of *Entamoeba* [11,12]. The β-chitin is still abundant in nature and can be found in mollusks, or other biomineralizing organisms, as *Foraminifera* [13,14]. Finally, the ɣ-chitin is extremely rare and its actual existence is still debatable. To date, this last polymorph has been documented in the cocoon fibers of the *Orgya dubia*, the stomach of *Loligo*, and some insects' peritrophic membranes [5,15].

The α-chitin is the most crystalline polymorph, with a crystallinity generally greater than 80% [16]. It is characterized by a strong network of hydrogen bonds that lead to a high mechanical modulus. On the other hand, the β-chitin has a lower crystallinity and fewer intermolecular forces. This has led to a special interest in this polymorph since it is more prone to functionalization and solubilization compared to α-chitin [15].

Chitin-based hydrogels have shown promising application prospects in the field of biomedicine [2]. The usual method for gelling native chitin involves cross-linking chitin molecules in solutions using physical or chemical methods [17]. However, the main difficulty in making chitin hydrogels is the lack of appropriate solvents due to chitin's insolubility. Several methods have been proposed to address this issue, including the use of specialized solvents to dissolve native chitin [18–23], hydrophilic modification [24,25], and the defibrillation of the material [1].

In Fan et al. (2008), a series of LiOH/KOH/urea aqueous solutions with different weight ratios were used to dissolve chitin structures with degrees of acetylation ranging from 5% to 94%. Then, coagulants were applied to these chitin/chitosan solutions to form robust hydrogels [16]. In Dang et al. (2020), the solubilization of chitin was carried out in a $CaCl_2$ methanol solution. Chitin hydrogels were then formed by adding excess water to the chitin solution and removing the methanol and calcium ions through dialysis or filtration [19]. In all these studies, organic solvents or other potentially toxic chemicals were used to achieve chitin solubilization.

Chitosan, an acid-soluble deacetylated derivative of chitin, allows hydrogels to be obtained by exploiting the interactions of the cationic amino groups of chitosan, with negatively charged molecules and anions. Chitosan can form an ionic complexation with small anionic molecules, such as sulfates, citrates, and phosphates [26,27], or metal anions such as $MoO_4^{2-}$ [28,29].

In contrast, in Ma, Qinyan, et al. (2019), a β-chitin fiber solution was obtained using ammonium persulfate as an oxidizing agent to introduce a carboxylic group at the C6 position of chitin [30].

Other oxidation methods are also reported in the literature. 2,2,6,6-Tetramethylpiperidine 1-oxyl (TEMPO) is often used as a primary oxidizing agent in combination with other co-oxidants, as in the system TEMPO/NaClO/NaBr [31,32]. However, the use of TEMPO to obtain soluble fibrils is a combined process often involving other steps such as mechanical disintegration, sonication, or the enzymatic, or acid hydrolysis method [33].

Oxidation with periodate is also reported. The reaction involves pre-treating chitin with KOH for 24 h and using periodic acid to ensure the correct amount of periodate ions in the reaction solution. The reaction requires long reaction times, such as 14 days, as reported by Liu et al. (2021) [34].

The carboxylic acid introduced with these methods facilitates the defibrillation of the system by creating negative charges that repel each other in a basic environment.

We chose to follow the oxidation method with ammonium persulfate as reported in Ma, Qinyan, et al. (2019), since our work represents a continuation of theirs. Additionally, the use of ammonium persulfate allows for chitin fibers to be obtained with fewer reaction steps and less time required, compared to other oxidants used.

The oxidized chitin fibers obtained by Ma, Qinyan, et al. (2019) were able to form hydrogels upon sonication. Following this method, the hydrogels could also potentially be formed by physical interactions (anion–cation and/or hydrogen bonding), avoiding the use of potentially toxic cross-linkers [35]. This potential was not explored in the 2019 paper.

Among biopolymers, oxidized chitin shows a similarity with alginate, as both structures have the C6 oxidized to a carboxylic group. However, in oxidized chitin, the degree of C6 oxidation is controlled and not complete as in alginate, which means the contribution of hydrogen bonding and apolar interactions is prevalent during gelation [36]. Moreover, alginate is solubilized as single molecules, while oxidized chitin dissolves/disperses as crystalline nano-fibrils. This difference affects the gelling capability, even if its mechanism is, in part, based on analogue interactions. Moreover, the presence of crystalline fibrils is expected to positively affect the mechanical resistance of the gel.

In this study, we aim to explore the potential preparation of hydrogels using both β-chitin and α-chitin as the starting material, aiming to explore their different reactivity. In Ma, Qinyan, et al. (2019), only β-chitin was studied. In addition to their work, our aim is to optimize their synthesis by controlling the starting material grain size and the oxidation conditions. By doing so, we expect to oxidize preferentially the chitin's low crystalline regions, leaving the core of the crystalline motifs almost unaltered. This would allow us to obtain hydrogel building blocks with a higher value. Finally, we want to explore the tunability of the hydrogel's mechanical properties by exposing it to diverse environments, as in the presence of metal ions or variable pHs.

These optimized hydrogels could lead to potential applications in diverse fields, including the biomedical one where a material's adaptation to a changing environment could be crucial.

## 2. Results and Discussion

### 2.1. Chitin Grain Size Optimization

The first step of the work was to optimize the material synthesis, to obtain soluble crystalline fibrils of oxidized chitin. To maximize the yield of production and fasten the kinetic of oxidation, we decided to work with chitin powder, rather than flakes, to have a higher initial exposed surface. While α-chitin was already purchased as a powder, the purchased β-chitin was milled to obtain a fine powder. Both powders were sieved to obtain diverse grain size: (i) from 600 μm to 150 μm, (ii) from 150 μm to 45 μm, and (iii) below 45 μm.

A study on the crystallinity and structure of α-chitin and β-chitin powders with diverse grain sizes was carried out. The aim was to reduce the grain size of the powder while preserving the crystallinity as much as possible. Table 1 reports the diffraction angles and the crystallite size (d) of the main reflections obtained from the analyses of X-ray powder diffraction (XRPD) patterns of α-chitin and β-chitin powders sieved at different grain sizes. The diffractograms are reported in Figure S1. Miller indices were attributed according to literature data [37,38]. Chitin's diffraction peaks are a convolution of different signals, and the Miller indices reported refers only to the most intense one, which contributes to most of the signal intensity.

**Table 1.** Diffraction angles and crystallite sizes (d) of the main reflections for the various grain sizes of α-chitin and β-chitin. The standard deviation of the measurements is reported in parentheses. Chitin's diffraction peaks are a convolution of different signals, the Miller indices reported refer only to the most intense signals which account for most of the signal intensity.

| | | 600–150 μm | | | 150–45 μm | | | <45 μm | | |
|---|---|---|---|---|---|---|---|---|---|---|
| **Sample** | | **$2\theta$ (°)** | **d (nm)** | **CI (%)** | **$2\theta$ (°)** | **d (nm)** | **CI (%)** | **$2\theta$ (°)** | **d (nm)** | **CI (%)** |
| α-chitin | (020) | 9.26 (0.01) | 7.05 (0.07) | 79.7 (0.4) | 9.16 (0.06) | 7.2 (0.2) | 78.0 (0.2) | 9.09 (0.03) | 7.0 (0.2) | 70.7 (0.7) |
| | (110) | 19.22 (0.01) | 4.82 (0.03) | 83.9 (0.2) | 19.13 (0.06) | 4.8 (0.2) | 81 (1) | 19.07 (0.04) | 4.48 (0.03) | 75.1 (0.7) |
| β-chitin | (010) | 8.2 (0.1) | 4.04 (0.09) | 69 (1) | 8.38 (0.06) | 3.78 (0.08) | 59 (3) | 8.07 (0.01) | 3.52 (0.07) | 46 (1) |
| | (100) | 19.7 (0.1) | 2.34 (0.08) | 68.7 (0.4) | 19.92 (0.03) | 2.17 (0.01) | 61 (1) | 19.62 (0.01) | 1.78 (0.01) | 49.5 (0.5) |

In the α-chitin powders, a shift of the (020) and (110) reflections towards lower diffraction angles was observed when reducing the grain size dimension from 600 μm down to below 45 μm. This indicates an increase in the unit cell parameters, suggesting a weakening of interchain interactions. This process was also associated with a mild decrease in crystallinity in the sample with a grain size < 45 µm, as indicated by the decrease in the crystal size along the zone axis associated to the (110) plane and the decrease in the CI calculated on both planes.

The β-chitin powder samples showed lower crystallinity than α-chitin, when compared in the same grain size ranges. Similarly, to that observed for α-chitin, a progressive reduction in the crystallinity occurred also for β-chitin. In this case, the decrease was observed both along the [010] and [100] zone axes. Moreover, for this polymorph, an increase in the lattice cell parameters was revealed by the shift of the diffraction peaks to lower angles which, as for α-chitin, can be associated with a weakening of the interplane and interchain interactions.

From the XRD analysis, for the β polymorph, a decrease in crystallite size corresponding to the (100) reflection is observed as the particle size decreases. An overall decrease in the material crystallinity was observed from the CI of both peaks decreasing the grain size.

A decrease in crystallinity decreasing particle size was also reported in Jorge A. et al. (2018) [39]. Both α-chitin and β-chitin were ground in a knife mill and sieved according to the particle sizes.

However, for the α polymorph, less significant variations are observed. This is consistent with the different crystalline packing of the two polymorphs, more compact for α-chitin [39].

Based on the obtained results, samples of α-chitin and β-chitin powders having grain sizes between 600 µm and 150 µm were used for further experiments, being the ones retaining the highest crystallinity.

### *2.2. Optimization of the Oxidation Time for β-Chitin*

The selected chitin samples, with a powder grain size of 600–150 µm, were oxidized by reacting with ammonium persulfate at a temperature of 40 °C following the procedure described in Section 3.4. This synthetic step was optimized in the reaction time.

An initial evaluation of the reaction progress was monitored through turbidity measurements, as the heterogeneous reaction proceeds with the dissolution of chitin particles. After just 3 h of reaction, the initial grains in the β-chitin powder reduced their dimensions, as evidenced by the rapid decrease in transmittance of the reaction batch (Figure S2). After 24 h, the reaction mixture showed a complete dissolution of chitin, while, after 45 h, an increment in turbidity was observed due to aggregate formation. In parallel, the yield of the reaction decreased progressively while increasing the reaction time; see Figure 1. This can be attributed to the formation of chitin fibers of nanometric sizes that were lost during the purification of the product or the degradation of chitin due to excessive oxidation. At 45 h, it was no longer possible to collect material, even by dialysis, suggesting a complete degradation of the polysaccharide chain. Considering the turbidity profile obtained and the yield associated with that, we decided to focus our attention on the following reaction times, 3 h, 6 h, 9 h, and 24 h, to sample along different positions of the turbidity profile. No time over 24 h was examined since the yield was considered too low.

The obtained oxidized chitin powders were examined using solid-state nuclear magnetic resonance (ss-NMR), Fourier-transform infrared spectroscopy (FT-IR), and XRPD.

The FT-IR spectra (see Figure S3b) showed all the absorption bands of chitin, plus a new weak absorption band at 1730 $cm^{-1}$. This band has been documented as a stretching of the C=O of carboxylic acids [30], demonstrating a positive functionalization of chitin. A ratio between this band and the band at 1073 $cm^{-1}$ (a C–O stretching associated to the sugar ring) was initially used to monitor the oxidation along the time; the results are reported in Figure S3c.

The ss-NMR spectra (see Figure S4) were used to calculate the degree of functionalization (%DF) of chitin. The %DF are reported in Figure 2 and show an incremental trend increasing the reaction time, showing an oxidation of about 10% of the C6 of the chitin monomers at 24 h. The trend observed is in accordance with the one extrapolated from the FT-IR spectra.

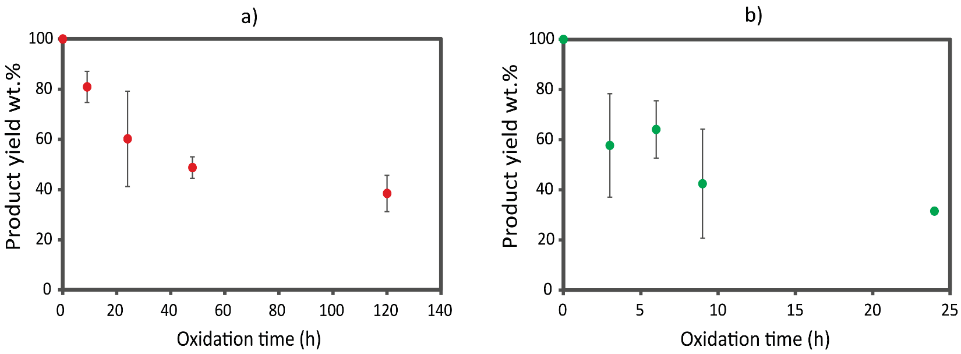

**Figure 1.** Product yield expressed as weight percentage obtained at the various oxidation times of (**a**) α-chitin and (**b**) β-chitin.

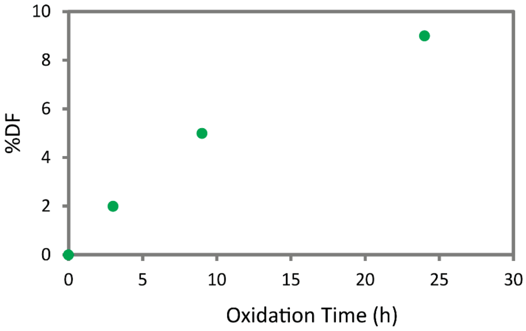

**Figure 2.** Degree of functionalization percentage (%DF) of C6 of β-chitin at different reaction times.

The XRPD analyses are reported in Table 2 and were used to identify the influence of oxidation on chitin's crystallographic organization. The diffraction patterns show that, along the [010] direction, a reduction in the cell parameter is observed, increasing the reaction time. This reduction is also associated with a decrease in crystallinity, revealed by a decrease in the crystal size. Conversely, along the [100] direction, the crystallinity and the dimension of the lattice parameter increased. This structural reorganization is likely due to the oxidation of C6 to a carboxylate group and a successive rearrangement of the hydrogen bond network in the crystal during the oxidation reaction.

**Table 2.** Diffraction angles and crystallite sizes (d) of the main reflections for the various oxidation time of β-chitin. The standard deviation of the measurements is reported in parentheses. Chitin's diffraction peaks are a convolution of different signals; the Miller indices reported refer only to the most intense signals which account for most of the signal intensity.

| | | **(010)** | | | **(100)** | |
|---|---|---|---|---|---|---|
| **Sample** | **2θ (°)** | **d (nm)** | **CI (%)** | **2θ (°)** | **d (nm)** | **CI (%)** |
| Control | 8.21 (0.04) | 4.0 (0.1) | 69 (1) | 19.70 (0.01) | 2.4 (0.1) | 68.7 (0.4) |
| 3 h | 8.32 (0.02) | 3.74 (0.08) | 74 (2) | 19.50 (0.05) | 2.60 (0.09) | 73 (3) |
| 6 h | 8.24 (0.01) | 3.65 (0.08) | 76 (2) | 19.44 (0.01) | 2.70 (0.04) | 73 (3) |
| 9 h | 8.62 (0.09) | 3.5 (0.3) | 65 (5) | 19.35 (0.07) | 2.73 (0.02) | 71 (1) |
| 24 h | 8.63 (0.07) | 3.3 (0.1) | 66 (3) | 19.26 (0.04) | 2.78 (0.07) | 75.4 (0.4) |

An increase in the average distance among the (100) plane agrees with what was expected with the C6 oxidation. In β-chitin, the C6 hydroxyl group is pointed along the a-axis and is involved in hydrogen bonding with the carbonyl group of the amide of the adjacent polymeric chain. Increasing the degree of functionalization is expected to increase the average distance along this direction since the carboxylate will require more space compared to a primary alcohol. Despite that, the carboxylate may act as a hydrogen bond receiver from the N-H of the amide. The hydrogen bond associated with a carboxylate group is expected to be stronger and more stable compared to that of an alcohol. Moreover, carboxylate has lower mobility due to its carbon hybridization and its higher steric hinderance compared to a primary alcohol. The combination of stabilization, new potential interactions, and a decrease in the mobility of this group may lead to the increase in crystallinity along this crystallographic axis.

On the other hand, a shrinkage of the cell parameters was observed along the [010] direction. This direction is perpendicular to the polymeric chains and does not present any direct hydrogen bonding between adjacent chains. The oxidation of the C6 may lead to the formation of direct hydrogen bonding in between polymeric chains, such as new hydrogen bonds involving the C=O of the carboxylate group, leading to a shortening of their average interplanar distance. Simultaneously, the relatively low degree of functionalization achieved will create small variations or kinks of the chains along this distance where the carboxylate group is, leading to an increase in the overall disorder of the crystal.

Based on the XRPD results, none of the rearrangement observed induced a significant loss in crystallinity.

In conclusion, combining the degree of functionalization calculated from the ss-NMR spectra (Figure 2) and the relative intensity of the FT-IR bands (Figure S3c), the 24 h time point was selected as the optimal reaction time. In fact, at 24 h, the reaction still shows a relevant product yield (32 wt.%), while the product has the highest degree of functionalization, approximately 10% of the C6 of β-chitin, with no significant loss in crystallinity.

### *2.3. Optimization of the Oxidation Time for α-Chitin*

In contrast to β-chitin, α-chitin shows a markedly different reactivity, coherent with what has previously been documented in the literature [5,15]. According to the turbidity measurements, the transmittance of the reaction batch decreases much more slowly compared to the β-chitin; see Figure S2. This suggests that α-chitin fibers are less accessible to ammonium persulfate, and defibrillation occurs over longer periods. At about 72 h, a complete dissolution of the chitin was observed. Basing on the turbidity measurement results, we decided to focus our attention on the following reaction times, 9 h, 24 h, 48 h, and 120 h, to sample along different positions of the turbidity profile. No time longer than 120 h were tested (even if it still showed a yield of about 40 wt.%.) since the reaction time would be too long and not compatible with practical applications.

A lower reactivity of α-chitin can also be deduced by FT-IR spectra analyses (Figure S3). As for β-chitin, an absorption band at 1730 cm$^{-1}$ is observed in the oxidized samples. A ratio between the intensity of this signal and the one at 1073 cm$^{-1}$ was calculated, as was carried out for the other polymorph. After 120 h, the relative intensity of the carboxylic acid band increases by only 27%, a value inferior to that obtained for β-chitin after 24 h of reaction (30%).

Compared to β-chitin, the FT-IR analyses on the oxidized α-chitin samples showed a smaller increment in oxidation in the first 24 h. No differences in the FT-IR relative intensity and yield (Figure 1a) were observed between 48 h and 120 h, suggesting the reaction reached a plateau, and the decrease in turbidity was probably due to slow solubilization processes.

The XRPD pattern was acquired for each of the α-chitin powder synthetized and the data are reported in Table 3 and Figure S5. Comparing the diffraction pattern, no significant variation was observed along the (110) or the (020) directions in the peak position. A mild increase in crystallinity was observed along the (020) plane, while no relevant trend in the crystallinity was identified along the (110) plane. The same result was also obtained by Jiang J. et al. [40], in which α-chitin is oxidized using the $O_2$/Laccase/TEMPO system, testing various concentrations of TEMPO. From the XRD analysis, it is observed that the structure of chitin remains mostly unchanged. Here, too, a slight increase in crystallinity is observed, probably due to the removal of the water-soluble amorphous zones during oxidation. These results suggest that oxidation occurs on the chitin fiber surface [40].

**Table 3.** Diffraction angles and crystallite sizes (d) of the main reflections for the various oxidation time of α-chitin. The standard deviation of the measurements is reported in parentheses. Chitin's diffraction peaks are a convolution of different signals; the Miller indices reported refer only to the most intense signals which account for most of the signal intensity.

| | **(020)** | | | **(110)** | | |
|---|---|---|---|---|---|---|
| **Sample** | **2θ (°)** | **d (nm)** | **CI (%)** | **2θ (°)** | **d (nm)** | **CI (%)** |
| Control | 9.26 (0.04) | 7.2 (0.1) | 79.7 (0.4) | 19.25 (0.01) | 5.23 (0.04) | 83.9 (0.2) |
| 9 h | 9.18 (0.07) | 7.6 (0.1) | 83.6 (0.4) | 19.13 (0.07) | 5.1 (0.1) | 89.2 (0.8) |
| 24 h | 9.21 (0.04) | 8.1 (0.4) | 83 (2) | 19.13 (0.01) | 5.3 (0.1) | 89.8 (0.8) |
| 48 h | 9.21 (0.04) | 8.1 (0.4) | 83.0 (0.1) | 19.2 (0.1) | 5.37 (0.06) | 91.6 (0.9) |
| 5 gg | 9.25 (0.09) | 8.0 (0.6) | 79.9 (0.2) | 19.22 (0.05) | 5.0 (0.3) | 91.0 (0.2) |

We chose to test only the β-chitin to produce oxidized chitin hydrogels, as α-chitin requires a long oxidation time to achieve a good degree of functionalization.

### 2.4. Rheological Analysis

Following the procedure described in Section 3.9, a hydrogel was obtained from the β-chitin grains in the range of 600–150 μm, oxidized for 24 h. The hydrogel prepared (1 wt.% concentration) appeared as a homogeneous material with a soft consistency, as is visible in the picture in Figure 3.

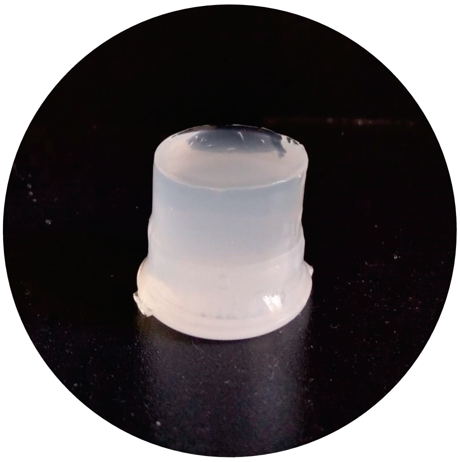

**Figure 3.** A β-chitin hydrogel camera picture. The hydrogel cylinder has a diameter of about 1 cm.

With the aim to modulate its mechanical resistance and test its chemical stability, we exposed the hydrogel to diverse environments. The conditions studied were mostly the following two: in the presence of calcium ions, and under different pH values.

The samples were prepared as described in Sections 3.9.1 and 3.9.2.

For the first study, various molar ratios between carboxylate groups and calcium ions ($Ca^{2+}$) were tested. Different addition methods of $Ca^{2+}$ were tested: (i) the surface addition of the calcium solution on the hydrogel, (ii) the mixing of the solution with the hydrogel, and (iii) the addition of $Ca^{2+}$ before sonication. Among them, the surface addition method was selected, as it produced samples with a higher storage modulus (G′) and better reproducibility compared with (ii) (as reported in Table S1), while method (iii) showed the formation of aggregates and hydrogel clumps.

### 2.4.1. Amplitude Sweep Tests

The viscoelastic behavior of the hydrogels in terms of storage (G′) and loss (G″) moduli, representing the elastic and the viscous portion of the viscoelastic behavior, respectively, was analyzed using rheological experiments. For all the tested samples, the G′ modulus is higher than the loss modulus G″, thus indicating that all the tested samples have a solid structure and can be classified as gels [41,42]. The linear viscoelastic region (LVE) indicates the range of strain where the sample is elastic and can recover its original state when the strain is removed. All the tested samples are very elastic, presenting a large LVE range and no crossover point (G′ = G″): none of the samples reaches the breaking point, where the material converts from solid to liquid.

$Ca^{2+}$ were added in different molar ratios compared to the carboxylate groups, quantified by ss-NMR (See Section 2.2). The molar ratios studied were $Ca^{2+}$: $COO^-$ equal to 1:3; 1:1; 3:1, and 5:1. These concentrations were chosen to explore different binding ratios between the carboxylate and the $Ca^{2+}$, assuming they would bind in a 1:1 or 1:2 ratio. Higher concentrations were studied to explore the presence of other binding sites.

The amplitude sweep curves of all tested samples are shown in Figure 4, while the numerical values derived from the analyses of the $Ca^{2+}$-treated samples are reported in Table 4. The data reveal that the incorporation of $Ca^{2+}$ results in a notable enhancement of the stiffness of the gels, which may be the consequence of a probable physical crosslinking between the $Ca^{2+}$ and the carboxylates present in the chain of the oxidized chitin [43]. Compared to the control, where the same volume of water was added, all the samples with $Ca^{2+}$ have a storage modulus one order of magnitude higher and show a better reproducibility, with reduced standard deviation values compared to the control.

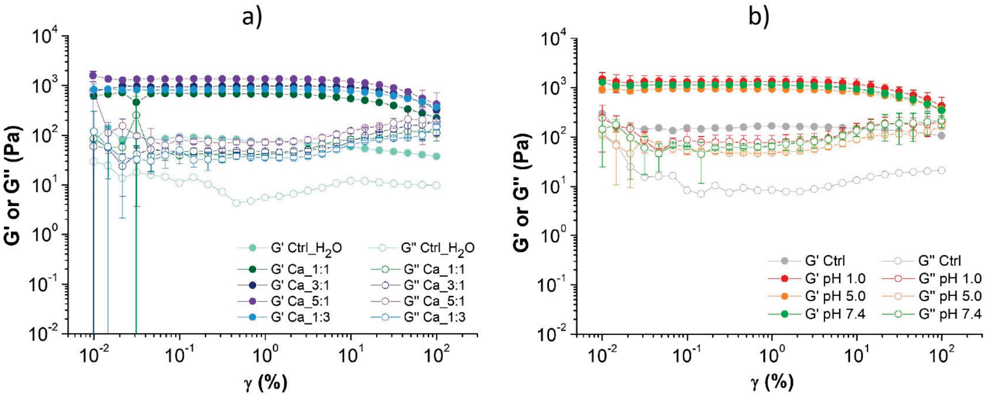

**Figure 4.** Amplitude sweep tests of the samples tested with (**a**) different molar ratios of $Ca^{2+}$ and (**b**) different pH conditions. The standard deviation of the Ctrl and Ctrl_$H_2O$ sample was omitted for clarity and its full graph can be seen in Figure S6.

**Table 4.** Table shows the values of G′ and G″ calculated at a shear strain value equal to 0.046%.

| Sample | Storage Modulus G′; (γ = 0.046%) | Loss Modulus G″; (γ = 0.046%) |
|---|---|---|
| | [Pa] | [Pa] |
| Ctrl_$H_2O$ | 80 ± 50 | 20 ± 10 |
| Ca_1:3 | 820 ± 30 | 30 ± 10 |
| Ca_1:1 | 690 ± 30 | 40 ± 20 |
| Ca_3:1 | 940 ± 50 | 50 ± 20 |
| Ca_5:1 | 1100 ± 300 | 60 ± 40 |

The increase in storage modulus rises with the increasing amount of added $Ca^{2+}$, resulting in a mechanically stronger material [44].

A similar increase in storage modulus was observed by modifying the type of bivalent metal ion, using magnesium ions in a 3:1 ratio (800 Pa). Furthermore, slightly lower $G'$ values (690 Pa) was observed when a NaCl solution with the same ionic strength was added (Table S2).

Comparing with the results found in the literature, the hydrogels obtained here show a superior performance compared to other hydrogels from natural polymers. In the work by Syverud, Kristin, et al. (2015), a cellulose nanofibril hydrogel obtained with TEMPO achieves a storage modulus $G'$ of 275 ± 62 Pa when using a 0.98 wt.% dispersion [45]. Additionally, in the work by Cuomo et al. (2019), an increase in the strength of the alginate hydrogel is reported, correlated to the quantity of added $Ca^{2+}$. However, using a 1 wt.% alginate solution, the maximum storage modulus reached is only 100 Pa [46]. Lower G′ values (about $10^2$ Pa) were also reported for gelatin gels (1 wt.%) blended with increasing amounts of chitosan (0.1–0.8 wt.%) with pH values between 3 and 4 [47]. Few examples of chitin gels were also reported, obtained by heating the polymer in ionic liquids. In these cases, the stiffness is highly dependent on the solvent used. Weak gels ($G'$ values in the range $10^1$–$10^2$ Pa) [48] were obtained from IL (1-allyl-3-methylimidazolium bromide) for relatively high chitin concentrations (5–7 wt.%). $G'$ values slightly higher than ours (about $10^4$ Pa) were instead reported by Deng et al. (2020) for 1 wt.% chitin gels obtained in [BMIM]Ac (1-butyl-3-metlimidazolium acetate) [19].

Successively the stability of the hydrogel at different pHs, specifically 1.0, 5.0, 7.4, and 9.0, was tested. These pHs were chosen due to their biological relevance, as pH 1.0 is the pH associated with digestion (specifically in the stomach), 7.4 is generally considered a healthy physiological pH, and pH 5.0 is usually associated with inflammation. pH 9.0 was tested as an alkaline counterpart. In order to reproduce the hydrogel stability in a physiological environment, PBS was used as a buffer solvent at pH 7.4.

For this test, each hydrogel was immersed in a buffered solution for 24 h, while a hydrogel stored in milliQ water was measured as a control. At the end of this exposure, the hydrogels immersed in milliQ water and carbonate buffer at pH 9.0 were not tested because the gel lost its structure and dissolved completely. Due to the absence of a control experiment in the same condition, the initial hydrogel was used as the control experiment.

The remaining samples were measured for their rheological properties and the results of the amplitude test are shown in the Figure 4b, while the numerical data are reported in Table 5. The hydrogels immersed in pH 1.0, pH 5.0, and pH 7.4 show a storage modulus ($G'$) five times greater than the starting hydrogel used as a control, as seen in Figure 4b, but no significant difference in the rheological properties was observed among these conditions. A mild increase in the loss modulus was also observed in these samples compared to the control. Even in this case, no crossover points ($G' = G''$) are detected: none of the tested samples reaches the breaking point in the tested shear strain range.

**Table 5.** Table shows the values of $G'$ and $G''$ calculated at a shear strain value equal to 0.046%.

| Sample | Storage Modulus $G'$; ($\gamma$ = 0.046%) | Loss Modulus $G''$; ($\gamma$ = 0.046%) |
|---|---|---|
| | [Pa] | [Pa] |
| Ctrl | 200 ± 100 | 20 ± 20 |
| pH 1 | 1300 ± 400 | 50 ± 10 |
| pH 5 | 950 ± 60 | 70 ± 10 |
| pH 7.4 | 1150 ± 30 | 50 ± 30 |

These results suggest that, within the oxidized chitin hydrogel, favorable interactions are formed at pH 1.0, 5.0, and 7.4. However, at very basic pH levels (pH 9.0), the interactions are so weak that they cause the collapse of the entire hydrogel structure. Indeed, at acidic pH levels, the deacetylated amines ($pK_a$ 6.3) [5] of chitin protonate and can interact with the carboxylate ions (with a $pK_a$ likely similar to that of alginate, 3.2 [49]) present in the polymer chains. Alternatively, since we do not know the actual $pK_a$ of this compound, at basic pH levels, the carboxylic acids may deprotonate, and the electrostatic repulsion between polymeric chains, combined with the higher polymer solubility, may lead to the collapse of the hydrogel structure.

The collapse of the hydrogel in water, on the other hand, suggests that it is probably unstable at pHs much lower than pH 9. Acid pHs may stabilize the material, inducing positive interactions by protonation, while PBS may stabilize the structure by cation ionic bridges, as already observed by adding NaCl, $MgCl_2$, or $CaCl_2$. Considering the composition of PBS, the ion bridges formed are likely due to $Na^+$ or $K^+$. Specifically, in the previous section, it was observed that $Na^+$ induced a toughening of the hydrogel, but its efficiency is lower compared to $Ca^{2+}$. The higher $G'$ observed at pH 7.4 (PBS) is likely due to the abundance of $Na^+$ in the PBS, which allowed us to saturate all the binding sites, maximizing the interactions in the hydrogel.

#### 2.4.2. Frequency Sweep Tests

Frequency sweep tests were carried out on the different hydrogel samples to describe their time-dependent behavior in the non-destructive deformation range (LVE). The shear strain value ($\gamma$= 0.1%) to perform the test was chosen within the LVE region, obtained from the amplitude sweep (see Section 3.10.1).

The results of the frequency sweep experiments (Figures S7 and S8) confirm the solid-like behavior of all the hydrogels ($G' > G''$). Some of the samples show a crossover point at high frequencies (always $\omega > 10$ rad/s) where $G' < G''$ and a probable breaking of the gel network occurs. The only samples where $G'$ and $G''$ are completely independent from the frequency and exhibit purely elastic properties [50] are the gel with Ca 5:1 and the one at pH 5.0, apart from the Ctrl, which has a lower value of $G'$. From this, it can also be deduced that the hydrogel right after the synthesis, Ctrl, is elastic, while the control sample with the addition of water, Ctrl_$H_2O$, shows a viscoelastic behavior. This is coherent with the solubilization observed when fully immersed in water. In all samples, $G'$ exhibits a constant trend for the majority of the tested frequencies. This indicates the presence of a stable cross-linked network [51].

### *2.5. Structural Characterization*

#### 2.5.1. Infrared Spectroscopy

The attenuated total reflectance (ATR) FT-IR spectra were performed on the freeze-dried hydrogels and used to investigate variations in the interactions in the hydrogel network in the different environments. In all samples, the same pattern of absorption bands was observed and only shifts and changes in relative intensity were observed.

In Figure 5, the spectra of the samples with an increased amount of $Ca^{2+}$ are reported. The addition of $Ca^{2+}$ was observed to induce changes in the O-H stretching (from 3435 to 3372 $cm^{-1}$) and in the shape of the amide I band, which exhibits two peaks (at 1630 and 1655 $cm^{-1}$), in the control that merge into a single peak as more $Ca^{2+}$ were added. Additionally, a shift in the peak of C-O stretching (from 1029 to 1025 $cm^{-1}$ and from 1067 to 1064 $cm^{-1}$) and N-H stretching is observed (from 3099 to 3108 $cm^{-1}$; from 3280 to 3255 $cm^{-1}$). No shift was observed in the absorption bands associated with the carbon backbone of the polymer (i.e., sugar ring vibration).

The shifts observed are mostly associated with functional groups involved in hydrogen bonding as a donor or receiver. According to that, $Ca^{2+}$ ions seem to interact in between polymeric chains and mediate hydrogen bonding between the chitin polymeric chains involving hydroxyl groups, and the amide N-H and carbonyl group. This intercalation does not appear to interfere with the polymer chain structure which appears unaltered, meaning no intramolecular difference in the degree of freedom of the polymeric chains is observed.

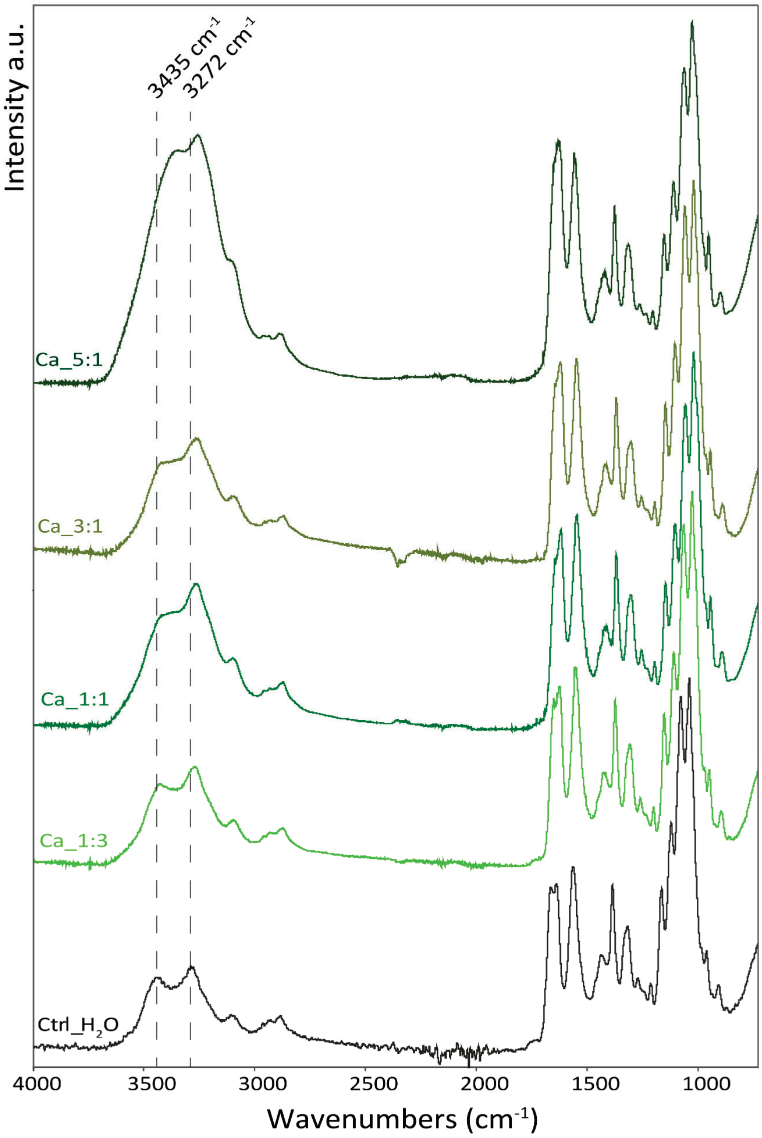

**Figure 5.** ATR-FTIR spectra of the samples with different $Ca^{2+}$/carboxylate groups molar ratios. The dashed lines indicate the stretching motion of O-H (3435 $cm^{-1}$) and N-H stretching (3281 $cm^{-1}$) referred to the control sample (Ctrl_$H_2O$).

In the hydrogels stored at different pH conditions, the O-H stretching band shifted to lower wavenumbers (from 3280 to 3255 $cm^{-1}$) along with the N-H stretching (from 3094 to 3090 $cm^{-1}$) as the pH decreases. Along with this shift, the two bands tend to merge into one; see Figure 6.

The amide I band exhibits the same trend observed in the hydrogels treated with calcium where the control shows a band split into two peaks that merge into one as the pH decreases.

The pH variation also affects the ring vibration, as evidenced by the shift of the ring stretching band from 894 to 900 $cm^{-1}$, increasing the pH. Other bands associated with the polymer backbone do not appear to show significant shifts (i.e., asymmetric bridge oxygen stretching, or asymmetric in phase ring stretching).

Contrary to the $Ca^{2+}$-treated hydrogels, a shift in the $CH_2$ bending and $CH_3$ deformation was observed from 1429 $cm^{-1}$ in the control to about 1419 $cm^{-1}$ for all the pH-treated samples. No other significant shift was observed in other apolar moieties.

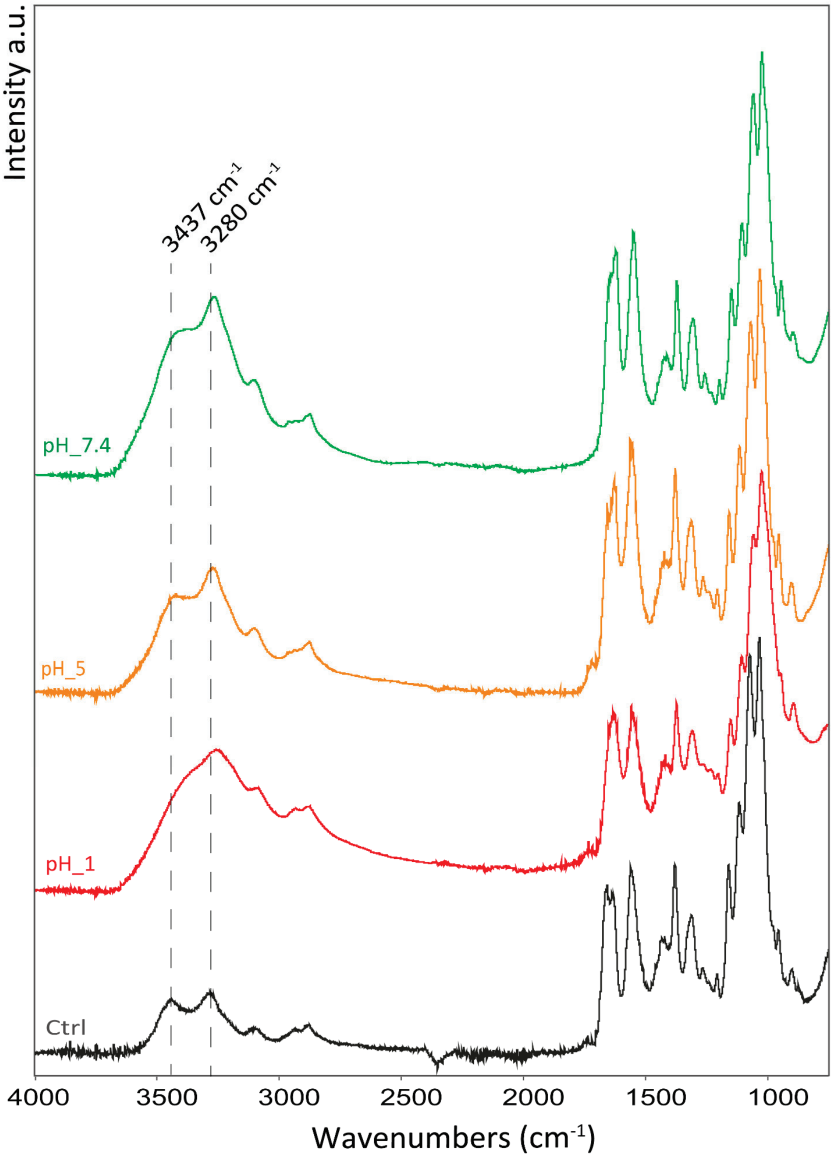

**Figure 6.** ATR-FTIR spectra of samples in different pH conditions. The dashed lines indicate the stretching motion of O-H (3437 cm$^{-1}$) and N-H stretching (3280 cm$^{-1}$) referred to the control sample (Ctrl).

As observed with the hydrogel treated with Ca$^{2+}$, an increase in the hydrogel rheological properties is associated with shifts to lower wavenumbers in the functional groups involved in hydrogen bonding (O-H, N-H, and C=O). This suggests a shortening of the hydrogen-bonding interactions, leading to more polarized functional groups and higher interactions between polymeric chains. Along with that, pH appears to also force additional interactions between apolar groups that affects the mobility of the chitin ring. This interaction is likely positively driven by the increment in the polarity and ionic strength of the solution.

All peak assignments are provided in the supporting information Table S3 [52].

### 2.5.2. X-ray Powder Diffraction Analysis

X-ray powder diffraction (XRPD) analysis was performed on the freeze-dried hydrogels to investigate their structural organization.

In the XRPD analyses of the hydrogels obtained with different Ca$^{2+}$ additions, reported in Figure 7a, an overall decrease in the crystallinity was observed, increasing the Ca amount.

This was observed as a decrease in the overall signal intensity; the XRPD were acquired on a similar amount of the sample.

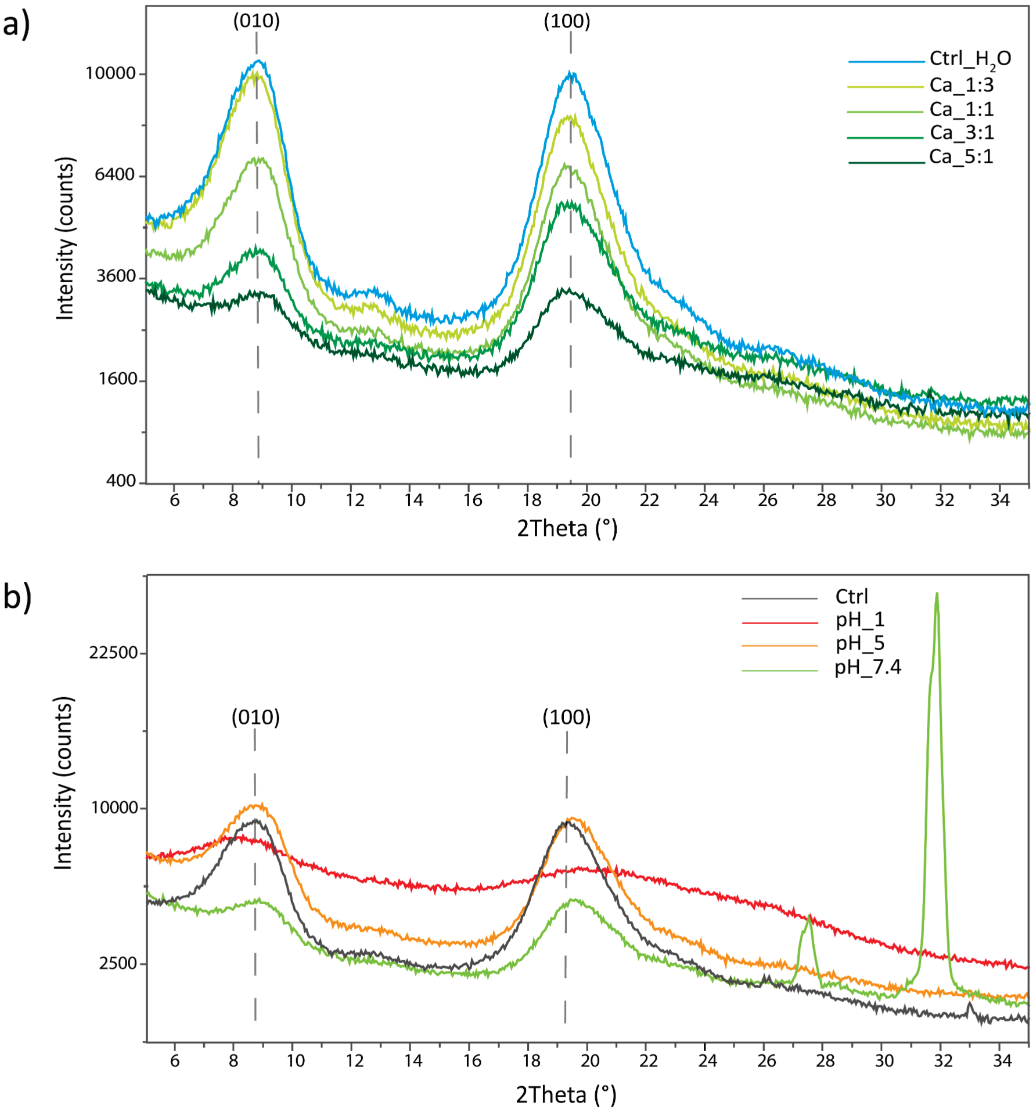

**Figure 7.** XRPD analyses on freeze-dried hydrogels treated (**a**) with different carboxylate group/calcium ion molar ratios (**b**) in different pH conditions. Chitin's diffraction peaks are a convolution of different signals; the Miller indices reported refer only to the most intense signals which account for most of the signal intensity. In the sample treated at pH 7.4, two additional peaks are visible; those peaks have been attributed to inorganic salts derived from traces of PBS in the hydrogel during freeze-drying.

A reduction in the unit cell parameter along the [010] direction was observed, increasing the $Ca^{2+}$. Indeed, the peak corresponding to the (010) reflection shifts from a value of 8.82° in the control sample treated with water to a value of 9.06° in the sample treated with Ca 5:1. This corresponds to a decrease in interplanar distance of 0.26 Å. The shift was associated with an increase in the crystallinity of this diffraction peak, visible as an increase in the crystal size. The results are reported in Table 6.

An increment in the a-axis unit cell parameter (0.02 Å), from 19.48° to 19.39°, was observed along the [100] direction, increasing the $Ca^{2+}$. In this case, a reduction in the crystallinity was observed along this direction. In this direction, an initial increase in crystallinity was observed, moving from the control to the sample treated with Ca 1:3 or 1:1.

**Table 6.** Diffraction angles and crystallite sizes (d) of the main reflections in the diffractograms obtained for the hydrogels containing different $Ca^{2+}$/carboxylate group molar ratios. Chitin's diffraction peaks are a convolution of different signals; the Miller indices reported refer only to the most intense signals which account for most of the signal intensity. * The values reported for the Ca_5:1 should be considered indicative, given the low quality of the diffraction peaks.

| | | (010) | | | (100) | |
|---|---|---|---|---|---|---|
| **Sample** | **2θ (°)** | **d (nm)** | **CI (%)** | **2θ (°)** | **d (nm)** | **CI (%)** |
| Ctrl_$H_2O$ | 8.82 | 3.59 | 73 | 19.48 | 3.08 | 72 |
| Ca_1:3 | 8.78 | 3.59 | 74 | 19.41 | 3.21 | 70 |
| Ca_1:1 | 8.87 | 3.69 | 69 | 19.41 | 3.17 | 68 |
| Ca_3:1 | 8.88 | 3.94 | 51 | 19.43 | 2.89 | 62 |
| Ca_5:1 * | 9.06 | 4.38 | 42 | 19.39 | 2.77 | 43 |

The results suggest that $Ca^{2+}$ ions intercalate in the crystal structure, disrupting its order and decreasing the overall polymer crystallinity. This intercalation is likely initially due to the chelation of the $Ca^{2+}$ by the carboxylate groups, and then probably affects different non-specific binding sites. A similar effect has also been reported in the preparation of a hydrogel starting from carboxymethylcellulose (CMC) crosslinked with calcium ions. In their work, the XRD analysis showed a crystallinity index (CI) of 32.77% for the CMC which becomes equal to only 4.24% when calcium is added [53].

In our case, this interaction is probably occurring along the a-axis (between the two planes of the sugar rings of adjacent polymeric chains) where we theorized the carboxylic group to be mostly located and involved as a hydrogen-bonding acceptor with the N-H of the amide in the adjacent chain. $Ca^{2+}$ is probably inserting in between the two parts of this hydrogen bond, inducing an enlargement of the cell parameter and introducing big defects in the crystal structure. The insertion of calcium ions along the a-axis in between polymeric chains could induce important modifications in the chain-to-chain interaction along the b-axis (where polymeric chains are positioned side-to-side). The presence of $Ca^{2+}$ could seize the carboxylate, eliminating the kinks and defects accumulated along this axis after the functionalization. On the other hand, the presence of a positive charge is probably acting as a bridge between the chains, inducing a contraction of the unit cell along this axis. Due to a lower steric hindrance along this plane and a higher interaction, the cell shrinks and becomes more ordered along this direction.

The XRPD acquired on the hydrogels exposed to different pHs are reported in Figure 7b. This set of samples showed a less clear trend compared to the $Ca^{2+}$-treated ones.

The overall intensity appeared to be comparable between the control and the sample at pH 5, while the sample at pH 7.4 showed an intensity intermediate to that of the samples treated with Ca 3:1 and 5:1. Finally, the sample treated at pH 1 showed the lowest overall crystallinity among all the hydrogel tested.

The same trend is also observed along the [100] direction where a reduction in the unit cell parameter is observed, moving from the control to pH 5, pH 7.4, and pH 1. The shift was also associated with a reduction in the crystal size. The results are reported in Table 7.

Along the [010] direction, a contraction of the cell parameter is observed at pH 5 and 7.4 along with an increase in crystal size. At pH 1, instead, a strong expansion of the unit cell and a decrease in crystallinity is observed along this direction.

In the sample at pH 7.4, two additional signals were observed at 27.51° and 31.87°. These signals were attributed to inorganic salts derived from the PBS solution entrapped in the hydrogel.

**Table 7.** Diffraction angles and crystallite sizes (d) of the main reflections in the diffractograms obtained for the hydrogels treated in different pH conditions. Chitin's diffraction peaks are a convolution of different signals; the Miller indices reported refer only to the most intense signals which account for most of the signal intensity. * The values reported for the pH_1 sample should be considered indicative, given the low quality of the diffraction peaks.

| | | (010) | | | (100) | |
|---|---|---|---|---|---|---|
| **Sample** | **2θ (°)** | **d (nm)** | **CI (%)** | **2θ (°)** | **d (nm)** | **CI (%)** |
| Ctrl | 8.71 | 3.59 | 73 | 19.39 | 3.14 | 73 |
| pH 1 * | 8.30 | 2.48 | 52 | 20.67 | 0.97 | 52 |
| pH 5 | 8.81 | 3.65 | 67 | 19.58 | 3.07 | 64 |
| pH 7.4 | 8.94 | 4.15 | 31 | 19.64 | 2.91 | 13 |

The XRPD results suggest a different interaction is governing the aggregation at pH 7.4 and 5 since a contraction is observed along the [100] direction, suggesting a positive contribution by the presence of ions to the interchain interactions. The carboxylate protonation in acid environment could, in fact, induce a change in the hydrogen-bonding pattern along the a-axis. It would likely interact with the C=O of the amide of the adjacent polymeric chain, restoring the native hydrogen bond pattern of β-chitin. Most likely, both ions' interactions, coherent with the observations in the (010) plane, and protonation are occurring, leading to the increase in disorder observed.

Contrary to all the previous samples, the sample at pH 1 appears strongly altered, up to almost complete amorphization. Due to that, the results concerning the peak position or the crystal size cannot be considered reliable. This strong alteration may be the result of a complete protonation of the carboxylic acids and/or the co-ordination of positive charges in the crystal in non-specific binding sites. In fact, β-chitin has already been reported as strongly swellable in acid pHs [7,54] and this amorphization may have been guided to the same interactions.

### 2.5.3. Scanning Electron Microscopy Analyses

Scanning electron microscopy (SEM) was used to analyze the morphology and aggregation of the freeze-dried hydrogels. After freeze-drying, all the samples retained their shape as hydrogels and showed a soft consistency; see Figure S9. The hydrogel treated at pH 1, instead, showed a strong shrinkage and a brittle consistency.

Observing the samples with SEM, all samples showed a porous structure with smooth sheet-like walls and filaments of fibers embedded in the matrix. The increment in the $Ca^{2+}$ addition was observed to be associated with a thickening of the pore walls and a reduction in the free fiber presence (Figure 8).

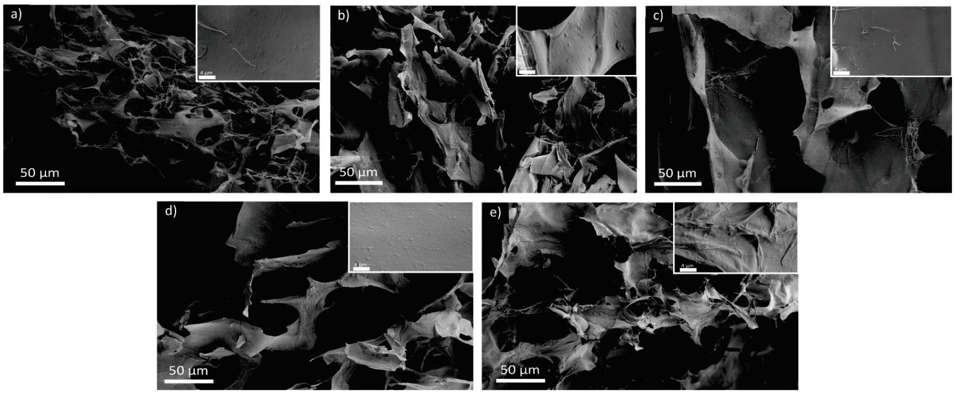

**Figure 8.** SEM images of the freeze-dried hydrogels: (**a**) Ctrl_$H_2O$; (**b**) Ca_1:3; (**c**) Ca_1:1; (**d**) Ca 3:1; and (**e**) Ca_5:1. For each condition, an insight with a higher magnification is reported.

A similar wall thickening and fiber reduction was observed also in the samples exposed to different pHs, as is visible in Figure 9. This effect followed the same trend observed in the XRPD, control sample, pH 5, pH 7.4, and, finally, pH 1. The latter showed the thickest walls among all samples and exhibited sharper and more delineated fractures.

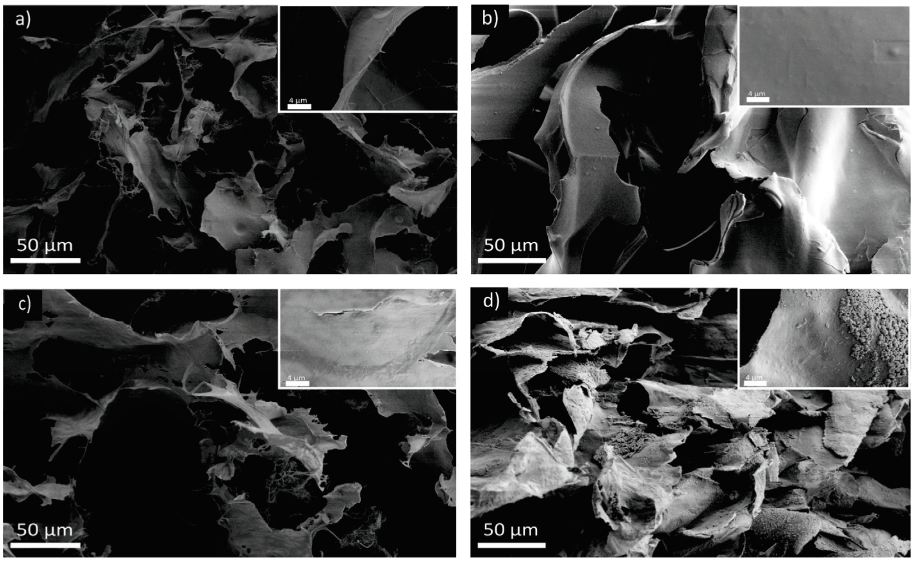

**Figure 9.** SEM images of the freeze-dried hydrogels exposed to different pHs: (**a**) Ctrl; (**b**) pH_1; (**c**) pH_5; and (**d**) pH_7.4. For each condition, an insight with a higher magnification is reported.

The sheet-like morphology observed could be an artifact of the sample freezing and may not be representative of the hydrogel organization in solution. Despite that, the SEM analyses suggests that an increase in the interactions of the hydrogel occurs, increasing the cation concentration in solution—we see a thickening of the laminar structures. This thickening is probably due to the aggregation of loosely bound fibers, which are then forced to interact with the hydrogel network.

### *2.6. Discussion on Hydrogel Tunability*

The characterizations performed on the hydrogels exposed to different environments showed how the rheological properties and the structure of the material can be rearranged based on diverse triggers. Such a rearrangement can increase the storage modulus of the gel from 5 to 10 times. These triggers are generally related to positively charged chemical species, such as metal cations or hydrogen ions.

These cations interact with the polymeric chains and even intercalate in the chitin's crystal structure. The cations seem to interact with groups generally involved in hydrogen bonding, namely, alcohols, amines, and amides (both N-H and C=O). A strong interaction is also likely occurring with the carboxylic group. These interactions probably see the cation involved in the dipolar interaction between these groups.

When the ions intercalate in the crystalline regions, this seems to happen along the a-axis, in between the sugar ring plane of the polymeric chains, causing a decrease in crystallinity. When $Ca^{2+}$ ions are intercalating, an expansion of the crystallographic unit cell in this direction is observed. On the other hand, a contraction is observed when monovalent cations, like $Na^+$, $K^+$, or $H^+$, interact with the hydrogel crystal units. This contraction is probably the reason why the $CH_2$ bending and the sugar ring stretching are affected.

Simultaneously, a contraction over the b-axis, where the polymeric chains are arranged side-to-side, is observed in all the conditions tested, along with an increase in crystallinity. This suggests an increment of the interactions over this direction, generally presenting very little direct interactions in β-chitin. Overall, the intercalation of cations in the crystal is associated with a decrease in crystallinity due to a disruption of the crystal structure order; this loss in crystallinity increases, increasing the ion concentration in solution.

The morphological examination of the freeze-dried hydrogels suggests an increase in the hydrogel network interaction, increasing the cation presence. It also shows how the fibrils in the hydrogel are only partially interacting in the control, and then increase their interaction when exposed to cations. This observation suggests that the cations induce the formation of additional linkage in the matrix, or favor the formation of the one already possible, forcing new fibrils to aggregate in the hydrogel network.

It is worth mentioning that the frequency sweep tests identified four samples with viscoelastic behavior instead of an elastic one. Except for one of the controls, the samples exhibiting a viscoelastic behavior are the ones exposed to the lowest and highest ion amounts—respectively, the Ca 1:3, the sample in PBS (pH 7.4), and the one at pH 1. This suggests an optimal ionic exposure that maximize the properties of the hydrogel, giving it an elastic behavior. This condition varies when different ions are used. Such a change in the rheological properties is probably due to an excessive aggregation of the fibrils, as visible in the SEM of the sample at pH 1, which confer a more brittle behavior.

## 3. Materials and Methods

### 3.1. Materials

The β-chitin flakes from the squid pens of *Loligo vulgaris* were purchased from BioLog Heppe® GmbH (Landsberg, Germany). The α-chitin powder from shrimp shells was purchased from Glentham Life Sciences (Planegg, Germany). All other chemical reagents were purchased from Merck and used without any additional purification.

### 3.2. Chitin Ball Milling

The initial β-chitin powder was ground with a ball mill 8000 Mixer Mill™ SPEX CertiPrep™ (Metuchen, NJ, USA). The jar used has a diameter of 3.85 cm and height 5.70 cm. The grinding was carried out with three small spheres with a diameter of 0.62 cm and three spheres with a diameter of 1.27 cm. Both the jar and the spheres are made of hardened steel. Then, 2 g of powder were ground at a time for 10 min. Subsequently, both β-chitin and α-chitin were sieved through 600, 150, and 45 μm sieves (GIULIANI Tecnologie srl, Turin, Italy) to separate different powder meshes.

### 3.3. X-ray Powder Diffraction Analysis

X-ray diffraction patterns were collected using a PanAnalytical X'Pert Pro diffractometer equipped with a multiarray X'Celerator detector using Cu Kα radiation generated at 40 kV and 40 mA ($\lambda = 1.54056$ Å).

The diffraction patterns were collected in the 2θ range between 5° and 35° with a step size ($\Delta 2\theta$) of 0.05° and time per step of 123 s.

The peak maximum and full width at half maximum (FWHM) measurements were calculated using the PanAnalytical X'Pert Data Viewer software (version 1.2d). The value was then used to determine the crystallite size (d) using the Sherrer equation.

The crystal index (CI) was determined as a percentage using the following equation [55,56]:

$$CI = [(I_{cryst} - I_{am})/I_{cryst}] \times 100$$

where $I_{cryst}$ is the intensity in counts at the maximum of the reflex and $I_{am}$ is the intensity of amorphous diffraction at $2\theta \cong 14°$.

### 3.4. Chitin Oxidation

For the oxidation reaction, 0.5 g of chitin powder (600–150 μm) were added in 50 mL of a 45 wt.% ammonium persulfate solution (APS) at 40 °C under stirring for diverse reaction times in a round bottom flask. For gel production, β-chitin was stirred for 24 h.

After that, the solution appears as an opalescent dispersion. The material in suspension was collected and washed with deionized water by consecutive centrifugation with an Eppendorf Centrifuge 5810 R at 8000 rpm for 5 min until it reached neutrality.

The powder was then resuspended in 30 mL of milliQ water and left under magnetic stirring overnight, to eliminate possible reaction residues. The next day, the powder was centrifuged, as was carried out previously, and resuspended in about 15 mL of milliQ water, frozen in the freezer, and desiccated by freeze-drying using a FreeZone 1 (Labconco Corp., Kansas City, MO, USA). The product was conserved dry at room temperature.

### *3.5. ss-NMR Measurements*

The $^{13}$C solid-state nuclear magnetic resonance (ss-NMR) experiments were performed on a Bruker 700 MHz Wide Bore spectrometer equipped with a 4 mm CP MAS X/Y/H DVT probe in a double-resonance H-X configuration. The analyses were performed operating at 260 K and MAS speed of 12 kHz. The CP contact time was 2 ms, and the recycle delay was 10 s. A typical number of 512 or 2048 scans were acquired for each spectrum.

The degree of functionalization (%$DF$) was calculated, setting the total integral for C3, C4, and C5 to 3 and measuring the C6 integral ($I_t$). The %$DF$ was then calculated using the following formula:

$$\%DF = \left(1 - \frac{I_t}{I_{t0}}\right) \times 100$$

where $I_t$ is the integral of the C6 signal attributed to the various oxidized chitin samples and it is the one of the initial chitins. The NMR signal attribution is reported in Figure S4 [15,57].

### *3.6. UV–Visible Spectroscopy*

Spectrophotometric measurements were carried out with a UV–vis spectrophotometer (Varian Cary 300 Bio UV–Visible Spectrophotometer, Santa Clara, CA, USA) using a spectral range of 300–900 nm, scan rate of 600 nm·min$^{-1}$, with a resolution of 1 nm. Turbidity measurements were measured at 500 nm.

### *3.7. FTIR-Spectroscopy*

The infrared spectra were collected using a Fourier-transform infrared spectroscopy (FTI) (Thermo Scientific Nicolet iS10, Waltham, MA, USA) and processed with Omnic software 9.8.286 (Thermo Electron Corp., Woburn, MA, USA).

The samples were prepared in KBr pellets (1 wt.% of sample) and the spectra were collected with 2 cm$^{-1}$ resolution and 70 scans.

The intensity of each peak was obtained by correcting the intensity on the baseline [30]. The oxidation degree was then evaluated by calculating the ratio between the carboxylic acid peak (1730 cm$^{-1}$) and the most intense peak of the glucosidic ring which falls at 1074 cm$^{-1}$ [58].

### *3.8. Product Yeld*

The product yield was calculated based on the initial mass ($mg_i$) of chitin powder and the final mass ($mg_f$) obtained from the oxidation reaction and calculated using the following formula:

$$product\ yield = \frac{mg_f}{mg_i} \times 100$$

### *3.9. Hydrogel Preparation*

Oxidized β-chitin powder (βchitOx) was dispersed in milliQ water to obtain a 1 wt.% dispersion. This was vigorously stirred using a magnetic stirrer for about 2 h at room temperature.

Once no visible aggregates were observed by the naked eye, the pH of the dispersion was between 3 and 4. A required volume of a 1 M NaOH solution was added to the dispersion to bring the pH between 8 and 9.

The obtained dispersion was divided into 2 mL aliquots inside sterilin tubes (Thermo Scientific™ Sterilin™ 7 mL Polystyrene Bijou Containers, Waltham, MA, USA) and sonicated at 10% amplitude with a tip sonicator (Branson Ultrasonics$^{TM}$ Brookfield, WI, USA; Sonifier 250; 20 kHz) equipped with a semimicro tip, with the container immersed in an ice bath to prevent overheating. The sonicated β-chitOx dispersion was then left to rest to obtain the βchitOx-hydrogel. Since only one type of unaltered (with $Ca^{2+}$ or pH) hydrogel was prepared in this study, we will refer to this sample as hydrogel or control.

#### 3.9.1. Metal Ion Addition to the Hydrogel

To investigate the effect of $Ca^{2+}$ on the hydrogel, different $CaCl_2$ solutions were prepared at concentrations of 16.6, 50, 150, and 250 mM. A volume equal to 196 µL of these solutions was used to obtain molar ratios of 1:3, 1:1, 3:1, and 5:1 with the carboxylate groups formed after the reaction of oxidation (quantified by ss-NMR measurement). The tests on $Mg^{2+}$ and $Na^{+}$ were performed using $MgCl_2$ and NaCl solutions.

Different addition methods were tested:

- Surface addition: Allowing the solution to drip from the walls of the sterilin tubes containing the hydrogel.
- Mixed addition: Inserting the solution into the hydrogel, and then mixing with the pipette tip. This process disrupts the hydrogel to better blend the solution.
- Calcium solution addition before the sonication step.

The hydrogel is then left to rest for 24 h to allow the $Ca^{2+}$ to diffuse homogenously.

#### 3.9.2. Study of pH Influence on the Hydrogel

The sterilins containing the hydrogels were immersed in beakers containing 90 mL of solutions at different pH values: 1 (0.1 M HCl); 5 (10 mM citrate buffer $Na_3C_6H_5O_7/C_6H_8O_7$); 7.4 (phosphate buffered saline, PBS); 9 (10 mM carbonate buffer $NaHCO_3$; $Na_2CO_3$); and MilliQ water used as control. The sterilins were left in solution with a mild stirring on a rocking table for 24 h; along this time, the buffer solution was changed twice to maintain a constant environment.

### *3.10. Hydrogel Characterization*

#### 3.10.1. Rheological Properties

The rheological properties of the different hydrogels were assessed using an Anton Paar (Graz, Austria) MCR102 rheometer. The tested hydrogels (2 mL) were directly prepared in 7 mL Sterilin™ polystyrene containers (Thermo Scientific™, Waltham, MA, USA) which fit in the rheometer. A cup and vane geometry was used, setting a gap of 2.1 cm. Oscillatory amplitude sweep experiments (ɣ: 0.01–100%) were performed using a constant angular frequency of 10 rad·s$^{-1}$. The frequency sweep experiments were performed at a constant shear strain of ɣ= 0.1% (within the LVE region) with an increasing angular frequency (ω) from 0.1 to 100 rad·s$^{-1}$. All tests were performed at a fixed temperature of 23 °C, controlled by an integrated Peltier system.

#### 3.10.2. FTIR-Spectroscopy

The hydrogels were analyzed using the FTIR equipment described in Section 3.7. The hydrogels were frozen with liquid nitrogen, and then dried by freeze-drying using a FreeZone 1 (Labconco Corp., Kansas City, MO, USA). The dry samples were measured in attenuated total reflectance (ATR) mode using 1 cm$^{-1}$ resolution and 200 scans. The data analysis was then performed using the OMNIC software 9.8.286.

#### 3.10.3. X-ray Powder Diffraction Analysis

For the X-ray powder analysis of the freeze-dried hydrogels (see Section 3.10.2), the same instrumentation described in Section 3.3 was used. The diffraction patterns were collected in the 2θ range between 5° and 35° with a step size (Δ2θ) of 0.05° and a time per step of 360 s.

### 3.10.4. Scanning Electron Microscopy Images

For the scanning electron microscopy (SEM) imaging, the samples were dried, as reported; see Section 3.10.2 (Figure S8) A piece of the dry samples was then cut with a scalpel, glued on a carbon tape, and coated with 10–20 nm of gold prior analyses. The images were collected with a SEM Zeiss LEOc1530 FEG using a voltage of 5 kV and an aperture of 20 µm.

## 4. Conclusions

In this study, we prepared tunable chitin hydrogels, exploring in detail, optimizing, and customizing a known synthetic process. The grain size of the starting material (between 600 µm and 150 µm) and the reaction time (24 h) were optimized to achieve highly crystalline oxidized β-chitin fibrils (having a %DF of 10%) with a yield of a 32 wt.%. Different reaction conditions were also tested on α-chitin, which exhibited a lower reactivity and a much longer reaction kinetic. Structural characterization (FT-IR and XRPD) was performed on all the reaction products to identify how the functionalization affects the structure of the biopolymer.

Successively, a hydrogel was obtained from the oxidized β-chitin. Such a hydrogel exhibited tunable rheological properties (up to a 10-times increment in $G'$) when exposed to cations ($Ca^{2+}$, $Mg^{2+}$, $Na^+$, or $H^+$), which induce structural rearrangements. The initial gelation is induced by a few minutes of sonication and occurs along the time, but it can be fastened if cations are present. Such a process could be compatible with an application as injectable gels for wound sealing or surgery since the physiological ion concentration would be enough to induce the formation of a tough hydrogel (as observed in PBS). Moreover, the hydrogel is stable in physiological environments, both healthy (pH 7.4), inflamed or unhealthy [59,60] (pH 5), and those connected to digestion (pH 1). This allows its use as a biomedical material for application with almost every human tissue. This also makes them a material of potential interest for the development of wound dressings. On the other hand, the instability of these hydrogels in alkaline environments and pure water make their disposal extremely easy and eco-friendly. Potentially, the hydrogel could even be dissolved at pH 9, and the fibrils could be recovered and recycled to produce a new hydrogel. Such a solubility could also be exploited to deliver biologically active compounds into the stomach of animals having an alkaline stomach pH, such as pests, like insects, or economically relevant animals, like sea urchins [61,62].

In conclusion, these negatively charged β-chitin fibrils could act as complementary materials to positively charged chitosan fibers. Additionally, their potential to obtain acid-stable tough hydrogels, that, alternatively, could be reinforced using metal cations, could represent an alternative to the structurally similar alginate hydrogels. This study sheds light on an alternative material with peculiar properties that could represent an important resource for the development of future technological materials, especially in the biomedical field.

**Supplementary Materials:** The following supporting information can be downloaded at: https://www.mdpi.com/article/10.3390/md22040164/s1, the full characterization of the oxidized chitins, missing rheological data or characterization of the hydrogel not reported in the main text (including frequency sweep tests), and the interpretation of the FT-IR bands.

**Author Contributions:** Conceptualization, G.F.; methodology, A.M., D.G., C.T., G.F. and D.M.; validation, A.M., D.G., C.T., G.F. and D.M.; formal analysis, A.M., D.G. and D.M.; investigation, A.M. and D.M.; resources, C.T. and G.F.; data curation, A.M., D.G. and D.M.; writing—original draft preparation, A.M.; writing—review and editing, A.M., D.G., C.T., G.F. and D.M.; visualization, G.F. and D.M.; supervision, D.G., C.T., G.F. and D.M.; project administration, G.F. and D.M.; funding acquisition, G.F. All authors have read and agreed to the published version of the manuscript.

**Funding:** G.F. thanks the National Recovery and Resilience Plan (NRRP), Mission 4 Component 2 Investment 1.4—Call for tender No. 3138 of 16 December 2021, rectified by Decree n.3175 of 18 December 2021 of Italian Ministry of University and Research funded by the European

Union—NextGenerationEU, project code CN_00000033, Concession Decree No. 1034 of 17 June 2022 adopted by the Italian Ministry of University and Research, Project title "National Biodiversity Future Center—NBFC".

**Data Availability Statement:** The data can be made available upon request to the corresponding author.

**Acknowledgments:** This work benefited from the support and the use of the resources of Instruct-ERIC, and, specifically, of the CERM/CIRMMP Italy Centre (VID:35740).

**Conflicts of Interest:** The authors declare no conflicts of interest.

## References

1. Liu, L.; Wang, R.; Yu, J.; Jiang, J.; Zheng, K.; Hu, L.; Wang, Z.; Fan, Y. Robust Self-Standing Chitin Nanofiber/Nanowhisker Hydrogels with Designed Surface Charges and Ultralow Mass Content via Gas Phase Coagulation. *Biomacromolecules* **2016**, *17*, 3773–3781. [CrossRef] [PubMed]
2. Liao, J.; Hou, B.; Huang, H. Preparation, Properties and Drug Controlled Release of Chitin-Based Hydrogels: An Updated Review. *Carbohydr. Polym.* **2022**, *283*, 119177. [CrossRef]
3. Ullah, F.; Othman, M.B.H.; Javed, F.; Ahmad, Z.; Akil, H.M. Classification, Processing and Application of Hydrogels: A Review. *Mater. Sci. Eng. C* **2015**, *57*, 414–433. [CrossRef]
4. Catoira, M.C.; Fusaro, L.; Di Francesco, D.; Ramella, M.; Boccafoschi, F. Overview of Natural Hydrogels for Regenerative Medicine Applications. *J. Mater. Sci. Mater. Med.* **2019**, *30*, 115. [CrossRef]
5. Montroni, D.; Marzec, B.; Valle, F.; Nudelman, F.; Falini, G. β-Chitin Nanofibril Self-Assembly in Aqueous Environments. *Biomacromolecules* **2019**, *20*, 2421–2429. [CrossRef]
6. Montroni, D. Hierarchically Organized Chitin-Based Matrices. Ph.D. Thesis, University of Bologna, Bologna, Italy, 2020.
7. Barbalinardo, M.; Biagetti, M.; Valle, F.; Cavallini, M.; Falini, G.; Montroni, D. Green Biocompatible Method for the Synthesis of Collagen/Chitin Composites to Study Their Composition and Assembly Influence on Fibroblasts Growth. *Biomacromolecules* **2021**, *22*, 3357–3365. [CrossRef] [PubMed]
8. Tamura, H.; Furuike, T.; Nair, S.V.; Jayakumar, R. Biomedical Applications of Chitin Hydrogel Membranes and Scaffolds. *Carbohydr. Polym.* **2011**, *84*, 820–824. [CrossRef]
9. Peralta Ramos, M.L.; González, J.A.; Albornoz, S.G.; Pérez, C.J.; Villanueva, M.E.; Giorgieri, S.A.; Copello, G.J. Chitin Hydrogel Reinforced with TiO2 Nanoparticles as an Arsenic Sorbent. *Chem. Eng. J.* **2016**, *285*, 581–587. [CrossRef]
10. Ahmad, S.I.; Ahmad, R.; Khan, M.S.; Kant, R.; Shahid, S.; Gautam, L.; Hasan, G.M.; Hassan, M.I. Chitin and Its Derivatives: Structural Properties and Biomedical Applications. *Int. J. Biol. Macromol.* **2020**, *164*, 526–539. [CrossRef]
11. Huang, W.; Montroni, D.; Wang, T.; Murata, S.; Arakaki, A.; Nemoto, M.; Kisailus, D. Nanoarchitected Tough Biological Composites from Assembled Chitinous Scaffolds. *Acc. Chem. Res.* **2022**, *55*, 1360–1371. [CrossRef]
12. Lee, J.E.; Connolloy, J.; Yang, W.; Freychet, G.; Wang, T.; Herrera, S.A.; Murata, S.; Dasika, P.S.; Montroni, D.; Pohl, A.; et al. Fibrous Anisotropy and Mineral Gradients Within the Radula Stylus of Chiton: Controlled Stiffness and Damage Tolerance in a Flexible Biological Composite. *J. Compos. Mater.* **2023**, *57*, 565–574. [CrossRef]
13. Montroni, D.; Zhang, X.; Leonard, J.; Kaya, M.; Amemiya, C.; Falini, G.; Rolandi, M. Structural Characterization of the Buccal Mass of Ariolimax Californicus (Gastropoda; Stylommatophora). *PLoS ONE* **2019**, *14*, e212249. [CrossRef] [PubMed]
14. Montroni, D.; Leonard, J.; Rolandi, M.; Falini, G. Morphology and Organization of the Internal Shell of Ariolimax Californicus (Gastropoda; Stylommatophora), an Asymmetric Two-Face Biomineralized Matrix. *J. Struct. Biol.* **2021**, *2013*, 107764. [CrossRef] [PubMed]
15. Jang, M.K.; Kong, B.G.; Jeong, Y., II; Lee, C.H.; Nah, J.W. Physicochemical Characterization of α-Chitin, β-Chitin, and γ-Chitin Separated from Natural Resources. *J. Polym. Sci. A Polym. Chem.* **2004**, *42*, 3423–3432. [CrossRef]
16. Fan, Y.; Saito, T.; Isogai, A. Chitin Nanocrystals Prepared by TEMPO-Mediated Oxidation of α-Chitin. *Biomacromolecules* **2008**, *9*, 192–198. [CrossRef]
17. Shen, X.; Shamshina, J.L.; Berton, P.; Gurau, G.; Rogers, R.D. Hydrogels Based on Cellulose and Chitin: Fabrication, Properties, and Applications. *Green Chem.* **2015**, *18*, 53–75. [CrossRef]
18. Fang, Y.; Zhang, R.; Duan, B.; Liu, M.; Lu, A.; Zhang, L. Recyclable Universal Solvents for Chitin to Chitosan with Various Degrees of Acetylation and Construction of Robust Hydrogels. *ACS Sustain. Chem. Eng.* **2017**, *5*, 2725–2733. [CrossRef]
19. Deng, L.; Zhang, L.M. Rheological Characteristics of Chitin/Ionic Liquid Gels and Electrochemical Properties of Regenerated Chitin Hydrogels. *Colloids Surf. A Physicochem. Eng. Asp.* **2020**, *586*, 124220. [CrossRef]
20. Tamura, H.; Nagahama, H.; Tokura, S. Preparation of Chitin Hydrogel under Mild Conditions. *Cellulose* **2006**, *13*, 357–364. [CrossRef]
21. Yilmaz, E.; Bengisu, M. Preparation and Characterization of Physical Gels and Beads from Chitin Solutions. *Carbohydr. Polym.* **2003**, *54*, 479–488. [CrossRef]
22. Mukesh, C.; Mondal, D.; Sharma, M.; Prasad, K. Choline Chloride-Thiourea, a Deep Eutectic Solvent for the Production of Chitin Nanofibers. *Carbohydr. Polym.* **2014**, *103*, 466–471. [CrossRef]

23. Montroni, D.; Kobayashi, T.; Hao, T.; Lublin, D.; Yoshino, T.; Kisailus, D. Direct Ink Write Printing of Chitin-Based Gel Fibers with Customizable Fibril Alignment, Porosity, and Mechanical Properties for Biomedical Applications. *J. Funct. Biomater.* **2022**, *13*, 83. [CrossRef] [PubMed]
24. Liang, K.; Chang, B.; Tsai, G.; Lee, J.; Fu, W.-R. Heterogeneous N-Deacetylation of Chitin in Alkaline Solution. *Carbohydr. Res.* **1997**, *303*, 327–332.
25. Liu, H.; Yang, Q.; Zhang, L.; Zhuo, R.; Jiang, X. Synthesis of Carboxymethyl Chitin in Aqueous Solution and Its Thermo- and PH-Sensitive Behaviors. *Carbohydr. Polym.* **2016**, *137*, 600–607. [CrossRef] [PubMed]
26. Shu, X.Z.; Zhu, K.J. Controlled Drug Release Properties of Ionically Cross-Linked Chitosan Beads: The Influence of Anion Structure. *Int. J. Pharm.* **2002**, *233*, 217–225. [CrossRef] [PubMed]
27. Shen, E.C.; Wang, C.; Fu, E.; Chiang, C.Y.; Chen, T.T.; Nieh, S. Tetracycline Release from Tripolyphosphate-Chitosan Cross-Linked Sponge: A Preliminary in Vitro Study. *J. Periodontal. Res.* **2008**, *43*, 642–648. [CrossRef] [PubMed]
28. Brack, H.P.; Tirmizi, S.A.; Risen, W.M. A Spectroscopic and Viscometric Study of the Metal Ion-Induced Gelation of the Biopolymer Chitosan. *Polymer* **1997**, *38*, 2351–2362. [CrossRef]
29. Dambies, L.; Vincent, T.; Domard, A.; Guibal, E. Preparation of Chitosan Gel Beads by Ionotropic Molybdate Gelation. *Biomacromolecules* **2001**, *2*, 1198–1205. [CrossRef] [PubMed]
30. Ma, Q.; Pang, K.; Wang, K.; Huang, S.; Ding, B.; Duan, Y.; Zhang, J. Ultrafine and Carboxylated β-Chitin Nanofibers Prepared from Squid Pen and Its Transparent Hydrogels. *Carbohydr. Polym.* **2019**, *211*, 118–123. [CrossRef]
31. Fan, Y.; Saito, T.; Isogai, A. TEMPO-Mediated Oxidation of β-Chitin to Prepare Individual Nanofibrils. *Carbohydr. Polym.* **2009**, *77*, 832–838. [CrossRef]
32. Kato, Y.; Kaminaga, J.; Matsuo, R.; Isogai, A. TEMPO-Mediated Oxidation of Chitin, Regenerated Chitin and N-Acetylated Chitosan. *Carbohydr. Polym.* **2004**, *58*, 421–426. [CrossRef]
33. Oun, A.A.; Rhim, J.W. Effect of Oxidized Chitin Nanocrystals Isolated by Ammonium Persulfate Method on the Properties of Carboxymethyl Cellulose-Based Films. *Carbohydr. Polym.* **2017**, *175*, 712–720. [CrossRef] [PubMed]
34. Liu, P.; Liu, H.; Schäfer, T.; Gutmann, T.; Gibhardt, H.; Qi, H.; Tian, L.; Zhang, X.C.; Buntkowsky, G.; Zhang, K. Unexpected Selective Alkaline Periodate Oxidation of Chitin for the Isolation of Chitin Nanocrystals. *Green Chem.* **2021**, *23*, 745–751. [CrossRef]
35. Montembault, A.; Tahiri, K.; Korwin-Zmijowska, C.; Chevalier, X.; Corvol, M.T.; Domard, A. A Material Decoy of Biological Media Based on Chitosan Physical Hydrogels: Application to Cartilage Tissue Engineering. *Biochimie* **2006**, *88*, 551–564. [CrossRef] [PubMed]
36. Ching, S.H.; Bansal, N.; Bhandari, B. Alginate Gel Particles–A Review of Production Techniques and Physical Properties. *Crit. Rev. Food Sci. Nutr.* **2017**, *57*, 1133–1152. [CrossRef] [PubMed]
37. Moussian, B. Chitin: Structure, Chemistry and Biology. In *Advances in Experimental Medicine and Biology*; Springer New York LLC.: New York, NY, USA, 2019; Volume 1142, pp. 5–18.
38. Nagahama, H.; Higuchi, T.; Jayakumar, R.; Furuike, T.; Tamura, H. XRD Studies of β-Chitin from Squid Pen with Calcium Solvent. *Int. J. Biol. Macromol.* **2008**, *42*, 309–313. [CrossRef] [PubMed]
39. De, J.A.; Delezuk, M.; Pavinatto, A.; Campana-Filho, S.P. Influence of the Process Parameters on β-Chitin and α-Chitin Extraction: Probing about the Grinding and Particles Size. *Mater. Today Proc.* **2019**, *14*, 722–732.
40. Jiang, J.; Ye, W.; Yu, J.; Fan, Y.; Ono, Y.; Saito, T.; Isogai, A. Chitin Nanocrystals Prepared by Oxidation of α-Chitin Using the O2/Laccase/TEMPO System. *Carbohydr. Polym.* **2018**, *189*, 178–183. [CrossRef] [PubMed]
41. Giuri, D.; Jurković, L.; Fermani, S.; Kralj, D.; Falini, G.; Tomasini, C. Supramolecular Hydrogels with Properties Tunable by Calcium Ions: A Bio-Inspired Chemical System. *ACS Appl. Bio. Mater.* **2019**, *2*, 5819–5828. [CrossRef]
42. Mezger, T.G. *Applied Rheology-with Joe Flow on Rheology Road*; Anton Paar: Graz, Austria, 2014.
43. Uraki, Y.; Fujii, T.; Matsuoka, T.; Miura, Y.; Tokura, S. Site Specific Binding of Calcium Ions to Anionic Chitin Derivatives. *Carbohydr. Polym.* **1993**, *20*, 139–143. [CrossRef]
44. Cofelice, M.; Messia, M.C.; Marconi, E.; Cuomo, F.; Lopez, F. Effect of the Xanthan Gum on the Rheological Properties of Alginate Hydrogels. *Food Hydrocoll.* **2023**, *142*, 108768. [CrossRef]
45. Syverud, K.; Pettersen, S.R.; Draget, K.; Chinga-Carrasco, G. Controlling the Elastic Modulus of Cellulose Nanofibril Hydrogels—Scaffolds with Potential in Tissue Engineering. *Cellulose* **2015**, *22*, 473–481. [CrossRef]
46. Cuomo, F.; Cofelice, M.; Lopez, F. Rheological Characterization of Hydrogels from Alginate-Based Nanodispersion. *Polymers* **2019**, *11*, 259. [CrossRef] [PubMed]
47. Derkach, S.R.; Voron'ko, N.G.; Sokolan, N.I. The Rheology of Hydrogels Based on Chitosan–Gelatin (Bio)Polyelectrolyte Complexes. *J. Dispers. Sci. Technol.* **2017**, *38*, 1427–1434. [CrossRef]
48. Prasad, K.; Murakami, M.A.; Kaneko, Y.; Takada, A.; Nakamura, Y.; Kadokawa, J.I. Weak Gel of Chitin with Ionic Liquid, 1-Allyl-3-Methylimidazolium Bromide. *Int. J. Biol. Macromol.* **2009**, *45*, 221–225. [CrossRef]
49. Sondermeijer, H.P.; Witkowski, P.; Woodland, D.; Seki, T.; Aangenendt, F.J.; Van Der Laarse, A.; Itescu, S.; Hardy, M.A. Optimization of Alginate Purification Using Polyvinylidene Difluoride Membrane Filtration: Effects on Immunogenicity and Biocompatibility of Three-Dimensional Alginate Scaffolds. *J. Biomater. Appl.* **2016**, *31*, 510–520. [CrossRef] [PubMed]
50. Tunn, I.; Harrington, M.J.; Blank, K.G. Bioinspired Histidine-Zn2+ Coordination for Tuning the Mechanical Properties of Self-Healing Coiled Coil Cross-Linked Hydrogels. *Biomimetics* **2019**, *4*, 25. [CrossRef] [PubMed]

51. Moura, M.J.; Figueiredo, M.M.; Gil, M.H. Rheological Study of Genipin Cross-Linked Chitosan Hydrogels. *Biomacromolecules* **2007**, *8*, 3823–3829. [CrossRef] [PubMed]
52. Montroni, D.; Fermani, S.; Morellato, K.; Torri, G.; Naggi, A.; Cristofolini, L.; Falini, G. β-Chitin Samples with Similar Microfibril Arrangement Change Mechanical Properties Varying the Degree of Acetylation. *Carbohydr. Polym.* **2019**, *207*, 26–33. [CrossRef]
53. Tuan Mohamood, N.F.A.Z.; Abdul Halim, A.H.; Zainuddin, N. Carboxymethyl Cellulose Hydrogel from Biomass Waste of Oil Palm Empty Fruit Bunch Using Calcium Chloride as Crosslinking Agent. *Polymers* **2021**, *13*, 4056. [CrossRef]
54. Montroni, D.; Sparla, F.; Fermani, S.; Falini, G. Influence of Proteins on Mechanical Properties of a Natural Chitin-Protein Composite. *Acta Biomater.* **2021**, *120*, 81–90. [CrossRef] [PubMed]
55. Pacheco, N.; Garnica-Gonzalez, M.; Gimeno, M.; Bárzana, E.; Trombotto, S.; David, L.; Shirai, K. Structural Characterization of Chitin and Chitosan Obtained by Biological and Chemical Methods. *Biomacromolecules* **2011**, *12*, 3285–3290. [CrossRef] [PubMed]
56. Kaya, M.; Baran, T.; Mentes, A.; Asaroglu, M.; Sezen, G.; Tozak, K.O. Extraction and Characterization of α-Chitin and Chitosan from Six Different Aquatic Invertebrates. *Food Biophys.* **2014**, *9*, 145–157. [CrossRef]
57. Wang, Q.; Yan, X.; Chang, Y.; Ren, L.; Zhou, J. Fabrication and Characterization of Chitin Nanofibers through Esterification and Ultrasound Treatment. *Carbohydr. Polym.* **2018**, *180*, 81–87. [CrossRef] [PubMed]
58. Duarte, M.L.; Ferreira, M.C.; Marvão, M.R.; Rocha, J. An Optimised Method to Determine the Degree of Acetylation of Chitin and Chitosan by FTIR Spectroscopy. *Int. J. Biol. Macromol.* **2002**, *31*, 1–8. [CrossRef] [PubMed]
59. Steen, K.H.; Steen, A.E.; Reeh', P.W. A Dominant Role of Acid PH in Inflammatory Excitation and Sensitization of Nociceptors in Rat Skin, In Vitro. *J. Neurosci.* **1995**, *15*, 3982–3989. [CrossRef] [PubMed]
60. Magnabosco, G.; Ianiro, A.; Stefani, D.; Soldà, A.; Rapino, S.; Falini, G.; Calvaresi, M. Doxorubicin-Loaded Squid Pen Plaster: A Natural Drug Delivery System for Cancer Cells. *ACS Appl. Bio. Mater.* **2020**, *3*, 1514–1519. [CrossRef] [PubMed]
61. Boudko, D.Y.; Moroz, L.L.; Linser, P.J.; Trimarchi, J.R.; Smith, P.J.S.; Harvey, W.R. In Situ Analysis of PH Gradients in Mosquito Larvae Using Non-Invasive, Self-Referencing, PH-Sensitive Microelectrodes. *J. Exp. Biol.* **2001**, *204*, 691–699. [CrossRef]
62. Stumpp, M.; Hu, M.Y.; Tseng, Y.C.; Guh, Y.J.; Chen, Y.C.; Yu, J.K.; Su, Y.H.; Hwang, P.P. Evolution of Extreme Stomach PH in Bilateria Inferred from Gastric Alkalization Mechanisms in Basal Deuterostomes. *Sci. Rep.* **2015**, *5*, 10421. [CrossRef]

marine drugs

Article

# Porous Nano-Fiber Structure of Modified Electrospun Chitosan GBR Membranes Improve Osteoblast Calcium Phosphate Deposition in Osteoblast-Fibroblast Co-Cultures

**Hengjie Su [1,2], Tomoko Fujiwara [3], Omar Skalli [4], Gretchen Schreyack Selders [2], Ting Li [1], Linna Mao [1] and Joel D. Bumgardner [2,*]**

[1] Institute of Biomedical Engineering, Chinese Academy of Medical Sciences & Peking Union Medical College, Tianjin 300192, China
[2] Department of Biomedical Engineering, University of Tennessee Health Science Center-Memphis Joint Graduate Biomedical Engineering Program, The University of Memphis, Memphis, TN 38152, USA
[3] Department of Chemistry, The University of Memphis, Memphis, TN 38152, USA; tfjiwara@memphis.edu
[4] Integrated Microscopy Center, The University of Memphis, Memphis, TN 38152, USA
[*] Correspondence: jbmgrdnr@memphis.edu

**Abstract:** Desirable characteristics of electrospun chitosan membranes (ESCM) for guided bone regeneration are their nanofiber structure that mimics the extracellular fiber matrix and porosity for the exchange of signals between bone and soft tissue compartments. However, ESCM are susceptible to swelling and loss of nanofiber and porous structure in physiological environments. A novel post-electrospinning method using di-tert-butyl dicarbonate (tBOC) prevents swelling and loss of nanofibrous structure better than sodium carbonate treatments. This study aimed to evaluate the hypothesis that retention of nanofiber morphology and high porosity of tBOC-modified ESCM (tBOC-ESCM) would support more bone mineralization in osteoblast-fibroblast co-cultures compared to $Na_2CO_3$ treated membranes ($Na_2CO_3$-ESCM) and solution-cast chitosan solid films (CM-film). The results showed that only the tBOC-ESCM retained the nanofibrous structure and had approximately 14 times more pore volume than $Na_2CO_3$-ESCM and thousands of times more pore volume than CM-films, respectively. In co-cultures, the tBOC-ESCM resulted in a significantly greater calcium-phosphate deposition by osteoblasts than either the $Na_2CO_3$-ESCM or CM-film ($p < 0.05$). This work supports the study hypothesis that tBOC-ESCM with nanofiber structure and high porosity promotes the exchange of signals between osteoblasts and fibroblasts, leading to improved mineralization in vitro and thus potentially improved bone healing and regeneration in guided bone regeneration applications

**Keywords:** chitosan; electrospinning; guided bone regeneration; calcium phosphate deposition; co-culture

## 1. Introduction

Guided bone regeneration (GBR) membranes are used in dental applications to prevent the invasion of gingival tissues into the bone-regenerating compartments. In addition to the shielding/barrier function of the membranes, the interconnected porosity and structure of the barrier membranes are reported as also playing important roles in healing by enabling an exchange of nutrients and growth factors between the gingival and bone compartments and mimicking extracellular matrix structure of newly forming tissues [1–5]. Electrospinning is one method to make GBR membranes that mimic the native nanofibrous extracellular matrix (ECM) structure and provide an interconnected porosity to allow the diffusion of nutrition, metabolites, and soluble factors between compartments that support healing [6].

Chitosan is a natural polysaccharide that has been widely researched as a GBR material due to its biocompatibility, homology to native ECM component hyaluronan, degradability, and ability to be electrospun [7]. However, electrospun chitosan membranes can be highly susceptible to swelling and loss of nanofibers and the interconnected porous structure [8,9]. Our group has successfully developed a novel post-electrospinning method that retains the nanofibrous structure of electrospun chitosan membranes (ESCM) better than other methods based on alkali treatments [7]. The post-spinning modification involves first removing acetate ions left over from the electrospinning process in the fibers using triethylamine (TEA) and then reacting di-tert-butyl dicarbonate (tBOC) with the chitosan amino groups to create a hydrophobic wrap on the outside of the electrospun chitosan fibers that prevents fiber swelling [7]. We demonstrated that the TEA/tBOC modified ESCM (TEA/tBOC-ESCM) exhibited little swelling and retained their nanofiber structure in physiological solutions, whereas a typical $Na_2CO_3$ treatment used to remove acetate ion salts resulted in extensive swelling and loss of nanofiber structure. The TEA/tBOC-ESCM were shown to be compatible with cultured cells, to degrade in vitro, to possess adequate mechanical properties for GBR applications, to provide effective barrier function, and to support bone healing in a rodent model.

This study aimed to further examine the hypothesis that the retained nanofiber morphology and porosity of the TEA/tBOC-ESCM improves in vitro cell performance as compared to $Na_2CO_3$ treated ESCMs ($Na_2CO_3$-ESCM) and solution-cast chitosan solid film membranes (CM-film). The membranes were characterized for surface morphology, porosity, water contact angle and ash and endotoxin content. Fibroblast and osteoblast cells in individual and co-cultures were used to evaluate the effect of nanofiber structure and porosity on cell growth as well as osteoblastic mineralization. The co-culture model was introduced to simulate the clinical application of GBR membrane treatments that aimed to separate and prevent the ingrowth of fibroblasts into sites of osteoblast growth and mineralization.

## 2. Results and Discussion

### 2.1. Membrane Characterizations

Results for the characterizations of the test membranes for fiber structure and diameter, porosity, hydrophobicity endotoxins and ash content are shown in Figure 1 and Table 1. The fiber diameter of the non-treated ESCM was 172 ± 48 nm, while that of the TEA/tBOC-ESCM was 219 ± 93 nm. There were no obvious fibers in the $Na_2CO_3$-ESCM, and no discernible structure in the CM-film. Consistent with previous reports, SEM microphotographs and analysis revealed that only the TEA/tBOC-ESCM were composed of well-defined nanometer diameter fibers, whereas the $Na_2CO_3$-ESCM exhibited significant fiber swelling, making the determination of individual fiber diameters difficult [7,10]. Because of the retained nanofiber structure, the TEA/tBOC-ESCM exhibited approximately 14 times greater porosity than the $Na_2CO_3$-ESCM (Table 1). As the CM-films were produced using a solution casting method, they lacked both fiber structure and significant porosity. The porosity of the GBR membranes is reported to be important for allowing nutrient and cell signaling exchange between osteogenic and soft/epithelial tissue compartments [11–14]. The significantly greater porosity of the TEA/tBOC-ESCM due to the retention of the nanofiber structure may be an advantage for improved nutrient and signal exchange as compared to the lower porosity $Na_2CO_3$-ESCM or essentially non-porous CM-film.

There was no significant difference in the median pore size of the two ESCM membranes, and even the solution-cast CM-film exhibited a range of pore sizes (Table 1). Since the CM-film becomes extremely brittle and stiff after neutralization, the small pores in the CM-film were attributed to minor defects that may arise in the casting, drying and neutralization of the films and or in manipulating films using forceps. The similarity in pore size between the TEA/tBOC-ESCM and $Na_2CO_3$-ESCM is more indicative of spaces between the randomly oriented fibers. Nevertheless, the range of pore sizes (~5 to ~44 μm) of both ESCMs is similar to other studies of electrospun membranes for GBR applications [11–14]. These studies report that these small pore sizes and the circuitous connections of the pores due to non-woven random fiber networks limit cell migration through the membranes, which is important to their barrier function while also allowing for nutrient and signal exchange.

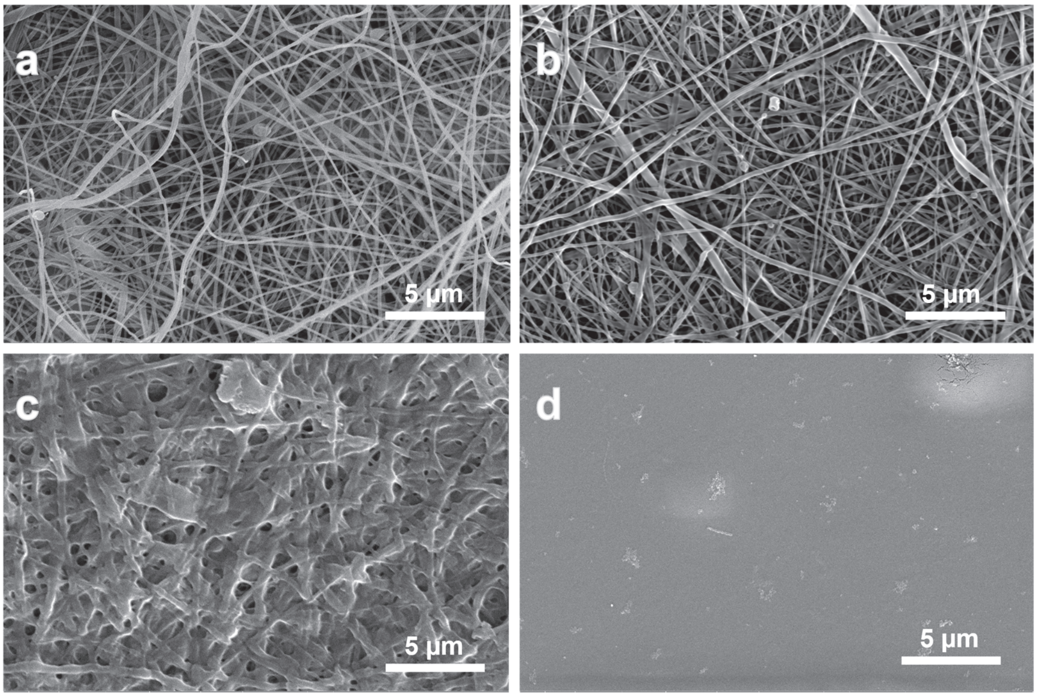

**Figure 1.** SEM images of the (**a**) non-treated chitosan electrospun membrane, (**b**) TEA/tBOC-ESCM, (**c**) $Na_2CO_3$-ESCM, and (**d**) the CM-film. The TEA/tBOC-ESCM exhibited similar nanofiber morphology and diameters as the as-spun membranes, whereas the $Na_2CO_3$-ESCM showed significant fiber swelling and loss of nanofiber morphology. The CM-film exhibited a smooth surface and no fibrous structure.

**Table 1.** Characteristics of TEA/tBOC-modified and $Na_2CO_3$-treated ESCM and solution-cast chitosan membrane films (CM-film). Data are expressed as mean ($n$ = 3) ± standard deviation except for pore size, which is expressed as a median and percentiles due to a skewed pore size distribution.

| | CM-Film | $Na_2CO_3$-ESCM | TEA/tBOC-ESCM |
|---|---|---|---|
| Median pore size (25th percentile, 75th percentile) (μm) | 11.4 (4.7, 41.7) | 12.2 (4.9, 42.5) | 15.1 (6.6, 44.1) |
| Total pore volume ($mm^3$/g) | $0.1 \pm 0.2^{a}$ | $32.4 \pm 47.1^{b}$ | $461.0 \pm 96.6^{c}$ |
| Water contact angle (degree) | $96.2 \pm 2.4^{a}$ | $76.0 \pm 10.8^{b}$ | $87.4 \pm 9.0^{b}$ |
| Endotoxin (EU/mL) | <0.1 | <0.1 | <0.1 |
| Ash (wt%) [&] | $<0.5\%^{a}$ | $1.9 \pm 0.5\%^{b}$ | $<0.5\%^{a}$ |

Letter superscripts indicate significant differences at α = 0.05 level of significance; [&] original chitosan powder ash content < 0.5%.

The CM-film had the statistically highest water contact angle, followed by the TEA/tBOC-ESCM and then the $Na_2CO_3$-ESCM, which had the statistically lowest contact angle (Table 1). The high hydrophobic character of the CM-film is attributed in part to the strong alkali treatment, which deprotonates the amino groups in the chitosan polymer in addition to neutralizing and removing acetate ions from the solution casting process. The increased hydrophobicity of TEA/tBOC-ESCM stems from the methyl groups within the tBOC group, contrasting with $Na_2CO_3$-ESCM, which retains residual carbonate salts contributing to its previously reported higher hydrophilicity [7]. Although hydrophobic biomaterial surfaces are often linked to reduced cellular attachment and spreading, this may not pose a significant concern for GBR applications, where the primary role is to serve as a barrier against cellular migration. However, due to the gradual hydrolysis of tBOC from the ESCM over a period of 7–10 days, and given that the membranes feature pores within the range of 40µm in diameter, which is sufficient for tissue ingrowth, the integration of the membrane into local tissues does occur [7,15,16]. The integration of the membrane within tissues is advantageous for stabilizing its placement and guiding tissue growth during healing.

Membranes were tested for endotoxin using a Limulus Amebocyte Lysate (LAL) based assay (Table 1). Endotoxin is a component of the outer cell wall of Gram-negative bacteria and may persist as a contaminant in chitosan powders after processing from the original biological source material and impact cellular and host tissue responses such as inflammation and or sepsis [17]. The results indicated that the endotoxin concentrations of the membranes were very low, remaining below the 0.1 EU/mL test kit limit. This value is also beneath the 0.5 EU/mL limit recommended by the US FDA for devices that come into contact with the cardiovascular and lymphatic systems, whether directly or indirectly [18].

The original source material for the chitosan used in this research is shrimp shells, which contain calcium carbonate as the main mineral component of the exoskeleton matrix. Since ash content represents the amount of residual minerals in chitosan after processing from the original source material, the ash content is largely due to residual calcium carbonate minerals but may also contain other elements from the environment like lead and mercury that can have adverse effects on host cells and tissues [17]. The ash content of the starting chitosan material as well as for both the CM-films and TEA/tBOC-ESCMs was determined to be <0.5%. This low ash content is indicative of chitosan with a low amount of contaminating minerals. On the other hand, the $Na_2CO_3$-ESCM exhibited an ash content of 2.0 ± 0.6%, which was a significant four-fold increase over the other groups. This increase in ash content is attributed to residual $Na_2CO_3$ salts in or on the membrane after soaking in the highly concentrated $Na_2CO_3$ solution. Compared with other studies, the ash contents of the chitosan powders were generally less than 2% [19–23]. Hence, the ash contents of this study were within the range of other chitosan materials.

### *2.2. Fibroblast and Osteoblast Co-Culture*

The dual cell culture setup was an initial attempt to mimic the cell growth environment of periodontal treatment, aiming to investigate whether a chitosan membrane with a porous structure is superior to one without pores. The insert of the dual cell culture provided a relatively individual fibroblast growth environment, with the only communication pathway being the bottom membrane, facilitating the nutrient exchange between fibroblasts and osteoblasts. When the chitosan membrane fully covered the insert bottom, the membrane's porosity determined the level of exchange. Despite the potential presence of chitosan extraction residues in all chitosan groups, the only variable across these groups was the presence of a porous structure in the membrane. A more porous membrane structure indicated a higher level of nutrient exchange between the two cell growth environments.

Focused on the aim of this study, which was to investigate whether a chitosan membrane with a porous structure was superior to one without pores, the selection of groups was aimed at minimizing variables. One control group consisted of samples without a chitosan membrane. This control was established to assess whether chitosan membranes effectively facilitated nutrient exchange, considering that the insert provides a clear pathway. The CM-film group was selected as another control to eliminate the potential influence of chitosan extraction residues and to focus on the variable of chitosan membrane porosity.

In the dual cell culture results, both the NIH 3T3 and MC3T3 E1 cells exhibited significant cell proliferation after 14 days, indicating that all the membranes were compatible with cell growth (Figure 2). In the previous study, Saos-2 osteosarcoma cells demonstrated significant proliferation after 5 days on both the TEA/tBOC-ESCM and the $Na_2CO_3$-ESCM [7]. Therefore, it can be inferred that the electrospun chitosan membranes and the cast film were compatible with both fibroblasts and osteoblasts.

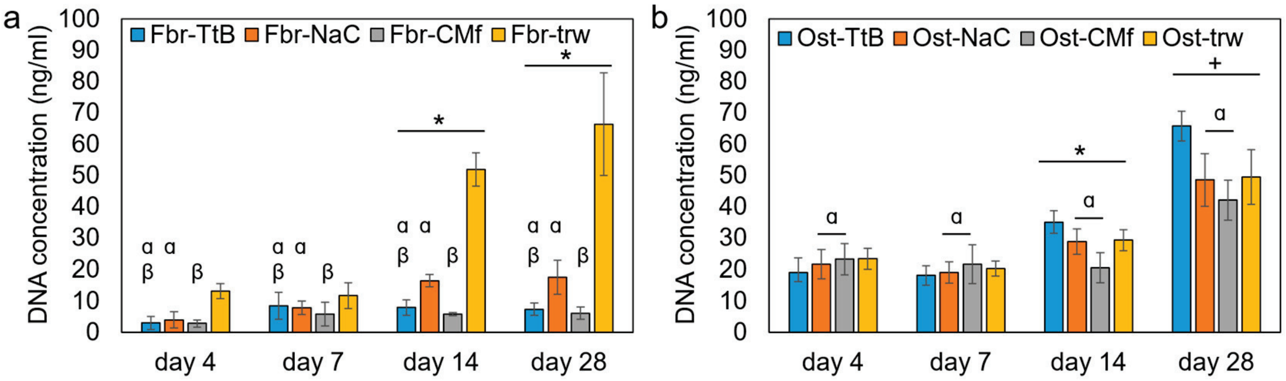

**Figure 2.** The dual cell culture results of (**a**) the top NIH 3T3 cell proliferation in the cell culture inserts and (**b**) the bottom MC3T3 cell proliferation on the well bottoms. * and + denote the significant difference in time points. α and β denote the significant differences among the cell culture groups. For abbreviations used in the graph, "Fbr-" indicates information regarding fibroblasts, while "Ost-" indicates information regarding osteoblasts. Regarding membrane types, "TtB" indicates the group with NIH 3T3 cells on the TEA/tBOC-ESCM, "NaC" indicates the group with NIH 3T3 cells on the $Na_2CO_3$-ESCM, "CMf" indicates the group with NIH 3T3 cells on the CM-Film, and "trw" indicates the group with NIH 3T3 cells on the insert with no membrane.

The NIH 3T3 fibroblasts exhibited significantly more growth in the control inserts (without chitosan membrane/film) compared to the cells in inserts with chitosan membranes (Figure 2a). This difference is primarily attributed to the transwell polycarbonate membranes, which are specifically treated to promote cell attachment and growth. Significantly greater fibroblast growth was observed on the $Na_2CO_3$-ESCM membranes (Fbr-NaC) compared to the CM-film. However, no difference in growth was detected between the fibroblasts on the TEA/tBOC-ESCM (Fbr-TtB) and the other two membranes, suggesting that the difference was small. Regarding porosity, the TEA/tBOC-ESCM exhibited approximately 10 times greater porosity, while the CM-films had approximately 100 times less porosity than the $Na_2CO_3$-ESCM. This is consistent with previous research, indicating that higher porosity contributes to increased cell growth [24]. Moreover, the hydrophobic nature of chitosan membranes may have influenced fibroblast growth. The $Na_2CO_3$-ESCM group, being more hydrophilic, showed significantly higher growth compared to the CM-film group, which is more hydrophobic. This aligns with the theory that a more hydrophilic surface promotes increased cell growth [25].

The MC3T3 E1 cells in co-culture with the TEA/tBOC-ESCM exhibited significantly different cell growth as compared to other chitosan membrane groups (Figure 2b). It showed that the cell proliferation below the TEA/tBOC-ESCM was lower than the other membrane groups at day 4 and day 7. However, it showed higher cell proliferation than the other membrane groups after 14 and 28 days. At the same time, there was no significant difference between the Ost-TtB group and Ost-trw group, which were prior to the non-porous structure membrane groups. It suggested that the TEA/tBOC-ESCM did not have a negative effect on bone cell proliferation. Its porous structure, similar to the ECM structure, facilitated a nutrient exchange between the NIH 3T3 and MC3T3 E1 cell growth environments, potentially promoting long-term MC3T3 E1 cell proliferation.

The ALP concentration normalized to the DNA amount exhibited significant increases in all groups after 14 and 28 days (Figure 3a). Osteoblasts in co-culture with the fibroblasts on the CM-film showed the highest ALP activity of the test groups on days 14 and 28, while osteoblasts in co-culture with fibroblasts on the ESCMs tended to have ALP activities that were either comparable or lower than osteoblasts cultured alone or in control co-culture.

However, the differences between these groups were not large since the osteoblasts cultured alone were not significantly different between all three membrane groups. It is further noted that ALP expression varies in a temporal fashion, and peaks in ALP expression may have been missed due to gaps between time points used. In a study by Ghuman et al., the ALP normalized to the control of the MC3T3 cells in the co-culture with gingival fibroblasts was significantly lower than the pure MC3T3 cell growth group [26], which implies that cross-talk between the fibroblasts and the MC3T3 cells might not stimulate ALP expression. In contrast, Zhu et al. showed that the relative ALP expression in MC3T3 E1 co-cultured with ephrinB2 transgenic periodontal ligament cells was significantly higher than in the pure MC3T3 E1 cell growth group [27]. Differences in these studies may be related to time points (day 3 vs. day 14) used to evaluate ALP in addition to differences in types of fibroblast cells [26,27]. Further research is still needed to explore the communication between fibroblasts and osteoblasts on osteoblastic differentiation and mineralization. Future studies may also be needed to consider the communication between gingival epithelial cells and osteoblasts.

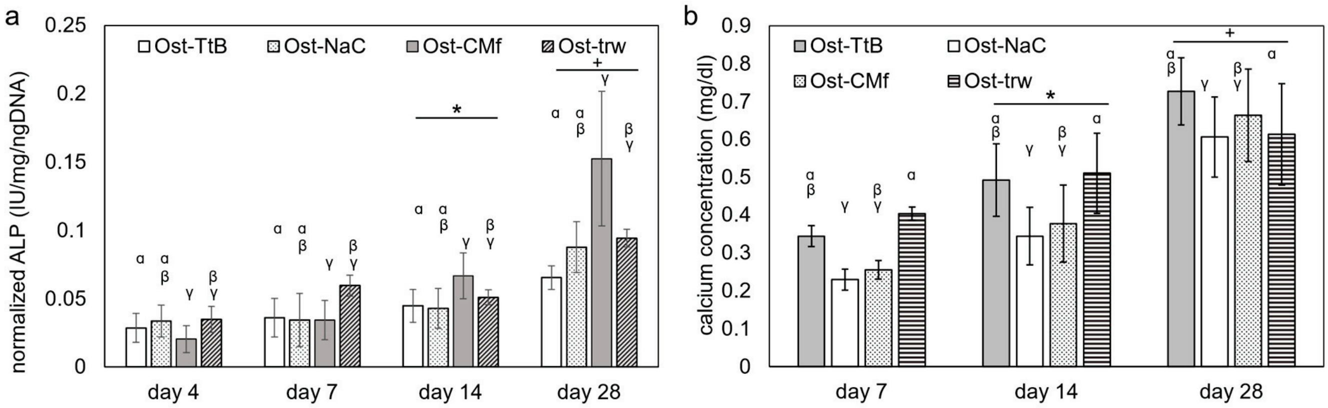

**Figure 3.** The dual cell culture results of (**a**) the ALP expression of the MC3T3 E1 cells and (**b**) the calcium deposit of the MC3T3 E1 cells at each time point. * and + denote the significant difference between day 4 and day 7. α, β and γ denote the significant difference among the cell culture groups. For abbreviations used in the graph, while "Ost-" indicates information regarding osteoblasts. Regarding membrane types, "TtB" indicates the group with NIH 3T3 cells on the TEA/tBOC-ESCM, "NaC" indicates the group with NIH 3T3 cells on the $Na_2CO_3$-ESCM, "CMf" indicates the group with NIH 3T3 cells on the CM-Film, and "trw" indicates the group with NIH 3T3 cells on the insert with no membrane.

The amount of calcium, serving as an indicator of calcium-phosphate deposition, exhibited a significant increase in all groups after 14 and 28 days (Figure 3b), indicating cells were able to differentiate and elaborate a mineralized matrix. Among the groups, the Ost-TtB and the Ost-trw groups displayed a significantly higher calcium concentration than the Ost-$NaCO_3$ group, while the Ost-CMf group showed a significantly lower calcium concentration than the Ost-trw group. The fluorescent stain graphs of osteocalcin (Figure 4) revealed increased production of osteocalcin after 14 days, serving as another indicator of heightened osteogenic activity similar to the calcium-phosphate deposition. The Ost-TtB group exhibited a significantly higher calcium concentration than the Ost-NaC group, suggesting that the TEA/tBOC-ESCM promotes cell mineralization better than the $Na_2CO_3$-ESCM. Although not statistically significant, the Ost-TtB group showed a trend of higher calcium concentration compared to the Ost-CMf group. Therefore, the TEA/tBOC-ESCM demonstrated similar or superior performance in cell mineralization compared to the CM-film. Since the TEA/tBOC-ESCM was the only type that preserved the fibrous structure, it could be inferred that the group with the nanostructure membrane showed improved support for osteogenic differentiation and elaboration of a mineralized matrix, which are important for regenerating bone. This supports the hypothesis that the porous electrospun membranes allow for better nutrient, small molecule and cell signal communication between the NIH 3T3 cells and the MC3T3 E1 cells. The higher calcium deposition observed in the Ost-trw group compared to the Ost-NaC and Ost-CMf groups further demonstrated the contribution of the mesh structure of the transwell, which provided optimal communication between the fibroblast and osteoblast growth environments. This suggests that the existing nutrient exchange between NIH 3T3 cells and MC3T3 E1 cells may have contributed to promoting calcium deposition. In Yang's study, MC3T3 E1 cells showed more mineralization ability on the fibrous membrane with a higher chitosan content compared to the fibrous membrane with more PCL [28]. This suggested that chitosan itself may promote cell mineralization beyond the porous structure. In this study, the MC3T3 E1 cells were not directly in contact with the chitosan membranes, which could explain why chitosan did not significantly promote cell mineralization.

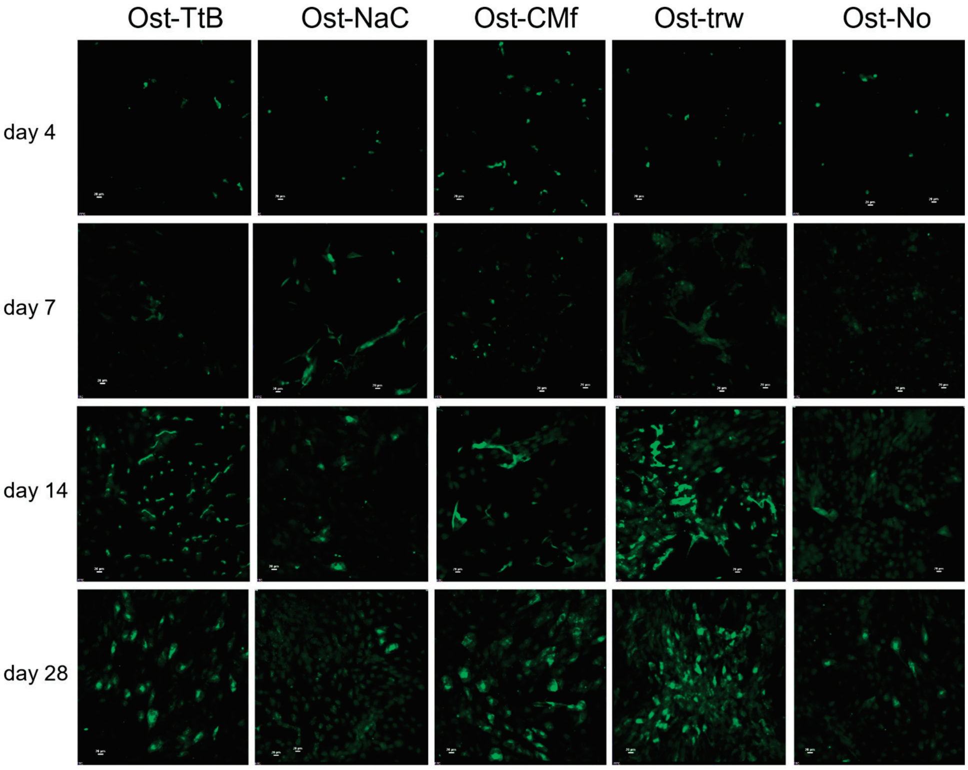

**Figure 4.** The fluorescent graphs of the anti-osteocalcin stained MC3T3 E1 cells at day 4, 7, 14 and 28. The osteocalcin increased from day 4 to day 28. For abbreviations used in the graph, while "Ost-" indicates information regarding osteoblasts. Regarding membrane types, "TtB" indicates the group with NIH 3T3 cells on the TEA/tBOC-ESCM, "NaC" indicates the group with NIH 3T3 cells on the $Na_2CO_3$-ESCM, "CMf" indicates the group with NIH 3T3 cells on the CM-Film, and "trw" indicates the group with NIH 3T3 cells on the insert with no membrane.

## 3. Materials and Methods

### 3.1. Chitosan Membrane and Film Preparation

Three types of chitosan-based membranes were prepared for this study: (a) TEA/tBOC-ESCM, (b) $Na_2CO_3$-ESCM and (c) a control CM-film treated with NaOH. The electrospun membranes were spun at 26 kV as described in previous studies using a 71% DDA chitosan (molecular weight = 311.5 kDa, Primex, Siglufjörður, Iceland) dissolved at 5.5 (*w*/*v*)% in 7:3 (*v*/*v*) trifluoroacetic acid (TFA, Thermo Fisher Scientific, Waltham, MA, USA) and dichloromethane (DCM, Sigma Aldrich, St. Louis, MI, USA). To make the TEA/tBOC-ESCM, membranes were first immersed in 10% (*v*/*v*) triethylamine/acetone solution for 24 h. After washing with acetone 3 times, membranes were immersed in the 0.1 g/mL tBOC solution for 48 h and then again washed with acetone 3 times [7]. Membranes were dried between two pieces of nylon mesh and under heavy weight to exclude the moisture in the air. To make the $Na_2CO_3$-ESCM, electrospun membranes were immersed in 5 M $Na_2CO_3$ solution for 3 h at room temperature and then dried between two pieces of nylon mesh [10].

To prepare CM-films, a 2 % (*w*/*v*) chitosan (71% DDA) in 2% acetic acid solution was prepared by stirring overnight. Twenty-eight millimeters of chitosan solution was pipetted into a petri dish (diameter = 8.5 cm) and allowed to dry for a few days at ambient conditions. For the neutralization, 2 M NaOH/DI $H_2O$ solution was pipetted into the petri dish to immerse films for 1 h. CM-film was rinsed with DI $H_2O$ for 30 min 3 to 5 times to remove excess NaOH and then dried in air at room temperature.

### 3.2. Membrane Characterizations

ESCM and solution-cast membranes were characterized for fiber structure and diameter, porosity, hydrophobicity, ash and endotoxin content. For fiber structure and diameter, specimens were examined using a scanning electron microscope (SEM, model EVO HD15, Carl Zeiss AG, Jena, Germany) from 2500× to 6000× after coating with 8 nm gold-palladium [7]. Fiber diameters were measured using image analysis software of the SEM. The porosity of test specimens was evaluated via porosimeter (Pascal 140 Mercury Porosimeter, Thermo Fisher Scientific, Waltham, MA, USA). Hydrophilic and hydrophobic character was measured by water contact angle using a VCA Optima measurement system (AST products, Inc, Billerica, MA, USA). Ash content of the test membranes was measured via combustion at 550 ± 20 °C to determine residual minerals from the original chitosan powder or as a result of the manufacture of ESCMs or the CM-films [29]. For endotoxin testing, gas-sterilized 1.5 cm diameter discs of test membrane samples were incubated in pyrogen-free water at a ratio of 1:100 (µg sample/µL water) for 24 h at 50 °C with constant shaking [30]. Endotoxin levels in pyrogen-free water extracts were determined using the Pierce LAL chromogenic endotoxin quantitation kit (Thermo Fisher Scientific, Waltham, MA, USA). For each material characterization method, three specimens of each test membrane type ($n$ = 3/membrane) were evaluated.

### 3.3. Fibroblast and Osteoblast Co-Culture

Before the co-culture, the membranes underwent gas sterilization with ethylene oxide. The culture media was formulated by mixing α-MEM-media (Corning, Cellgro) with 5 mM β-glycerophosphate, 50 µg/mL ascorbic acid, 10 nM dexamethasone, 10% fetal bovine serum (FBS), 500 I.U./mL penicillin, 500 µg/mL streptomycin, and 25 µg/mL amphotericin-B.

Standard 24-well plates (Costar$^{TM}$ flat bottom cell culture microplates, Corning, Glendale, AZ, USA) were used to seed osteoblasts and support inserts. First, MC3T3 E1 cells were seeded at $2 \times 10^4$ cells/well of a 24-well plate in the medium and allowed to attach overnight. Medium was removed, and a Falcon$^{TM}$ Transwell cell culture insert (pore size = 0.4 µm, Corning, Glendale, AZ, USA) was placed into each well. Next, a disc-shaped test or control chitosan membrane (diameter = 6 mm) was placed in the insert, and then fresh culture medium was added to the wells to cover the membranes. After about 24 h, the medium was removed, and $1 \times 10^4$ NIH 3T3 cells/insert were seeded on either the test or control membranes and fresh medium was added to the wells to cover the cells in the wells and in the transwell inserts (Figure 5).

The co-culture groups are described in Table 2. Cells were co-cultured for 28 days, with the medium being changed every 2–3 days. At days 4, 7, 14, and 28, osteoblast and fibroblast cell growth were evaluated using the Quant-iT$^{TM}$ PicoGreen$^{TM}$ dsDNA Assay kit (Thermo Fisher Scientific, Waltham, MA, USA) ($n$ = 3/membrane or film/time point). The osteoblast cells were evaluated for alkaline phosphatase (ALP) enzyme activity as an early marker of bone cell differentiation using the QuantiChrome$^{TM}$ Alkaline Phosphatase Assay Kit (BioAssay Systems) normalized to dsDNA, and mineral deposition on days 7, 14 and 28 via the Calcium Assay (Pointe Scientific, Inc., Canton, MI, USA) as a terminal indicator of differentiation. ($n$ = 3/membrane or film/time point). For qualitative assessment of a late marker for bone cell differentiation ($n$ = 1/membrane or film/time point), immunostaining of the bone cell matrix for osteocalcin was performed using a primary anti-osteocalcin antibody (BGLAP Picoband™, Boster Biological Technology, Pleasanton, CA, USA), followed by a Donkey anti-rabbit IgG ReadyProbes™ secondary antibody conjugated with Alexa Fluor 488 (Thermo Fisher Scientific, Waltham, MA, USA). Wells were then treated with ProLong™ Diamond Antifade Mountant with DAPI (Thermo Fisher Scientific, Waltham, MA, USA) prior to viewing on a Nikon Eclipse microscope (Nikon, Melville, NY, USA). Images were collected under the same brightness and contrast conditions to facilitate qualitative comparisons.

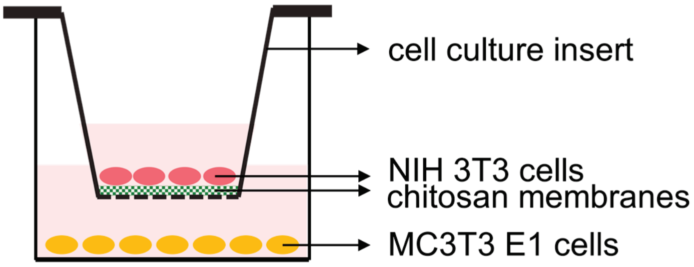

**Figure 5.** Diagram of co-culture arrangement of bone and fibroblast cells separated by a chitosan membrane. The MC3T3 E1 osteoblasts were seeded on the bottom of wells. After over-night incubation for osteoblast cell attachment, culture inserts containing a test chitosan membrane or no chitosan membrane (insert only) as a control were placed into the wells. Then, the NIH3T3 fibroblasts were seeded on the membrane/film samples.

**Table 2.** Co-culture group descriptions.

| Group | TEA/tBOC-ESCM | $Na_2CO_3$-ESCM | CM-Film | Control |
|---|---|---|---|---|
| Cell culture insert | NIH 3T3 cells on the TEA/tBOC-ESCM (Fbr-TtB) | NIH 3T3 cells on the $Na_2CO_3$-ESCM (Fbr-NaC) | NIH 3T3 cells on the CM-film (Fbr-CMf) | No membrane, NIH 3T3 cells only (Fbr-trw) |
| Well plate bottom | MC 3T3 (Ost-TtB) | MC 3T3 (Ost-NaC) | MC 3T3 (Ost-CMf) | MC 3T3 (Ost-trw) |

### *3.4. Statistical Analysis*

The data for fiber diameter, water contact angle and ash content were analyzed by one-way analysis of variance (ANOVA) at the 0.05 level of significance. The cell culture data were analyzed by the two-way ANOVA ($\alpha$ = 0.05). As appropriate, Tukey's post-hoc tests were used to distinguish significantly different groups at $\alpha$ = 0.05 level of significance.

## 4. Conclusions

In conclusion, the TEA/tBOC-ESCM preserved the nanofibrous and highly porous structure, whereas the $Na_2CO_3$-ESCM did not, and the CM-film did not have any fibrous structure and lacked porosity. Hence, the TEA/tBOC-ESCM had more pore volume than the other two. The CM-film was more hydrophobic than the other two electrospun membranes, and the TEA/tBOC-ESCM was more hydrophobic than the $Na_2CO_3$-ESCM. The ash contents of all the membranes were under 0.5% except for the $Na_2CO_3$-ESCM, which was under 2%. All the membranes/films had extremely low endotoxin concentrations, which were considered suitable for the FDA requirements. The in vitro evaluation showed that all the membranes were osteoblast- and fibroblast-compatible. The TEA/tBOC-ESCM showed more MC3T3 E1 cell proliferation and more or similar deposited calcium amount than the other two membranes/films. The higher amount of deposited calcium indicated faster mineralization with the TEA/tBOC-ESCM membrane. In clinical treatment, faster mineralization indicates faster bone formation. Hence, these results indicate that the highly porous nanofiber structure of the TEA/tBOC membranes may have an advantage in improving the bone healing/regeneration time in GBR clinical treatments.

**Author Contributions:** Conceptualization, methodology, paper revision, and funding acquisition, J.D.B.; conceptualization, methodology, project administration, data analysis, paper writing, and revision, H.S.; porosity test, G.S.S.; chemical analysis, T.F.; osteocalcin staining test, O.S.; resources, L.M. and T.L. All authors have read and agreed to the published version of the manuscript.

**Funding:** This research was supported by the Biomaterials Applications of Memphis (BAM) Laboratories (Project #2013_0124) in the Biomedical Engineering Department at the University of Memphis and a grant (Project# 09 2016-2017) from the FedEx Institute of Technology, Memphis, TN, USA, Chinese Academy of Medical Science health innovation project (grant nos. 2021-I2M-1-058 and 2021-I2M-1-042), CAMS Innovation Fund for medical sciences (2021-I2M-C&T-B-095), Key Project of Construction of Drug Regulatory Science System (RS2024X007), STI 2030-Major Projects (2021ZD0200406) and Fundamental Research Funds for the Central Universities (3332023070).

**Data Availability Statement:** The data presented in this study are available on request from the corresponding author.

**Acknowledgments:** This work was performed as part of the requirements to complete a Ph.D. in Biomedical Engineering at the University of Memphis and in the UofM-UTHSC Joint BME Graduate Program.

**Conflicts of Interest:** Authors Hengjie Su, Tomoko Fujiwara and Joel D Bumgardner have a patent on the TEA/tBOC-ESCMs that were used in this study (U.S. Patent No. 11,878,088; Chitosan Nanofiber Compositions, Compositions Comprising Modified Chitosan, and Methods of Use).

## References

1. Bee, S.-L.; Hamid, Z.A.A. Asymmetric Resorbable-Based Dental Barrier Membrane for Periodontal Guided Tissue Regeneration and Guided Bone Regeneration: A Review. *J. Biomed. Mater. Res. Part B Appl. Biomater.* **2022**, *110*, 2157–2182. [CrossRef]
2. Sanz, M.; Dahlin, C.; Apatzidou, D.; Artzi, Z.; Bozic, D.; Calciolari, E.; De Bruyn, H.; Dommisch, H.; Donos, N.; Eickholz, P.; et al. Biomaterials and Regenerative Technologies Used in Bone Regeneration in the Craniomaxillofacial Region: Consensus Report of Group 2 of the 15th European Workshop on Periodontology on Bone Regeneration. *J. Clin. Periodontol.* **2019**, *46*, 82–91. [CrossRef]
3. Kim, K.; Su, Y.; Kucine, A.J.; Cheng, K.; Zhu, D. Guided Bone Regeneration Using Barrier Membrane in Dental Applications. *ACS Biomater. Sci. Eng.* **2023**, *9*, 5457–5478. [CrossRef]
4. Caballé-Serrano, J.; Munar-Frau, A.; Ortiz-Puigpelat, O.; Soto-Penaloza, D.; Peñarrocha, M.; Hernández-Alfaro, F. On the Search of the Ideal Barrier Membrane for Guided Bone Regeneration. *J. Clin. Exp. Dent.* **2018**, *10*, e477–e483. [CrossRef]
5. Liang, C.; Wang, G.; Liang, C.; Li, M.; Sun, Y.; Tian, W.; Liao, L. Hierarchically Patterned Triple-Layered Gelatin-Based Electrospun Membrane Functionalized by Cell-Specific Extracellular Matrix for Periodontal Regeneration. *Dent. Mater.* **2024**, *40*, 90–101. [CrossRef]
6. Qian, M.; Li, S.; Xi, K.; Tang, J.; Shen, X.; Liu, Y.; Guo, R.; Zhang, N.; Gu, Y.; Xu, Y.; et al. ECM-Engineered Electrospun Fibers with an Immune Cascade Effect for Inhibiting Tissue Fibrosis. *Acta Biomater.* **2023**, *171*, 308–326. [CrossRef]
7. Su, H.; Liu, K.-Y.; Karydis, A.; Abebe, D.G.; Wu, C.; Anderson, K.M.; Ghadri, N.; Adatrow, P.; Fujiwara, T.; Bumgardner, J.D. In Vitro and in Vivo Evaluations of a Novel Post-Electrospinning Treatment to Improve the Fibrous Structure of Chitosan Membranes for Guided Bone Regeneration. *Biomed. Mater.* **2016**, *12*, 015003. [CrossRef]
8. Cooper, A.; Bhattarai, N.; Kievit, F.M.; Rossol, M.; Zhang, M. Electrospinning of Chitosan Derivative Nanofibers with Structural Stability in an Aqueous Environment. *Phys. Chem. Chem. Phys.* **2011**, *13*, 9969–9972. [CrossRef]
9. Sangsanoh, P.; Supaphol, P. Stability Improvement of Electrospun Chitosan Nanofibrous Membranes in Neutral or Weak Basic Aqueous Solutions. *Biomacromolecules* **2006**, *7*, 2710–2714. [CrossRef]
10. Norowski, P.A.; Fujiwara, T.; Clem, W.C.; Adatrow, P.C.; Eckstein, E.C.; Haggard, W.O.; Bumgardner, J.D. Novel Naturally Crosslinked Electrospun Nanofibrous Chitosan Mats for Guided Bone Regeneration Membranes: Material Characterization and Cytocompatibility. *J. Tissue Eng. Regen. Med.* **2015**, *9*, 577–583. [CrossRef]
11. Masoudi Rad, M.; Nouri Khorasani, S.; Ghasemi-Mobarakeh, L.; Prabhakaran, M.P.; Foroughi, M.R.; Kharaziha, M.; Saadatkish, N.; Ramakrishna, S. Fabrication and Characterization of Two-Layered Nanofibrous Membrane for Guided Bone and Tissue Regeneration Application. *Mater. Sci. Eng. C Mater. Biol. Appl.* **2017**, *80*, 75–87. [CrossRef]
12. Yang, F.; Both, S.K.; Yang, X.; Walboomers, X.F.; Jansen, J.A. Development of an Electrospun Nano-Apatite/PCL Composite Membrane for GTR/GBR Application. *Acta Biomater.* **2009**, *5*, 3295–3304. [CrossRef]
13. Dos Santos, V.I.; Merlini, C.; Aragones, Á.; Cesca, K.; Fredel, M.C. In Vitro Evaluation of Bilayer Membranes of PLGA/Hydroxyapatite/β-Tricalcium Phosphate for Guided Bone Regeneration. *Mater. Sci. Eng. C Mater. Biol. Appl.* **2020**, *112*, 110849. [CrossRef]

14. Ebrahimi, L.; Farzin, A.; Ghasemi, Y.; Alizadeh, A.; Goodarzi, A.; Basiri, A.; Zahiri, M.; Monabati, A.; Ai, J. Metformin-Loaded PCL/PVA Fibrous Scaffold Preseeded with Human Endometrial Stem Cells for Effective Guided Bone Regeneration Membranes. *ACS Biomater. Sci. Eng.* **2021**, *7*, 222–231. [CrossRef]
15. Su, H.; Fujiwara, T.; Anderson, K.M.; Karydis, A.; Ghadri, M.N.; Bumgardner, J.D. A Comparison of Two Types of Electrospun Chitosan Membranes and a Collagen Membrane In Vivo. *Dent. Mater.* **2021**, *37*, 60–70. [CrossRef]
16. Su, H. In Vitro and In Vivo Evaluation and Mechanical Improvement of the Electrospun Chitosan Membrane. Ph.D. Thesis, The University of Memphis, Memphis, TN, USA, 2020.
17. Jennings, J.A.; Bumgardner, J.D. (Eds.) *Chitosan Based Biomaterials*; Woodhead Publishing Series in Biomaterials; Elsevier/Woodhead Publishing: Amsterdam, The Netherlands, 2017; ISBN 978-0-08-100230-8.
18. Pang, E.-K.; Paik, J.-W.; Kim, S.-K.; Jung, U.-W.; Kim, C.-S.; Cho, K.-S.; Kim, C.-K.; Choi, S.-H. Effects of Chitosan on Human Periodontal Ligament Fibroblasts In Vitro and on Bone Formation in Rat Calvarial Defects. *J. Periodontol.* **2005**, *76*, 1526–1533. [CrossRef]
19. Islam, M.d.S.; Yeum, J.H. Electrospun Pullulan/Poly(Vinyl Alcohol)/Silver Hybrid Nanofibers: Preparation and Property Characterization for Antibacterial Activity. *Colloids Surf. A Physicochem. Eng. Asp.* **2013**, *436*, 279–286. [CrossRef]
20. Pipattanawarothai, A.; Suksai, C.; Srisook, K.; Trakulsujaritchok, T. Non-Cytotoxic Hybrid Bioscaffolds of Chitosan-Silica: Sol-Gel Synthesis, Characterization and Proposed Application. *Carbohydr. Polym.* **2017**, *178*, 190–199. [CrossRef]
21. Sibaja, B.; Culbertson, E.; Marshall, P.; Boy, R.; Broughton, R.M.; Solano, A.A.; Esquivel, M.; Parker, J.; Fuente, L.D.L.; Auad, M.L. Preparation of Alginate–Chitosan Fibers with Potential Biomedical Applications. *Carbohydr. Polym.* **2015**, *134*, 598–608. [CrossRef]
22. Haider, S.; Park, S.-Y. Preparation of the Electrospun Chitosan Nanofibers and Their Applications to the Adsorption of Cu(II) and Pb(II) Ions from an Aqueous Solution. *J. Membr. Sci.* **2009**, *328*, 90–96. [CrossRef]
23. Phongying, S.; Aiba, S.; Chirachanchai, S. Direct Chitosan Nanoscaffold Formation via Chitin Whiskers. *Polymer* **2007**, *48*, 393–400. [CrossRef]
24. Wang, Y.; Xu, R.; Luo, G.; Lei, Q.; Shu, Q.; Yao, Z.; Li, H.; Zhou, J.; Tan, J.; Yang, S.; et al. Biomimetic Fibroblast-Loaded Artificial Dermis with "Sandwich" Structure and Designed Gradient Pore Sizes Promotes Wound Healing by Favoring Granulation Tissue Formation and Wound Re-Epithelialization. *Acta Biomater.* **2016**, *30*, 246–257. [CrossRef]
25. Boyan, B.D.; Lotz, E.M.; Schwartz, Z. Roughness and Hydrophilicity as Osteogenic Biomimetic Surface Properties. *Tissue Eng. Part A* **2017**, *23*, 1479–1489. [CrossRef]
26. Ghuman, M.S.; Al-Masri, M.; Xavier, G.; Cobourne, M.T.; McKay, I.J.; Hughes, F.J. Gingival Fibroblasts Prevent BMP-Mediated Osteoblastic Differentiation. *J. Periodontal Res.* **2019**, *54*, 300–309. [CrossRef]
27. Zhu, S.Y.; Wang, P.L.; Liao, C.S.; Yang, Y.Q.; Yuan, C.Y.; Wang, S.; Dissanayaka, W.L.; Heng, B.C.; Zhang, C.F. Transgenic Expression of ephrinB2 in Periodontal Ligament Stem Cells (PDLSCs) Modulates Osteogenic Differentiation via Signaling Crosstalk between ephrinB2 and EphB4 in PDLSCs and between PDLSCs and Pre-Osteoblasts within Co-Culture. *J. Periodontal. Res.* **2017**, *52*, 562–573. [CrossRef]
28. Yang, X.; Chen, X.; Wang, H. Acceleration of Osteogenic Differentiation of Preosteoblastic Cells by Chitosan Containing Nanofibrous Scaffolds. *Biomacromolecules* **2009**, *10*, 2772–2778. [CrossRef]
29. Hamilton, V.; Yuan, Y.; Rigney, D.A.; Puckett, A.D.; Ong, J.L.; Yang, Y.; Elder, S.H.; Bumgardner, J.D. Characterization of Chitosan Films and Effects on Fibroblast Cell Attachment and Proliferation. *J. Mater. Sci. Mater. Med.* **2006**, *17*, 1373–1381. [CrossRef]
30. Nakagawa, Y.; Murai, T.; Hasegawa, C.; Hirata, M.; Tsuchiya, T.; Yagami, T.; Haishima, Y. Endotoxin Contamination in Wound Dressings Made of Natural Biomaterials. *J. Biomed. Mater. Res. Part B Appl. Biomater.* **2003**, *66*, 347–355. [CrossRef]

marine drugs

Article

# Effects of Shrimp Shell-Derived Chitosan on Growth, Immunity, Intestinal Morphology, and Gene Expression of Nile Tilapia (*Oreochromis niloticus*) Reared in a Biofloc System

**Nguyen Vu Linh [1,2], Anisa Rilla Lubis [1], Nguyen Dinh-Hung [3], Supreya Wannavijit [1], Napatsorn Montha [1], Camilla Maria Fontana [1], Phattawin Lengkidworraphiphat [4], Orranee Srinual [1,2], Won-Kyo Jung [5], Marina Paolucci [6] and Hien Van Doan [1,2,*]**

[1] Department of Animal and Aquatic Sciences, Faculty of Agriculture, Chiang Mai University, Chiang Mai 50200, Thailand; linhvu.n@cmu.ac.th (N.V.L.); anisarillalubis@gmail.com (A.R.L.); phoooooooooo10@gmail.com (S.W.); napatsorn.m@cmu.ac.th (N.M.); camillamaria.fontana@phd.unipd.it (C.M.F.); orranee.s@cmu.ac.th (O.S.)
[2] Functional Feed Innovation Center (FuncFeed), Faculty of Agriculture, Chiang Mai University, Chiang Mai 50200, Thailand
[3] Aquaculture Pathology Laboratory, School of Animal & Comparative Biochemical Sciences, The University of Arizona, Tucson, AZ 85721, USA; dinhhung@arizona.edu
[4] Multidisciplinary Research Institute, Chiang Mai University, 239 Huay Keaw Rd., Suthep, Muang, Chiang Mai 50200, Thailand; junjira_l@cmu.ac.th
[5] Marine Integrated Biomedical Technology Center, The National Key Research Institutes in Universities, Pukyong National University, Busan 48513, Republic of Korea; wkjung@pknu.ac.kr
[6] Department of Science and Technologies, University of Sannio, 82100 Benevento, Italy; paolucci@unisannio.it
* Correspondence: hien.d@cmu.ac.th; Tel.: +66-992-971888

**Abstract:** Chitosan (CH) shows great potential as an immunostimulatory feed additive in aquaculture. This study evaluates the effects of varying dietary CH levels on the growth, immunity, intestinal morphology, and antioxidant status of Nile tilapia (*Oreochromis niloticus*) reared in a biofloc system. Tilapia fingerlings (mean weight 13.54 ± 0.05 g) were fed diets supplemented with 0 (CH0), 5 (CH5), 10 (CH10), 20 (CH20), and 40 (CH40) $\text{mL}\cdot\text{kg}^{-1}$ of CH for 8 weeks. Parameters were assessed after 4 and 8 weeks. Their final weight was not affected by CH supplementation, but CH at 10 $\text{mL}\cdot\text{kg}^{-1}$ significantly improved weight gain (WG) and specific growth rate (SGR) compared to the control ($p < 0.05$) at 8 weeks. Skin mucus lysozyme and peroxidase activities were lower in the chitosan-treated groups at weeks 4 and 8. Intestinal villi length and width were enhanced by 10 and 20 $\text{mL}\cdot\text{kg}^{-1}$ CH compared to the control. However, 40 $\text{mL}\cdot\text{kg}^{-1}$ CH caused detrimental impacts on the villi and muscular layer. CH supplementation, especially 5–10 $\text{mL}\cdot\text{kg}^{-1}$, increased liver and intestinal expressions of interleukin 1 (*IL-1*), interleukin 8 (*IL-8*), LPS-binding protein (*LBP*), glutathione reductase (*GSR*), glutathione peroxidase (*GPX*), and glutathione S-transferase (*GST-α*) compared to the control group. Overall, dietary CH at 10 $\text{mL}\cdot\text{kg}^{-1}$ can effectively promote growth, intestinal morphology, innate immunity, and antioxidant capacity in Nile tilapia fingerlings reared in biofloc systems.

**Keywords:** by-product; feed additive; growth performance; immune response; mRNA expression

---

## 1. Introduction

The rapid growth of aquaculture has led to an increased demand for improved diets and feed supplements for farmed fish [1]. Feed represents one of the largest costs for aquaculture producers. Determining the specific nutritional requirements, optimal feeding strategies, and nutrient utilization of each fish species is, therefore, critical to enable sustainable and scalable production [2]. Nile tilapia (*Oreochromis niloticus*) has become one of the most widely farmed aquaculture species because of its rapid growth, ability to adapt to different environments, disease resistance, and high protein content in the flesh [3,4]. Recently, tilapia farming practices have shifted from extensive to intensive commercial production systems [5,6]. However, disease outbreaks have emerged as the main obstacle to sustainable intensive tilapia farming globally. Finding ways to prevent diseases will be crucial to address this challenge as tilapia production continues to intensify [6]. Antibiotics have traditionally been used in commercial fish farms to prevent disease transmission. However, concerns over antibiotic usage in aquaculture have led to investigating replacements to reduce reliance on these treatments [7,8]. This has sparked great interest in finding new, innovative feed additives for tilapia, such as probiotics [9,10], prebiotics [11–13], and synbiotics [14,15]. These additives have been reported to enhance growth performance, health status, immune function, antioxidant defenses, and immune-related gene expression in tilapia. Such improvements could positively impact overall production. Replacing antibiotics with alternative feed supplements, particularly bioactive compounds derived from seafood products, may provide health benefits for tilapia while addressing issues surrounding antibiotic use in aquaculture.

Shrimp, one of the many varieties of seafood, is a popular and healthful dietary choice globally. Its output reached 8.25 million metric tons in 2015 and reached 9.66 million metric tons in 2019, with an annual growth rate of 2–3% [16], resulting in 6–8 million tons of waste [17,18]. The majority of shrimp waste is discarded publicly in landfills [19], burned, or dumped into the oceans [20,21]. Only a small portion is utilized as food and feed for animals and aquaculture [22,23]. The shrimp disposal sites could be major sources of offensive odors, as well as dust, gases, and fumes [18,24]. The rapid breakdown of shrimp waste can result in the appearance and spread of infections by flies, mosquitoes, and rats, endangering human health [25,26]. Nonetheless, this waste stream also includes beneficial natural substances, chief among them being chitin, which is an essential component in the production of chitosan [27–29]. Chitosan (CH) has been shown to have anti-cancer [30,31], anti-inflammatory [32,33], and neuroprotective [34] activities, in addition to having antioxidant, anti-diabetic, anti-hypertensive, and wound-healing [35] properties. Additionally, chitosan has antibacterial properties against the majority of bacteria, molds, and yeasts [36]. Furthermore, chitosan is a nontoxic, biodegradable, and biocompatible biopolymer. These characteristics make chitosan and its derivatives suitable for usage in a wide range of sectors, including the food, pharmaceutical, and agricultural industries [37–39].

Biofloc technology (BFT) has emerged as a sustainable aquaculture practice that enables fishponds to self-nitrify without water exchange [40,41]. In BFT systems, flocs formed from organic particulate matter and diverse microorganisms serve as an in situ food source. Fish can directly consume these protein-rich flocculants, reducing the need for fishmeal and soybean meal in feeds [42–45]. By substituting commercial diets with biofloc, the risks of mycotoxin and antinutrient exposure are also decreased, lowering feed costs [46,47]. Tilapia is especially well-suited for biofloc farming, as the species can effectively utilize biofloc for nutrition [48,49]. Given the benefits of BFT for tilapia production, this study aimed to evaluate how chitosan feed supplementation influences the growth, immune function, intestinal histology, and expression of key immune-antioxidant genes in Nile tilapia reared in a biofloc system. The overarching goal was to assess the potential of CH as a feed additive for enhancing tilapia health and productivity under sustainable BFT conditions.

## 2. Results

### 2.1. Growth Performance

The growth performance of Nile tilapia fingerlings fed the chitosan supplemented diets is shown in Table 1. After 4 weeks, FW was significantly higher ($p < 0.05$) in the CH10 group compared to the control group, while no significant differences were detected among groups at 8 weeks ($p > 0.05$). Weight gain did not differ significantly between the control and treatments at 4 weeks ($p > 0.05$). However, at 8 weeks, fish fed the CH10 diet showed significantly increased weight gain compared to the control group ($p < 0.05$) (Table 1). The

CH10 group also exhibited the highest SGR at both 4 weeks (2.83 ± 0.07) and 8 weeks (2.29 ± 0.03) (Table 1). No significant differences in FCR were observed between groups at any time (Table 1). The survival rate exceeded 95% in all treatments after the 8-week feeding trial.

**Table 1.** Growth performances and feed efficiency in Nile tilapia (*Oreochromis niloticus*) fingerlings fed diets with increasing chitosan (CH) levels for 4 and 8 weeks. Data is shown as mean ± SEM. Different letters (a–b) indicate significant differences between dietary groups. Diets: CH0, 0 mL·kg$^{-1}$ COS (control); CH5, 5 mL·kg$^{-1}$; CH10, 10 mL·kg$^{-1}$; CH20, 20 mL·kg$^{-1}$; CH40, 40 mL·kg$^{-1}$ of chitosan.

| | **CH0** | **CH5** | **CH10** | **CH20** | **CH40** | ***p*-Value** |
|---|---|---|---|---|---|---|
| **IW (g)** | 13.48 ± 0.03 | 13.66 ± 0.05 | 13.55 ± 0.03 | 13.56 ± 0.08 | 13.47 ± 0.05 | 0.499 |
| **FW (g)** | | | | | | |
| 4 weeks | 29.45 ± 1.33 | 28.97 ± 0.98 | 31.72 ± 0.28 | 29.06 ± 0.38 | 28.87 ± 1.27 | 0.470 |
| 8 weeks | 50.44 ± 0.67 $^{b}$ | 50.23 ± 0.62 $^{b}$ | 50.69 ± 0.54 $^{a}$ | 50.60 ± 1.20 $^{b}$ | 50.29 ± 1.95 $^{b}$ | 0.049 |
| **WG (g)** | | | | | | |
| 4 weeks | 15.97 ± 1.26 | 15.30 ± 0.93 | 18.17 ± 0.44 | 15.49 ± 0.45 | 15.40 ± 1.20 | 0.228 |
| 8 weeks | 36.96 ± 1.30 $^{b}$ | 36.56 ± 0.04 $^{b}$ | 40.14 ± 0.83 $^{a}$ | 37.03 ± 0.85 $^{b}$ | 36.81 ± 0.47 $^{b}$ | 0.050 |
| **SGR (%/day)** | | | | | | |
| 4 weeks | 2.60 ± 0.13 $^{ab}$ | 2.50 ± 0.10 $^{b}$ | 2.83 ± 0.07 $^{a}$ | 2.54 ± 0.06 $^{ab}$ | 2.54 ± 0.13 $^{ab}$ | 0.032 |
| 8 weeks | 2.20 ± 0.04 $^{b}$ | 2.17 ± 0.00 $^{b}$ | 2.29 ± 0.03 $^{a}$ | 2.19 ± 0.04 $^{b}$ | 2.19 ± 0.01 $^{b}$ | 0.047 |
| **FCR** | | | | | | |
| 4 weeks | 0.76 ± 0.03 $^{a}$ | 0.76 ± 0.01 $^{a}$ | 0.75 ± 0.03 $^{a}$ | 0.75 ± 0.02 $^{a}$ | 0.75 ± 0.02 $^{a}$ | 0.479 |
| 8 weeks | 1.02 ± 0.01 $^{a}$ | 1.07 ± 0.04 $^{a}$ | 1.08 ± 0.04 $^{a}$ | 1.02 ± 0.03 $^{a}$ | 1.07 ± 0.08 $^{a}$ | 0.855 |
| **SR (%)** | | | | | | |
| 4 weeks | 96.67 ± 1.67 $^{a}$ | 95.00 ± 2.89 $^{a}$ | 98.33 ± 3.33 $^{a}$ | 98.33 ± 1.67 $^{a}$ | 98.33 ± 1.67 $^{a}$ | 0.046 |
| 8 weeks | 96.67 ± 1.67 $^{a}$ | 95.00 ± 2.89 $^{a}$ | 98.33 ± 3.33 $^{a}$ | 98.33 ± 1.67 $^{a}$ | 98.33 ± 1.67 $^{a}$ | 0.046 |

IW (g) = initial weight; FW (g) = final weight; WG (g) = weight gain; SGR (%) = specific growth rate; FCR = feed conversion ratio; SR (%) = survival rate.

### 2.2. Immunological Response

Lysozyme and peroxidase activities of skin mucus in Nile tilapia after 4 and 8 weeks of feeding are shown in Table 2. At both time points, skin mucus lysozyme activity (SMLA) and skin mucus peroxidase activity (SMPA) were significantly higher in the control group compared to all dietary CH treatments ($p < 0.05$). No significant differences were detected between the various CH-supplemented diets for either enzyme activity ($p > 0.05$).

**Table 2.** Skin mucus lysozyme and peroxidase activities in Nile tilapia (*Oreochromis niloticus*) fingerlings fed diets with increasing chitosan (CH) levels for 4 and 8 weeks. Data is shown as mean ± SEM. Different letters (a–b) indicate significant differences between dietary groups. Diets: CH0, 0 mL·kg$^{-1}$ (control); CH5, 5 mL·kg$^{-1}$; CH10, 10 mL·kg$^{-1}$; CH20, 20 mL·kg$^{-1}$; CH40, 40 mL·kg$^{-1}$ of chitosan.

| | | **CH0** | **CH5** | **CH10** | **CH20** | **CH40** | ***p*-Value** |
|---|---|---|---|---|---|---|---|
| 4 weeks | SMLA | 0.217 $^{a}$ ± 0.01 | 0.205 $^{b}$ ± 0.01 | 0.211 $^{ab}$ ± 0.01 | 0.195 $^{b}$ ± 0.01 | 0.201 $^{b}$ ± 0.01 | 0.048 |
| | SMPA | 0.313 $^{a}$ ± 0.02 | 0.287 $^{b}$ ± 0.01 | 0.304 $^{ab}$ ± 0.01 | 0.261 $^{b}$ ± 0.02 | 247 $^{b}$ ± 0.03 | 0.050 |
| 8 weeks | SMLA | 0.249 $^{a}$ ± 0.01 | 0.215 $^{b}$ ± 0.01 | 0.220 $^{ab}$ ± 0.01 | 0.201 $^{b}$ ± 0.01 | 0.215 $^{b}$ ± 0.01 | 0.001 |
| | SMPA | 0.213 $^{a}$ ± 0.04 | 0.193 $^{b}$ ± 0.06 | 0.204 $^{ab}$ ± 0.06 | 0.181 $^{b}$ ± 0.02 | 147 $^{b}$ ± 0.02 | 0.036 |

SMLA (μg mL$^{-1}$) = skin mucus lysozyme activity; SMPA (μg mL$^{-1}$) = skin mucus peroxidase activity.

Serum lysozyme and peroxidase activities are illustrated in Table 3. Serum lysozyme activity (SL) was higher in the control group at 4 weeks. Serum peroxidase activity (SP) was significantly higher in CH 10 at week 4 ($p < 0.05$). However, this difference was not significant at 8 weeks. In contrast, the CH20 and CH40 groups exhibited notably reduced SP at both sampling times.

**Table 3.** Serum lysozyme and peroxidase activities in Nile tilapia (*Oreochromis niloticus*) fingerlings fed diets with increasing chitosan (CH) levels for 4 and 8 weeks. Data is shown as mean ± SEM. Different letters (a–c) indicate significant differences between dietary groups by one-way ANOVA and Duncan's test ($p < 0.05$). Diets: CH0, 0 mL·kg$^{-1}$ COS (control); CH5, 5 mL·kg$^{-1}$; CH10, 10 mL·kg$^{-1}$; CH20, 20 mL·kg$^{-1}$; CH40, 40 mL·kg$^{-1}$ of chitosan.

| | | CH0 | CH5 | CH10 | CH20 | CH40 | *p*-Value |
|---|---|---|---|---|---|---|---|
| 4 weeks | SL | $0.297^{a} \pm 0.01$ | $0.275^{bc} \pm 0.01$ | $0.289^{ab} \pm 0.01$ | $0.258^{c} \pm 0.01$ | $0.286^{b} \pm 0.01$ | 0.038 |
| | SP | $0.443^{b} \pm 0.02$ | $0.449^{b} \pm 0.02$ | $0.501^{a} \pm 0.01$ | $0.388^{c} \pm 0.01$ | $0.392^{c} \pm 0.01$ | 0.015 |
| 8 weeks | SL | $0.248^{a} \pm 0.01$ | $0.225^{bc} \pm 0.01$ | $0.240^{ab} \pm 0.01$ | $0.212^{c} \pm 0.01$ | $0.231^{b} \pm 0.01$ | 0.049 |
| | SP | $0.477^{b} \pm 0.05$ | $0.438^{abc} \pm 0.04$ | $0.522^{a} \pm 0.03$ | $0.377^{c} \pm 0.02$ | $0.392^{bc} \pm 0.03$ | 0.041 |

SL: serum lysozyme activity (μg mL$^{-1}$); SP: serum peroxidase activity (μg mL$^{-1}$).

### 2.3. Histological Analysis

Intestinal morphology and related parameters of Nile tilapia fingerlings are presented in Figures 1 and 2. Villus length and width were significantly increased in the CH10 treatment group compared to the control group and the other treatment groups ($p < 0.05$). Fish fed the CH20 diet also exhibited greater villus length and width compared to the control. Additionally, the muscularis layer was the thickest in the CH10 group among all diets ($p < 0.05$). In contrast, the CH40 diet resulted in noticeable morphological alterations, including decreased villus length, villus width, and reduced muscularis thickness ($p < 0.05$).

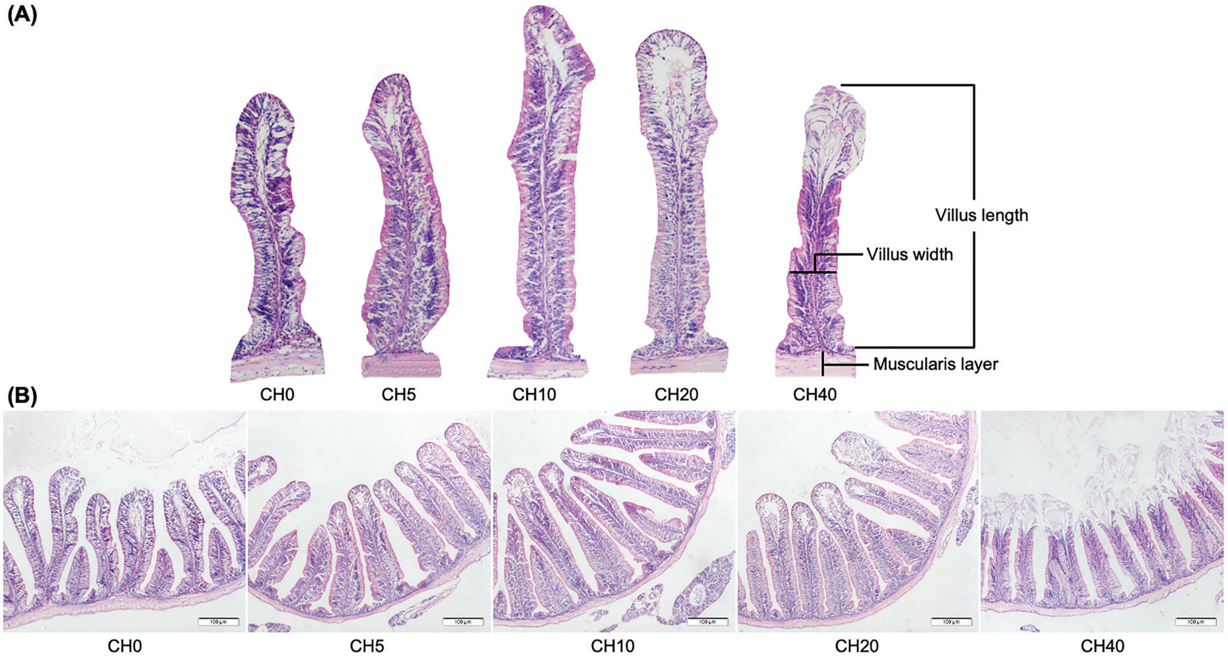

**Figure 1.** Intestinal morphology in Nile tilapia (*Oreochromis niloticus*) fingerlings fed diets with increasing chitosan (CH) levels after 8 weeks compared to the non-supplemented control diet. (**A**) A comparison of the length and width of the villus and thickness of the muscularis layer. (**B**) The cross-section through the microanatomy of the anterior intestine. Diets: CH0, 0 mL·kg$^{-1}$ COS (control); CH5, 5 mL·kg$^{-1}$; CH10, 10 mL·kg$^{-1}$; CH20, 20 mL·kg$^{-1}$; CH40, 40 mL·kg$^{-1}$ of chitosan. The tissue was stained with hematoxylin and eosin (H&E). The bars in the pictures are 100 μm.

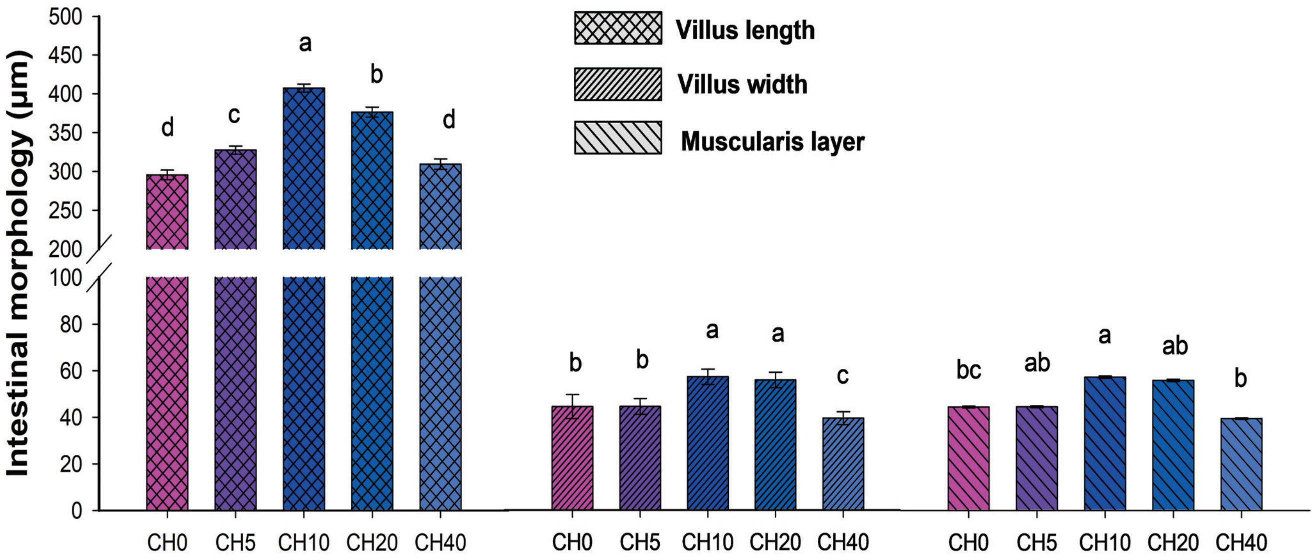

**Figure 2.** The measurements of the intestinal morphology of Nile tilapia (*Oreochromis niloticus*) fingerlings fed diets with increasing chitosan (CH) levels. Diets: CH0, 0 mL·kg$^{-1}$ COS (control); CH5, 5 mL·kg$^{-1}$; CH10, 10 mL·kg$^{-1}$; CH20, 20 mL·kg$^{-1}$; CH40, 40 mL·kg$^{-1}$ of chitosan. Five sections were randomly selected for measurement for each fish, with three fish per treatment. Values are means ± SEM ($n$ = 15, microfields). Values in the same row with different superscripts indicate a significant difference between the CH-containing groups ($p < 0.05$).

### 2.4. Immune and Antioxidant-Related Gene Expressions

The effects of dietary CH-supplemented on the expression of immune-related (*IL-1*, *IL-8*, *LBP*) and antioxidant-related (*GSR*, *GPX*, *GST-α*) genes in the liver and intestine of tilapia are shown in Figures 3 and 4. In both tissues, all supplemented diets appeared to upregulate these genes compared to the control. In the liver, the CH5 diet induced the greatest increase in most of the genes, with IL-8 expression being significantly higher than the control and the other diets ($p < 0.05$). For *IL-1*, *GSR*, and *GST-α*, there were no significant differences among supplemented groups ($p > 0.05$). *GPX* expression was significantly higher in the CH5 compared to the CH40 group ($p < 0.05$). Additionally, the CH5 and CH10 diet groups elicited increased *LBP* expression compared to the control and CH20 and CH40 groups ($p < 0.05$).

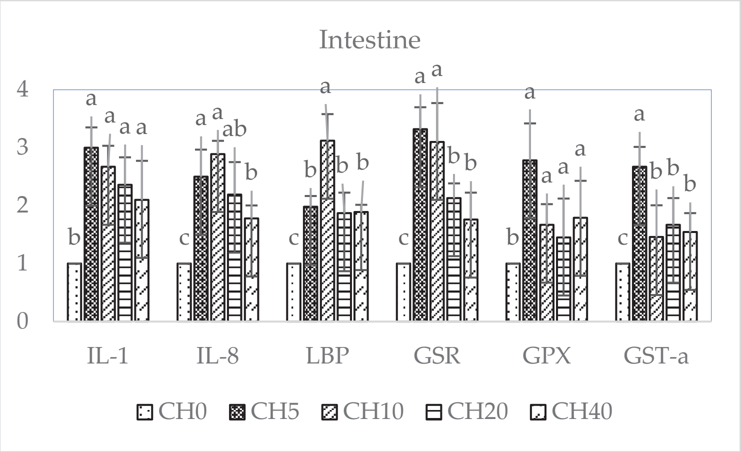

**Figure 3.** Expression transcript levels of interleukin-1 (*IL-1*), interleukin-8 (*IL-8*), lipopolysaccharide-binding protein (*LBP*), glutathione reductase (*GSR*), glutathione peroxidase (*GPX*), and glutathione

S-transferase-α (*GST-α*) in the liver of Nile tilapia (*Oreochromis niloticus*) fingerlings fed diets with increasing chitosan (CH) levels for 4 and 8 weeks ($n = 6$). Data is shown as mean ± SEM. Different letters (a–c) indicate significant differences between dietary groups by one-way ANOVA and Duncan's test ($p < 0.05$). Diets: CH0, 0 mL·kg$^{-1}$ COS (control); CH5, 5 mL·kg$^{-1}$; CH10, 10 mL·kg$^{-1}$; CH20, 20 mL·kg$^{-1}$; CH40, 40 mL·kg$^{-1}$ of chitosan.

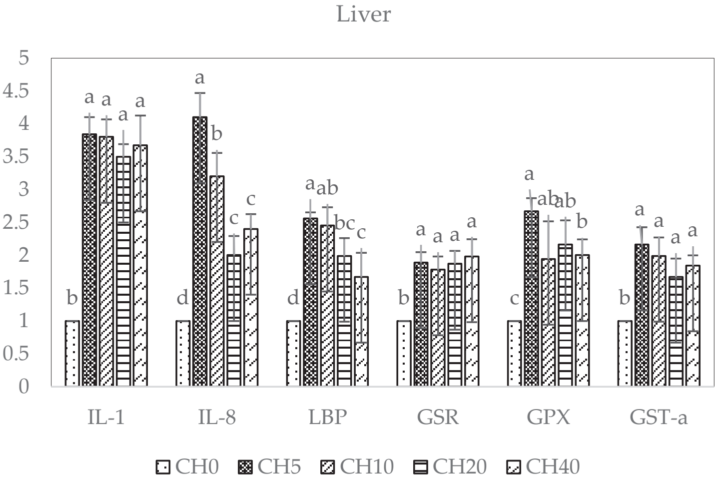

**Figure 4.** Expression transcript levels of interleukin-1 (*IL-1*), interleukin-8 (*IL-8*), lipopolysaccharide-binding protein (*LBP*), glutathione reductase (*GSR*), glutathione peroxidase (*GPX*), and glutathione S-transferase-α (*GST-α*) in intestine of Nile tilapia (*Oreochromis niloticus*) fingerlings fed diets with increasing chitosan (CH) levels for 4 and 8 weeks ($n = 6$). Data is shown as mean ± SEM. Different letters (a–c) indicate significant differences between dietary groups by one-way ANOVA and Duncan's test ($p < 0.05$). Diets: CH0, 0 mL·kg$^{-1}$ COS (control); CH5, 5 mL·kg$^{-1}$; CH10, 10 mL·kg$^{-1}$; CH20, 20 mL·kg$^{-1}$; CH40, 40 mL·kg$^{-1}$ of chitosan.

In the intestine, expression of *IL-1* and *GPX* was significantly higher in all dietary CH-treated groups compared to the control group ($p < 0.05$), with no statistically significant differences among supplemented diets ($p > 0.05$). Interestingly, the highest *LBP* expression occurred in the CH10 group, which was significantly different from the control and other treated groups ($p < 0.05$). *GSR* expression was significantly higher in the CH5 and CH10 groups compared to the control and CH20 and CH40 groups ($p < 0.05$). Additionally, CH5 and CH10 diets elicited clear increases in *IL-8* and CH-5 increased *GST-α* expression compared to the control and the other CH-supplemented groups.

## 3. Discussion

The current study demonstrated the beneficial effects of dietary-supplemented CH on the growth of Nile tilapia (*Oreochromis niloticus*) fingerlings cultured in a biofloc system. Influences of dietary chitosan on growth have been evaluated in various aquatic species with variable results [10,50–52]. Specifically in Nile tilapia, previous findings on chitosan's effects as a feed additive have been heterogeneous. Shiau and Yu [53] found that 2–10% of dietary chitosan inhibited tilapia growth, while Romana-Eguia et al. [54] showed no impact on growth. However, other studies [55,56] reported improved growth and meat quality with chitosan supplementation in Nile tilapia. Interestingly, this study indicated that only the 10 mL·kg$^{-1}$ CH diet significantly increased FW, WG, and SGR of Nile tilapia fingerlings, suggesting that the benefits are dose-dependent, with excessive amounts conferring no added growth effects. Indeed, multiple studies have evidenced the detrimental impacts of immunostimulant over-supplementation on aquaculture species, including immune exhaustion and slowed growth [57,58]. Shiau and Yu [53] reported decreased weight gain in Nile tilapia with chitosan, potentially due to reduced nutrient digestibility and absorption. Chitosan particle size may also influence Nile tilapia growth [59]. Several lines of evidence suggest that chito-oligosaccharides can improve growth performance in tilapia through various interrelated mechanisms. As prebiotics, CH can modify intestinal microbial communities in a beneficial manner, supporting gut health and likely enhancing nutrient digestion and absorption [60]. The immunostimulatory effects of chito-oligosaccharides are also thought to play a key role by reducing the susceptibility to infectious diseases, allowing tilapia to allocate more energy towards growth rather than mounting inflammatory responses [61]. Chito-oligosaccharides have additionally been shown to increase the activities of digestive enzymes like protease, lipase, and amylase in tilapia, which could lead to greater utilization of feed for growth [62]. Finally, mitigation of oxidative stress by the antioxidant properties of CH enables available energy to be used for anabolism rather than neutralizing reactive oxygen species, supporting growth [63,64]. The growth-promoting effects of immunostimulants like CH are influenced by numerous factors, including dosage, molecular weight, feeding duration, temperature, administration route, and species difference [65]. Our results demonstrated that the benefits of CH on growth were dose-dependent in Nile tilapia, with 10 $\text{mL}\cdot\text{kg}^{-1}$ being the optimal supplementation level for improving performance. While the precise modes of action have yet to be elucidated, this study provides valuable insights into appropriate CH dosing strategies for maximizing growth in tilapia aquaculture. Further research is still needed to fully understand the biological pathways and key factors mediating the effects of CH on increasing fish growth rate.

Innate immunity serves as the first line of defense against pathogens in fish [66]. The body's surface mucosa provides a physical and immunological barrier, playing crucial roles in protection, sensory function, and ion regulation [67,68]. Mucosal responses are key in early infection control, as many pathogens initially adhere to mucosal surfaces during invasion [69]. Lysozyme, found in mucus, fluids, and tissues, is an important component of teleost innate immunity due to its bactericidal and opsonizing effects [70,71]. Serum lysozyme can indicate the innate status of the host by initiating the complement cascade [69,70]. CH's free radical scavenging amino groups can boost unstable lysozyme [72], and oral chitosan has been shown to increase lysozyme activity in various fish species [73,74]. Peroxidase, another key innate immune enzyme, helps to maintain redox homeostasis in immune cells and acts as a microbicidal agent by destroying $H_2O_2$ [75,76]. In this study, our results demonstrated that dietary CH supplementation at 5–40 $\text{mL}\cdot\text{kg}^{-1}$ significantly decreased peroxidase and lysozyme activities in the skin mucus after 4 weeks, declining further by 8 weeks. Interestingly, 10 $\text{mL}\cdot\text{kg}^{-1}$ CH increased blood serum peroxidase activity at 4 and 8 weeks of the feeding trial. These results align with Yu et al. [58], who showed 10 g/kg CH reduced lysozyme in golden pompano (*Trachinotus ovatus*). The contrasting blood and mucus enzyme responses reveal the complex immunomodulatory effects of CH in fish. Achieving optimal benefits likely requires careful dosage optimization. Our findings highlight the need for further research into appropriate CH supplementation strategies to support mucosal and systemic innate defenses in aquaculture species.

Oligosaccharide supplementation in fish diets promotes feed conversion and enhances intestinal microanatomy, improves mucosal epithelium health, and defends against opportunistic bacterial infections [77]. This optimization of intestinal morphology may increase the absorption area of the intestine, facilitating efficient nutrient absorption [78]. In the present study, it was observed that the treatment with CH resulted in an increase in villus height and width, along with an increase in the thickness of the muscularis layer, which was particularly pronounced in the CH10 and CH20 groups. Since the proportion of villi is related to the ability to absorb nutrients through the available surface area, the surface increase could potentially improve nutrient utilization and storage [79]. Our results are consistent with previous studies, such as those showing an increase in villus length following supplementation of hybrid grouper diets with CH oligosaccharides [80] or after supplementation of hybrid catfish diets with mannan oligosaccharides [81]. It has also been reported that various other oligosaccharides can significantly increase villus length in numerous fish species, as shown by 1% galacto-oligosaccharide in the diet for red drum [82] or 2% fructo-oligosaccharide in the diet for bluntnose seabream [83]. However, it is worth noting that the effects of oligosaccharides on the villi structure may vary depending on the fish species, oligosaccharide type and concentration, and the fish species' own microbiota. In this study, the CH40-containing treatments resulted in some undesirable changes in the intestinal morphology of the fish, including degeneration of the villi and morphological disorders. This outcome may be attributed to an imbalance of amino acids in the diet, possibly triggered by an incorrect ratio when replacing fish meal with CH, which is consistent with previous studies [80,84]. Since dietary amino acids are primarily used to meet growth requirements and build fish tissue, an imbalance of these amino acids may lead to dysplasia in fish intestinal morphology [85,86]. Overall, our results indicate that CH supplementation at 10–20 $\mathrm{mL{\cdot}kg^{-1}}$ may beneficially enhance the intestinal morphology and the absorptive capacity in tilapia, yet higher doses could negatively impact the intestine structure.

Pro-inflammatory cytokine *IL-1* is essential for innate immunity, stimulating lymphocytes, phagocytes, and infection resistance in fish [87]. *IL-8*, released during inflammation, activates inflammatory cells as a neutrophil chemoattractant and mediator [88]. *IL-1* and *IL-8* coordinate innate inflammatory defenses and pathogen clearance by phagocytes [89,90]. The acute-phase protein lipopolysaccharide-binding protein (*LBP*) also has key innate immune functions, binding lipopolysaccharides and eliciting responses to Gram-negative bacteria [91]. In our study, all CH doses markedly increased hepatic and intestinal expression of the immune genes *IL-1*, *IL-8*, and *LBP* compared to the control, indicating activation of innate immune responses in tilapia. These results align with previous observations reporting *IL-1* and *IL-8* upregulation following immunostimulant feeding in tilapia [92]. However, in golden pompano, CH reduced *IL-8* expression [57], highlighting species-specific differences. Antioxidant supplements can improve fish health by reducing oxidative stress. Glutathione peroxidase (*GPX*) and glutathione reductase (*GSR*) remove hydrogen peroxide using glutathione [13,93]. Glutathione S-transferase (*GST*) detoxifies electrophiles, enhancing their elimination [94]. In this study, we found dietary CH-supplemented significantly increased antioxidant gene (*GSR*, *GPX*, *GST-α*) expression in tilapia liver and intestine, similar to previous tilapia studies [13] and golden pompano [57]. This suggests that CH may mitigate oxidative damage. Overall, our gene expression analyses indicate that CH can stimulate innate immune and antioxidant responses in tilapia.

The growth benefits of CH in this study may have been enhanced by using a biofloc production system [95], which consists of suspended microbial biomass that acts as a natural food source [46,96–98]. This seems to stem from the fact that the prebiotic effects of CH selectively enriched beneficial biofloc species, maximizing natural productivity. Their immunostimulatory properties likely complemented immune activation by biofloc microbes. The combination of bioavailable nutrients from biofloc consumption and improved digestibility and gut health from CH may have synergistically augmented tilapia growth.

The limitations of this study include the absence of a priori power analysis and the use of non-standard reporting of chitosan concentration in volume units (mL/kg diet) instead of mass units (g/kg diet). The lack of a priori power analysis may serve to hide the true effects of chitosan supplementation, potentially leading to underpowered circumstances that are unable to identify statistically significant results. To address these issues, we propose the use of power analysis in the study design phase as a mean to precisely ascertain the necessary sample sizes. Furthermore, standardizing the reporting of chitosan concentrations in mass units will greatly enhance the reproducibility of research findings and streamline the process of comparing them across different investigations.

## 4. Materials and Methods

### 4.1. Nile Tilapia Husbandry

Healthy Nile tilapia fingerlings were acquired from a tilapia farm in Chiang Mai Province, Thailand. The fish were first acclimated for two weeks under standard aquaculture conditions and fed on commercial diets twice daily. The tilapia was then moved into fifteen 150 L fiberglass tanks for the feeding trials. Water quality parameters, including temperature (°C), pH, dissolved oxygen (mg·L$^{-1}$), and ammonium, were maintained within optimal ranges for Nile tilapia [99] throughout the experiment as follows: T° = 28.5 ± 0.07; pH = 7.81 ± 0.03; dissolved oxygen = 5.76 ± 0.02 mg·L$^{-1}$, and ammonium = 0.12 ± 0.002 mg·L$^{-1}$.

## *4.2. Diet Preparation and Experimental Design*

### 4.2.1. Preparation of Chitosan (CH)

The CH supplement used in this study was obtained from Olizac Technologies Co., Ltd., Khlong Nueng, Khlong Luang District, Pathum Thani, Thailand. It was extracted from shrimp shell via enzymatic hydrolysis as described previously [100]. Briefly, shrimp shells underwent deproteinization, demineralization, and depigmentation before being deacetylated with 50% sodium hydroxide to achieve over 90% degree of deacetylation. The CH was then precipitated and lyophilized. A mixture of chitinase and chitosanase enzymes was applied to produce CH with a molecular weight of approximately 10 kDa, as determined by gel permeation chromatography.

### 4.2.2. Experimental Design

Five experimental diets containing different levels of CH were prepared. The diet formulations are shown in Table 4 The dry ingredients were thoroughly mixed and then pelletized with the addition of oil and water into 2 mm pellets. Feeds were stored at 4 °C until use. After a two-week acclimation, 300 healthy tilapia fingerlings (13.54 ± 0.05 g) were randomly distributed into the following treatment groups ($n$ = 20 fish per tank, 3 replicate tanks per treatment): CH0, 0 mL·kg$^{-1}$ CH as control; CH5, 5 mL·kg$^{-1}$; CH10, 10 mL·kg$^{-1}$; CH20, 20 mL·kg$^{-1}$; and CH40, 40 mL·kg$^{-1}$. Fish were fed the experimental diets twice daily for 8 weeks while water quality parameters were monitored daily as described previously [99].

**Table 4.** The formulation and proximate composition of the experimental diets (g/kg of the basal diets).

| | **CH0** | **CH5** | **CH10** | **CH20** | **CH40** |
|---|---|---|---|---|---|
| Fish meal | 200 | 200 | 200 | 200 | 200 |
| Corn meal | 150 | 150 | 150 | 150 | 150 |
| Soybean meal | 390 | 390 | 390 | 390 | 390 |
| Wheat flour | 70 | 70 | 70 | 70 | 70 |
| Rice bran | 150 | 150 | 150 | 150 | 150 |
| Soybean oil | 2 | 2 | 2 | 2 | 2 |
| Chitosan solution (mL) | 0 | 5 | 10 | 20 | 40 |
| Binder | 20 | 20 | 20 | 20 | 20 |
| Premix [1] | 10 | 10 | 10 | 10 | 10 |
| Vitamin C 98% | 8 | 8 | 8 | 8 | 8 |
| Total (g) | 1000 | 1000 | 1000 | 1000 | 1000 |
| Proximate composition of the experimental diets (%) | | | | | |
| Crude protein | 32.80 | 32.00 | 32.60 | 32.40 | 32.50 |
| Crude lipid | 2.85 | 2.75 | 2.63 | 2.78 | 2.88 |
| Fiber | 3.68 | 3.74 | 3.44 | 3.72 | 3.55 |
| Ash | 7.59 | 7.86 | 7.75 | 7.35 | 7.91 |
| Dry matter | 99.16 | 98.40 | 98.35 | 97.77 | 97.54 |
| Gross Energy (cal/g) | 4273.00 | 4261.50 | 4253.90 | 4262.00 | 4245.00 |

[1] Vitamin and trace mineral mix supplemented as follows (IU kg$^{-1}$ or g kg$^{-1}$ diet): retinyl acetate 1,085,000 IU; cholecalciferol 217,000 IU; D, L-a-tocopherol acetate 0.5 g; thiamin nitrate 0.5 g; pyridoxine hydrochloride 0.5 g; niacin 3 g; folic 0.05 g; cyanocobalamin 10 g; Ca pantothenate 1 g kg$^{-1}$; inositol 0.5 g; zinc 1 g; copper 0.25 g; manganese 1.32 g; iodine 0.05 g; sodium 7.85 g.

## *4.3. Biofloc Water Preparation*

Biofloc was established in the experimental tanks 3 weeks prior to starting the feeding trial. Coarse salt (400 g), molasses (5 g), dolomite (5 g), and control feed (2 g) were added to each tank to initiate floc formation. The carbon-to-nitrogen (C:N) ratio was maintained at 15:1 by supplementing with molasses (40% carbon) 2 h after each feeding [40]. The C/N ratio was monitored by measuring residual nitrogen levels in the tanks and determining the carbon and nitrogen content of the feed.

### *4.4. Growth Performance*

After 4 and 8 weeks of feeding the experimental diets, all fish were weighed to assess growth performance. Parameters were calculated as follows:

Weight gain (WG, g) = final weight (FW) − initial weight (IW);
Specific growth rate (SGR, %) = 100 × (ln FW − ln IW)/number of experimental days;
Feed conversion ratio (FCR) = amount of feed given (dry weight)/WG (wet weight);
Survival rate (SR, %) = (final number of fish/initial number of fish) × 100.

### *4.5. Immunological Analysis*

#### 4.5.1. Sample Collection

Skin mucus and serum samples were collected to analyze immunological parameters. For skin mucus, 3 fish were randomly selected from each tank and anesthetized with clove oil (200 ppm) to minimize stress and discomfort. Following anesthesia, the fish were humanely euthanized in accordance with ethical guidelines for the collection of skin mucus and serum samples. Individuals were placed in plastic bags containing 10 mL of 50 mM NaCl. The fish were gently rubbed for 1 min to collect skin mucus. The mucus–salt mixture was centrifuged at 1500× *g* for 10 min at 4 °C. The supernatant was stored at −80 °C until analysis.

Blood samples were collected as previously described [99]. Briefly, 1 mL of blood was drawn from the caudal vein of each fish using a 1 mL syringe and immediately transferred into new sterilized tubes (without anticoagulants). Blood samples were kept at room temperature for 1 h and then incubated for 4 h at 4 °C. Serum samples were collected after centrifugation (15 min, 4 °C at 10,000× *g*) and stored at −80 °C until analysis.

#### 4.5.2. Immunological Parameter Analysis

Lysozyme and peroxidase activities in undiluted serum and skin mucus samples were performed according to the previously described method [101]. Briefly, 25 µL of serum or 100 µL of skin mucus from each fish was added in triplicate to 96-well plates, followed by 175 µL of a 0.3 mg.mL$^{-1}$ Micrococcus lysodeikticus suspension (in 0.1 M citrate phosphate buffer, pH 5.8). Plates were rapidly mixed, and the decrease in turbidity was measured every 30 s for 10 min at 540 nm using a microplate reader (Synergy H1, BioTek, Santa Clara, CA 95051, USA). A standard curve was generated using known concentrations of hen egg white lysozyme (0–20 µg.mL$^{-1}$, Sigma-Aldrich Inc., St. Louis, MO 68178, USA).

### *4.6. Histopathology Analysis*

To examine intestinal morphology, the anterior intestine from 3 fish per treatment was sampled at the end of the trial. Tissues were fixed in 10% neutral buffered formalin for 24 h, then transferred to 70% ethanol. Samples were processed using an automated tissue processor, involving dehydration in graded ethanol, clearing with xylene, and embedding in paraffin wax. The tissues were sectioned at 4–5 µm thickness using a microtome (Leica Biosystems, Deer Park, IL 60010, USA) and stained with hematoxylin and eosin (H and E). Slides were viewed and photographed using a light microscope (BX51 Olympus, Tokyo, Japan). Morphometric analysis was performed by measuring villus length, villus width, and muscularis thickness on 5 randomly selected microfields per fish.

### *4.7. Quantitative Real-Time PCR (qPCR)*

#### 4.7.1. Tissue Sampling, Total RNA Isolation, and cDNA Synthesis

Expressions of immune-related (*IL-1*, *IL-8*, and *LBP*) and antioxidant-related (*GST-α*, *GPX*, and *GSR*) genes were analyzed in the liver and intestine after 8 weeks. Examined organs (20–40 mg) were collected from two fish in each tank ($n$ = 6) and stored in sterilized tubes supplemented with 500 µL Trizol (Invitrogen, Waltham, MA, USA) at −80 °C for further analysis. Total RNA was isolated using the PureLink$^{TM}$ RNA Mini Kit (Invitrogen, Thermo Fisher Scientific, Waltham, MA, USA) following the manufacturer's protocol. RNA quantity and quality were assessed by spectrophotometry (NanoDrop$^{TM}$ 2000, Thermo Scientific, Waltham, MA, USA). One µg of total RNA was used for cDNA synthesis with the iScript$^{TM}$ cDNA kit (BIO-RAD, Hercules, CA, USA).

### 4.7.2. Quantitative Real-Time PCR

Gene expression was quantified by qPCR using the primer sequences listed in Table 5. Reactions contained 1 µL cDNA (100 ng), 0.4 µL each primer (10 µM), 10 µL 2× SYBR Green Mastermix (BIO-RAD, USA) and nuclease-free water to 20 µL total volume. qPCR was performed on a CFX ConnectTM system (BIO-RAD, USA) as described previously [13]. Relative mRNA levels were calculated using the $2^{-\Delta\Delta Ct}$ method [102] with *18S rRNA* as the internal reference gene.

**Table 5.** Primer sequences used for quantitative real-time PCR.

| Genes | Primer Sequence (5′-3′) | Tm (°C) | Product Size (bp) | Reference |
|---|---|---|---|---|
| *18S-rRNA* | GTGCATGGCCGTTCTTAGTT<br>CTCAATCTCGTGTGGCTGAA | 60 | 150 | XR_003216134 |
| *IL-1* | GTCTGTCAAGGATAAGCGCTG<br>ACTCTGGAGCTGGATGTTGA | 59 | 200 | XM_019365844 |
| *IL-8* | CTGTGAAGGCATGGGTGTG<br>GATCACTTTCTTCACCCAGGG | 59 | 196 | NM_001279704 |
| *LBP* | ACCAGAAACTGCGAGAAGGA<br>GATTGGTGGTCGGAGGTTTG | 59 | 200 | XM_013271147 |
| *GST-α* | ACTGCACACTCATGGGAACA<br>TTAAAAGCCAGCGGATTGAC | 60 | 190 | NM_001279635 |
| *GPX* | GGTGGATGTGAATGGAAAGG<br>CTTGTAAGGTTCCCCGTCAG | 60 | 190 | NM_001279711 |
| *GSR* | CTGCACCAAAGAACTGCAAA<br>CCAGAGAAGGCAGTCCACTC | 60 | 172 | XM_005467348 |

### *4.8. Statistical Analyses*

The Shapiro–Wilk test was used to assess the normality of the data. One-way analysis of variance (ANOVA) was performed to determine statistically significant differences among the dietary treatment groups. The distribution of the sample variables was considered normal ($p > 0.05$) and was evaluated using a one-way ANOVA. Statistical significance among groups ($p < 0.05$) was compared using post hoc LSD analysis and non-normal distribution ($p < 0.05$). All data were analyzed using Statistix (Analytical Software, v10.0 Tallahassee, FL 32312, USA) statistical software.

## 5. Conclusions

In summary, this study demonstrates that dietary supplementation with 10 mL·kg$^{-1}$ CH can effectively improve the growth, health, and productivity of Nile tilapia fingerlings reared in biofloc systems. CH also stimulated innate immunity, as shown by increased serum peroxidase activity at 4 weeks. Most notably, CH feeding markedly upregulated the expression of immune and antioxidant genes in the liver and intestine. This indicates that CH can beneficially modulate the immune status and oxidative stress resistance in Nile tilapia. Our findings highlight the potential of CH as a feed additive to improve Nile tilapia fingerlings' health and productivity in sustainable biofloc aquaculture.

**Author Contributions:** Methodology, Writing, review, and editing, formal analysis, data curation, software analysis, validation, N.V.L.; writing—original draft, A.R.L.; writing, review, and editing, N.D.-H.; investigation, methodology, S.W.; formal analysis, methodology, N.M.; writing, review, and editing, C.M.F.; methodology, P.L.; methodology, O.S.; supervision, validation, W.-K.J.; review and editing, M.P.; conceptualization, data curation, funding acquisition, supervision, validation, and project administration, H.V.D. All authors have read and agreed to the published version of the manuscript.

**Funding:** This research was funded by the National Research Council of Thailand (PMUC), grant number 640000060128, and partially supported by Chiang Mai University, grant number CoE2566.

**Institutional Review Board Statement:** All animal care and experimental procedures followed AAALAC (Association for Assessment and Accreditation of Laboratory Animal Care) guidelines and were approved by the Chiang Mai University Research Ethics Committee (Approved No. AG03002-2565).

**Data Availability Statement:** The data presented in this study are available on request from the corresponding author.

**Acknowledgments:** The authors would like to thank the National Research Council of Thailand (PMUC) for their support and assistance with this study.

**Conflicts of Interest:** The authors declare no conflicts of interest.

## References

1. Sampathkumar, K.; Yu, H.; Loo, S.C.J. Valorisation of Industrial Food Waste into Sustainable Aquaculture Feeds. *Future Foods* **2023**, *7*, 100240. [CrossRef]
2. Gule, T.T.; Geremew, A. Dietary Strategies for Better Utilization of Aquafeeds in Tilapia Farming. *Aquac. Nutr.* **2022**, *2022*, 9463307. [CrossRef]
3. Abdel-Aziz, M.F.A.; Hassan, H.U.; Yones, A.-M.; Abdel-Tawwab, Y.A.; Metwalli, A.A.A.-T. Assessing the Effect of Different Feeding Frequencies Combined with Stocking Density, Initial Weight, and Dietary Protein Ratio on the Growth Performance of Tilapia, Catfish and Carp. *Sci. Afr.* **2021**, *12*, e00806. [CrossRef]
4. Syed, R.; Masood, Z.; Hassan, H.U.; Khan, W.; Mushtaq, S.; Ali, A.; Gul, Y.; Jafari, H.; Habib, A.; Shah, M.I.A. Growth Performance, Haematological Assessment and Chemical Composition of Nile Tilapia, *Oreochromis niloticus* (Linnaeus, 1758) Fed Different Levels of Aloe Vera Extract as Feed Additives in a Closed Aquaculture System. *Saudi J. Biol. Sci.* **2022**, *29*, 296–303. [CrossRef] [PubMed]
5. El-Sayed, A.-F.M.; Fitzsimmons, K. From Africa to the World—The Journey of Nile Tilapia. *Rev. Aquac.* **2023**, *15*, 6–21. [CrossRef]
6. Delphino, M.; Joshi, R.; Alvarez, A.T. Economic Appraisal of Using Genetics to Control *Streptococcus agalactiae* in Nile Tilapia under Cage and Pond Farming System in Malaysia. *Sci. Rep.* **2022**, *12*, 8754. [CrossRef] [PubMed]
7. Suyamud, B.; Chen, Y.; Quyen, D.T.T.; Dong, Z.; Zhao, C.; Hu, J. Antimicrobial Resistance in Aquaculture: Occurrence and Strategies in Southeast Asia. *Sci. Total Environ.* **2024**, *907*, 167942. [CrossRef]
8. Henriksson, P.J.; Rico, A.; Troell, M.; Klinger, D.H.; Buschmann, A.H.; Saksida, S.; Chadag, M.V.; Zhang, W. Unpacking Factors Influencing Antimicrobial Use in Global Aquaculture and Their Implication for Management: A Review from a Systems Perspective. *Sustain. Sci.* **2018**, *13*, 1105–1120. [CrossRef]
9. Guimarães, M.C.; Cerezo, I.M.; Fernandez-Alarcon, M.F.; Natori, M.M.; Sato, L.Y.; Kato, C.A.; Moriñigo, M.A.; Tapia-Paniagua, S.; Dias, D.d.C.; Ishikawa, C.M. Oral Administration of Probiotics (*Bacillus subtilis* and *Lactobacillus plantarum*) in Nile Tilapia (*Oreochromis niloticus*) Vaccinated and Challenged with *Streptococcus agalactiae*. *Fishes* **2022**, *7*, 211. [CrossRef]
10. Nurmalasari; Liu, C.-H.; Maftuch, I.M.; Hu, S.-Y. Dietary Supplementation with Prebiotic Chitooligosaccharides Enhances the Growth Performance, Innate Immunity and Disease Resistance of Nile Tilapia (*Oreochromis niloticus*). *Fishes* **2022**, *7*, 313. [CrossRef]
11. Wang, T.; Wu, H.-X.; Li, W.; Xu, R.; Qiao, F.; Du, Z.-Y.; Zhang, M.-L. Effects of Dietary Mannan Oligosaccharides (MOS) Supplementation on Metabolism, Inflammatory Response and Gut Microbiota of Juvenile Nile Tilapia (*Oreochromis niloticus*) Fed with High Carbohydrate Diet. *Fish Shellfish Immunol.* **2022**, *130*, 550–559. [CrossRef] [PubMed]
12. Kakavand, F.; Iri, A.; Rezaei Shadegan, M.; Bigdeli, M.; Heydarzadeh Barzegar, D.; Zamani, V.; Barkhordar, M.; Houshmand, P.; Zare Mehrabadi, E.; Hedayati, A. Toxicity Effect of Silver Nitrate on Some Hematological Indices of Nil Tilapia (*Oreochromis niloticus*) Fed with Different Levels of Prebiotic Oyster Mushroom (*Pleurotus ostreatus*). *J. Aquat. Physiol. Biotechnol.* **2022**, *9*, 141–160.
13. Outama, P.; Le Xuan, C.; Wannavijit, S.; Lumsangkul, C.; Linh, N.V.; Montha, N.; Tongsiri, S.; Chitmanat, C.; Van Doan, H. Modulation of Growth, Immune Response, and Immune-Antioxidant Related Gene Expression of Nile Tilapia (*Oreochromis niloticus*) Reared under Biofloc System Using Mango Peel Powder. *Fish Shellfish Immunol.* **2022**, *131*, 1136–1143. [CrossRef] [PubMed]

14. del Valle, J.C.; Bonadero, M.C.; Gimenez, A.V.F. Saccharomyces Cerevisiae as Probiotic, Prebiotic, Synbiotic, Postbiotics and Parabiotics in Aquaculture: An Overview. *Aquaculture* **2023**, *569*, 739342. [CrossRef]
15. Khanjani, M.H.; da Silva, L.O.B.; Fóes, G.K.; Vieira, F.d.N.; Poli, M.A.; Santos, M.; Emerenciano, M.G.C. Synbiotics and Aquamimicry as Alternative Microbial-Based Approaches in Intensive Shrimp Farming and Biofloc: Novel Disruptive Techniques or Complementary Management Tools? A Scientific-Based Overview. *Aquaculture* **2023**, *567*, 739273. [CrossRef]
16. Amiri, H.; Aghbashlo, M.; Sharma, M.; Gaffey, J.; Manning, L.; Moosavi Basri, S.M.; Kennedy, J.F.; Gupta, V.K.; Tabatabaei, M. Chitin and Chitosan Derived from Crustacean Waste Valorization Streams Can Support Food Systems and the UN Sustainable Development Goals. *Nat. Food* **2022**, *3*, 822–828. [CrossRef] [PubMed]
17. FAO. *The State of World Fisheries and Aquaculture 2022*; FAO: Rome, Italy, 2022.
18. Wani, A.K.; Akhtar, N.; Mir, T.u.G.; Rahayu, F.; Suhara, C.; Anjli, A.; Chopra, C.; Singh, R.; Prakash, A.; El Messaoudi, N.; et al. Eco-Friendly and Safe Alternatives for the Valorization of Shrimp Farming Waste. *Environ. Sci. Pollut. Res.* **2023**. [CrossRef] [PubMed]
19. Ravanipour, M.; Bagherzadeh, R.; Mahvi, A.H. Fish and Shrimp Waste Management at Household and Market in Bushehr, Iran. *J. Mater. Cycles Waste Manag.* **2021**, *23*, 1394–1403. [CrossRef]
20. Mao, X.; Guo, N.; Sun, J.; Xue, C. Comprehensive Utilization of Shrimp Waste Based on Biotechnological Methods: A Review. *J. Clean. Prod.* **2017**, *143*, 814–823. [CrossRef]
21. Yadav, M.; Goswami, P.; Paritosh, K.; Kumar, M.; Pareek, N.; Vivekanand, V. Seafood Waste: A Source for Preparation of Commercially Employable Chitin/Chitosan Materials. *Bioresour. Bioprocess.* **2019**, *6*, 8. [CrossRef]
22. Mansyur, N.; Hanudin, E.; Purwanto, B.; Utami, S. The Nutritional Value of Shrimp Waste and Its Response to Growth and N Uptake Efficiency by Corn. *IOP Conf. Ser. Earth Environ. Sci.* **2021**, *748*, 012013. [CrossRef]
23. Liu, Z.; Liu, Q.; Zhang, D.; Wei, S.; Sun, Q.; Xia, Q.; Shi, W.; Ji, H.; Liu, S. Comparison of the Proximate Composition and Nutritional Profile of Byproducts and Edible Parts of Five Species of Shrimp. *Foods* **2021**, *10*, 2603. [CrossRef] [PubMed]
24. Susetyaningsih, R.; Suntoro, S.; Gunawan, T.; Budiastuti, M.T.S. Impact of Shrimp Pond Waste on Water Quality (Case Study of Trisik Lagoon in Yogyakarta). *AIP Conf. Proc.* **2020**, *2296*, 020050.
25. Dauda, A.B.; Ajadi, A.; Tola-Fabunmi, A.S.; Akinwole, A.O. Waste Production in Aquaculture: Sources, Components and Managements in Different Culture Systems. *Aquac. Fish.* **2019**, *4*, 81–88. [CrossRef]
26. El Amri, H.; Boukharta, M.; Zakham, F.; Ennaji, M.M. Emergence and Reemergence of Viral Zoonotic Diseases: Concepts and Factors of Emerging and Reemerging Globalization of Health Threats. In *Emerging and Reemerging Viral Pathogens*; Elsevier: Amsterdam, The Netherlands, 2020; pp. 619–634.
27. Yan, N.; Chen, X. Sustainability: Don't Waste Seafood Waste. *Nature* **2015**, *524*, 155–157. [CrossRef]
28. Hosney, A.; Ullah, S.; Barčauskaitė, K. A Review of the Chemical Extraction of Chitosan from Shrimp Wastes and Prediction of Factors Affecting Chitosan Yield by Using an Artificial Neural Network. *Mar. Drugs* **2022**, *20*, 675. [CrossRef] [PubMed]
29. de Queiroz Antonino, R.S.C.M.; Lia Fook, B.R.P.; de Oliveira Lima, V.A.; de Farias Rached, R.Í.; Lima, E.P.N.; da Silva Lima, R.J.; Peniche Covas, C.A.; Lia Fook, M.V. Preparation and Characterization of Chitosan Obtained from Shells of Shrimp (*Litopenaeus vannamei* Boone). *Mar. Drugs* **2017**, *15*, 141. [CrossRef] [PubMed]
30. Xu, Q.; Wang, W.; Qu, C.; Gu, J.; Yin, H.; Jia, Z.; Song, L.; Du, Y. Chitosan Oligosaccharides Inhibit Epithelial Cell Migration through Blockade of N-Acetylglucosaminyltransferase V and Branched GlcNAc Structure. *Carbohydr. Polym.* **2017**, *170*, 241–246. [CrossRef] [PubMed]
31. Zou, P.; Yuan, S.; Yang, X.; Zhai, X.; Wang, J. Chitosan Oligosaccharides with Degree of Polymerization 2–6 Induces Apoptosis in Human Colon Carcinoma HCT116 Cells. *Chem.-Biol. Interact.* **2018**, *279*, 129–135. [CrossRef]
32. Jitprasertwong, P.; Khamphio, M.; Petsrichuang, P.; Eijsink, V.G.H.; Poolsri, W.; Muanprasat, C.; Rangnoi, K.; Yamabhai, M. Anti-Inflammatory Activity of Soluble Chitooligosaccharides (CHOS) on VitD3-Induced Human THP-1 Monocytes. *PLoS ONE* **2021**, *16*, e0246381. [CrossRef]
33. Muanprasat, C.; Wongkrasant, P.; Satitsri, S.; Moonwiriyakit, A.; Pongkorpsakol, P.; Mattaveewong, T.; Pichyangkura, R.; Chatsudthipong, V. Activation of AMPK by Chitosan Oligosaccharide in Intestinal Epithelial Cells: Mechanism of Action and Potential Applications in Intestinal Disorders. *Biochem. Pharmacol.* **2015**, *96*, 225–236. [CrossRef] [PubMed]
34. Dai, X.; Chang, P.; Li, X.; Gao, Z.; Sun, Y. The Inhibitory Effect of Chitosan Oligosaccharides on β-Site Amyloid Precursor Protein Cleaving Enzyme 1 (BACE1) in HEK293 APPswe Cells. *Neurosci. Lett.* **2018**, *665*, 80–85. [CrossRef] [PubMed]
35. Muanprasat, C.; Chatsudthipong, V. Chitosan Oligosaccharide: Biological Activities and Potential Therapeutic Applications. *Pharmacol. Ther.* **2017**, *170*, 80–97. [CrossRef] [PubMed]
36. Bezrodnykh, E.A.; Antonov, Y.A.; Berezin, B.B.; Kulikov, S.N.; Tikhonov, V.E. Molecular Features of the Interaction and Antimicrobial Activity of Chitosan in a Solution Containing Sodium Dodecyl Sulfate. *Carbohydr. Polym.* **2021**, *270*, 118352. [CrossRef] [PubMed]
37. Tabatabaei, M.; Ebrahimi, B.; Rajaei, A.; Movahednejad, M.H.; Rastegari, H.; Taghavi, E.; Aghbashlo, M.; Gupta, V.K.; Lam, S.S. Producing Submicron Chitosan-Stabilized Oil Pickering Emulsion Powder by an Electrostatic Collector-Equipped Spray Dryer. *Carbohydr. Polym.* **2022**, *294*, 119791. [CrossRef] [PubMed]
38. Liang, F.; Li, C.; Hou, T.; Wen, C.; Kong, S.; Ma, D.; Sun, C.; Li, S. Effects of Chitosan–Gentamicin Conjugate Supplement on Non-Specific Immunity, Aquaculture Water, Intestinal Histology and Microbiota of Pacific White Shrimp (*Litopenaeus vannamei*). *Mar. Drugs* **2020**, *18*, 419. [CrossRef] [PubMed]

39. Vázquez, J.A.; Rodríguez-Amado, I.; Montemayor, M.I.; Fraguas, J.; del Pilar González, M.; Murado, M.A. Chondroitin Sulfate, Hyaluronic Acid and Chitin/Chitosan Production Using Marine Waste Sources: Characteristics, Applications and Eco-Friendly Processes: A Review. *Mar. Drugs* **2013**, *11*, 747–774. [CrossRef] [PubMed]
40. Avnimelech, Y. *Biofloc Technology: A Practical Guide Book*; World Aquaculture Society: Sorrento, LA, USA, 2009; ISBN 1-888807-16-4.
41. McCusker, S.; Warberg, M.B.; Davies, S.J.; Valente, C.d.S.; Johnson, M.P.; Cooney, R.; Wan, A.H. Biofloc Technology as Part of a Sustainable Aquaculture System: A Review on the Status and Innovations for Its Expansion. *Aquac. Fish Fish.* **2023**, *33*, 331–352. [CrossRef]
42. Kuhn, D.D.; Boardman, G.D.; Craig, S.R.; Flick, G.J., Jr.; McLean, E. Use of Microbial Flocs Generated from Tilapia Effluent as a Nutritional Supplement for Shrimp, *Litopenaeus vannamei*, in Recirculating Aquaculture Systems. *J. World Aquac. Soc.* **2008**, *39*, 72–82. [CrossRef]
43. Crab, R.; Defoirdt, T.; Bossier, P.; Verstraete, W. Biofloc Technology in Aquaculture: Beneficial Effects and Future Challenges. *Aquaculture* **2012**, *356*, 351–356. [CrossRef]
44. Khanjani, M.H.; Mohammadi, A.; Emerenciano, M.G.C. Microorganisms in Biofloc Aquaculture System. *Aquac. Rep.* **2022**, *26*, 101300. [CrossRef]
45. Ogello, E.O.; Outa, N.O.; Obiero, K.O.; Kyule, D.N.; Munguti, J.M. The Prospects of Biofloc Technology (BFT) for Sustainable Aquaculture Development. *Sci. Afr.* **2021**, *14*, e01053. [CrossRef]
46. Luo, G.; Gao, Q.; Wang, C.; Liu, W.; Sun, D.; Li, L.; Tan, H. Growth, Digestive Activity, Welfare, and Partial Cost-Effectiveness of Genetically Improved Farmed Tilapia (*Oreochromis niloticus*) Cultured in a Recirculating Aquaculture System and an Indoor Biofloc System. *Aquaculture* **2014**, *422*, 1–7. [CrossRef]
47. Xu, W.-J.; Morris, T.C.; Samocha, T.M. Effects of C/N Ratio on Biofloc Development, Water Quality, and Performance of *Litopenaeus vannamei* Juveniles in a Biofloc-Based, High-Density, Zero-Exchange, Outdoor Tank System. *Aquaculture* **2016**, *453*, 169–175. [CrossRef]
48. Yu, Y.-B.; Lee, J.-H.; Choi, J.-H.; Choi, Y.J.; Jo, A.-H.; Choi, C.Y.; Kang, J.-C.; Kim, J.-H. The Application and Future of Biofloc Technology (BFT) in Aquaculture Industry: A Review. *J. Environ. Manag.* **2023**, *342*, 118237. [CrossRef]
49. Chutia, A.; Xavier, K.M.; Shamna, N.; Rani, A.B. Application of Bioflocculating Agent in Inoculum Enhances Quality of Biofloc and Influences Growth, Feed Utilization and Stress Responses of GIFT Tilapia Reared *in-situ*. *Aquaculture* **2022**, *553*, 738050. [CrossRef]
50. Qin, C.; Zhang, Y.; Liu, W.; Xu, L.; Yang, Y.; Zhou, Z. Effects of Chito-Oligosaccharides Supplementation on Growth Performance, Intestinal Cytokine Expression, Autochthonous Gut Bacteria and Disease Resistance in Hybrid Tilapia *Oreochromis niloticus*♀× *Oreochromis aureus*♂. *Fish Shellfish Immunol.* **2014**, *40*, 267–274. [CrossRef]
51. Rahimnejad, S.; Yuan, X.; Wang, L.; Lu, K.; Song, K.; Zhang, C. Chitooligosaccharide Supplementation in Low-Fish Meal Diets for Pacific White Shrimp (*Litopenaeus vannamei*): Effects on Growth, Innate Immunity, Gut Histology, and Immune-Related Genes Expression. *Fish Shellfish Immunol.* **2018**, *80*, 405–415. [CrossRef]
52. Abdel-Ghany, H.M.; Salem, M.E.-S. Effects of Dietary Chitosan Supplementation on Farmed Fish; a Review. *Rev. Aquac.* **2020**, *12*, 438–452. [CrossRef]
53. Shiau, S.-Y.; Yu, Y.-P. Dietary Supplementation of Chitin and Chitosan Depresses Growth in Tilapia, *Oreochromis niloticus* × *O. aureus*. *Aquaculture* **1999**, *179*, 439–446. [CrossRef]
54. Romana-Eguia, M.R.R.; Parado-Estepa, F.D.; Salayo, N.D.; Lebata-Ramos, M.J.H. *Resource Enhancement and Sustainable Aquaculture Practices in Southeast Asia: Challenges in Responsible Production of Aquatic Species: Proceedings of the International Workshop on Resource Enhancement and Sustainable Aquaculture Practices in Southeast Asia 2014 (RESA)*; Aquaculture Department, Southeast Asian Fisheries Development Center: Bangkok, Thailand, 2015; ISBN 971-9931-04-3.
55. Kamali Najafabad, M.; Imanpoor, M.R.; Taghizadeh, V.; Alishahi, A. Effect of Dietary Chitosan on Growth Performance, Hematological Parameters, Intestinal Histology and Stress Resistance of Caspian Kutum (*Rutilus frisii Kutum* Kamenskii, 1901) Fingerlings. *Fish Physiol. Biochem.* **2016**, *42*, 1063–1071. [CrossRef]
56. Wang, Y.; Li, J. Effects of Chitosan Nanoparticles on Survival, Growth and Meat Quality of Tilapia, *Oreochromis nilotica*. *Nanotoxicology* **2011**, *5*, 425–431. [CrossRef]
57. Yu, W.; Yang, Y.; Chen, H.; Zhou, Q.; Zhang, Y.; Huang, X.; Huang, Z.; Li, T.; Zhou, C.; Ma, Z. Effects of Dietary Chitosan on the Growth, Health Status and Disease Resistance of Golden Pompano (*Trachinotus ovatus*). *Carbohydr. Polym.* **2023**, *300*, 120237. [CrossRef]
58. Yu, W.; Yang, Y.; Zhou, Q.; Huang, X.; Huang, Z.; Li, T.; Wu, Q.; Zhou, C.; Ma, Z.; Lin, H. Effects of Dietary Astragalus Polysaccharides on Growth, Health and Resistance to *Vibrio harveyi* of *Lates calcarifer*. *Int. J. Biol. Macromol.* **2022**, *207*, 850–858. [CrossRef]
59. Abd El-Naby, F.S.; Naiel, M.A.; Al-Sagheer, A.A.; Negm, S.S. Dietary Chitosan Nanoparticles Enhance the Growth, Production Performance, and Immunity in *Oreochromis niloticus*. *Aquaculture* **2019**, *501*, 82–89. [CrossRef]
60. Denji, K.A.; Mansour, M.R.; Akrami, R.; Ghobadi, S.; Jafarpour, S.; Mirbeygi, S. Effect of Dietary Prebiotic Mannan Oligosaccharide (MOS) on Growth Performance, Intestinal Microflora, Body Composition, Haematological and Blood Serum Biochemical Parameters of Rainbow Trout (*Oncorhynchus mykiss*) Juveniles. *J. Fish. Aquat. Sci.* **2015**, *10*, 255.
61. Wang, Y.; Zhao, K.; Li, L.; Song, X.; He, Y.; Ding, N.; Li, L.; Wang, S.; Liu, Z. A Review of the Immune Activity of Chitooligosaccharides. *Food Sci. Technol.* **2023**, *43*, e97822. [CrossRef]

62. Abd El-Naby, A.S.; Al-Sagheer, A.A.; Negm, S.S.; Naiel, M.A. Dietary Combination of Chitosan Nanoparticle and Thymol Affects Feed Utilization, Digestive Enzymes, Antioxidant Status, and Intestinal Morphology of *Oreochromis niloticus*. *Aquaculture* **2020**, *515*, 734577. [CrossRef]
63. Fernandes, J.C.; Eaton, P.; Nascimento, H.; Gião, M.S.; Ramos, Ó.S.; Belo, L.; Santos-Silva, A.; Pintado, M.E.; Malcata, F.X. Antioxidant Activity of Chitooligosaccharides upon Two Biological Systems: Erythrocytes and Bacteriophages. *Carbohydr. Polym.* **2010**, *79*, 1101–1106. [CrossRef]
64. Anraku, M.; Gebicki, J.M.; Iohara, D.; Tomida, H.; Uekama, K.; Maruyama, T.; Hirayama, F.; Otagiri, M. Antioxidant Activities of Chitosans and Its Derivatives in in Vitro and in Vivo Studies. *Carbohydr. Polym.* **2018**, *199*, 141–149. [CrossRef]
65. Dalmo, R.A.; Bøgwald, J. SS-Glucans as Conductors of Immune Symphonies. *Fish Shellfish Immunol.* **2008**, *25*, 384–396. [CrossRef]
66. Alves, A.P.d.C.; Paulino, R.R.; Pereira, R.T.; da Costa, D.V.; e Rosa, P.V. Nile Tilapia Fed Insect Meal: Growth and Innate Immune Response in Different Times under Lipopolysaccharide Challenge. *Aquac. Res.* **2021**, *52*, 529–540. [CrossRef]
67. Conforto, E.; Vílchez-Gómez, L.; Parrinello, D.; Parisi, M.G.; Esteban, M.Á.; Cammarata, M.; Guardiola, F.A. Role of Mucosal Immune Response and Histopathological Study in European Eel (*Anguilla anguilla* L.) Intraperitoneal Challenged by *Vibrio anguillarum* or *Tenacibaculum soleae*. *Fish Shellfish Immunol.* **2021**, *114*, 330–339. [CrossRef]
68. Marshall, W.S.; Bellamy, D. The 50 Year Evolution of in Vitro Systems to Reveal Salt Transport Functions of Teleost Fish Gills. *Comp. Biochem. Physiol. Part A Mol. Integr. Physiol.* **2010**, *155*, 275–280. [CrossRef]
69. McNeilly, T.N.; Naylor, S.W.; Mahajan, A.; Mitchell, M.C.; McAteer, S.; Deane, D.; Smith, D.G.; Low, J.C.; Gally, D.L.; Huntley, J.F. Escherichia Coli O157: H7 Colonization in Cattle Following Systemic and Mucosal Immunization with Purified H7 Flagellin. *Infect. Immun.* **2008**, *76*, 2594–2602. [CrossRef]
70. Magnadóttir, B. Innate Immunity of Fish (Overview). *Fish Shellfish Immunol.* **2006**, *20*, 137–151. [CrossRef]
71. Galagarza, O.A.; Smith, S.A.; Drahos, D.J.; Eifert, J.D.; Williams, R.C.; Kuhn, D.D. Modulation of Innate Immunity in Nile Tilapia (*Oreochromis niloticus*) by Dietary Supplementation of *Bacillus subtilis* Endospores. *Fish Shellfish Immunol.* **2018**, *83*, 171–179. [CrossRef]
72. Park, Y.-K.; Kim, M.-H.; Park, S.-C.; Cheong, H.-S.; Jang, M.-K.; Nah, J.-W.; Hahm, K.-S. Investigation of the Antifungal Activity and Mechanism of Action of LMWS-Chitosan. *J. Microbiol. Biotechnol.* **2008**, *18*, 1729–1734.
73. Chang, Q.; Liang, M.; Wang, J.; Sun, J. Influence of Chitosan on the Growth and Non-Specific Immunity of Japanese Sea Bass (*Lateolabrax japonicus*). *Mar. Fish. Res.* **2006**, *27*, 17–22.
74. Gopalakannan, A.; Arul, V. Immunomodulatory Effects of Dietary Intake of Chitin, Chitosan and Levamisole on the Immune System of *Cyprinus carpio* and Control of *Aeromonas hydrophila* Infection in Ponds. *Aquaculture* **2006**, *255*, 179–187. [CrossRef]
75. Guardiola, F.A.; Cuesta, A.; Arizcun, M.; Meseguer, J.; Esteban, M.A. Comparative Skin Mucus and Serum Humoral Defence Mechanisms in the Teleost Gilthead Seabream (*Sparus aurata*). *Fish Shellfish Immunol.* **2014**, *36*, 545–551. [CrossRef]
76. Srichaiyo, N.; Tongsiri, S.; Hoseinifar, S.H.; Dawood, M.A.; Jaturasitha, S.; Esteban, M.Á.; Ringø, E.; Van Doan, H. The Effects Gotu Kola (*Centella asiatica*) Powder on Growth Performance, Skin Mucus, and Serum Immunity of Nile Tilapia (*Oreochromis niloticus*) Fingerlings. *Aquac. Rep.* **2020**, *16*, 100239. [CrossRef]
77. Dimitroglou, A.; Merrifield, D.; Moate, R.; Davies, S.; Spring, P.; Sweetman, J.; Bradley, G. Dietary Mannan Oligosaccharide Supplementation Modulates Intestinal Microbial Ecology and Improves Gut Morphology of Rainbow Trout, *Oncorhynchus mykiss* (Walbaum). *J. Anim. Sci.* **2009**, *87*, 3226–3234. [CrossRef]
78. Geda, F.; Rekecki, A.; Decostere, A.; Bossier, P.; Wuyts, B.; Kalmar, I.; Janssens, G. Changes in Intestinal Morphology and Amino Acid Catabolism in Common Carp at Mildly Elevated Temperature as Affected by Dietary Mannanoligosaccharides. *Anim. Feed Sci. Technol.* **2012**, *178*, 95–102. [CrossRef]
79. Daniels, C.L.; Merrifield, D.L.; Boothroyd, D.P.; Davies, S.J.; Factor, J.R.; Arnold, K.E. Effect of Dietary *Bacillus* spp. and Mannan Oligosaccharides (MOS) on European Lobster (*Homarus gammarus* L.) Larvae Growth Performance, Gut Morphology and Gut Microbiota. *Aquaculture* **2010**, *304*, 49–57. [CrossRef]
80. Chen, G.; Yin, B.; Liu, H.; Tan, B.; Dong, X.; Yang, Q.; Chi, S.; Zhang, S. Supplementing Chitosan Oligosaccharide Positively Affects Hybrid Grouper (*Epinephelus fuscoguttatus*♀× *E. lanceolatus*♂) Fed Dietary Fish Meal Replacement with Cottonseed Protein Concentrate: Effects on Growth, Gut Microbiota, Antioxidant Function and Immune Response. *Front. Mar. Sci.* **2021**, *8*, 707627.
81. Hahor, W.; Thongprajukaew, K.; Suanyuk, N. Effects of Dietary Supplementation of Oligosaccharides on Growth Performance, Gut Health and Immune Response of Hybrid Catfish (*Pangasianodon gigas* × *Pangasianodon hypophthalmus*). *Aquaculture* **2019**, *507*, 97–107. [CrossRef]
82. Zhou, Q.-C.; Buentello, J.A.; Gatlin III, D.M. Effects of Dietary Prebiotics on Growth Performance, Immune Response and Intestinal Morphology of Red Drum (*Sciaenops ocellatus*). *Aquaculture* **2010**, *309*, 253–257. [CrossRef]
83. Wu, Y.; Liu, W.; Li, H.; Xu, W.; He, J.; Li, X.; Jiang, G. Effects of Dietary Supplementation of Fructooligosaccharide on Growth Performance, Body Composition, Intestinal Enzymes Activities and Histology of Blunt Snout Bream (*Megalobrama amblycephala*) Fingerlings. *Aquac. Nutr.* **2013**, *19*, 886–894. [CrossRef]
84. Wang, K.; Jiang, W.; Wu, P.; Liu, Y.; Jiang, J.; Kuang, S.; Tang, L.; Zhang, Y.; Zhou, X.; Feng, L. Gossypol Reduced the Intestinal Amino Acid Absorption Capacity of Young Grass Carp (*Ctenopharyngodon idella*). *Aquaculture* **2018**, *492*, 46–58. [CrossRef]
85. Yamamoto, T.; Matsunari, H.; Sugita, T.; Furuita, H.; Masumoto, T.; Iwashita, Y.; Amano, S.; Suzuki, N. Optimization of the Supplemental Essential Amino Acids to a Fish Meal-Free Diet Based on Fermented Soybean Meal for Rainbow Trout *Oncorhynchus mykiss*. *Fish. Sci.* **2012**, *78*, 359–366. [CrossRef]

86. Morales, A.; Gómez, T.; Villalobos, Y.D.; Bernal, H.; Htoo, J.K.; González-Vega, J.C.; Espinoza, S.; Yáñez, J.; Cervantes, M. Dietary Protein-Bound or Free Amino Acids Differently Affect Intestinal Morphology, Gene Expression of Amino Acid Transporters, and Serum Amino Acids of Pigs Exposed to Heat Stress. *J. Anim. Sci.* **2020**, *98*, skaa056. [CrossRef]
87. Sakai, M.; Hikima, J.; Kono, T. Fish Cytokines: Current Research and Applications. *Fish. Sci.* **2021**, *87*, 1–9. [CrossRef]
88. Zlotnik, A.; Yoshie, O. The Chemokine Superfamily Revisited. *Immunity* **2012**, *36*, 705–716. [CrossRef]
89. Dinarello, C.A. Overview of the IL-1 Family in Innate Inflammation and Acquired Immunity. *Immunol. Rev.* **2018**, *281*, 8–27. [CrossRef]
90. Hirayama, D.; Iida, T.; Nakase, H. The Phagocytic Function of Macrophage-Enforcing Innate Immunity and Tissue Homeostasis. *Int. J. Mol. Sci.* **2017**, *19*, 92. [CrossRef]
91. Fu, G.H.; Liu, F.; Xia, J.H.; Yue, G.H. The LBP Gene and Its Association with Resistance to *Aeromonas hydrophila* in Tilapia. *Int. J. Mol. Sci.* **2014**, *15*, 22028–22041. [CrossRef]
92. Fath El-Bab, A.F.; Majrashi, K.A.; Sheikh, H.M.; Shafi, M.E.; El-Ratel, I.T.; Neamat-Allah, A.N.; El-Raghi, A.A.; Elazem, A.Y.A.; Abd-Elghany, M.F.; Abdelnour, S.A. Dietary Supplementation of Nile Tilapia (*Oreochromis niloticus*) with β-Glucan and/or *Bacillus coagulans*: Synergistic Impacts on Performance, Immune Responses, Redox Status and Expression of Some Related Genes. *Front. Vet. Sci.* **2022**, *9*, 1011715. [CrossRef]
93. Imai, H.; Nakagawa, Y. Biological Significance of Phospholipid Hydroperoxide Glutathione Peroxidase (PHGPx, GPx4) in Mammalian Cells. *Free Radic. Biol. Med.* **2003**, *34*, 145–169. [CrossRef]
94. Ahlf, W.; Heise, S. Sediment Toxicity Assessment: Rationale for Effect Classes (5 Pp). *J. Soils Sediments* **2005**, *5*, 16–20. [CrossRef]
95. De Schryver, P.; Crab, R.; Defoirdt, T.; Boon, N.; Verstraete, W. The Basics of Bio-Flocs Technology: The Added Value for Aquaculture. *Aquaculture* **2008**, *277*, 125–137. [CrossRef]
96. Azim, M.E.; Little, D.C. The Biofloc Technology (BFT) in Indoor Tanks: Water Quality, Biofloc Composition, and Growth and Welfare of Nile Tilapia (*Oreochromis niloticus*). *Aquaculture* **2008**, *283*, 29–35. [CrossRef]
97. Mirzakhani, N.; Ebrahimi, E.; Jalali, S.A.H.; Ekasari, J. Growth Performance, Intestinal Morphology and Nonspecific Immunity Response of Nile Tilapia (*Oreochromis niloticus*) Fry Cultured in Biofloc Systems with Different Carbon Sources and Input C: N Ratios. *Aquaculture* **2019**, *512*, 734235. [CrossRef]
98. Khanjani, M.H.; Sharifinia, M.; Hajirezaee, S. Recent Progress towards the Application of Biofloc Technology for Tilapia Farming. *Aquaculture* **2022**, *552*, 738021. [CrossRef]
99. Linh, N.V.; Van Nguyen, D.; Khongdee, N.; Wannavijit, S.; Outama, P.; Le Xuan, C.; Mahatheeranont, S.; Sookwong, P.; Le, T.D.; Hoseinifar, S.H. Influence of Black Rice (*Oryza sativa* L.) Bran Derived Anthocyanin-Extract on Growth Rate, Immunological Response, and Immune-Antioxidant Gene Expression in Nile Tilapia (*Oreochromis niloticus*) Cultivated in a Biofloc System. *Fish Shellfish Immunol.* **2022**, *128*, 604–611. [CrossRef] [PubMed]
100. Suthongsa, S.; Pichyangkura, R.; Kalandakanond-Thongsong, S.; Thongsong, B. Effects of Dietary Levels of Chito-Oligosaccharide on Ileal Digestibility of Nutrients, Small Intestinal Morphology and Crypt Cell Proliferation in Weaned Pigs. *Livest. Sci.* **2017**, *198*, 37–44. [CrossRef]
101. Keereelang, J.; Mangumphan, K.; Chitmanat, C.; Tongsiri, S.; Linh, N.V.; Van Doan, H. Dietary Effect of *Lactobacillus plantarum* (TISTR 912) on Digestive Enzyme Activity, Growth Performance, Immune Response, and Disease Resistance of Black Sharkminnow (*Labeo chrysophekadion*) against *Aeromonas hydrophila* Infection. *Aquac. Rep.* **2022**, *27*, 101409. [CrossRef]
102. Livak, K.J.; Schmittgen, T.D. Analysis of Relative Gene Expression Data Using Real-Time Quantitative PCR and the $2^{-\Delta\Delta Ct}$ Method. *Methods* **2001**, *25*, 402–408. [CrossRef]

marine drugs

Article

# Isolation and Purification of Chitosan Oligosaccharides ($Mw \leq 1000$) and Their Protective Effect on Acute Liver Injury Caused by $CCl_4$

**Kai Wang [1,2,†], Dawei Yu [1,2,†], Yan Bai [3], Hua Cao [4], Jiao Guo [2,*] and Zhengquan Su [1,*]**

[1] Guangdong Provincial University Engineering Technology Research Center of Natural Products and Drugs, Guangdong Pharmaceutical University, Guangzhou 510006, China; wk972023826@163.com (K.W.); ydw65038@163.com (D.Y.)
[2] Guangdong Metabolic Disease Research Center of Integrated Chinese and Western Medicine, Guangdong Pharmaceutical University, Guangzhou 510006, China
[3] School of Public Health, Guangdong Pharmaceutical University, Guangzhou 510310, China; angell_bai@163.com
[4] School of Chemistry and Chemical Engineering, Guangdong Pharmaceutical University, Zhongshan 528458, China; caohua@gdpu.edu.cn
* Correspondence: gyguoyz@163.com (J.G.); suzhq@scnu.edu.cn (Z.S.); Tel.: +86-20-3935-2345 (Z.S.); Fax: +86-20-3935-2067 (Z.S.)
† These authors contributed equally to this work.

**Abstract:** Chitosan oligosaccharides are the degradation products of chitin obtained from the shell extracts of shrimps and crabs. Compared with chitosan, chitosan oligosaccharides have better solubility and a wider application range. In this study, high-molecular-weight chitosan oligosaccharides (COST, chitosan oligosaccharides, $MW \leq 1000$) were isolated and purified by a GPC gel column, and the molecular weight range was further reduced to obtain high-purity and low-molecular-weight chitosan (COS46). Compared with COST, COS46 is better at inhibiting $CCl_4$-induced cell death, improving cell morphology, reducing ALT content, and improving cell antioxidant capacity. The effects of COST and COS46 on $CCl_4$-induced acute liver injury were further verified in mice. Both COS46 and COST improved the appearance of the liver induced by $CCl_4$, decreased the levels of ALT and AST in serum, and decreased the oxidation/antioxidant index in the liver. From the liver pathological section, the effect of COS46 was better. In addition, some indicators of COS46 showed a dose-dependent effect. In conclusion, compared with COST, low-molecular-weight COS46 has better antioxidant capacity and a better therapeutic effect on $CCl_4$-induced acute liver injury.

**Keywords:** acute liver injury; $CCl_4$; chitosan oligosaccharide; oxidation resistance

## 1. Introduction

At present, the shells of crabs and shrimps in marine arthropods are often ignored and underutilized, which are important sources of chitin. After a series of compound chemical treatments, chitosan and chitosan oligosaccharides are obtained, which have important application value in medical care and food [1]. Chitosan oligosaccharide itself has a variety of physiological activities, such as antibacterial properties [2,3], anti-tumor properties [4,5], antioxidant [3,6] and anti-inflammatory effects [7], etc. There are also studies using chitosan oligosaccharides as a drug carrier [8,9] or as a prebiotic to explore their influence on intestinal flora in different diseases [10,11]. It has also been revealed to have anti-diabetes [12], anti-obesity [13], anti-HIV-1 [14], and anti-Alzheimer's disease [15] effects and promote calcium absorption [16].

The excellent antioxidant properties of chitosan oligosaccharides have been the focus of related research, and it has been proven that it can reduce oxidative stress injury by scavenging free radicals and reactive oxygen species and maintaining the activity of antioxidant enzymes [17,18]. Therefore, the antioxidant properties of chitosan oligosaccharides can be identified from two aspects: the ability to scavenge free radicals and the ability to improve the level of antioxidant substances in vivo. However, the exact mechanism has not been explained. According to existing studies and the chemical structure of chitosan oligosaccharides, it is speculated that its amino group can combine with unstable free radicals to form a stable structure, which shows antioxidant properties.

Recent studies have indicated that the biological activity of chitosan oligosaccharides is primarily influenced by DP (degree of polymerization) and Mw (molecular weight). Therefore, it is difficult to determine which parts of chitosan oligosaccharides play a major role in biological activity [19]. Although there is no exact evidence to directly show the relationship between chitosan oligosaccharides' antioxidant properties and molecular weight, it is speculated from the existing relevant studies that a low molecular weight and a high degree of deacetylation can equip chitosan oligosaccharides with a better antioxidant effect [20], and the relationship between the two needs to be further explored.

Currently, chitosan oligosaccharides available in the market are typically synthesized from monosaccharides or extracted from hydrolyzed products. Researchers selectively synthesize the necessary oligosaccharides through specific chemical or enzymatic reactions. However, the synthesis process involves numerous steps and is costly. Therefore, it is more convenient to extract chitosan oligosaccharides [21–23]. Combined with the relationship between the properties of chitosan oligosaccharides and molecular weight, it is of great significance to narrow the molecular weight range through specific technical means, and even obtain chitosan oligosaccharides with a specific degree of polymerization. It is important not only to clarify the pharmacodynamic mechanism of chitosan oligosaccharides with different polymerization degrees but also to develop and utilize chitosan oligosaccharides more effectively. Due to the small difference in charge density and molecular weight between chitosan oligosaccharide monomers, the separation and purification of chitosan oligosaccharides are very challenging, especially when the degree of polymerization is greater than 4. This makes it a hotspot in the field of sugar science.

In the existing research, many methods for recovering and purifying chitosan oligosaccharides, such as gel filtration or size exclusion chromatography, have been found to purify and obtain specific chitosan oligosaccharides, and the molecular weight difference between different polymerization degrees of chitosan oligosaccharides is the basis for separation. It has been reported that chitosan oligosaccharides with a polymerization degree of 2–6 were separated from the hydrolysate of chitosan by gel filtration chromatography and ion exchange chromatography [24]. In an experiment of enzymatic hydrolysis of chitosan, the separation ability of size-exclusion chromatography (SEC) was used to help researchers fully understand the composition of the enzymatic hydrolysate [25]. Ultrafiltration [26] and nanofiltration [27] are also applied to the purification of chitosan oligosaccharides. Ion exchange chromatography [28] and metal affinity chromatography [29] are also widely used to detect and separate chitosan oligosaccharides.

High-performance liquid chromatography (HPLC) is often used for chitosan oligosaccharide analysis and purification [30]. HPLC is often combined with an ultraviolet detector, and the acetyl amino group of chitosan oligosaccharides can form a conjugated structure with the sugar ring, and the absorbance of chitosan oligosaccharides can be detected at a wavelength of approximately 210 nm. A differential refraction detector is preferred for the HPLC analysis of N-acetylated and N-deacetylated chitosan oligosaccharides, but its sensitivity is low and it is not suitable for gradient washing [31]. It is difficult to separate chitosan oligosaccharides by conventional HPLC, mainly because of its strong hydrophilicity and poor retention on HPLC columns [32]. Hydrophilic-interaction chromatography (HILIC) is a technique that can effectively separate polar and hydrophilic compounds. Some studies have successfully separated and purified chitosan oligosaccharides with a polymerization degree of 2–6 from a chitosan oligosaccharides mixture by using HILIC technology and used it to judge the influence of each component on RSC96 cells [32].

N- acetyl chitotriose and N, N′- diacetyl chitotriose can be separated from acetylated chitotriose by a cation exchange gel column [21]. For partially acetylated chitosan oligosaccharides, HPLC-ESI-MS can be used for separation and detection [33].

Capillary Electrophoresis (CE) has the advantage of high separation ability. Compared with HPLC, it has the characteristics of less sample loading, but it is precisely because of the small sample loading that a large number of chitosan oligosaccharides cannot be obtained by CE technology. When used to separate and detect chitosan oligosaccharides, electrophoretic mobility depends on the number of unit structures in an acidic aqueous solution, which is similar to other oligomeric electrolytes [28,34]. In many studies, chitosan oligosaccharides have been successfully separated using this technique [34,35].

$CCl_4$ is a typical substance with hepatotoxicity, which will remove halogen atoms in liver microsomes through a redox reaction to generate the trichloromethyl radical and its derivative trichloromethyl peroxyradical active intermediate. These free radicals bind to phospholipid molecules on the endoplasmic reticulum (ER) through covalent bonds. This can inhibit protein synthesis, destroy the function and morphology of the cell membrane, and cause hepatotoxicity, fibrosis, lipid peroxidation, and ERS (Endoplasmic reticulum stress) reaction [36,37].

Acute liver injury induced by $CCl_4$ in animals is very similar to acute chemical liver injury in humans, so it is widely used in the study of potential hepatoprotective drug activity [38]. $CCl_4$ not only exerts strong toxicity on the liver but also causes damage to other parts of the body [39], including the kidneys [40], nervous system [41], and testes [42].

Currently, there is no research on the role of DP4-6 chitosan oligosaccharides in liver metabolic diseases. This paper proposes a hypothesis that the antioxidant properties of chitosan oligosaccharides are related to their molecular weight. It is speculated that low-molecular-weight chitosan oligosaccharides have a better protective effect on the liver. The paper also describes the process of obtaining DP4-6 chito-oligosaccharides by separating and purifying COST and named the product COS46. The hypothesis was confirmed through cell and animal experiments. The study investigated the difference in antioxidant properties and efficacy of COST in protecting against liver injury before and after separation. These findings are expected to aid in the further development and utilization of chitosan oligosaccharides.

## 2. Results

### *2.1. Isolation and Purification of COST*

### 2.1.1. COST Component and DP4-6 COS Content

The results of the TLC analysis of COST are shown in Figure 1A. The selected developer system has a good separation effect on COST, with obvious separation at each point and no obvious tailing phenomenon. According to TLC, compared with the mixed standard (1–7), COST contains chitosan oligosaccharides with a degree of polymerization of 3–7, but there are still a large number of substances piled up at the starting line of the thin layer, which cannot be separated. It is speculated that chitosan oligosaccharides with a higher degree of polymerization than chito-seven sugars exist in COST.

As shown in Table S1, the retention times of COS4, COS5, and COS6 are approximately 6 min, 8 min, and 12 min, respectively, and the standard curve is drawn according to the peak area of the concentration of each chitosan oligosaccharide standard series. The target principal component of COST is integral, and the peak area was 6166, 2267, and 3521, which was substituted into the standard curve for calculation. See the Supplementary Materials for the LC-MS spectrum and data on each standard product and COST (Figure S7, Table S2).

The component concentration of DP = 4(COS4) in COST was 0.99 mg/mL, and the content was 28.78%. The concentration of DP = 5(COS5) was 0.37 mg/mL and the content was 10.76%. The component concentration of DP = 6(COS6) was 0.61 mg/mL and the content was 17.73%. Therefore, in the COST of raw materials, the component content of DP4-6(COS46) is 57.27%.

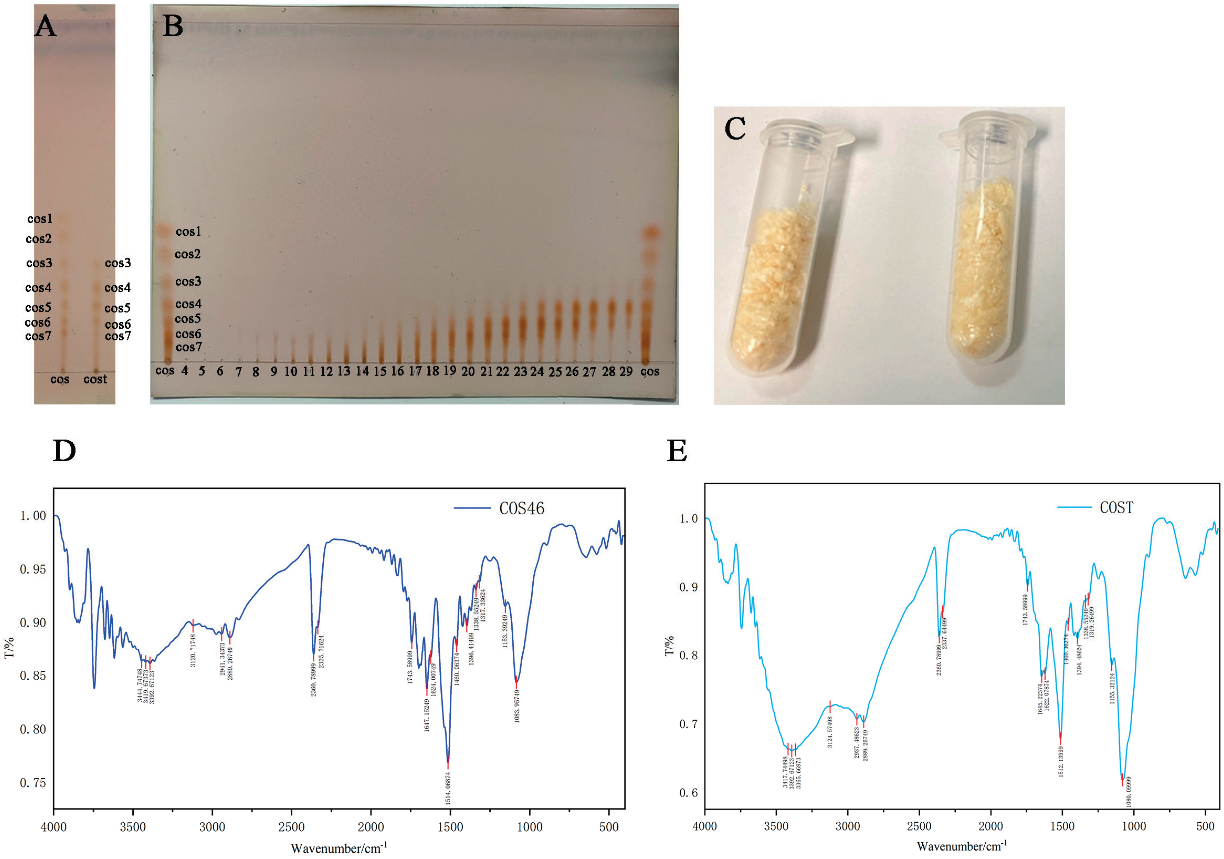

**Figure 1.** Thin layer diagram of COST and COS (Chitosan oligosaccharides mixed standard DP 1–7) (**A**); TLC thin-layer chromatography at different time periods. Serial number of collected eluate (4–29) (**B**); isolated COS46 freeze-dried powder (**C**); COS46 infrared spectrum (**D**); COST infrared spectrum (**E**).

### 2.1.2. Gel Chromatographic Separation Yield

TLC chromatography of each tube is shown in Figure 1B. Chitosan oligosaccharides of the target polymerization degree appeared from 19#. The lyophilized product was light yellow, as shown in Figure 1C. As can be seen from Table 1, when the sample size at COST is approximately 0.3 g, approximately 0.1 g of COS46 can be harvested. The COS46 obtained by five times of separation is calculated, and the yield is 30.39 ± 1.57%.

**Table 1.** Yield of COS46 obtained from GPC separation and purification.

| $\text{Mass}_{\text{COST}}$ (g) | $\text{Mass}_{\text{COS46}}$ (g) | Yield (%) | Average Yield (%) |
|---|---|---|---|
| 0.3059 | 0.0891 | 29.13 | 30.39 ± 1.57 |
| 0.3343 | 0.1002 | 29.97 | |
| 0.3290 | 0.1055 | 28.72 | |
| 0.3289 | 0.1055 | 32.08 | |
| 0.3228 | 0.1035 | 32.06 | |

### 2.1.3. COS46 Purity and Infrared Spectrum

The target component of COS46 was also integrated, and the peak area was 4524, 2340, and 2783, which was substituted into the standard curve for calculation. See the Supplementary Materials for the LC-MS atlas and data on COS46 (Figure S6, Table S2).

In COS46, the component concentration of COS4 was 0.73 mg/mL and the content was 40.11%. The concentration of COS5 was 0.39 mg/mL and the content was 21.43%. The component concentration of COS6 was 0.49 mg/mL and the content was 26.92%. Therefore, the total proportion of the target component in COS46 was 88.46%.

The infrared spectra of COS46 and COST are shown in Figure 1D,E. Compared with the COST of raw materials, COS46 shows an obvious peak shape change at 3400 cm$^{-1}$, where infrared absorption is mainly generated by hydrogen bonds. It is speculated that the reason is that the polymerization degree of COS46 decreases, and the chain length becomes shorter after purification by gel chromatography. The decrease in intramolecular and intermolecular hydrogen bonds in the molecular chains of chitosan oligosaccharides resulted in increased infrared absorption at this wave number. The C-O-C stretching vibration in the range of 1200–1050 cm$^{-1}$ is the ether bond stretching vibration band in the pyran ring of the chitosan oligosaccharide unit structure, and the band intensity of COST is slightly higher in the figure. This may be due to the separation process affecting the ether bond, resulting in a decrease in the intensity of stretching vibrations in the separated product. Finally, the existence of such a wide peak in the figure may be caused by some water remaining in the sample.

### 2.1.4. Determination of Deacetylation Degree

The results are shown in Figure 2A. Among the three, only GlcNAc had an obvious maximum absorption peak, GlcN had no obvious absorption, and COS46 showed a weak absorption peak. Then the three were scanned at a 200–215 nm wavelength and the first derivative was plotted. The results are shown in Figure 2B. The maximum absorption peak of GlcNAc and COS46 appeared near 202 nm, and the absorption of GlcNAc was significantly greater than that of COS46.

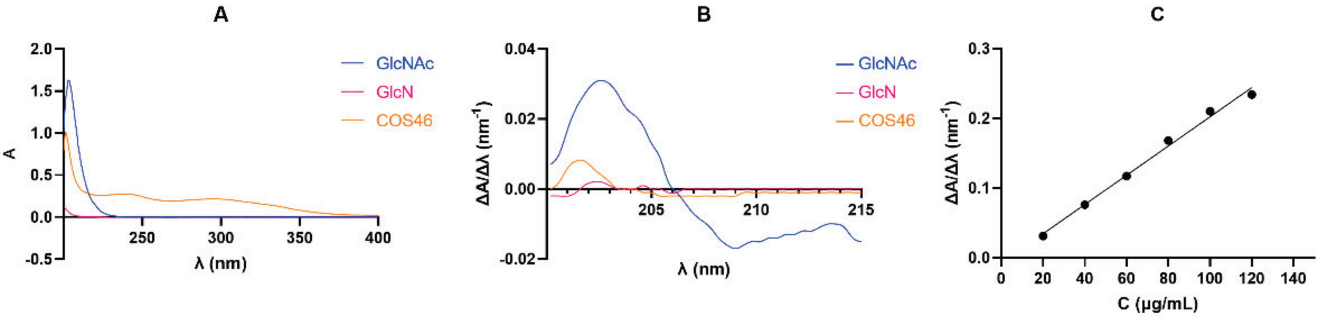

**Figure 2.** (**A**) Full sweep spectra of GlcNAc, GlcN, and COS46 at 200−400 nm wavelength; (**B**) GlcN and COS46 were mapped with the first derivative at 200–215 nm wavelength scanning; (**C**) the first derivative of GlcNAc (20.0−120.0 μg/mL) in 0.3 mol/L HCl ($y = 0.002097x - 0.007467$, $R^2 = 0.9924$).

The content of GlcNAc In COS46 was calculated using the standard curve. According to the formula, the degree of deacetylation of COS46 is 97.71%, as shown in Table 2.

**Table 2.** Degrees of deacetylation of COS46.

| Sample | Concentration cos$_{46}$ (μg/mL) | Deacetylation Degree (DD)% | Average DD (%) |
|---|---|---|---|
| COS46-1 | 705.3 | 97.23 | 97.71 |
| COS46-2 | 705.3 | 97.33 | |
| COS46-3 | 705.3 | 98.58 | |

### 2.1.5. Molecular Weight of COS46 and COST

The established photometric standard curve is shown in Figure S20. The linear regression equation of the standard curve is $y = 0.4555x + 0.05216$, and $R^2 = 0.9789$.

The measurement results of COS46 and COST are shown in Tables 3 and 4. Both OD1 and OD2 are within the linear range of the standard curve. By substituting the formula, the average molecular weight of COS46 is 628.50 and that of COST is 906.12.

The average molecular weight decreased, which proved that chitosan oligosaccharides with a narrower molecular weight range were successfully obtained in the previous gel chromatography separation.

**Table 3.** Average molecular weight of COS46.

| OD1-COS46 | | OD2-COS46 | | DP | Average Molecular Weight |
|---|---|---|---|---|---|
| Absorbance | Average | Absorbance | Average | | |
| 0.2706<br>0.2676<br>0.2752 | 0.2711 | 0.1021<br>0.1040<br>0.1023 | 0.1028 | 3.79 | 628.50 |

**Table 4.** Average molecular weight of COST.

| OD1-COST | | OD2-COST | | DP | Average Molecular Weight |
|---|---|---|---|---|---|
| Absorbance | Average | Absorbance | Average | | |
| 0.2342<br>0.2536<br>0.1445 | 0.2108 | 0.1131<br>0.1175<br>0.1098 | 0.1135 | 5.38 | 906.12 |

### 2.2. *Oxidation Resistance of COS46 and COST*

The scavenging rates of hydroxyl radicals and DPPH radicals by COS46 and COST are shown in Figure 3. For hydroxyl radical scavenging efficiency, within the experimental concentration range, except for the initial concentration of 0.2 mg/mL, the scavenging capacity of COS46 was higher than that of COST. The DPPH radical scavenging efficiency was better on COST and gradually improved with the increase in concentration. As one of the reactive oxygen species in the human body, the harm caused by the hydroxyl radical in the human body has long been recognized by the public. COS46 is more efficient than COST in reducing the formation of the hydroxyl radical, and it is more suitable as an exogenous antioxidant.

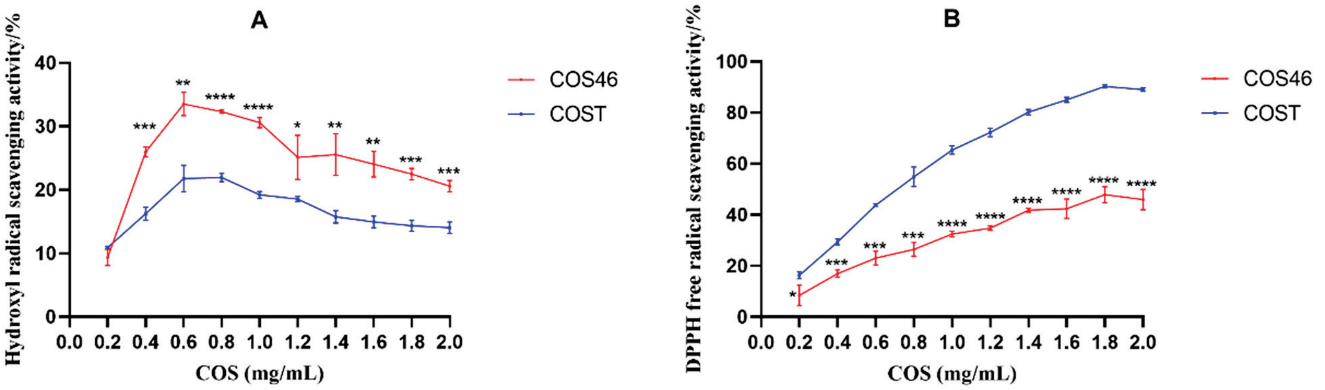

**Figure 3.** The hydroxyl radical scavenging activity (**A**); the DPPH free radical scavenging ability (**B**); * $p < 0.05$, ** $p < 0.01$, *** $p < 0.001$, **** $p < 0.0001$.

### 2.3. *Effects of COS46 and COST on Hepatocyte Injury of L02*

#### 2.3.1. Modeling Conditions of Hepatocyte Injury and Dose Concentration

As shown in Figure 4A, with the increase in the DMSO concentration, the cell viability decreased gradually. When it reached 0.12%, the cell survival rate showed a significant difference compared with no DMSO administration. Therefore, in the follow-up experiment, the proportion of DMSO selected in the modeling solution system was 0.10%.

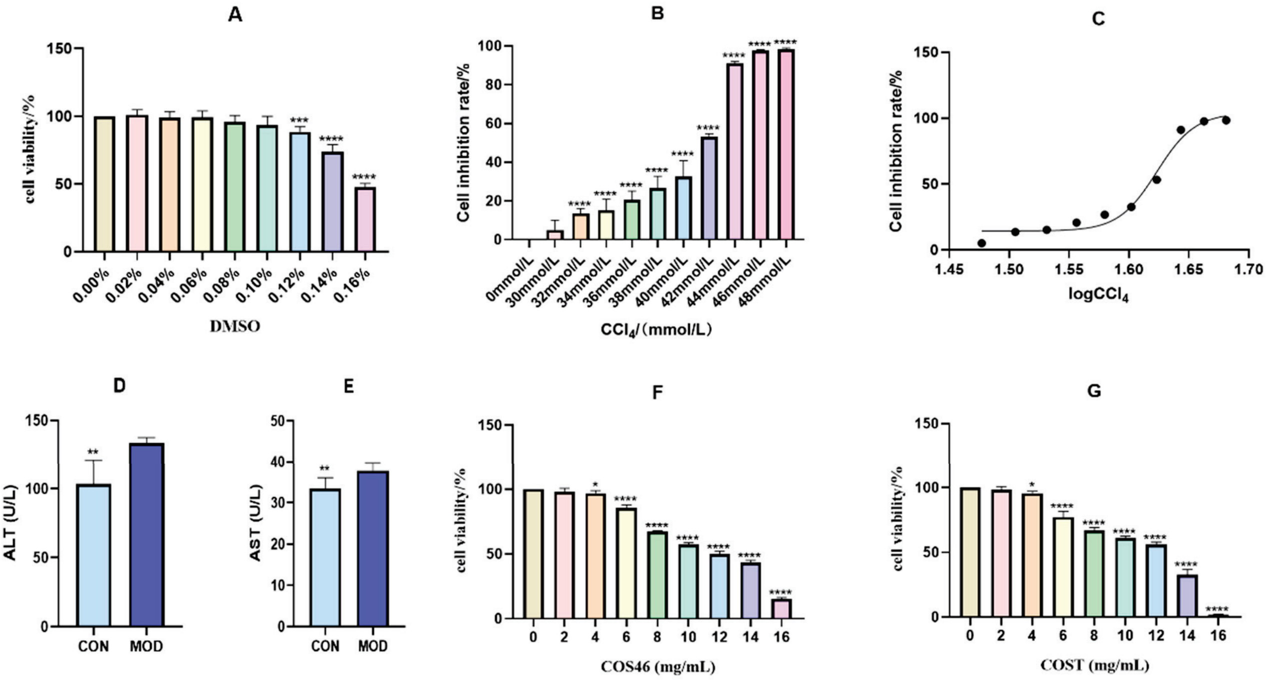

**Figure 4.** Effect of different percentage concentrations of DMSO on cell viability (**A**); inhibition rate of $CCl_4$ in different concentrations (**B**); the $IC_{50}$ curve of $CCl_4$ (**C**); contents of ALT (**D**) and AST (**E**) in cell medium after 24 h treatment with $CCl_4$; effect of different concentrations of COS46 (**F**) and COST (**G**) on viability of L02 cells (n = 6, mean ± SD); * $p < 0.05$, ** $p < 0.01$, *** $p < 0.001$, **** $p < 0.0001$.

As shown in Figure 4B,C, the cell inhibition rate increased with the increase in the $CCl_4$ concentration. The modeling concentration is selected according to the principle of $IC_{50}$, which is 42 mmol/L, and this concentration is selected as the modeling concentration.

After the modeling concentration was determined according to the IC50 curve, $CCl_4$ cells attached to the wall for 24 h were further incubated for 24 h, and ALT and AST were measured in the culture medium. As shown in Figure 4D,F, ALT and AST in the MOD group were significantly increased, L02 hepatocytes were damaged, and a large number of transaminases were transferred to the culture medium. The results showed that the model of hepatocyte injury was successfully established.

As shown in Figure 4F,G. The cell survival rate decreased with the increase in the drug concentration. When the concentration of COS46 and COST reached 4 mg/mL, the cell survival rate was reduced by approximately 5% compared with the cells without drug administration, and the difference was statistically significant. When the dose was 2 mg/mL, the cell survival rate was more than 98%. Taking this as the selection standard, the high-, medium-, and low-dose concentrations of COS46 and COST were determined to be 2 mg/mL, 1 mg/mL, and 0.5 mg/mL, respectively.

### 2.3.2. Cell Viability and Biochemical Indices

As shown in Figure 5A, the cell survival rate in the groups given COS46 and COST was significantly improved compared with the MOD group. Among them, the COS46-H,M,L had the same improvement effect on cell survival rate, and the effect was better than that of COST-H,M.

As shown in Figure 5B,C, compared with the MOD group, AST activity in each group decreased, but there was no significant difference. COS46-L and COST-M had the most obvious effect on the reduction in AST, and the effect was similar. COS46-H,M,L could reduce ALT activity, and the three doses were significantly different from the MOD group, and COS46-L was the best. Although COST-H,M,L can also affect ALT, only COST-M showed a significant difference.

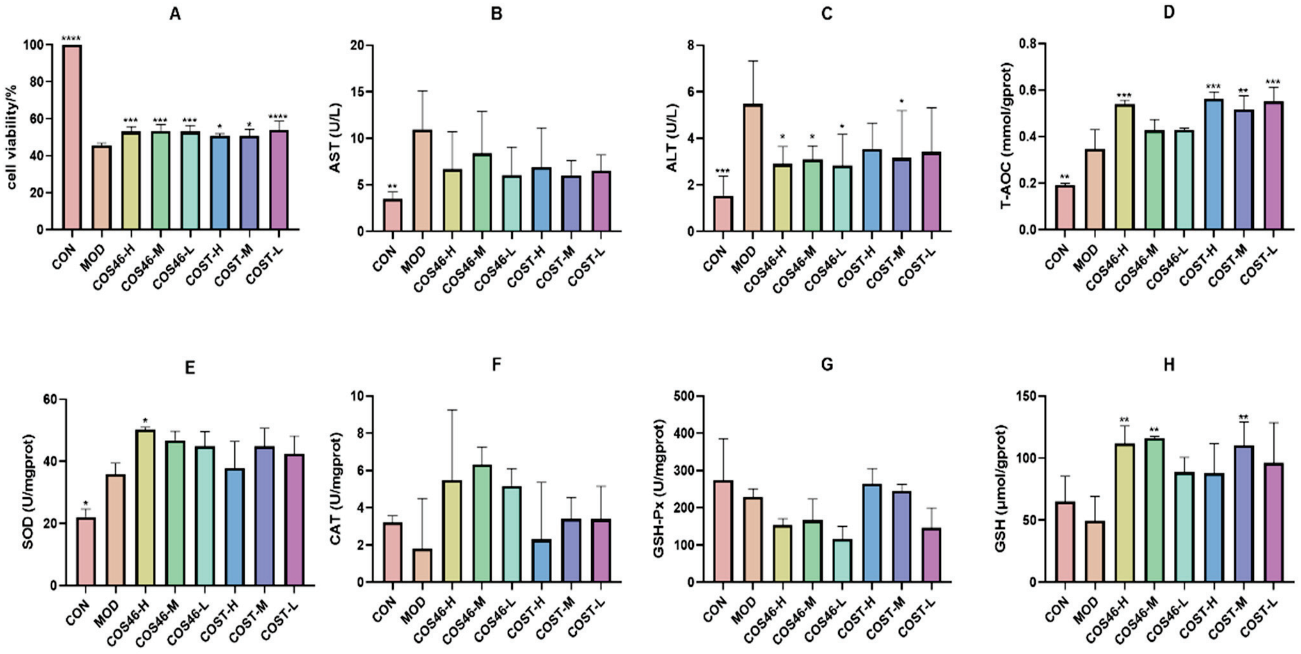

**Figure 5.** Effect of COS46 and COST on viability of L02 cells treated with $CCl_4$ (**A**); effect of COS46 and COST on AST (**B**) and ALT (**C**) levels in cell medium (n = 6, mean ± SD). Effects of COS46 and COST on T-AOC (**D**), SOD (**E**), CAT (**F**), GSH-Px (**G**), and GSH (**H**) in L02 cells (n = 3, mean ± SD); * $p < 0.05$, ** $p < 0.01$, *** $p < 0.001$, **** $p < 0.0001$.

The results of T-AOC, SOD, CAT, GSH-Px, and GSH levels in cells are shown in Figure 5D,H. Compared with the CON group, the T-AOC and SOD levels in the MOD group increased, and the values in each administration group were further increased than those in the MOD group. For T-AOC, COS46 showed significant differences only at high doses, while COST showed significant differences at all three doses. In terms of SOD measurement, only the COS46-H group showed a significant difference.

Compared with the CON group, the activity of CAT in the MOD group decreased, and the activity of CAT in different doses of COST and COS46 groups increased. Although there was no significant difference between the two groups, the increase in COS46 was higher than that of COST.

Compared with the CON group, the activity of GSH-Px in the MOD group decreased. After COS46 pretreatment, GSH-Px had not increased, while it had increased in COST-H,M groups, but there was no significant difference.

Compared with the CON group, the activity of GSH in the MOD group decreased, but after COS46 and COST pretreatment, the activity of GSH increased. There were significant differences between the COS46-H group and the COS46-M group, as well as between the COST-M groups.

In short, COS46 showed more obvious improvement in SOD, CAT, and GSH, but COST has a greater influence on T-AOC and the GSH-Px index. Both COS46 and COST can reduce the oxidative damage of $CCl_4$ to hepatocytes. Combined with the experimental results, COS46 has a more favorable improvement effect.

## *2.4. Effects of COS46 and COST on Mice with Liver Injury*

### 2.4.1. Effects of COS46 and COST on Liver Appearance, Liver Index, and Serum AST and ALT

As shown in Figure 6A, the livers of mice in the CON group were ruddy in appearance and exquisite in texture, and no granular feeling was observed. The livers of the MOD group showed obvious yellow granules, a yellow surface, and decreased elasticity. Yellow particles were also observed on the liver surfaces of the positive drug group, but no yellowing or redness was restored compared with the MOD group. $CCl_4$-caused liver lesions were improved in all groups given chitosan oligosaccharides. As the dosage of COS46 increased, the effect became more obvious, and the particle sensation was lighter than that of COST.

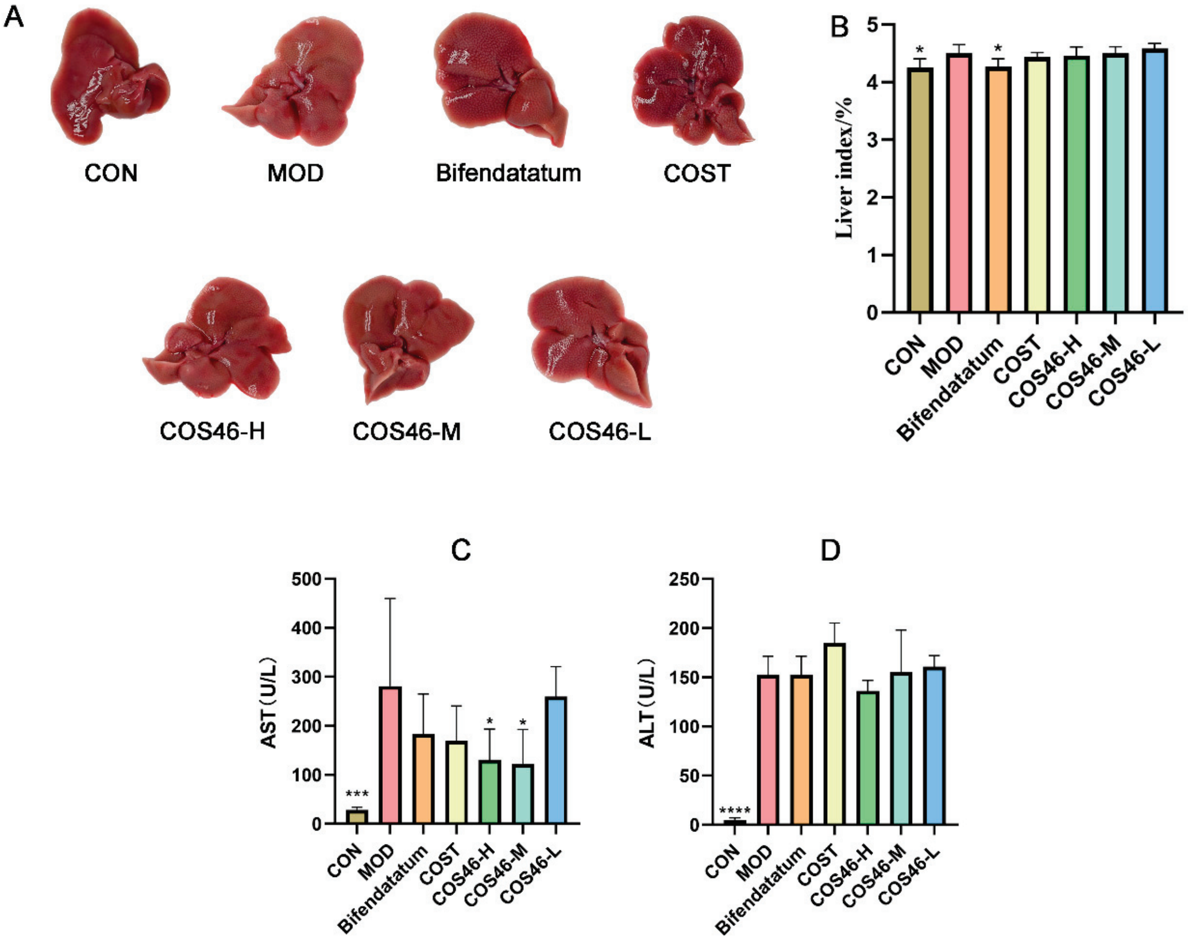

**Figure 6.** Appearance of mouse liver (**A**); liver index (**B**); AST (**C**) and ALT (**D**) in serum (n = 6, mean ± SD); * $p < 0.05$, *** $p < 0.001$, **** $p < 0.0001$.

As shown in Figure 6B, the liver index of the CON group was significantly lower than that of the MOD group, indicating that liver swelling and other conditions occurred after the administration of $CCl_4$. The liver index of COS46 dose groups decreased in a dose-dependent manner, but there was no significant difference compared with the MOD group.

As shown in Figure 6C,D, compared with the CON group, AST and ALT indexes in the MOD group significantly increased, indicating that $CCl_4$ caused liver cell damage. After pretreatment for 7 days, the serum AST value of each group decreased, and the COS46-H group and the COS46-M group showed significant differences. The ALT index did not decrease significantly, but the COS46 group showed dose dependency.

### 2.4.2. Mouse Liver Biochemical Indexes and HE Staining

Figure 7A–F shows the detection results of antioxidant enzyme activity and oxidative damage indexes in the livers of mice in each group. Compared with the CON group, the total antioxidant capacity of the MOD group significantly decreased, while T-AOC did not significantly increase in all administration groups, but the values of COS46-H and COS46-L groups increased slightly. There was no significant difference in SOD levels among all groups.

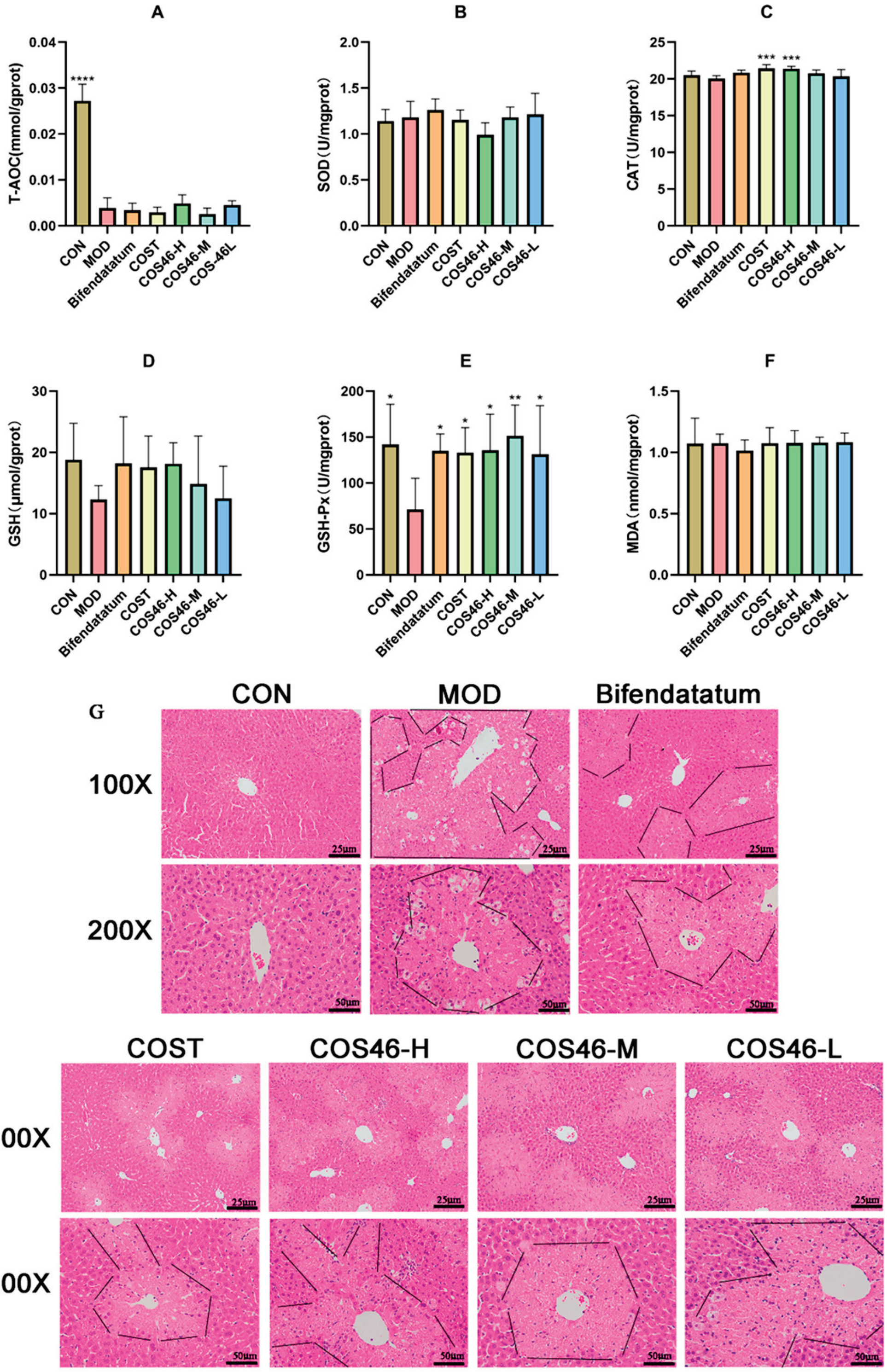

**Figure 7.** The antioxidant–oxidative index of liver (n = 6, mean ± SD), T-AOC (**A**), SOD (**B**), CAT (**C**), GSH (**D**), GSH-Px (**E**), and MDA (**F**); liver HE staining (**G**); * $p < 0.05$, ** $p < 0.01$, *** $p < 0.001$, **** $p < 0.0001$. Black indicates the outline of the damaged part.

Compared with the CON group, CAT enzyme activity in the MOD group decreased slightly, but there was no significant difference. In each administration group, the enzyme activity of the COST group and the COS46-H group increased compared with that of the MOD group and showed a significant difference. Meanwhile, COS46 showed a dose-dependent increase in CAT enzyme activity.

The content of GSH in the MOD group was much lower than that in the CON group, which showed no significant difference. In each administration group, the GSH content in the liver increased, and COS46 increased the GSH content in a dose-dependent manner, but there was no significant difference. The activity of the GSH-Px enzyme in the MOD group significantly decreased, while the activity of GSH-Px significantly increased in all administration groups, and COS46-M showed the best effect. In short, COS46 is better than COST in improving GSH and GSH-Px.

The levels of MDA in the CON group and the MOD group were close to each other, but there was no change trend in MDA content in each administration group.

The HE staining results of mouse livers in each group are shown in Figure 7G. The liver structure of the CON group was normal, and cells were arranged uniformly and in order, with the central vein as the center in a single radial arrangement. In the MOD group, there were obvious abnormalities, such as vacuolar degeneration, necrosis, nuclear ruptures, and cytoplasmic staining of hepatocytes. After 7 days of bifendatatum pretreatment, liver pathological sections showed some improvement in liver abnormalities and no obvious vacuole-like degeneration, and the degree of cytoplasmic redness was reduced. The COST group and the COS46-H group also had the effect of alleviating liver injury and the degree of the two groups was like that of the positive-drug group under visual observation, and both were slightly weaker than the positive-drug group. Similarly, the effects of COS46-M and COS46-L groups on liver injury were similar, with no significant difference, but compared with the MOD group, they could still improve the damage caused by $CCl_4$.

## 3. Materials and Methods

### 3.1. Materials

COST was purchased from AK Biotech Co., Ltd. (Chengdu, China) (detailed parameters can be found in the certificate of analysis in supplementary data).

The COS4 standard, COS5 standard, COS6 standard, and chitosan oligosaccharides mixed standard (DP1-7) were purchased from Huizhou Changlong Biotechnology Co., Ltd. (Guangdong, China).

The biochemical index kits used in this paper were purchased from Nanjing Jiancheng Bioengineering Institute.

The chemicals used are commercially available products.

### 3.2. COST Component Analysis and Purification of COS46

#### 3.2.1. COST Component Analysis and DP4-6 Component Content Determination

(1) Qualitative analysis of COST components by TLC thin layer

COST and chitosan oligosaccharides mixed standards (dp1-7) were used to prepare the solution with the appropriate concentration. Plate: Merck high-efficiency silicone plate (1.05553). Development height: 9.5 cm. Developer system: isopropanol: ammonia: pure water = 15:7.5:1. After unfolding, the plate was dried, soaked in anisaldehyde sulfate colorant for 2 min, dried, and heated in an oven at 110 °C for 10 min to develop color.

(2) The content of DP4-6 components in COST was analyzed by LC-MS

The COST sample and chitosan oligosaccharides standard were weighed and a series of solutions were prepared as follows:

The COS4 standard was weighed as 2.80 mg, dissolved in (acetonitrile: water = 3:7) to make a 1.40 mg/mL solution, and diluted to 0.7, 0.35, 0.175, and 0.0875 mg/mL, respectively.

The COS5 standard was weighed as 2.10 mg, dissolved in (acetonitrile: water = 3:7) to make a 1.40 mg/mL solution, and diluted to 0.35, 0.175, 0.0875, and 0.04375 mg/mL, respectively.

The COS6 standard was weighed as 1.80 mg, dissolved in (acetonitrile: water = 3:7) to make a 1.40 mg/mL solution, and diluted to 0.45, 0.225, 0.1125, and 0.05625 mg/mL, respectively.

The COST standard was weighed as 3.4 mg and dissolved in (acetonitrile: water = 3:7) to make a 3.44 mg/mL solution.

Ten microliters of each solution were extracted for analysis and the standard curve was established.

Table 5 lists the experimental parameters of LC-MS.

**Table 5.** Experimental conditions of liquid chromatography–mass spectrometry (LC-MS).

| | Item | Condition |
|---|---|---|
| LC | Column | GL Sciences Inertsil $NH_2$ 3.0 mm × 150 mm, 5 μm |
| | T | 35 °C |
| | μ | 0.6 mL/min |
| | Mobile phase | $CH_3CN$:0.3%$NH_3 \cdot H_2O$ = 65:35 |
| MS | Spray Voltage | 3200 V |
| | Capillary Temperature | 270.00 °C |
| | Sheath Gas | 40.00 Arb |
| | Aux Gas | 8.00 Arb |
| | Max Spray Current | 100.00 μA |
| | Probe Heater Temp. | 250.00 °C |
| | Ion Source | ESI + ms |

### 3.2.2. Isolation and Identification of COS46

(1) GPC

The Sephadex G-15 was used as column packing, which was fully swelled in a 90 °C water bath and cleaned and had the gas removed, and the chromatographic column was installed by the wet method.

The G15 column was used at a flow rate of 3 mL/h to separate. Then it was collected and lyophilized. The collection frequency was once every 20 min until the reception was completed. This part of the operation is based on TLC operation described in Section 3.2.1 (1). The effluents containing chitosan oligosaccharides with DP = 4–6 were selected for consolidation and freeze-dried, and the yield was calculated according to the mass.

(2) LC-MS

The experimental conditions of LC-MS were the same as in Section 3.2.1 (2).

First, 1.82 mg COS46 was weighed and dissolved (acetonitrile: pure water = 3:7) into a 1.82 mg/mL solution, and 10 μL was injected for analysis.

(3) FT-IR

The COS46 and COST samples were mixed with dry potassium bromide, and then placed in an agate mortar. After grinding and mixing, the tablets were pressed on an oil press. The baseline was calibrated with dry potassium bromide. The scanning range was 400–4000 $cm^{-1}$, the resolution was 4 $cm^{-1}$, and the number of scans was 16. The infrared spectra of COS46 and COST were obtained.

### 3.2.3. Determination of Deacetylation Degree

The deacetylation degree of COS46 was determined by first-derivative ultraviolet spectrophotometry established in the laboratory [43].

(1) Determination of maximum absorption wavelength

GlcNAc (N-acetylglucosamine), GlcN (aminoglucose), and COS46 solutions were prepared in a 0.3 mol/L HCl solution. The scanning wavelength range was 200–400 nm, the slit width was 2 nm, the scanning speed was 20 nm/min, the time constant was 4S, and the recording speed was 10 cm/min. The optical path of the quartz cuvette is 1 cm. Then, under spectral scanning in the range of 200–215 nm, the absorbance of the solution was recorded, and the absorbance was converted into first-order differential calculation.

(2) First-derivative ultraviolet spectrophotometry was established

GlcNAc standard solutions with different concentrations were prepared in a HCl solution. The absorbance of each standard solution was recorded at the main wavelength of 204 nm and the baseline wavelength of 202 nm, and $\frac{\Delta A}{\Delta \lambda}$ (ΔA = A204 nm–A202 nm, Δλ = 2 nm) was calculated. The concentration of the standard solution was the abscissa, and $\frac{\Delta A}{\Delta \lambda}$ was the ordinate to establish the standard curve.

(3) Determination of deacetylation degree of COS46

$$DD(\%) = \frac{C_{46} - C_{GlcNAc}}{C_{46} - \frac{42}{203}C_{GlcNAc}} \times 100$$

*C46* is the concentration of COS46 (μg/mL); $C_{GlcNAc}$ is the concentration of the N-acetylglucosamine unit in the sample, which is obtained according to the standard curve (μg/mL); 203 is the molecular weight of the *GlcNAc* fragment in COS46, calculated according to $C_8H_{13}NO_5$; 42 is the relative molecular weight difference between *GlcNAc* and GlcN fragments.

### 3.2.4. Determination of Number Average Molecular Weight of COST and COS46

A 1 mg/mL glucosamine standard solution was prepared as solutions of different concentrations and added to different glass tubes. Each glass tube was filled with distilled water to 1 mL, 1 mL of the DNS reagent was added, it was placed in a boiling water bath for 5 min, 8 mL of distilled water was added, and 200 μL was removed and placed in a 96-well plate. *OD1* (optical density) was measured at 520 nm by a microplate reader.

Then, 1 mg/mL COST and COS46 solutions were prepared. The remaining operations were the same as above. The *OD1* value was determined at 520 nm with an enzyme-labeled instrument.

Next, we took 1 mL of 1 mg/mL COST and COS46, added 3 mL of 6 mol/L HCl, bathed it in boiling water for 2 h, neutralized the mixture with 6 mol/L NaOH, and diluted the solution to 10 mL with water. We then took 1 mL of diluted hydrolysate, added 1 mL of the DNS reagent, bathed the mixture in boiling water for 5 min, and added 8 mL of distilled water after cooling. Finally, we removed 200 μL and measured the *OD2* value with an enzyme-labeled instrument at 520 nm.

If both *OD1* and *OD2* are in the range of the scalar curve, the average degree of polymerization of the sample is:

$$\mathrm{n} = 10 \times \frac{OD1}{OD2}$$

The average relative molecular mass of the sample is:

$$\mathrm{M_W} = \mathrm{n} \times 179 - (\mathrm{n} - 1) \times 18$$

## *3.3. Determination of Oxidation Resistance of COS46 and COST*

### 3.3.1. Determination of Hydroxyl Radical Scavenging Ability

In each test tube, 1 mL of COS46 and COST (in concentrations of 0.2, 0.4, 0.6, 0.8, 1.0, 1.2, and 1.4 mg/mL) was added, followed by the sequential addition of 1 mL of 6 mmol/L $FeSO_4$, 2 mL of 6 mmol/L $H_2O_2$, and mixing. The mixture was then left in the dark at room temperature for 10 min. Subsequently, 1 mL of a 6 mmol/L salicylic acid-ethanol solution was added, and after mixing, the reaction was held in the dark at 37 °C for 60 min in a water bath. After cooling to room temperature, the absorbance was measured at 517 nm, yielding the absorbance value *A1*. For the blank group, an equivalent amount of water served as the substitute for the sample, yielding the absorbance value *A0*. Each group underwent three parallel measurements. The hydroxyl radical scavenging rate was then calculated using the formula below:

$$\text{Hydroxyl radical scavenging activity}(\%) = \frac{A_0 - A_1}{A_0} \times 100\%$$

### 3.3.2. Determination of DPPH Free Radical Scavenging Ability

First, we added 2 mL of the 0.1 mmol/L DPPH (1,1-Diphenyl-2-picrylhydrazyl radical)-EtOH solution and 2 mL of different concentrations of COS46 and COST (0.2, 0.4, 0.6, 0.8, 1.0, 1.2, 1.4, 1.6, 1.8, and 2.0 mg/mL) to each test tube, mixed well, and reacted the solution in a dark water bath at 37 °C for 60 min. After cooling to room temperature, we measured the absorbance at 517 and recorded it as *A1*. The control group used the same amount of absolute ethanol instead of the DPPH-EtOH solution, which was recorded as *A2*, and the blank group used the same amount of distilled water instead of the sample to be tested. We then calculated the DPPH radical scavenging rate according to the following formula:

$$\text{DPPH free radical scavenging activity}(\%) = \left(1 - \frac{A_1 - A_2}{A_0}\right) \times 100\%$$

### *3.4. Cell Experiment*

#### 3.4.1. L02 Cell Culture

L02 cells were cultivated in a constant-temperature and -humidity environment at 37 °C and 5% $CO_2$ in a complete medium containing RPMI-1640, fetal bovine serum (9:1, *v*/*v*), streptomycin (100 μg/mL), and penicillin (100 U/mL), with a 1% double-antibody ratio. The culture medium was replaced every two days, and the experiment was initiated when the cell fusion rate reached 80%.

#### 3.4.2. Establishment of Liver Injury Model Induced by CCl4 (Determination of DMSO and CCl4 Concentrations)

First, 0.02%, 0.04%, 0.06%, 0.08%, 0.10%, 0.12%, 0.14%, 0.16%, and 0.18% DMSO were used to treat cells.

Next, 10, 20, 30, 40, 50, 60, 70, 80, and 90 mmol/L $CCl_4$ were used to treat cells. CCK-8 was used to determine the cell survival rate, and IC50 was calculated to determine the modeling concentration.

#### 3.4.3. The Concentrations of COS46 and COST

First, 2, 4, 6, 8, 10, 12, 14, and 16 mg/mL COS46 and COST were given to cells, respectively, and then they were cultured for 24 h. The CCK-8 method was used to determine the cell inhibition rate and the dosage of COS46 and COST.

#### 3.4.4. Effects of COS46 and COST on Survival Rate of L02 Cells Treated with $CCl_4$

L02 cells at the logarithmic growth stage were inoculated into 96-well culture plates with $2.0 \times 10^4$ cells per well. The CON group, MOD group, COS46-H/M/L group, and COST-H/M/L group were set up and cultured for 24 h. The administration group was added with different concentrations of drugs and continued to culture for 24 h. In addition to CON, each group was added with the modeling concentration of $CCl_4$ and continued to be treated for 24 h. CCK-8 measured the cell survival rate.

#### 3.4.5. Culture Medium and Antioxidant and Oxidation Indices Detection

As described in Section 3.4.4, the supernatant of the medium was collected and the contents of ALT and AST were measured.

L02 cells at the logarithmic growth stage were inoculated into 6-well culture plates with $4 \times 10^5$ cells per well. The cells were then lysed, and the lysate was collected to determine the levels of T-AOC (Total antioxidant capacity), SOD (Superoxide dismutase), CAT (Catalase), GSH-Px (Glutathione peroxidase), and GSH (glutathione.).

### *3.5. Animal Experimental*

#### 3.5.1. Animal

Seventy SPF male C57BL/6J mice, 18–22 g, were purchased from Guangdong Sijia Jingda Biological Co., LTD., Production License No.: SCXK (Guangdong, China) 2020-0052; Reared in Animal Center of Guangdong Pharmaceutical University, License No. SYXK (Guangdong, China) 2022-0125. The feeding conditions of the animal experiment were 24.0 ± 2.0 °C, relative humidity of 54–65%, air change times > 15 times /h, and alternating light and dark for 12 h. The experimental animals are kept in the pathogen-free laboratory of the Experimental Animal Center of Guangdong Pharmaceutical University. This experiment was approved by the Experimental Animal Ethics Committee of Guangdong Pharmaceutical University and strictly followed the requirements of the Guidelines for Ethical Review of Experimental Animal Welfare (GB/T35892-2018) to fully protect the welfare of experimental animals.

#### 3.5.2. Administration and Establishment of Acute Liver Injury Model

Seventy male C57BL/6J mice were randomly divided into 7 groups after 1 week of adaptive feeding. They were the blank control group (CON), model control group (MOD), positive drug control group (Bifendatatum), COST administration group (COST), COS46 high-dose group (COS46-H), COS46 medium-dose group (COS46-M), and COS46 low-dose group (COS46-L). There were 10 mice in each group, and they all had a free diet.

The COST dose was 250 mg/kg, and the COS46 high, medium and low doses were 500 mg/kg, 250 mg/kg, and 125 mg/kg, respectively. The blank control group and the model control group were intragastric with distilled water instead, and intragastric administration continued for 7 days. After the end of the 7th day, the liver injury model was induced by a one-time gavage of a 5 mL/kg 1% $CCl_4$ oil solution in each dose group and the model control group and the corresponding volume of olive oil was given to the blank control group, and then the tested animals were fasted for 16 h. The mice were then anesthetized by an intraperitoneal injection of a 60 mg/kg BW sodium pentobarbital solution, and blood was taken from the orbit. The animals were sacrificed by cervical dislocation after blood collection. The appropriate amount of liver was taken for embedding, fixed with 4%PFA for 24 h, and the remaining liver was stored at −80 °C for use.

(1) Liver index

Mouse body weight and liver weight were weighed, and the liver index was calculated.

$$\text{Liver index } (\%) = \frac{\text{liver weight (g)}}{\text{body weight (g)}}$$

(2) Biochemical index

Serum: ALT and AST

Liver: T-AOC, SOD, MDA, CAT, GSH, GSH-Px

The above indexes were measured by the Nanjing Jiancheng Kit.

(3) Liver HE staining

The liver was embedded in paraffin wax and cut into 4 μm pathological sections for HE staining (Leagene Biotechnology, Beijing, China, DH0006).

### *3.6. Statistical Analysis*

The data obtained in this experiment were analyzed and mapped by GraphPad Prism 9.0, and the result of the data was expressed as the mean ± SD. The data significance analysis was conducted using One-Way ANOVA for multi-group data and T-tests for the data significance analysis between the two groups. $p < 0.05$ indicated statistical significance.

## 4. Discussions and Conclusions

Traditionally, chitosan oligosaccharides are a mixture prepared from chitin or chitosan. When using such chitosan oligosaccharides to explore their biological activity, the repeatability of the experiment is poor, and the results may be divided, so the study of separating chitosan oligosaccharides will definitely become a trend in the future. In addition, because chitosan oligosaccharides with different polymerization degrees have different biological activities [44], a detailed study on chitosan oligosaccharides with different polymerization degrees is conducive to the safer and more reasonable use of chitosan oligosaccharides and will further expand the application scope of chitosan oligosaccharides.

In this study, COS46 contains a tetramer, a pentamer, and a hexamer, and it is regarded as a whole as the research object, and the effect of each component is not analyzed in detail. However, according to the results provided by TLC, G-15 was selected as chromatographic column packing, according to its retention effect on chitosan oligosaccharides with different molecular weights. Reevaluating the height, diameter, and flow rate of the packing, it is possible to further separate the three components (COS4, COS5, and COS6) of COS46.

During the antioxidant activity test, it was observed that chito-oligosaccharides, both before and after separation, demonstrated a superior scavenging ability of free radicals. Hydroxyl free radicals, which are considered harmful to the human body, can form within the body. COS46 was found to be more effective in scavenging hydroxyl free radicals. When foreign substances stimulate the human body, hydrogen peroxide is produced. This then reacts with $Fe^{2+}$ to generate reactive oxygen through the Fenton reaction. It is speculated that COS46 can chelate with Fe2+ more effectively to prevent their reaction [45,46]. Therefore, COS46 may have more potential as an antioxidant.

After using $CCl_4$ to establish liver injury modeling, this experiment only explored the effects of COST and COS46 on L02 hepatocyte injury, antioxidant and oxidative effects, and effects on the Keap-1/Nrf2/HO-1 pathway in L02 hepatocytes. The change in related indexes after drug administration was not discussed further. Based on the experiment, it was found that SOD and CAT enzyme activities were higher in the cell administration groups compared to the CON group. This, combined with the existing research, suggests that COS46 and COST treatment may activate the signaling pathway, increase the expression of related antioxidant proteins, and improve the activity of SOD, CAT, and other antioxidant enzymes to some extent. When cells are exposed to toxic substances, they can quickly develop protective mechanisms to reduce damage and prevent cell death. The MOD group showed higher T-AOC and SOD indexes compared to the CON group. This may be due to the insufficient concentration of $CCl_4$ used in the liver toxicity model to cause cell death in all cells, and the surviving cells were able to respond positively and significantly improve their enzyme activity, allowing them to survive in the presence of $CCl_4$.

Many studies have verified the protective effect of chitosan oligosaccharides on the liver [47–49]. However, their administration time is usually more than 4 weeks, and studies on the short-term effect of chitosan oligosaccharides are very rare. Therefore, in animal experiments, we chose to verify the protective effect of administration for one week on acute liver injury.

After seven days of pretreatment and gavage with $CCl_4$, the MOD group of mice exhibited liver damage, including an increased liver index, apparent granulation, and elevated serum AST and ALT levels. Each administration group was able to alleviate the injury’s deterioration. Additionally, it was observed that administration could reverse the effects of $CCl_4$, leading to a reduction in liver GSH and Gsh-Px content and resistance to oxidative damage. However, the detection of related oxidation indexes yielded slightly different trends between the results of the cell experiment and the animal experiment. It is speculated that there may be differences between human hepatocytes and mouse cells in vitro, resulting in varying sensitivities to drugs and a slight deviation in the experimental results of the two cell types. It is also possible that the administration time in animal experiments is insufficient, which shows that chitosan oligosaccharides can only be used as a dietary supplement for a long time, and its short-term liver protection effect is not significant enough.

In summary, this paper demonstrates that the process of obtaining COS46 through GPC separation and purification has good process stability and high product purity. This method overcomes the current difficulties in preparing low-molecular-weight chitosan oligosaccharides to some extent. Simultaneously, COS46 and COST can act as exogenous antioxidants and improve the body’s antioxidant levels. This can effectively prevent damage to human hepatocytes and mouse livers caused by $CCl_4$ to a certain extent. Low-molecular-weight COS46 is superior to COST in some aspects of antioxidation.

**Supplementary Materials:** The following supporting information can be downloaded at: https://www.mdpi.com/article/10.3390/md22030128/s1, Figure S1: 0.0875 mg/mL COS4 (A), 0.04375 mg/mL COS5 (B), 0.05625 mg/mL COS6 (C) chromatograms of standard products; Figure S2: 0.175 mg/mL COS4 (A), 0.0875 mg/mL COS5 (B), 0.1125 mg/mL COS6 (C) chromatograms of standard products; Figure S3: 0.350 mg/mL COS4 (A), 0.175 mg/mL COS5 (B), 0.225 mg/mL COS6 (C) chromatograms of standard products; Figure S4: 0.700 mg/mL COS4 (A), 0.350 mg/mL COS5 (B), 0.450 mg/mL COS6 (C) chromatograms of standard products; Figure S5: 1.400 mg/mL COS4 (A), 0.700 mg/mL COS5 (B), 0.900 mg/mL COS6 (C) chromatograms of standard products; Figure S6: Liquid phase diagram of 1.820 mg/mL COS46; Figure S7: Liquid phase diagram of 3.440 mg/mL COST; Figure S8: Mass spectrum of COS46 when RT = 3.60 min; Figure S9: Mass spectrum of COS46 when RT = 4.78 min; Figure S10: Mass spectrum of COS46 when RT = 6.44 min; Figure S11: Mass spectrum of COS46 when RT = 8.83 min; Figure S12: Mass spectrum of COS46 when RT = 12.65 min; Figure S13: Mass spectrum of COS46 when RT=18.10min; Figure S14: Mass spectrum of COST when RT = 3.55 min; Figure S15: Mass spectrum of COST when RT = 4.83min; Figure S16: Mass spectrum of COST when RT = 6.56 min; Figure S17: Mass spectrum of COST when RT = 9.01 min; Figure S18: Mass spectrum of COST when RT = 12.98 min; Figure S19: Mass spectrum of COST when RT = 18.67 min; Figure S20: Standard curve of photometric method; Table S1: Standard curves of retention time (RT) and concentrations of COS4, COS5 and COS6; Table S2: Liquid phase data of COS46 and COST target components.

**Author Contributions:** Methodology, software, data curation, writing—original draft preparation, K.W. and D.Y.; software, visualization, investigation, Y.B. and H.C.; supervision, J.G. and Z.S.; validation, Y.B. and H.C.; writing—reviewing and editing, K.W.; funding acquisition, Z.S. All authors have read and agreed to the published version of the manuscript.

**Funding:** This work was financially supported by the Science and Technology Program of Guangzhou, China (NO. 202103000089), the Science Foundation for Distinguished Young Scholars of Guangdong (2020B1515020026).

**Institutional Review Board Statement:** The animal study protocol was approved by the Ethics Committee of the Experimental Animal Center of Guangdong Pharmaceutical University for studies involving animals. The animal ethical review number is (No. SYXK (Guangdong) 2022-0125).

**Data Availability Statement:** The data from the present study are available in the article.

**Conflicts of Interest:** The authors declare no conflict of interest.

## Abbreviations

| | |
|---|---|
| COS | chitosan oligosaccharides |
| COST | chitosan oligosaccharides (Mw $\leq$ 1000) |
| COS46 | chitosan oligosaccharides with degree of 4–6 polymerization |
| COS4 | chitotetraose |
| COS5 | chitopentaose |
| COS6 | chitohexaose |
| DD | degree of deacetylation |
| DP | degree of polymerization |
| GlcNAc | acetylglucosamine |
| GlcN | aminoglucose |

## References

1. Pellis, A.; Guebitz, G.M.; Nyanhongo, G.S. Chitosan: Sources, Processing and Modification Techniques. *Gels* **2022**, *8*, 393. [CrossRef] [PubMed]
2. Zhao, X.-P.; Liu, J.; Sui, Z.-J.; Xu, M.-J.; Zhu, Z.-Y. Preparation and antibacterial effect of chitooligosaccharides monomers with different polymerization degrees from crab shell chitosan by enzymatic hydrolysis. *Biotechnol. Appl. Biochem.* **2023**, *70*, 164–174. [CrossRef] [PubMed]
3. Xia, W.; Wei, X.Y.; Xie, Y.Y.; Zhou, T. A novel chitosan oligosaccharide derivative: Synthesis, antioxidant and antibacterial properties. *Carbohydr. Polym.* **2022**, *291*, 119608. [CrossRef] [PubMed]
4. Zou, P.; Yuan, S.; Yang, X.; Guo, Y.; Li, L.; Xu, C.; Zhai, X.; Wang, J. Structural characterization and antitumor effects of chitosan oligosaccharides against orthotopic liver tumor via NF-κB signaling pathway. *J. Funct. Foods* **2019**, *57*, 157–165. [CrossRef]

5. Zhai, X.; Li, C.; Ren, D.; Wang, J.; Ma, C.; Abd El-Aty, A.M. The impact of chitooligosaccharides and their derivatives on the in vitro and in vivo antitumor activity: A comprehensive review. *Carbohydr. Polym.* **2021**, *266*, 118132. [CrossRef]
6. Wang, L.; Liu, X.; Tan, W.; Li, Q.; Guo, Z.; Zhang, J. Preparation and antioxidant activity of novel chitosan oligosaccharide quinolinyl urea derivatives. *Carbohydr. Res.* **2022**, *521*, 108678. [CrossRef]
7. Zhang, Y.; Wang, Y.; Liu, Y.; Gong, T.; Hou, M. The Anti-inflammatory Effect of Chitosan Oligosaccharide on Heart Failure in Mice. *Biomed. Res. Int.* **2022**, *2022*, 8746530. [CrossRef]
8. Antonov, Y.A.; Zhuravleva, I.L.; Bezrodnykh, E.A.; Berezin, B.B.; Kulikov, S.N.; Tikhonov, V.E. Complexation of oligochitosan with sodium caseinate in alkalescent and weakly acidic media. *Carbohydr. Polym.* **2023**, *302*, 120391. [CrossRef]
9. Jing, W.; Chen, C.; Wang, G.; Han, M.; Chen, S.; Jiang, X.; Shi, C.; Sun, P.; Yang, Z.; Shi, B.; et al. Metabolic Modulation of Intracellular Ammonia via Intravesical Instillation of Nanoporter-Encased Hydrogel Eradicates Bladder Carcinoma. *Adv. Sci.* **2023**, *10*, e2206893. [CrossRef]
10. Na, K.; Wei, J.; Zhang, L.; Fang, Y.; Li, X.; Lu, S.; Guo, X. Effects of chitosan oligosaccharides (COS) and FMT from COS-dosed mice on intestinal barrier function and cell apoptosis. *Carbohydr. Polym.* **2022**, *297*, 120043. [CrossRef] [PubMed]
11. Ji, X.; Zhu, L.; Chang, K.; Zhang, R.; Chen, Y.; Yin, H.; Jin, J.; Zhao, L. Chitooligosaccahrides: Digestion characterization and effect of the degree of polymerization on gut microorganisms to manage the metabolome functional diversity in vitro. *Carbohydr. Polym.* **2022**, *275*, 118716. [CrossRef]
12. Tzeng, H.P.; Liu, S.H.; Chiang, M.T. Antidiabetic Properties of Chitosan and Its Derivatives. *Mar. Drugs* **2022**, *20*, 784. [CrossRef]
13. He, N.; Wang, S.; Lv, Z.; Zhao, W.; Li, S. Low molecular weight chitosan oligosaccharides (LMW-COSs) prevent obesity-related metabolic abnormalities in association with the modification of gut microbiota in high-fat diet (HFD)-fed mice. *Food Funct.* **2020**, *11*, 9947–9959. [CrossRef]
14. Karadeniz, F. In Vitro Anti-HIV-1 Activity of Chitosan Oligomers N-Conjugated with Asparagine and Glutamine. *BioTech* **2023**, *12*, 18. [CrossRef] [PubMed]
15. Ouyang, Q.Q.; Zhao, S.; Li, S.D.; Song, C. Application of Chitosan, Chitooligosaccharide, and Their Derivatives in the Treatment of Alzheimer's Disease. *Mar. Drugs* **2017**, *15*, 322. [CrossRef] [PubMed]
16. Muanprasat, C.; Wongkrasant, P.; Satitsri, S.; Moonwiriyakit, A.; Pongkorpsakol, P.; Mattaveewong, T.; Pichyangkura, R.; Chatsudthipong, V. Activation of AMPK by chitosan oligosaccharide in intestinal epithelial cells: Mechanism of action and potential applications in intestinal disorders. *Biochem. Pharmacol.* **2015**, *96*, 225–236. [CrossRef]
17. Tao, W.; Wang, G.; Pei, X.; Sun, W.; Wang, M. Chitosan Oligosaccharide Attenuates Lipopolysaccharide-Induced Intestinal Barrier Dysfunction through Suppressing the Inflammatory Response and Oxidative Stress in Mice. *Antioxidants* **2022**, *11*, 1384. [CrossRef]
18. Sun, Y.; Ji, X.; Cui, J.; Mi, Y.; Zhang, J.; Guo, Z. Synthesis, Characterization, and the Antioxidant Activity of Phenolic Acid Chitooligosaccharide Derivatives. *Mar. Drugs* **2022**, *20*, 489. [CrossRef] [PubMed]
19. Mourya, V.K.; Inamdar, N.N.; Choudhari, Y.M. Chitooligosaccharides: Synthesis, characterization and applications. *Polym. Sci. Ser. A* **2011**, *53*, 583–612. [CrossRef]
20. Aghbashlo, M.; Amiri, H.; Moosavi Basri, S.M.; Rastegari, H.; Lam, S.S.; Pan, J.; Gupta, V.K.; Tabatabaei, M. Tuning chitosan's chemical structure for enhanced biological functions. *Trends Biotechnol.* **2022**, *41*, 785–797. [CrossRef]
21. Li, K.; Liu, S.; Xing, R.; Qin, Y.; Li, P. Preparation, characterization and antioxidant activity of two partially N-acetylated chitotrioses. *Carbohydr. Polym.* **2013**, *92*, 1730–1736. [CrossRef]
22. Lodhi, G.; Kim, Y.-S.; Hwang, J.-W.; Kim, S.-K.; Jeon, Y.-J.; Je, J.-Y.; Ahn, C.-B.; Moon, S.-H.; Jeon, B.-T.; Park, P.-J. Chitooligosaccharide and its derivatives: Preparation and biological a pplications. *BioMed. Res. Int.* **2014**, *2014*, 654913. [CrossRef]
23. Bonin, M.; Sreekumar, S.; Cord-Landwehr, S.; Moerschbacher, B.M. Preparation of Defined Chitosan Oligosaccharides Using Chitin Deacetyl ases. *Int. J. Mol. Sci.* **2020**, *21*, 7835. [CrossRef]
24. Xiong, C.; Wu, H.; Wei, P.; Pan, M.; Tuo, Y.; Kusakabe, I.; Du, Y. Potent angiogenic inhibition effects of deacetylated chitohexaose sepa rated from chitooligosaccharides and its mechanism of action in vitro. *Carbohydr. Res.* **2009**, *344*, 1975–1983. [CrossRef] [PubMed]
25. Sørbotten, A.; Horn, S.J.; Eijsink, V.G.H.; Vårum, K.M. Degradation of chitosans with chitinase B from Serratia marcescens. Pr oduction of chito-oligosaccharides and insight into enzyme processivit y. *FEBS J.* **2005**, *272*, 538–549. [CrossRef] [PubMed]
26. Wu, Y.; Lin, Q.L.; Chen, Z.X.; Wu, W.; Xiao, H.X. Preparation of chitosan oligomers COS and their effect on the retrogra dation of intermediate amylose rice starch. *J. Food Sci. Technol.* **2012**, *49*, 695–703. [CrossRef] [PubMed]
27. Dong, H.; Wang, Y.; Zhao, L.; Zhou, J.; Xia, Q.; Jiang, L.; Fan, L. Purification of DP 6 to 8 chitooligosaccharides by nanofiltration from the prepared chitooligosaccharides syrup. *Bioresour. Bioprocess.* **2014**, *1*, 20. [CrossRef]
28. Dong, X.; Shen, A.; Gou, Z.; Chen, D.; Liang, X. Hydrophilic interaction/weak cation-exchange mixed-mode chromatography for chitooligosaccharides separation. *Carbohydr. Res.* **2012**, *361*, 195–199. [CrossRef]
29. Le Dévédec, F.; Bazinet, L.; Furtos, A.; Venne, K.; Brunet, S.; Mateescu, M.A. Separation of chitosan oligomers by immobilized metal affinity chromat ography. *J. Chromatogr. A* **2008**, *1194*, 165–171. [CrossRef] [PubMed]
30. Wang, B.; Wang, L.; Qu, Y.; Lu, J.; Xia, W. Chitosan oligosaccharides exert neuroprotective effects via mod ulating the PI3K/Akt/Bcl-2 pathway in a Parkinsonian model. *Food Funct.* **2022**, *13*, 5838–5853. [CrossRef] [PubMed]
31. Cao, L.; Wu, J.; Li, X.; Zheng, L.; Wu, M.; Liu, P.; Huang, Q. Validated HPAEC-PAD Method for the Determination of Fully Deacetylated Chitooligosaccharides. *Int. J. Mol. Sci.* **2016**, *17*, 1699. [CrossRef] [PubMed]

32. Jiang, M.; Guo, Z.; Wang, C.; Yang, Y.; Liang, X.; Ding, F. Neural activity analysis of pure chito-oligomer components separated from a mixture of chitooligosaccharides. *Neurosci. Lett.* **2014**, *581*, 32–36. [CrossRef] [PubMed]
33. Zhu, X.-Y.; Zhao, Y.; Zhang, H.-D.; Wang, W.-X.; Cong, H.-H.; Yin, H. Characterization of the Specific Mode of Action of a Chitin Deacetylas e and Separation of the Partially Acetylated Chitosan Oligosaccharides. *Mar. Drugs* **2019**, *17*, 74. [CrossRef]
34. Hattori, T.; Anraku, N.; Kato, R. Capillary electrophoresis of chitooligosaccharides in acidic solution: Simple determination using a quaternary-ammonium-modified column and indirect photometric detection with crystal violet. *J. Chromatogr. B Anal. Technol. Biomed. Life Sci.* **2009**, *878*, 477–480. [CrossRef] [PubMed]
35. Beaudoin, M.-E.; Gauthier, J.; Boucher, I.; Waldron, K.C. Capillary electrophoresis separation of a mixture of chitin and chitos an oligosaccharides derivatized using a modified fluorophore conjugati on procedure. *J. Sep. Sci.* **2005**, *28*, 1390–1398. [CrossRef]
36. Boll, M.; Lutz, W.D.; Becker, E.; Stampfl, A. Mechanism of Carbon Tetrachloride-Induced Hepatotoxicity. Hepatocellular Damage by Reactive Carbon Tetrachloride Metabolites. *Z. Für Naturforschung C* **2001**, *56*, 649–659. [CrossRef]
37. Sun, J.; Wen, X.; Liu, J.; Kan, J.; Qian, C.; Wu, C.; Jin, C. Protective effect of an arabinogalactan from black soybean against carbon tetrachloride-induced acute liver injury in mice. *Int. J. Biol. Macromol.* **2018**, *117*, 659–664. [CrossRef]
38. Li, S.; Zhou, J.; Xu, S.; Li, J.; Liu, J.; Lu, Y.; Shi, J.; Zhou, S.; Wu, Q. Induction of Nrf2 pathway by Dendrobium nobile Lindl. alkaloids protects against carbon tetrachloride induced acute liver injury. *Biomed. Pharmacother.* **2019**, *117*, 109073. [CrossRef]
39. Unsal, V.; Cicek, M.; Sabancilar, I. Toxicity of carbon tetrachloride, free radicals and role of antioxidants. *Rev. Environ. Health* **2021**, *36*, 279–295. [CrossRef]
40. He, S.; Zhao, W.; Chen, X.; Li, J.; Zhang, L.; Jin, H. Ameliorative Effects of Peptide Phe-Leu-Ala-Pro on Acute Liver and Kidney Injury Caused by $CCl_4$ via Attenuation of Oxidative Stress and Inflammation. *ACS Omega* **2022**, *7*, 44796–44803. [CrossRef]
41. Ismail, A.F.; Salem, A.A.; Eassawy, M.M. Modulation of gamma-irradiation and carbon tetrachloride induced oxidative stress in the brain of female rats by flaxseed oil. *J. Photochem. Photobiol. B* **2016**, *161*, 91–99. [CrossRef]
42. Mazani, M.; Ojarudi, M.; Banaei, S.; Salimnejad, R.; Latifi, M.; Azizi, H.; Rezagholizadeh, L. The protective effect of cinnamon and ginger hydro-alcoholic extract on carbon tetrachloride-induced testicular damage in rats. *Andrologia* **2020**, *52*, e13651. [CrossRef]
43. Jiang, Y.; Fu, C.; Wu, S.; Liu, G.; Guo, J.; Su, Z. Determination of the Deacetylation Degree of Chitooligosaccharides. *Mar. Drugs* **2017**, *15*, 332. [CrossRef] [PubMed]
44. Hao, W.; Li, K.; Li, P. Review: Advances in preparation of chitooligosaccharides with heteroge neous sequences and their bioactivity. *Carbohydr. Polym.* **2021**, *252*, 117206. [CrossRef]
45. Hao, W.; Li, K.; Ma, Y.; Li, R.; Xing, R.; Yu, H.; Li, P. Preparation and Antioxidant Activity of Chitosan Dimers with Different Sequences. *Mar. Drugs* **2021**, *19*, 366. [CrossRef]
46. Liu, Y.; Zhong, Z.; Bao, L.; Wen, F.; Yang, H. The preparation and antioxidant activities of four 2-aminoacyl-chitooligosaccharides. *Carbohydr. Res.* **2022**, *521*, 108667. [CrossRef]
47. Xiang, J.; Wang, J.; Xie, H.; Liu, Y.; Bai, Y.; Che, Q.; Cao, H.; Huang, G.; Guo, J.; Su, Z. Protective effect and mechanism of chitooligosaccharides on acetaminop hen-induced liver injury. *Food Funct.* **2021**, *12*, 9979–9993. [CrossRef] [PubMed]
48. Liu, P.; Li, H.; Xu, H.; Gong, J.; Jiang, M.; Qian, J.; Xu, Z.; Shi, J. Chitooligosaccharides Attenuated Hepatic Encephalopathy in Mice throug h Stabilizing Gut-Liver-Brain Disturbance. *Mol. Nutr. Food Res.* **2023**, *67*, e2200158. [CrossRef] [PubMed]
49. Liu, P.; Li, H.; Gong, J.; Geng, Y.; Jiang, M.; Xu, H.; Xu, Z.; Shi, J. Chitooligosaccharides alleviate hepatic fibrosis by regulating the pol arization of M1 and M2 macrophages. *Food Funct.* **2022**, *13*, 753–768. [CrossRef]

marine drugs

Article

# Phenolic Acid Functional Quaternized Chitooligosaccharide Derivatives: Preparation, Characterization, Antioxidant, Antibacterial, and Antifungal Activity

**Yan Sun [1,2,3,†], Jingmin Cui [1,2,†], Liguang Tian [4], Yingqi Mi [1,2,3] and Zhanyong Guo [1,2,*]**

1 Key Laboratory of Coastal Biology and Bioresource Utilization, Yantai Institute of Coastal Zone Research, Chinese Academy of Sciences, Yantai 264003, China; sunyan20@mails.ucas.ac.cn (Y.S.); jmcui@yic.ac.cn (J.C.); yqmi@yic.ac.cn (Y.M.)
2 University of Chinese Academy of Sciences, Beijing 100049, China
3 Shandong Saline-Alkali Land Modern Agriculture Company, Dongying 257300, China
4 Yantai Agricultural Technology Extension Center, Yantai 265499, China; tianliguang@yt.shandong.cn
* Correspondence: zhanyongguo@hotmail.com; Tel.: +86-535-2109171; Fax: +86-535-2109000
† These authors contributed to the work equally.

**Abstract:** As a promising biological material, chitooligosaccharide (COS) has attracted increasing attention because of its unique biological activities. In this study, fourteen novel phenolic acid functional COS derivatives were successfully prepared using two facile methods. The structures of derivatives were characterized by FT-IR and $^1$H NMR spectra. The in vitro antioxidant activity experiment results demonstrated that the derivatives presented stronger 1,1-Diphenyl-2-picryl-hydrazyl (DPPH), superoxide, hydroxyl radical scavenging activity and reducing power, especially the *N,N,N*-trimethylated chitooligosaccharide gallic acid salt (GLTMC), gallic acid esterified *N,N,N*-trimethylated chitooligosaccharide (GL-TMC) and caffeic acid *N,N,N*-trimethylated chitooligosaccharide (CFTMC) derivatives. Furthermore, the antifungal assay was carried out and the results indicated that the salicylic acid esterified *N,N,N*-trimethylated chitooligosaccharide (SY-TMC) had much better inhibitory activity against *Botrytis cinerea* and *Fusarium graminearum*. Additionally, the results of the bacteriostasis experiment showed that the caffeic acid esterified *N,N,N*-trimethylated chitooligosaccharide (CF-TMC) had the potential ability to inhibit *Escherichia coli* and *Staphylococcus aureus* bacteria. Altogether, this study may provide a neoteric method to produce COS derivatives with significantly increased biological activities, which have potential use in food, medicine, and health care products and other related industries.

**Keywords:** chitooligosaccharide; chitooligosaccharide quaternary ammonium salt derivatives; phenolic acid; antioxidant activity; antibacterial activity; antifungal activity

## 1. Introduction

Chitosan is the only natural cationic basic polysaccharide on earth and the second most abundant natural polysaccharide after cellulose [1]. Chitooligosaccharide (COS) is the degradation product of chitosan and usually produced by acid hydrolysis, physical hydrolysis or enzymatic degradation methods [2]. It is mainly a linear oligomer of glucosamine linked by a β-1,4 glycosidic bond, with a small amount of acetylglucosamine. The degree of polymerization ranges from 2 to 20 [3]. Due to the low degree of polymerization, COS has more excellent biological activities compared with chitosan. Previous research confirmed that COS not only has good water solubility [4], biocompatibility and biodegradability, but also has anti-inflammatory, anticancerogenic, antidiabetic, antimicrobial, anti-HIV-1, antioxidant, antiangiogenic, neuroprotective, and immunostimulatory effects [5–9]. Owning to these good activities, COS is becoming the focus of studies to develop products that can be used for humans, such as in the medicine, food, cosmetic, health care and agriculture industries [10]. Among the various studies, chemical modification is one of the most important research directions as the amino and hydroxyl groups of COS provide possible reaction sites to synthesize novel compounds [11]. And favorable substitution can further improve the biological activity and utilization value of COS.

Phenolic acids are natural products that are derived from plant secondary metabolism [12]. They are widely found in numerous plants and are easy to obtain [13]. Studies have shown that phenolic acids possess excellent antioxidant activity. The hydroxyl group of phenolic acids is the main functional group that exerts antioxidant activity because it can deliver hydrogen atoms to free radicals, interfere with the chain propagation reactions and chelate metal ions. In addition, the structural diversity of phenolic acids can affect the antioxidant capacity. Phenolic acids also have other biological activities, such as anti-inflammatory, immunoregulatory, anti-allergic, anti-atherogenic, anti-microbial, anti-thrombotic, cardioprotective, anti-cancer and antidiabetic properties [14–18]. Based on these multiple biological activities, phenolic acids are becoming a kind of potential biomaterial that can be used in the pharmaceutical, food and biomedicine industries, among others [19]. However, the low water solubility of phenolic acids limits their application.

So, based on the above characteristics of COS and phenolic acids, we want to synthesize new compounds with their combined activities. There has been much research on the synthesis of phenolic acid chitosan or COS derivatives. Tae-kil et al. selected eight phenolic acids (protocatechuic, 4-hydroxybenzoic, vanillic, syringic, *p*-coumaric, caffeic, ferulic and sinapinic acid) to synthesize eight acylated COS derivatives by the DCC/HOBt grafting system and demonstrated that caffeic acid-c-COS had the highest antioxidant activity [20]. Thanh et al. adopted a DCC grafting system to synthesize gallic acid acylated chitooligosaccharide and verified that it has a more enhanced inhibitory effect against allergic reactions in RBL-2H3 mast cells than COS [21]. Chen et al. prepared gallic acid grafted carboxymethyl chitosan through an ascorbic acid/hydrogen peroxide initiated graft copolymerization reaction and proved it can notably modulate intestinal microcirculation [22]. Sun et al. prepared 14 phenolic acid COS derivatives using seven phenolic acids and demonstrated that the derivatives had stronger antioxidant activity than COS [23]. Dai et al. used gallic acid to synthesize gallate-COS via carbodiimide and proved it had obvious antioxidant activity [24]. Mi et al. selected eight organic acids (cumaric acid, ascorbic acid, ferulic acid, p-coumaric acid, caffeic acid, gallic acid, salicylic acid, hydroxybenzoic acid) and synthesized eight hydroxypropyltrimethyl ammonium chitosan derivatives by the ion exchange method. The antioxidant activity test demonstrated these derivatives had dramatic enhancements in free radical scavenging activity [25]. Xing et al. prepared several organic acid COS salts by microwave method and tested their effect on NO secretion of macrophages. The results demonstrated that different salt chitooligosaccharides had different effects on promoting NO secretion [26]. To sum up, phenolic acid grafted chitosan or COS used to prepare new compounds can further enhance their biological activities, and the new compounds have great application potential. Moreover, quaternized chitosan is a widely used chitosan derivative. Because of the increased positive charge density, the quaternized chitosan has much better biocompatibility, solubility, antioxidant and antibacterial activities than chitosan [27]. Therefore, we speculate that the biological activity of derivatives prepared by quaternizing COS and grafting phenolic acids could also be improved.

In this study, we designed two synthetic routes and chose seven phenolic acids to prepare quaternized chitooligosaccharide phenolic acid derivatives. First, the *N,N,N*-trimethylated chitooligosaccharide phenolic acid salt derivatives were synthesized by ion exchange methods: the amino group of COS was first quaternized and then different phenolic acids were introduced through ion exchange. Seven derivatives were synthesized successfully: *N,N,N*-trimethylated chitooligosaccharide gallic acid salt (GLTMC), *N,N,N*-trimethylated chitooligosaccharide ferulic acid salt (FUTMC), *N,N,N*-trimethylated chitooligosaccharide *p*-coumaric acid salt (CMTMC), *N,N,N*-trimethylated chitooligosaccharide caffeic acid salt (CFTMC), *N,N,N*-trimethylated chitooligosaccharide protocatechuic acid salt (PCTMC), *N,N,N*-trimethylated chitooligosaccharide sinapic acid salt (SPTMC), *N,N,N*-trimethylated chitooligosaccharide salicylic acid salt (SYTMC). Second, the phenolic acid esterified *N,N,N*-trimethylated chitooligosaccharides were synthesized by the CDI catalytic system: the carboxyl group of phenolic acids was catalyzed by CDI and then reacted with the hydroxyl group of *N,N,N*-trimethylated chitooligosaccharide to form an ester bond. Seven derivatives were finally synthesized: gallic acid esterified *N,N,N*-trimethylated chitooligosaccharide (GL-TMC), ferulic acid *N,N,N*-trimethylated esterified chitooligosaccharide (FU-TMC), *p*-coumaric acid esterified *N,N,N*-trimethylated chitooligosaccharide (CM-TMC), caffeic acid esterified *N,N,N*-trimethylated chitooligosaccharide (CF-TMC), protocatechuic acid esterified *N,N,N*-trimethylated chitooligosaccharide (PC-TMC), sinapic acid esterified *N,N,N*-trimethylated chitooligosaccharide (SP-TMC) and salicylic acid esterified *N,N,N*-trimethylated chitooligosaccharide (SY-TMC). The structures and thermal stability of these derivatives were characterized by FT-IR, $^1$H NMR spectra and thermal analysis methods. The degree of substitution in derivatives was also calculated and analyzed by $^1$H NMR spectra. Moreover, the antioxidant activity of these derivatives was evaluated by the DPPH radical scavenging activity, superoxide radical scavenging activity, the hydroxyl radical scavenging activity and the reducing power experiments in vitro. Antifungal and antibacterial assay experiments were also implemented to detect the antimicrobial activities of derivatives. In addition, the cytotoxicity of derivatives was tested by L929 cells using the MTT method in vitro. This study may provide a novel method to synthesize COS phenolic acid derivatives, and the new green substances prepared in this paper can serve as antimicrobial or antioxidant agents for use in many fields.

## 2. Results and Discussion

### 2.1. Chemical Synthesis and Characterization

The synthesis procedure for phenolic acid TMC salt derivatives is shown in Route 1 of Scheme 1. In the first step of the reaction, in the presence of NaI and NaOH, TMCI was formed by the COS and $CH_3I$ reaction. In the second step of the reaction, phenolic acids reacted with NaOH and formed a carboxylate anion. After TMCI was added, the carboxylic acid anion of phenolic acid replaced $I^-$ and combined with the dissociated TMC cation by electrostatic attraction through ion exchange to form the desired products [28].

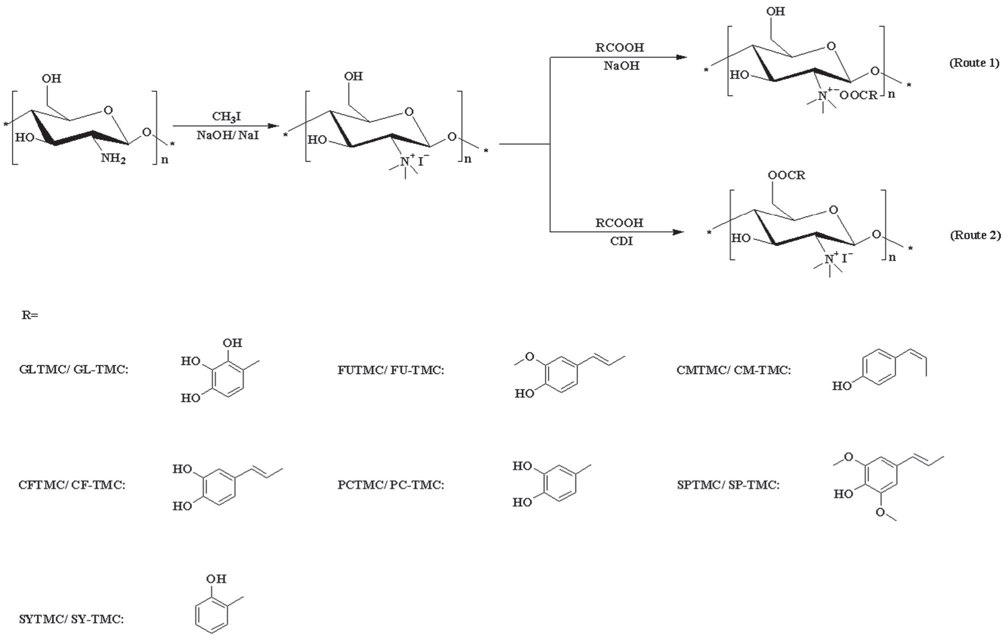

**Scheme 1.** Synthesis routes for phenolic acid COS derivatives.

The synthesis procedure for the phenolic acid esterified TMC derivatives is shown in Route 2 of Scheme 1. CDI is an imidazole derivative with high reactive activity due to the structure of double heterocycles. Herein, CDI reacted with the carboxyl groups in phenolic acids to form carbonyl imidazole. After TMCI was added, carbonyl imidazole reacted with the hydroxyl group of TMCI to form an ester bond; thus, the desired products were obtained [29,30].

### 2.2. FT-IR Spectra

The FT-IR spectra of the TMC phenolic acid salt derivatives are shown in Figure 1a. As exhibited in the figure, for COS, the wavenumber of 3395 $cm^{-1}$ can be attributed to the O-H and N-H bending, and the 2924 $cm^{-1}$ wavenumber is the stretching vibration of O-H. The band at 1582 $cm^{-1}$ represents the amino group and the characteristic peak at 1415 $cm^{-1}$ is the deformation vibration of $-CH_2$ and $-CH_3$. The absorption peak at 1084 $cm^{-1}$ is the C-O-C stretching vibration [31]. For TMCI, a new spike appearing at 1472 $cm^{-1}$ can be attributed to the $-N^+(CH_3)_3$, and the absorbance at 1644 $cm^{-1}$ can be assigned to the band of $N-CH_3$ [32]. This demonstrates the successful synthesis of the TMCI derivatives. Moreover, for the TMC phenolic acid salt derivatives, the spikes at 1470 $cm^{-1}$ and 1640 $cm^{-1}$ are obvious, which prove the presence of $N^+(CH_3)_3$. In addition, the new spikes at 1549, 1516, 1554, 1554, 1553, 1554, 1504, 1596 and 1589 $cm^{-1}$ of GLTMC, FUTMC, CMTMC, CFTMC, PCTMC, SPTMC and SYTMC can be attributed to the characteristic absorption of the C-C stretching vibration of the benzene ring [33]. Meanwhile, the peaks appearing at GLTMC (740, 798 $cm^{-1}$), FUTMC (702, 820, 852 $cm^{-1}$), CMTMC (721, 800 $cm^{-1}$), CFTMC (706, 820 $cm^{-1}$), PCTMC (790, 897 $cm^{-1}$), SPTMC (723, 828 $cm^{-1}$) and SYTMC (766, 813 $cm^{-1}$) are the C-H out-of-plane bending vibrations of the benzene ring [34]. Comprehensively, the FT-IR spectra characterization primarily demonstrates that the derivatives were successfully synthesized.

The FT-IR spectra of phenolic acid esterified TMC derivatives are shown in Figure 1b. It can be seen that the derivatives retain the characteristic absorption of COS and TMCI. The reaction displays an obvious characteristic spike around 1720 $cm^{-1}$, which can be attributed to the C=O stretching vibration of the ester bond. And the absorption at 1280–1050 $cm^{-1}$ can be assigned to the C-O-C stretching vibration of the ester bond, which proves the successful synthesis of esterified derivatives. Furthermore, the spikes at 1555 (GL-TMC), 1508 (FU-TMC), 1506 (CM-TMC), 1554 (CF-TMC), 1555 (PC-TMC), 1504 (SP-TMC) and 1613 $cm^{-1}$ (SY-TMC) represent the skeleton vibration absorption peak of the benzene ring, and the spikes at 700–850 $cm^{-1}$ represent the C-H out-of-plane bending vibration absorption peak of the benzene ring. Therefore, the characteristic absorptions demonstrate the successful introduction of phenolic acids.

### 2.3. $^1H$ NMR Spectra

In order to further determine the structures of the products, $^1H$ NMR spectra were implemented in this study and the results are shown in Figure 2. The chemical shift at δ 4.79 ppm of the products can be attributed to the $D_2O$ solvents. The chemical shift at δ 2.50 ppm of the products can be attributed to the DMSO solvents. In addition, the characterization of unmodified COS is as follows: the δ 4.48 ppm can be attributed to [H1], δ 2.69 ppm is [H2] and δ 3.21–4.08 ppm is [H2]-[H6]. As for TMCI, there is an obvious signal at δ 3.22 ppm, which can be assigned to the $N^+(CH_3)_3$ bond [35]. After the reaction with the phenolic acids, the $^1H$ NMR spectra of the derivatives obviously changes. The new shifts appearing at δ 6.0–9.0 ppm prove the successful synthesis of COS phenolic acid derivatives.

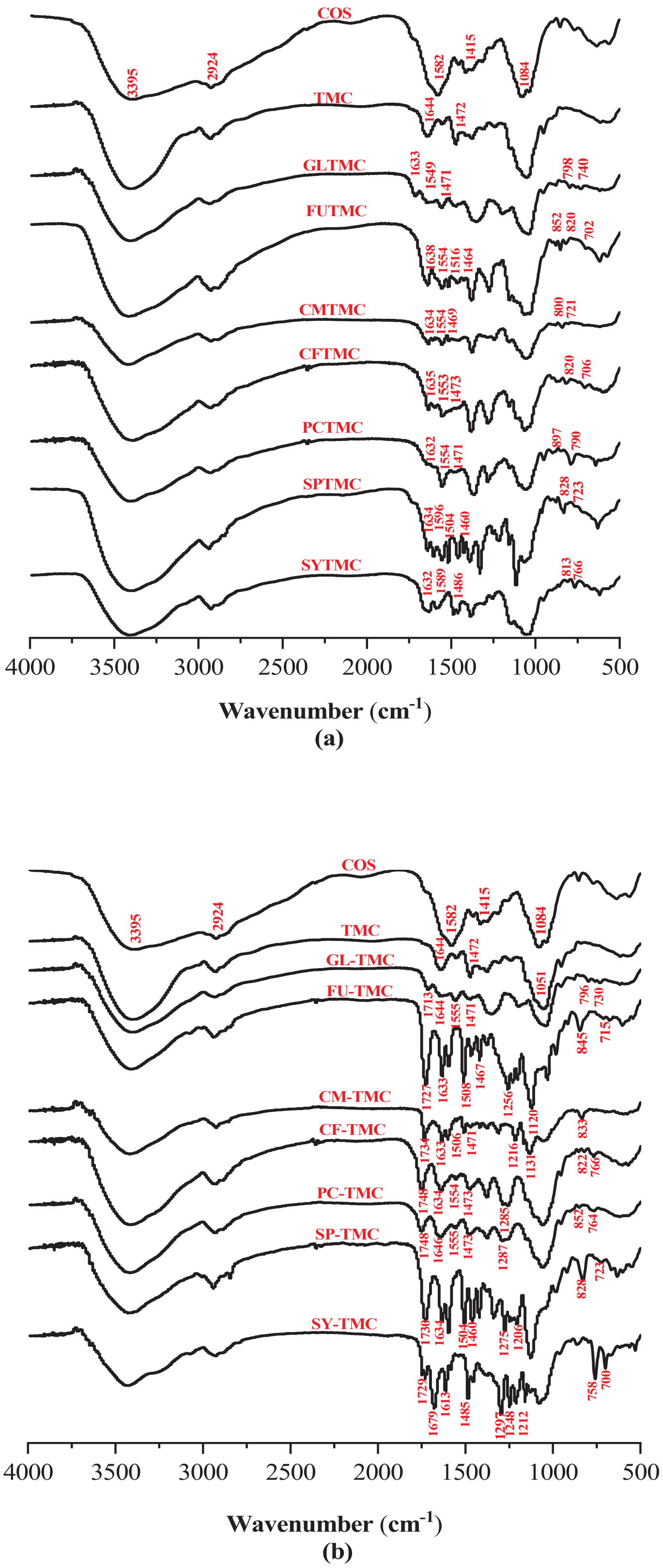

**Figure 1.** (**a**) FT-IR spectra of COS, TMCI and TMC phenolic acid salt derivatives; (**b**) FT-IR spectra of COS, TMCI and phenolic acid esterified TMC derivatives.

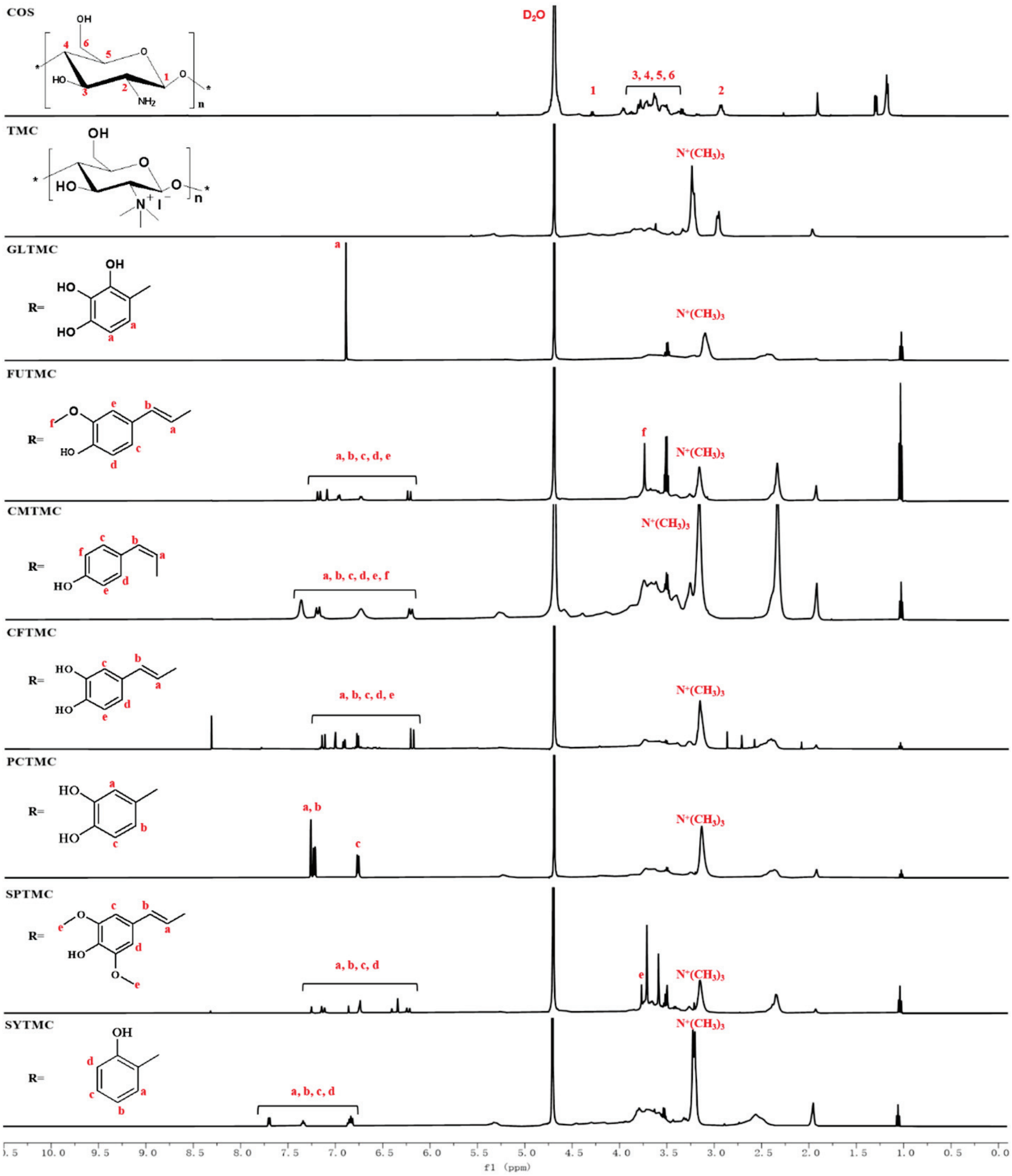

(**a**)

**Figure 2.** *Cont.*

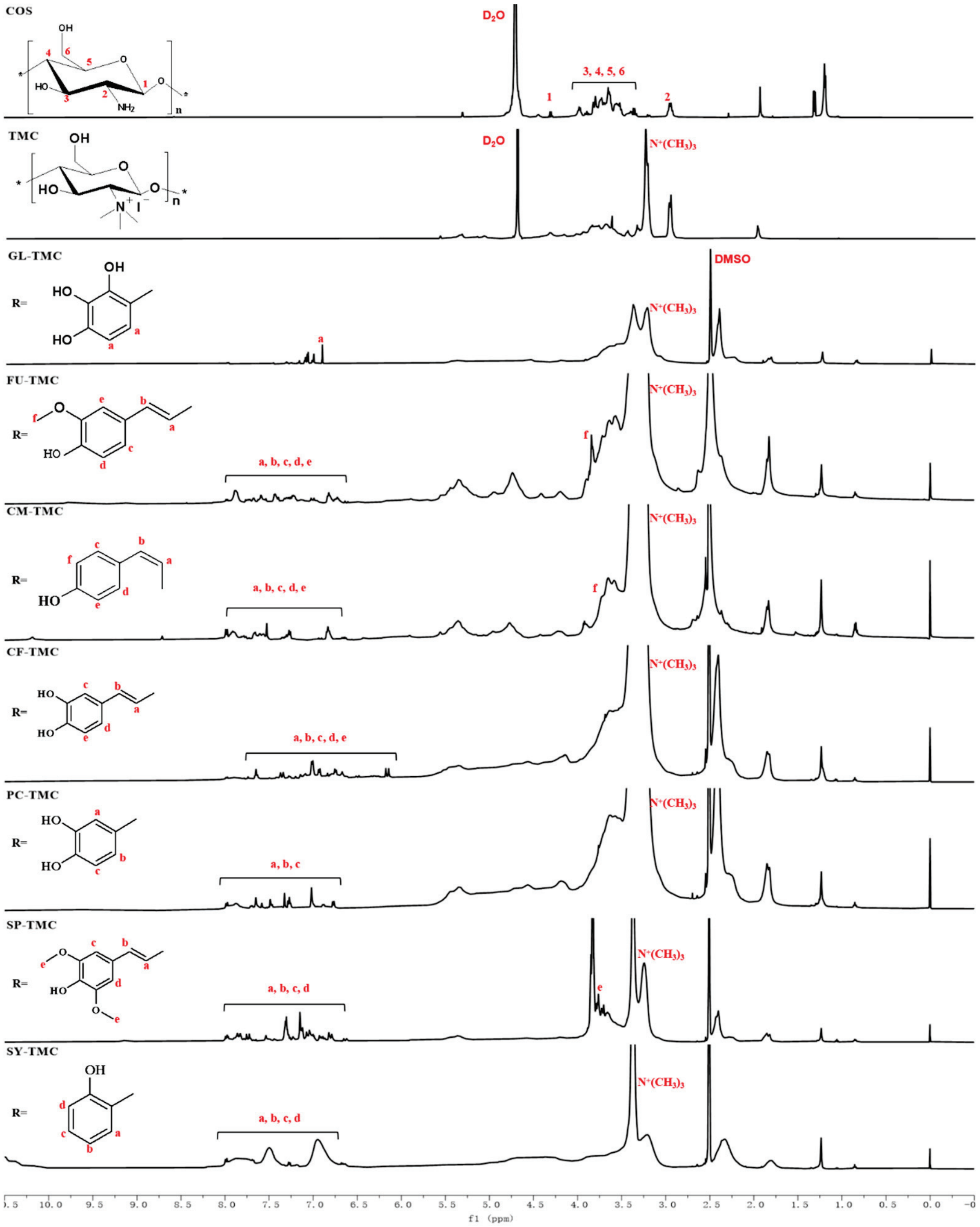

(**b**)

**Figure 2.** (**a**) $^1$H NMR spectra of COS, TMCI and TMC phenolic acid salt derivatives; (**b**) $^1$H NMR spectra of COS, TMCI and phenolic acid esterified TMC derivatives.

### *2.4. Yields and the DS of Chitosan Derivatives*

After obtaining the desired products, we calculated their yields, and the result is shown in Table 1. In addition, according to the $^1$H NMR spectra, the [H1] of COS was chosen as the integral standard peak and the DS of each derivative was determined by the ratio of the peak area. The result is also shown in Table 1.

**Table 1.** The yields and DS of COS derivatives.

| Compounds | Yields (%) | DS (%) | Compounds | Yields (%) | DS (%) |
|---|---|---|---|---|---|
| COS | - | - | TMC | 78.57 | 94.88 |
| GLTMC | 86.47 | 80.00 | GL-TMC | 58.96 | 32.00 |
| FUTMC | 24.20 | 66.00 | FU-TMC | 39.42 | 43.00 |
| CMTMC | 20.40 | 51.00 | CM-TMC | 32.40 | 41.00 |
| CFTMC | 68.97 | 54.00 | CF-TMC | 59.88 | 15.00 |
| PCTMC | 44.49 | 36.00 | PC-TMC | 53.16 | 12.00 |
| SPTMC | 65.42 | 46.00 | SP-TMC | 64.34 | 47.00 |
| SYTMC | 73.60 | 41.00 | SY-TMC | 73.40 | 43.00 |

### *2.5. Thermal Gravimetric Analysis (TGA) and Derivative Thermogravimetry (DTG)*

With the temperature ranging from 25 to 700 °C, COS had three mass loss steps (Figure 3). The first stage in the range of 30–100 °C with about 8% weight loss was mainly caused by the evaporation of water. And the second stage from 100–200 °C with 17.80% weight loss was caused by the decomposition of the amine and hydroxyl group [36]. The third weight loss in the range of 200–700 °C was mainly caused by the decomposition of the saccharide rings [37]. The final weight loss of COS was about 70.90% of the initial weight. As for the derivatives, it can be seen from the figure that the decomposition temperature of the derivatives was higher compared with COS. In the first stage of 25–200 °C, they obviously showed more stability and less weight loss. In the stage of 200–700 °C, the decomposition rate of derivatives was lower than COS, which demonstrated the better thermal stability. The reason may be that after being introduced into the COS, the phenolic acid formed a hydrogen bond with COS, which strengthened the thermal stability of derivatives. The quaternary ammonium group and the amide group also enhanced the thermal stability of the derivatives. The final mass loss of each derivative was as follows: TMC: 75.80%, GLTMC: 71.74%, FUTMC: 50.1167%, CM-TMC: 63.14%, CFTMC: 66.16%, PCTMC: 69.32%, SPTMC: 50.90%, SYTMC: 71.08%, GL-TMC: 67.02%, FU-TMC: 73.30%, CM-TMC: 69.09%, CF-TMC: 74.81%, PC-TMC: 73.14%, SP-TMC: 70.94%, SY-TMC: 62.66%.

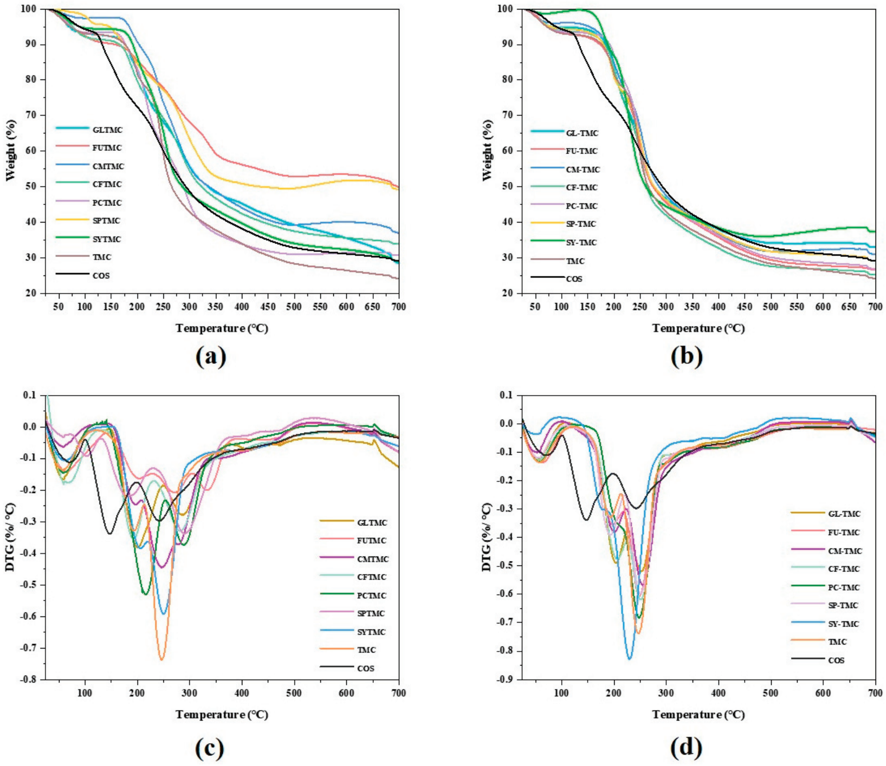

**Figure 3.** TGA (**a**,**b**) and DTG (**c**,**d**) curves of COS and its derivatives.

### *2.6. Antioxidant Activity*

#### 2.6.1. Scavenging Ability of the DPPH Radical

1,1-Diphenyl-2-picryl-hydrazyl (DPPH), as a nitrogen-centered synthetic radical with a lone pair of electrons, is one of the most common free radicals used to detect the antioxidant activity of substances. As a stable radical, DPPH radical ethanol solution is purple and has a maximum absorption wavelength at 517 nm. When added to the solution, antioxidants can deliver electrons or hydrogen to DPPH to generate the DPPH-H compound, which is more stable, and the color of the solution turns yellow. The degree of discoloration of the solution is quantitatively related to the number of electrons it accepts. The smaller the absorbance is, the stronger the antioxidant capacity of the substance is [38].

The DPPH radical scavenging activity of all products is concentration-related (Figure 4a,b). For TMC phenolic acid salt derivatives, it can be observed that the GLTMC, CMTMC, CFTMC, PCTMC, and SYTMC derivatives had obviously enhanced scavenging activity over COS within the range of tested concentrations. And GLTMC had the highest scavenging activity among these derivatives, achieving nearly 100%. So GLTMC is a potentially suitable antioxidant for DPPH radicals. As for FUTMC and SPTMC, at the concentration of 0.10 mg/mL, their scavenging effect reached more than 70%. But with the augmenting of concentration, the scavenging effect declined, and the possible reason may be as follows: with the increase in concentration, the color of the solution gradually deepened, which made its absorbance increase and the scavenging effect decline. As for phenolic acid esterified TMC derivatives, the DPPH radical scavenging activity of all products increased in a dose-dependent manner (Figure 4b). After being modified with phenolic acids, the DPPH radical scavenging activity of COS derivatives was significantly increased. Comprehensively, at the concentration of 1.60 mg/mL, the order of the DPPH radical scavenging activity of derivatives can be ranked as follows: VC > SY-TMC > SP-TMC > GL-TMC > PC-TMC > FU-TMC > CF-TMC > CM-TMC.

#### 2.6.2. Scavenging Ability of Superoxide Radical

A superoxide anion is formed in almost all aerobic cells and is harmful to cellular components as a precursor to more active oxides. Superoxide anion radicals are more dangerous because they have a longer life span and can travel over greater distances than other oxygen radicals [39]. Therefore, it is necessary to develop antioxidants that can effectively scavenge this free radical. In this study, the NADH-PMS-NBT system was used in the superoxide radical scavenging assay experiment. In the presence of NADH and oxygen the in air, PMS can react with them and form a superoxide anion radical. Then the superoxide anion radical reacts with NBT to generate blue substances, which cause the solution to reach the maximum absorption wavenumber at 520 nm. But if there are antioxidants in the system, the superoxide anion radicals will react with the antioxidants first and the solvent will not turn blue, thus the absorbance at 520 nm will decrease. The smaller the absorbance of the solvent, the stronger the superoxide radical scavenging activity [39].

The superoxide radical scavenging ability of the samples is shown in Figure 4c,d. Several conclusions can be drawn from the figure. First, with the increase in concentration, the scavenging activity of all samples was enhanced. Moreover, for the phenolic acid TMC salt derivatives, all derivatives had a higher scavenging effect at the concentrations of 0.10, 0.20, 0.40 and 0.80 mg/mL. GLTMC and CFTMC in particular had outstanding scavenging effects, which reached 100%. The superoxide radical scavenging activity result of phenolic acid esterified TMC derivatives was similar to the salt derivatives. Compared to COS, the antioxidant activity of these derivatives was obviously enhanced. Moreover, among these derivatives, GL-TMC, CF-TMC and PC-TMC had significantly higher antioxidant activity than COS at all tested concentrations and could be developed into excellent antioxidants. The order of the scavenging activity at the concentration of 0.80 mg/mL can be sorted as follows: GLTMC = CFTMC = GL-TMC > CF-TMC > PCTMC > SPTMC > FUTMC > PC-TMC > CM-TMC > SY-TMC > SP-TMC > FU-TMC > CMTMC > SYTMC > TMC > COS. The analysis demonstrates the effective modification of the phenolic acids.

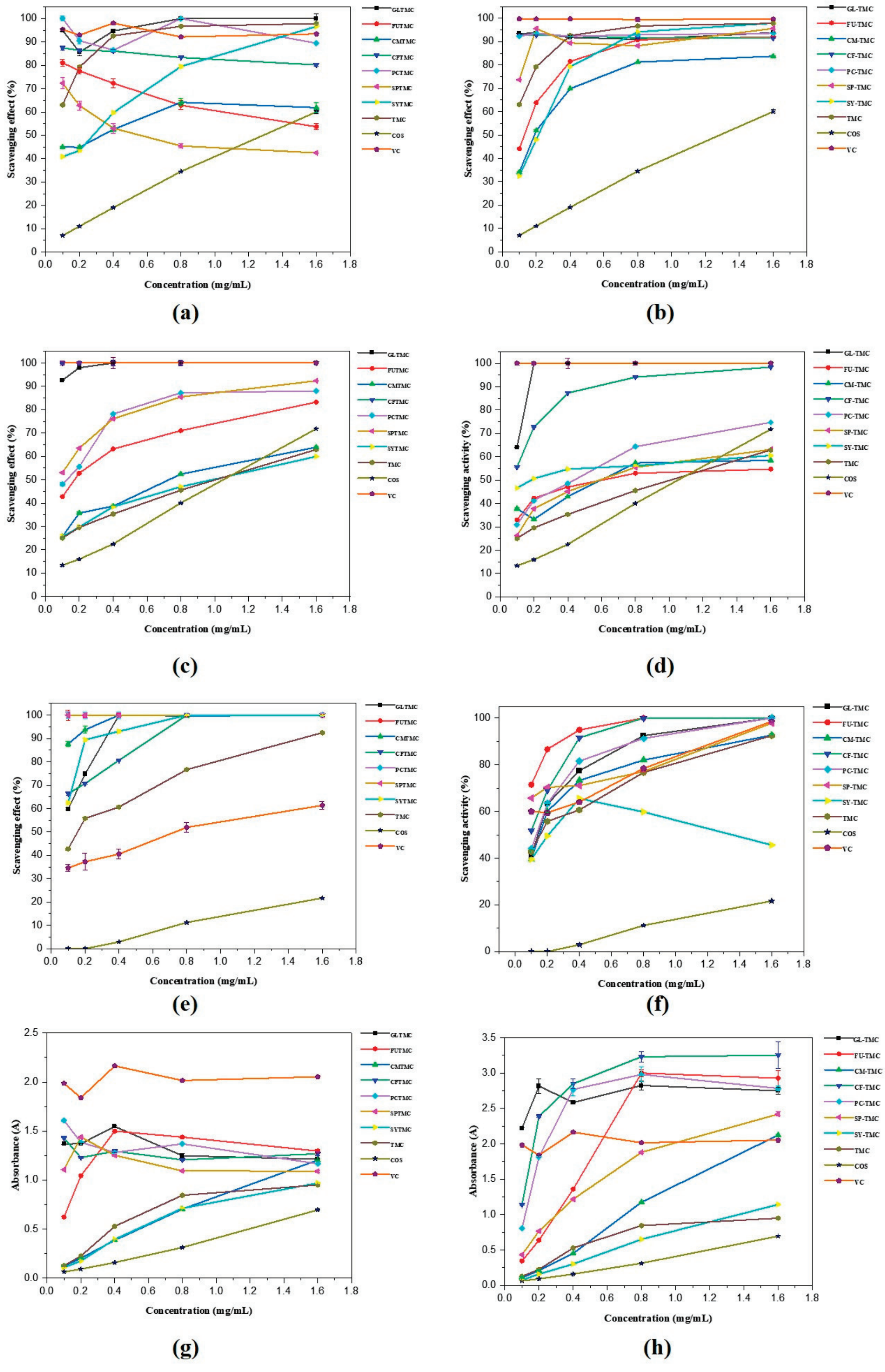

**Figure 4.** Antioxidant activity of COS and its derivatives: DPPH radical scavenging activity (**a**,**b**); Superoxide radical scavenging activity (**c**,**d**); Hydroxyl radical scavenging activity (**e**,**f**); and reducing power (**g**,**h**).

### 2.6.3. Scavenging Ability of Hydroxyl Radical

The hydroxyl radical is the most reactive free radical, which can react with non-selective compounds such as proteins, nucleic acids, unsaturated fatty acids and almost all biofilms. It can cause damage to macromolecules and organisms [40]. The hydroxyl radical scavenging activity of the samples is shown in Figure 4e,f. As we can see from the figure, augmentation of scavenging activity was identified for all the samples at increasing concentrations. COS had the lowest scavenging effect, which was only 21.66% at the concentration of 1.60 mg/mL. And the scavenging activity of all the derivatives was obviously enhanced at the tested concentrations compared to COS. For example, the scavenging activity of GLTMC reached 100% at the concentration of 0.40 mg/mL.

#### 2.6.4. Reducing Power

Reducing power is usually used to measure the electron-donating capacity of substances, which is also a manifestation of their antioxidant activity [41]. Here the tested system consisted of ferric ions ($Fe^{3+}$). When substances with reducing power are added to the test system, they deliver electrons to $Fe^{3+}$ and are reduced to $Fe^{2+}$. As a result, the color of the solution turns green and has the largest absorbance at a wavelength of 700 nm. The greener the color of the solution, the greater the absorbance value, which represents the stronger reducing power of the substance [42]. So, as the result shows (Figure 4g,h), most of the derivatives had higher absorbance than the COS at tested concentrations, which means a stronger reducing power than COS. On the whole, the reducing power of the derivatives at 1.60 mg/mL concentration can be ranked as follows: CF-TMC > FU-TMC > PC-TMC > GL-TMC > SP-TMC > CM-TMC > VC > FUTMC > CFTMC > GLTMC > CMTMC > PCTMC > SY-TMC > SPTMC > SYTMC > TMC > COS.

In this part, the antioxidant activity of products was measured in vitro by testing the scavenging activity of the DPPH radical, superoxide radical, hydroxyl radical and reducing power. As the above result shows, the antioxidant activity of both the TMC phenolic acid salt derivatives and the phenolic acid esterified TMC derivatives was increased to some extent compared with COS. This demonstrated the significant modification of phenolic acids into COS. Additionally, it can be seen that among these derivatives, GLTMC and GL-TMC had the strongest antioxidant activity, which proves that the number of hydroxyl groups is the key factor that determines the antioxidant activity of phenolic acids. The antioxidant activity of phenolic acids increases with the increase in the hydroxyl group number [43]. Moreover, the structural differences of phenolic acids also affect their antioxidant activity. The existence of the C=C bond in phenolic acids can make the formed free radicals more stable through the resonance effect. And the presence of the methoxy group is also beneficial to improving the antioxidant activity of phenolic acids [44]. So the CFTMC and CF-TMC have much higher antioxidant activity. Furthermore, quaternized COS with positive charges can react with free radicals and is also beneficial to improving the antioxidant activity. Therefore, through this part of experiment, we screened several derivatives with excellent antioxidant activity, which we hope to further develop into new antioxidants.

### *2.7. Antibacterial Activity*

With the progress in science and technology and the exploration of human diseases, many antimicrobial drugs have been developed and utilized for humans, which have greatly improved the cure rate of diseases and are beneficial to human health. But because of enhanced bacterial resistance, existing antibacterial agents are facing a serious challenge. Development of novel antibacterial drugs is still a big challenge for humans. *E. coli* is a common Gram-negative bacterium that is widely found in the intestinal tract and other sites in human and animals. Studies have shown that *E. coli* can cause many diseases such as diarrhea, dysentery, urinary tract infection, meningitis and sepsis [45]. *S. aureus* is a typical Gram-positive bacterium that can cause infections and many diseases, seriously threatening human physical health [46]. In this part, we selected these two kinds of pathogenic bacteria and detected the antibacterial activity of COS and its derivatives. The result is shown in Tables 2 and 3.

**Table 2.** The antibacterial activity of COS, TMCI and TMC phenolic acid salt derivatives.

| **Bacterial Species** | | **Samples** | | | | | | | | |
|---|---|---|---|---|---|---|---|---|---|---|
| | | **COS** | **TMC** | **GLTMC** | **FUTMC** | **CMTMC** | **CFTMC** | **PCTMC** | **SPTMC** | **SYTMC** |
| ***S. aureus*** | **MIC (mg/mL)** | >8 | >8 | 0.5 | 0.25 | 0.5 | 0.25 | 0.25 | 0.25 | 2 |
| | **MBC (mg/mL)** | >8 | >8 | 1 | 0.5 | 1 | 0.5 | 0.5 | 0.5 | 4 |
| ***E. coli*** | **MIC (mg/mL)** | >8 | >8 | 0.25 | 1 | 0.0625 | 0.5 | 1 | 0.5 | >8 |
| | **MBC (mg/mL)** | >8 | >8 | 0.5 | 2 | 0.125 | 1 | 2 | 1 | >8 |

**Table 3.** The antibacterial activity of COS, TMCI and phenolic acid esterified TMC derivatives.

| **Bacterial Species** | | **Samples** | | | | | | | | |
|---|---|---|---|---|---|---|---|---|---|---|
| | | **COS** | **TMC** | **GL-TMC** | **FU-TMC** | **CM-TMC** | **CF-TMC** | **PC-TMC** | **SP-TMC** | **SY-TMC** |
| ***S. aureus*** | **MIC (mg/mL)** | >8 | >8 | 4 | 0.25 | 0.125 | 0.25 | 2 | 1 | 0.25 |
| | **MBC (mg/mL)** | >8 | >8 | 8 | 0.5 | 0.25 | 0.5 | 4 | 2 | 0.5 |
| ***E. coli*** | **MIC (mg/mL)** | >8 | >8 | 0.125 | 0.125 | 0.03125 | 0.5 | 1 | 0.5 | 0.25 |
| | **MBC (mg/mL)** | >8 | >8 | 0.25 | 0.25 | 0.0625 | 1 | 2 | 1 | 0.5 |

Several conclusions can be drawn from the data in Tables 2 and 3. First, COS and TMCI showed no antibacterial activity. However, after being characterized by phenolic acids, the antibacterial activity of the derivatives was greatly enhanced. Second, the antibacterial activity of different COS phenolic acid derivatives was different. Moreover, the inhibition activity of derivatives against *S. aureus* and *E. coli* was different. For example, the MIC value of GL-TMC against *S. aureus* was 4 mg/mL while against *E. coli* it was 0.125 mg/mL. The possible reason is the difference in the cell wall between *S. aureus* and *E. coli*. Furthermore, among these derivatives, CMTMC and CM-TMC exhibited the best antibacterial activity.

### *2.8. Antifungal Analysis*

*B. cinerea* is a widely host-borne plant fungus that causes a variety of Botrytis cinerea diseases. It can infest the rhizomes, leaves, flowers and fruits of plants and can be pathogenic at all times of growth. It can cause more than 500 plant pathologies, affecting many economically valuable crops and causing great losses in the postharvest stage of plants. It is one of the most extensively studied necroptotic pathogens [47]. Figure 5a shows the TMC phenolic acid salt derivative inhibitory index of *B. cinerea*. As we can see, carbendazim had the optimal inhibitory effect, where the inhibitory index reached 100%. COS had the lowest inhibitory effect, which was only 25.65% at the concentration of 1.0 mg/mL. As for the derivatives, all the inhibitory indexes were obviously enhanced compared with COS. At the concentration of 0.1 mg/mL, the inhibitory index of the samples can be ranked as follows: SPTMC 48.95%, FUTMC 45.23%, GLTMC 44.17%, SYTMC 41.19%, CFTMC 40.99%, TMC 40.46%, CMTMC 39.73%, PCTMC 37.96%, COS 0.0%. The antifungal activity of the phenolic acid esterified TMC derivatives is shown in Figure 5b. Similar to the TMC phenolic acid salt derivatives, all the derivatives had more enhanced inhibitory activity than COS. Specifically among these derivatives, CM-TMC and SY-TMC presented outstanding inhibitory activity, achieving 85.49% and 89.71%, respectively.

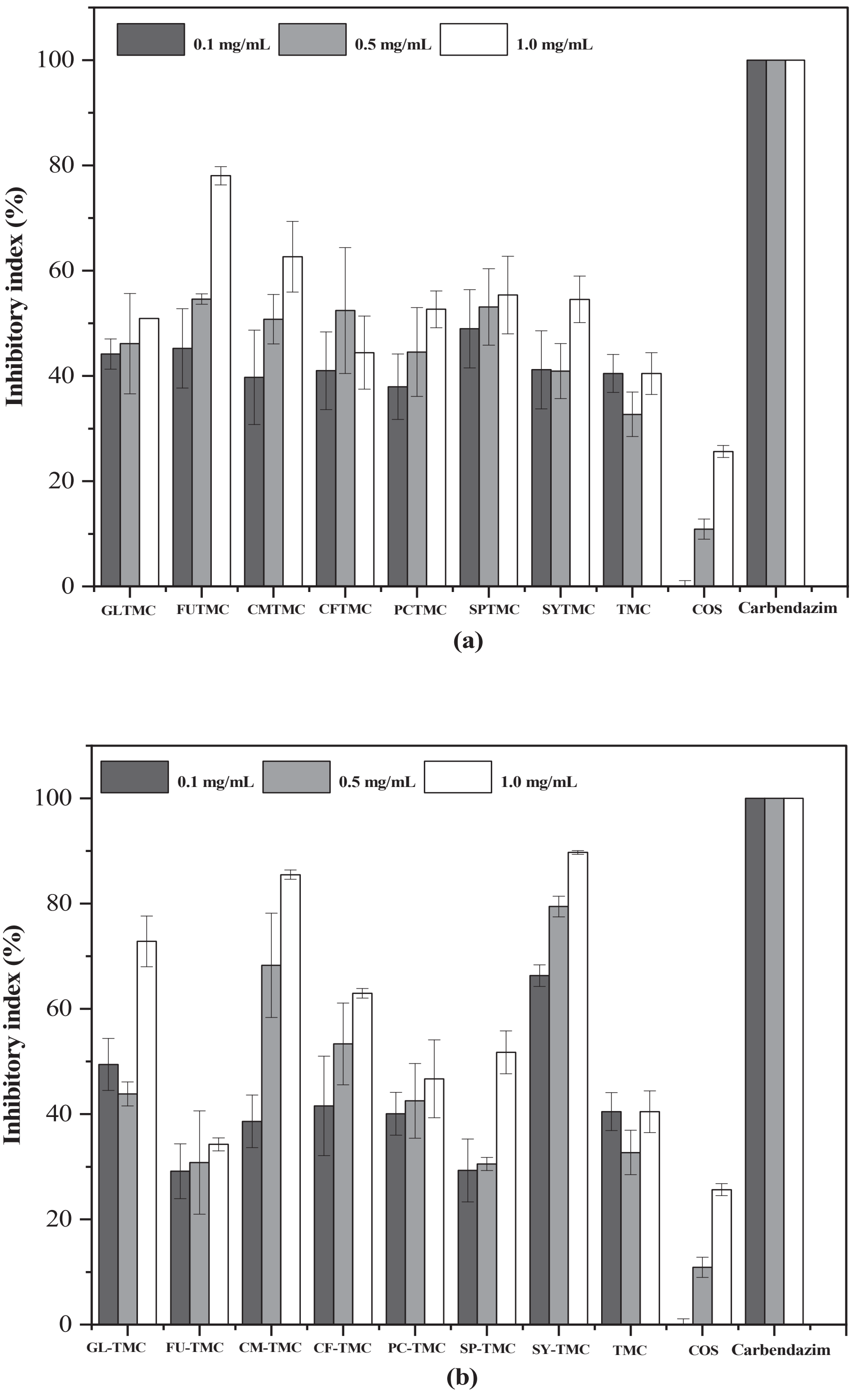

**Figure 5.** *Cont*.

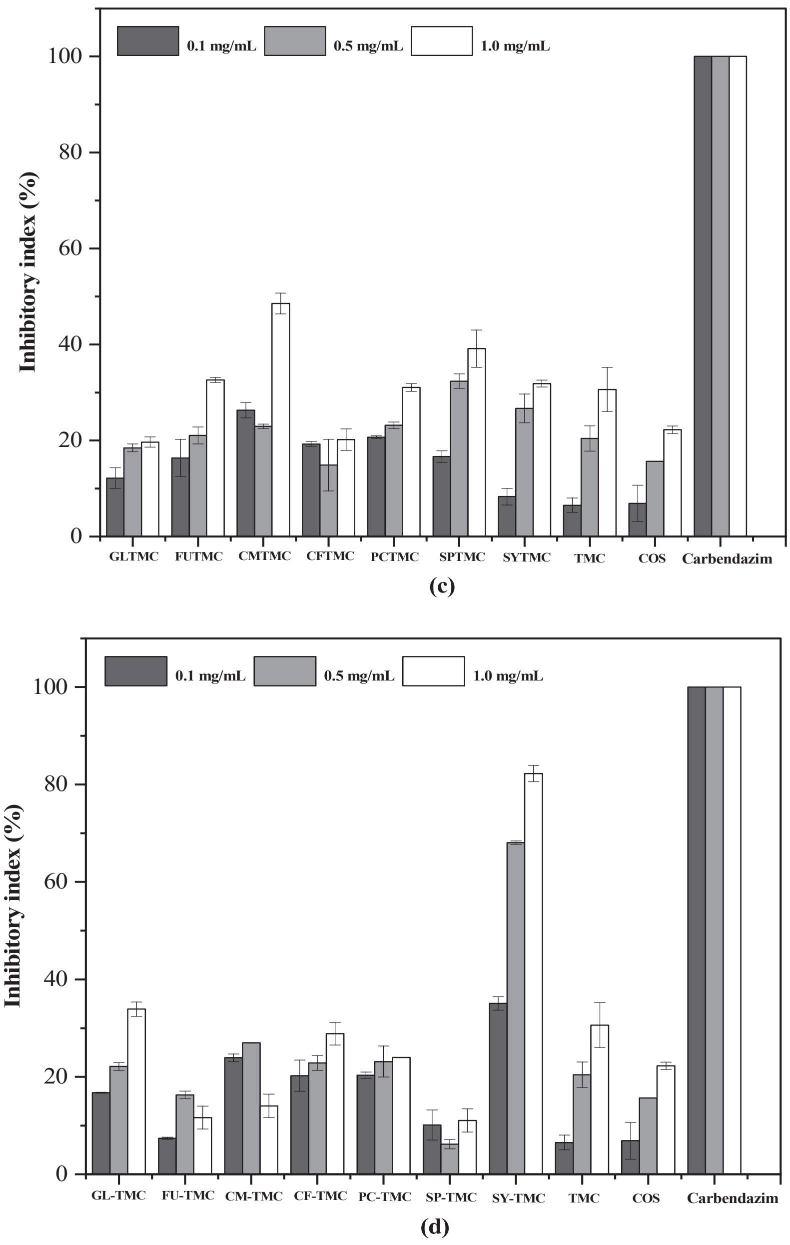

**Figure 5.** The antifungal activity of carbendazim, COS and its derivatives against *Botrytis cinerea* (**a**,**b**) and *Gibberella saubinetii* (**c**,**d**).

*F. graminearum*, once ranked as one of the top 10 phytopathogenic fungi worldwide, can cause diseases of wheat. Not only does it cause severe wheat yield loss, but its production of mycotoxins can also contaminate cereals, leading to poor grain quality. It causes immune function to decline after human and animal ingestion, causing acute or chronic poisoning, which can seriously harm zoonotic health [48]. The antifungal activity of COS phenolic acid derivatives against *F. graminearum* is shown in Figure 5c,d. As shown in the figure, carbendazim had the best inhibitory activity. The inhibitory index of COS at the concentrations of 0.1, 0.5 and 1.0 mg/mL was 6.86%, 15.24% and 22.86%, respectively. Compared to COS, the derivatives were increased in different degrees. For instance, at the concentration of 1.0 mg/mL, the inhibitory index of each derivative was as follows: GLTMC: 19.67%, FUTMC: 32.62%, CMTMC: 48.54%, CFTMC: 20.19%, PCTMC: 30.04%, SPTMC: 39.13%, SYTMC: 31.85%, GL-TMC: 33.90%, FU-TMC: 11.61%, CM-TMC: 14.01%, CF-TMC: 28.87%, PC-TMC: 23.60%, SP-TMC: 11.03%, SY-TMC: 82.25%, TMC: 30.62%. It can be seen from the data that the antifungal activities of different COS phenolic acid derivatives were different, and the activity of SY-TMC was the most significantly improved. The antifungal activity experiment demonstrated that the introduction of phenolic acids can effectively improve the antifungal activity of COS.

### *2.9. Cytotoxicity Analysis*

The cytotoxicity of COS phenolic acid derivatives is shown in Figure 6a. As we can see from the figure, when the concentration of the derivatives varied from 62.5, 125, 250, 500 to 1000 μg/mL, the FUTMC, PCTMC and SYTMC derivatives showed a high cell viability, which proves that these derivatives have low cytotoxicity and good biocompatibility. As for other derivatives, CMTMC, CFTMC and SPTMC had high cell viability at concentrations of 62.5, 125, 250 and 500 μg/mL. GLTMC showed an obvious tendency of increasing cytotoxicity with the increase in concentration. The cytotoxicity of phenolic acid esterified TMC derivatives is shown in Figure 6b. It can be observed that FU-TMC, CMTMC, CFTMC and SP-TMC had high cell viability at all tested concentrations. And GL-TMC, SY-TMC had high cell viability at the concentrations of 62.5, 125, 250 and 500 μg/mL, which proves their low cytotoxicity and good biocompatibility. Furthermore, the cell viability of GL-TMC, PC-TMC and SY-TMC showed a descending trend with the increase in concentration. Totally speaking, through this part of the experiment, we screened several derivatives with high antioxidant, antibacterial and antifungal activity and good biocompatibility.

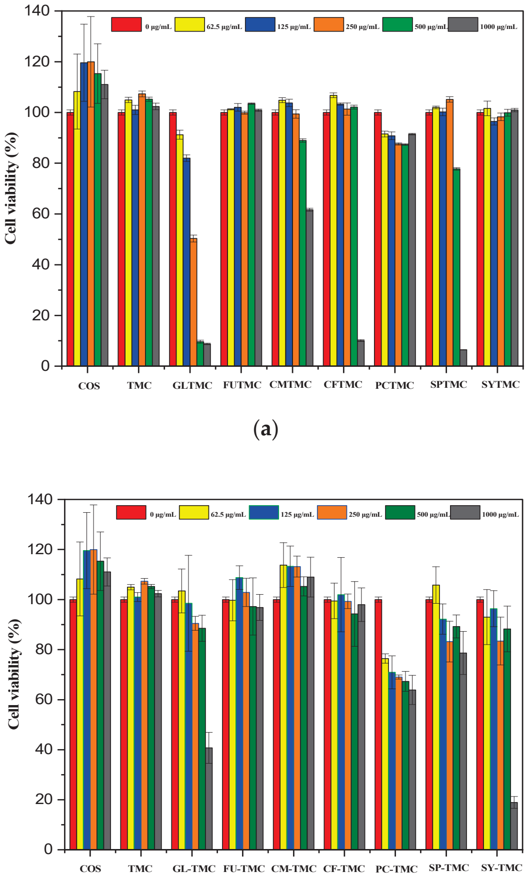

(**a**)

(**b**)

**Figure 6.** (**a**) the cytotoxicity of COS, TMCI and TMC phenolic acid salt derivatives; (**b**) the cytotoxicity of COS, TMCI and phenolic acid esterified TMC derivatives.

## 3. Materials and Methods

### 3.1. Materials

Chitooligosaccharide (molecular weight of 2000 Da, deacetylation degree of 95%) was purchased from Shandong Weikang Biomedical Technology Co., Ltd. (Linyi, China). L929 cells (GDC0034) were obtained from the China Center for Type Culture Collection. Gallic acid monohydrate, ferulic acid, *p*-coumaric acid, caffeic acid, protocatechuic acid, sinapic acid, salicylic acid, *N,N′*-Carbonyldiimidazole (CDI), sodium hydroxide 1-Methyl-2-pyrrolidinone (NMP) and other used chemical reagents were provided by Sigma-Aldrich Chemical Corp. (Shanghai, China). All chemical reagents were of analytical grade and no further purification was required.

### 3.2. Chemical Synthesis of COS Derivatives

#### 3.2.1. Synthesis of *N,N,N*-Trimethylated Chitooligosaccharide

According to Zhang [49], the synthesis procedure of *N,N,N*-trimethylated chitooligosaccharide (TMCI) was slightly modified and implemented as follows: 20 mmol COS was distributed into 60 mL NMP with 30 mL 15% NaOH solution and 9 g NaI and stirred for 30 min in a round-bottom flask. Then 30 mL $CH_3I$ was added into the flask drop by drop under freezing conditions. After that, the reaction system was refluxed at 60 °C for 2 h. The TMCI product was precipitated and washed by anhydrous ethanol and anhydrous diethyl ether and obtained after freeze-drying at $-50$ °C for 24 h.

#### 3.2.2. Synthesis of COS Derivatives—TMC Phenolic Acid Salts

First, 30 mmol NaOH and 30 mmol phenolic acids (gallic acid monohydrate, ferulic acid, *p*-coumaric acid, caffeic acid, protocatechuic acid, sinapic acid, and salicylic acid) were dissolved in 10 mL deionized water and stirred for 2 h. Second, 10 mmol TMCI with 10 mL deionized water was added into the system drop by drop and stirred for 4 h at room temperature. After the reaction, anhydrous ethanol and anhydrous diethyl ether were used to precipitate and wash the products. Finally, the products were obtained after freeze-drying at $-50$ °C for 24 h [23,25].

#### 3.2.3. Synthesis of COS Derivatives—Phenolic Acid Esterified TMC

First, 20 mmol of different phenolic acids (gallic acid monohydrate, ferulic acid, *p*-coumaric acid, caffeic acid, protocatechuic acid, sinapic acid, and salicylic acid) and CDI was dissolved in DMSO solution and stirred for 12 h at 60 °C. After that, 10 mmol TMCI was added to the reaction system and stirred for 12 h. Finally, the desired products were precipitated and washed with anhydrous ethanol and anhydrous diethyl ether. After freeze-drying at $-50$ °C for 24 h these derivatives were obtained.

### 3.3. Analytical Methods

#### 3.3.1. Fourier Transform Infrared (FT-IR) Spectroscopy

Fourier transform infrared (FT-IR) spectroscopy (Nicolet IS 50 Fourier Transform Infrared Spectrometer, provided by Thermo Fisher Scientific, Thermo, Waltham, WA, USA) was used at 4000–400 $cm^{-1}$ to analyze the FT-IR structure of the desired products. The products were mixed with KBr disks at a 1:100 ratio and scanned 32 times at 25 °C.

#### 3.3.2. Nuclear Magnetic Resonance (NMR) Spectroscopy

The $^1H$ NMR spectra of the desired products were tested and recorded by a Bruke AVIII 500 Spectrometer (500 MHz, Bruker Switzerland, Fällanden, Switzerland) at 25 °C. The products were dissolved in $D_2O$ or DMSO and the chemical shift values are given in δ (ppm).

#### 3.3.3. Yields and Degree of Substitution (DS) Analysis

In order to estimate the reaction efficiency, the production yield and DS were calculated in this part. Yield represents the ratio (%) of the actual weight (g) of the products to the theoretical weight (g).

The calculation formulation of DS is as follows:

$$\mathrm{DS} = \mathrm{H_s}/\mathrm{H_1}(\%)$$

where Hs represents the integral area of the hydrogen atom in the benzene ring of the derivatives, $H_1$ represents the integral area of the 1-position carbon-bonded hydrogen proton on the main chain of the chitosan.

#### 3.3.4. Thermal Stability

The thermal stability characterization of COS and its derivatives was characterized by a Mettler 5 MP thermogravimetric analyzer (Mettler Toledo, Greifensee, Switzerland). After being vacuum-dried for 24 h, the samples were heated in a range of 30–700 °C at 10 °C /min under a nitrogen atmosphere.

### *3.4. Antioxidant Activity Assay*

#### 3.4.1. DPPH Radical Scavenging Activity Assay

According to Li [50], the 1,1-Diphenyl-2-picryl-hydrazyl (DPPH) scavenging activity of products was slightly modified and tested as follows. After lyophilizing to constant weight, the samples were prepared into a solution at an initial concentration of 10 mg/mL. A total of 17.75 mg 1,1-Diphenyl-2-picryl-hydrazyl was dissolved in anhydrous ethanol and placed in a 500 mL volumetric flask. The product solutions were finally diluted into different concentration solutions (0.1, 0.2, 0.4, 0.8, 1.6 mg/mL) with deionized water and 2.0 mL DPPH solution. Then they were incubated together for 20 min and the absorbance of the solution was measured and recorded at 517 nm by a microplate reader. As for the control group, DPPH was replaced by 2.0 mL of the anhydrous group, and the sample was replaced by 1.0 mL deionized water as the blank group. Three replicates for every sample concentration were measured and the scavenging effect was calculated by the following equation:

$$Scavenging\ activity(\%) = \left[\frac{A_{sample-}A_{control}}{A_{blank}}\right] \times 100$$

where $A_{sample}$, $A_{control}$, $A_{blank}$ respectively represent the absorbance of the sample, the control and the blank at 517 nm.

#### 3.4.2. Superoxide Radical Scavenging Activity Assay

The superoxide radical scavenging activity of the products was tested as follows. After lyophilizing to constant weight, the samples to be tested were prepared into a solution at an initial concentration of 10 mg/mL. Tris-HCl buffer (16 mM, pH = 8.0), nicotinamide adenine dinucleotide reduced (NADH, 338 μM NADH dissolved in Tris-HCl buffer), nitro blue tetrazolium (NBT, 72 μM NBT dissolved in Tris-HCl buffer), phenazine methosulfate (PMS, 30 μM PMS dissolved in Tris-HCl buffer) were prepared for the experiment. Measured sample solutions (0.03, 0.06, 0.12, 0.24, 0.48 mL) were added with 0.5 mL NADH, 0.5 mL NBT, and 0.5 mL PMS, and then the volume was fixed to 2 mL with deionized water. After that, the solution was incubated for 5 min under dark condition at room temperature and the absorbance was measured at 560 nm with a microplate reader. In the control group, the NADH was replaced with an equal amount of Tris-HCl buffer, and in the blank group, the sample solution was replaced with an equal amount of deionized water. The scavenging effect was calculated by the following equation:

$$Scavenging\ activity(\%) = \left[1 - \frac{A_{sample} - A_{control}}{A_{control}}\right] \times 100$$

where $A_{sample}$, $A_{control}$ and $A_{blank}$ respectively represent the absorbance of the sample, the control and the blank at 560 nm [51].

### 3.4.3. Hydroxyl Radical Scavenging Activity Assay

The hydroxyl radical scavenging activity of products was tested as follows. After lyophilizing to constant weight, the samples were prepared into a solution at an initial concentration of 10 mg/mL. In addition, potassium phosphate buffer (pH = 7.4) $H_2O_2$ (60 µM dissolved in potassium phosphate buffer), EDTA-$Fe^{2+}$ (220 µM, potassium phosphate buffer), and safranine O (0.23 µM, potassium phosphate buffer) were prepared for the experiment. Sample solutions (0.045, 0.09, 0.18, 0.36, 0.72 mL) with 0.50 mL EDTA-$Fe^{2+}$, 1.00 mL potassium phosphate buffer, 1.00 mL safranine O, 1.00 mL $H_2O_2$ solution were incubated without light at 37 °C for 30 min. Meanwhile, the control group contained 1.00 mL deionized water, 0.50 mL EDTA-$Fe^{2+}$, 2.00 mL potassium phosphate buffer, 1.00 mL safranine O, and the blank group constituted 1.00 mL deionized water, 0.50 mL EDTA-$Fe^{2+}$, 1.00 mL potassium phosphate buffer, 1.00 mL safranine O and 1.00 mL $H_2O_2$. Finally, the absorbance of all solutions was measured at 520 nm with a microplate reader, and the scavenging effect was calculated by the following equation:

$$Scavenging\ activity(\%) = \left[\frac{A_{sample} - A_{blank}}{A_{control} - A_{blank}}\right] \times 100$$

where $A_{sample}$, $A_{control}$ and $A_{blank}$ respectively represent the absorbance of the sample, the control and the blank at 520 nm [52].

### 3.4.4. Reducing Power Assay

The reducing power of products was tested as follows. After lyophilizing to constant weight, the samples were prepared into a solution at an initial concentration of 10 mg/mL. In addition, sodium phosphate buffer (pH = 6.6), potassium ferricyanide solution (1%, dissolved in sodium phosphate buffer), trichloroacetic acid (10%, dissolved in sodium phosphate buffer), and ferric chloride solution (0.1%, dissolved in sodium phosphate buffer) were prepared for the experiment. First, sample solutions (0.03, 0.06, 0.12, 0.24, 0.48 mL) and 0.50 mL potassium ferricyanide reacted at 50 °C for 20 min, and then 0.50 mL trichloroacetic acid was added to terminate the reaction. Second, the solution was centrifuged and 0.75 mL supernatant was added into 0.60 mL deionized water with 0.15 mL ferric chloride solution. The reaction system was incubated at room temperature for 10 min. The absorbance of the reaction system was measured at 700 nm and the data represent the reducing power of products [53].

## *3.5. Evaluation of Antibacterial Activity*

### 3.5.1. Preparation of Solutions

The samples were dissolved in sterile water at an initial concentration of 16 mg/mL. Then 100 µL of stock solutions was added to the 96-well plate and continuously diluted 11 times.

### 3.5.2. Minimum Inhibitory Concentration and Minimum Biocidal Concentration

The antibacterial activity of the samples was tested by the method of minimum inhibitory concentration (MIC) and minimum biocidal concentration (MBC). *Escherichia coli* (*E. coli*) and *Staphylococcus aureus* (*S. aureus*) bacteria were cultivated to test the antibacterial activity, as they were the epitome of Gram-positive bacteria and Gram-negative bacteria, respectively. The experimental process was implemented as follows. First, the bacteria species were incubated in Luria Bertani (LB) medium at 37 °C. And the well-grown bacteria were diluted to 105–106 cell/mL with LB medium. Then the bacterial suspension was added to the 96-well plates containing samples of different concentrations prepared in advance. The volume added to each well was 100 µL, and it was incubated at 37 °C for 24 h. In the meantime, the MIC and MBC were observed by the naked eye. The MIC is the lowest concentration of samples that can completely inhibit visible bacteria growth after 12 h and the MBC is the lowest concentration of the experimental samples that can completely inhibit visible bacteria growth after 24 h. All experimental operations were completed under sterile conditions [54].

### *3.6. Antifungal Assay*

Herein, two kinds of plant fungus were cultured to test the antifungal activity of COS and its derivatives. The first one was *Botrytis cinerea* (*B. cinerea*) and the other was *Fusarium graminearum* (*F. graminearum*).

#### 3.6.1. Preparation of Solutions

First, the samples were dissolved in sterile water at an initial concentration of 10 mg/mL. Then the potato dextrose agar (PDA) medium was prepared and sterilized at 120 °C for 25 min to prepare the sample medium. After that, sample solutions of different volumes (2.0, 1.0 and 0.2 mL) were mixed with different volumes of medium (18.0, 19.0 and 19.8 mL) and then poured into disposable Petri dishes. The sample culture medium at concentrations of 0.10, 0.50 and 1.00 mg/mL was formed after solidification. Here in the positive control group, the sample was replaced by carbendazim and the blank control group was deionized water.

#### 3.6.2. Implementation of the Antifungal Experiment

The mycelial growth rate method was used in this experiment. The well-cultivated strains were coated on a PDA medium and cultured in a fungus incubator (28 °C, RH = 60%) for 48 h. After that, a fungi mycelia disk with a diameter of 5 mm was made and carefully inoculated on the sample medium. They were then placed into the fungus incubator for culture. When the mycelia of the blank group grew to the inner edge of the Petri dish, the diameter of the mycelia in all the sample culture media could be measured using the cross crossing method. Three values were measured in parallel for each sample concentration. All experiments were performed under aseptic conditions. Finally, the inhibition rate was measured as follows:

$$Inhibitory\ index(\%) = \left[1 - \frac{\mathrm{D_s} - 5}{\mathrm{D_b} - 5}\right] \times 100$$

where $\mathrm{D_s}$ is the diameter of the growth zone in the sample plates and $\mathrm{D_b}$ is the diameter of the growth zone in the blank control plates [37,55].

### *3.7. Cytotoxicity Assay*

L929 cells were chosen in this part to test the cytotoxicity of these derivatives by MTT method in vitro. First, L929 cells were incubated in DEMO medium with 10% fetal calf serum and 1% mixture of penicillin and streptomycin at 37 °C with a 5% $CO_2$ atmosphere. After passing through twice, the well-incubated cells at a concentration of $5 \times 10^4$/mL were added to 96-well plates and incubated for 24 h. Then the derivative solutions at different concentrations were added to the wells and incubated until the cells in control wells multiplied to 90%; the MTT with 0.5 mg/mL was added to the wells and the absorbance was detected at 490 nm with a microplate reader after 4 h with DMSO solution. The cell viability was calculated by the following equation:

$$Cell\ viability = \left[\frac{A_{sample} - A_{blank}}{A_{control} - A_{blank}}\right] \times 100$$

where $A_{sample}$, $A_{control}$ and $A_{blank}$ respectively represent the absorbance of the sample, the negative control and the blank group at 490 nm.

### *3.8. Statistical Analysis*

All experiments above were conducted at least three times and data are presented as the mean ± standard deviation (SD). Significant differences between the groups were assessed using one-way ANOVA followed by Duncan's test using PASW Statistics 21.0 (SPSS Inc., Chicago, IL, USA). Differences were considered statistically significant at $p < 0.05$.

## 4. Conclusions

In this study, several COS phenolic acid derivatives were successfully synthesized by chemical modification. COS, as a leading compound, was the first to be quaternized and then modified with phenolic acids by two different methods. The structures and DS of these derivatives were characterized by FT-IR and $^1$H NMR spectra. The thermal stability of the derivatives was studied and the results proved they were more stable than COS. Additionally, the antioxidant activity of the derivatives was explored in vitro according to four typical methods. The results demonstrated that the antioxidant activity of the derivatives was greatly improved. Subsequently, the antifungal and antibacterial activities of derivatives were also detected, and among them, derivatives of CMTMC, CM-TMC and SY-TMC had excellent antibacterial and antifungal activities. The cytotoxicity of these derivatives was explored by L929 cells in vitro and the results showed that the cytotoxicity of the derivatives exhibited concentration dependence. Therefore, this study confirms that introducing phenolic acid into COS can significantly improve its biological activity. The derivatives with outstanding activities can be further developed and utilized as antioxidants or bacteriostats in the fields of food, medicine, cosmetics, agriculture and environmental protection. However, the structure–activity relationship and antioxidant mechanism of the products still need further study.

**Author Contributions:** Formal analysis, Y.S. and J.C.; Funding acquisition, L.T. and Z.G.; Methodology, Y.S. and Z.G.; Project administration, Z.G.; Resources, L.T. and Z.G.; Software, Y.S., J.C. and Y.M.; Validation, Y.S., J.C. and Y.M.; Visualization, Y.S.; Writing—original draft, Y.S.; Writing—review and editing, Z.G. All authors have read and agreed to the published version of the manuscript.

**Funding:** This work was supported by the Shandong Key R&D Plan, Major Scientific and Technological Innovation Project (2022CXGC020413), the Science & Technology Specific Projects in the Agricultural High-Tech Industrial Demonstration Area of the Yellow River Delta (2022SZX01), the Key Deployment Project of the Center for Ocean Mega-Science of CAS (COMS2020J04) and the 2022 Central Guiding Local Science and Technology Development Fund Project in Shandong Province (YDZX2022007).

**Institutional Review Board Statement:** Not applicable.

**Informed Consent Statement:** Not applicable.

**Data Availability Statement:** All data contained in the manuscript are available from the authors.

**Acknowledgments:** The authors thank the support of the Yellow River Delta Saline-Alkali Agroecosystem Observation and Research Station.

**Conflicts of Interest:** The authors declare that there are no competing financial interests or conflicting relationships.

## References

1. Joseph, S.M.; Krishnamoorthy, S.; Paranthaman, R.; Moses, J.A.; Anandharamakrishnan, C. A review on source-specific chemistry, functionality, and applications of chitin and chitosan. *Carbohydr. Polym. Technol. Appl.* **2021**, *2*, 100036. [CrossRef]
2. Naveed, M.; Phil, L.; Sohail, M.; Hasnat, M.; Baig, M.M.F.A.; Ihsan, A.U.; Shumzaid, M.; Kakar, M.U.; Khan, T.M.; Akabar, M.; et al. Chitosan oligosaccharide (COS): An overview. *Int. J. Biol. Macromol.* **2019**, *129*, 827–843. [CrossRef] [PubMed]
3. Liaqat, F.; Eltem, R. Chitooligosaccharides and their biological activities: A comprehensive review. *Carbohydr. Polym.* **2018**, *184*, 243–259. [CrossRef] [PubMed]
4. Zhai, X.; Li, C.; Ren, D.; Wang, J.; Ma, C.; Abd El-Aty, A.M. The impact of chitooligosaccharides and their derivatives on the in vitro and in vivo antitumor activity: A comprehensive review. *Carbohydr. Polym.* **2021**, *266*, 118132. [CrossRef] [PubMed]
5. Liu, X.; Xia, W.; Jiang, Q.; Yu, P.; Yue, L. Chitosan oligosaccharide-N-chlorokojic acid mannich base polymer as a potential antibacterial material. *Carbohydr. Polym.* **2018**, *182*, 225–234. [CrossRef] [PubMed]
6. Park, H.-H.; Ko, S.-C.; Oh, G.-W.; Jang, Y.-M.; Kim, Y.-M.; Park, W.S.; Choi, I.-W.; Jung, W.-K. Characterization and biological activity of PVA hydrogel containing chitooligosaccharides conjugated with gallic acid. *Carbohydr. Polym.* **2018**, *198*, 197–205. [CrossRef]

7. Oh, G.-W.; Kim, S.-C.; Kim, T.-H.; Jung, W.-K. Characterization of an oxidized alginate-gelatin hydrogel incorporating a COS-salicylic acid conjugate for wound healing. *Carbohydr. Polym.* **2021**, *252*, 117145. [CrossRef] [PubMed]
8. Karagozlu, M.Z.; Karadeniz, F.; Kim, S.-K. Anti-HIV activities of novel synthetic peptide conjugated chitosan oligomers. *Int. J. Biol. Macromol.* **2014**, *66*, 260–266. [CrossRef]
9. Zhang, J.; Dai, X.; Jiang, Z. Research Progress in Functions of Bioactive Chitooligosaccharides in Prevention and Treatment of Alzheimers Disease. *Food Sci.* **2013**, *34*, 316–320.
10. Liang, S.; Sun, Y.; Dai, X. A Review of the Preparation, Analysis and Biological Functions of Chitooligosaccharide. *Int. J. Mol. Sci.* **2018**, *19*, 2197. [CrossRef]
11. Je, J.-Y.; Kim, S.-K. Chitooligosaccharides as potential nutraceuticals: Production and bioactivities. *Adv. Food Nutr. Res.* **2012**, *65*, 321–336.
12. Boz, H. Ferulic Acid in Cereals—A Review. *Czech J. Food Sci.* **2015**, *33*, 1–7. [CrossRef]
13. Anantharaju, P.G.; Gowda, P.C.; Vimalambike, M.G.; Madhunapantula, S.V. An overview on the role of dietary phenolics for the treatment of cancers. *Nutr. J.* **2016**, *15*, 99. [CrossRef]
14. Bialecka-Florjanczyk, E.; Fabiszewska, A.; Zieniuk, B. Phenolic Acids Derivatives—Biotechnological Methods of Synthesis and Bioactivity. *Curr. Pharm. Biotechnol.* **2018**, *19*, 1098–1113. [CrossRef]
15. Insaward, A.; Duangmal, K.; Mahawanich, T. Mechanical, Optical, and Barrier Properties of Soy Protein Film As Affected by Phenolic Acid Addition. *J. Agric. Food Chem.* **2015**, *63*, 9421–9426. [CrossRef]
16. Perez-Jimenez, J.; Lluis Torres, J. Analysis of Nonextractable Phenolic Compounds in Foods: The Current State of the Art. *J. Agric. Food Chem.* **2011**, *59*, 12713–12724. [CrossRef] [PubMed]
17. Heleno, S.A.; Martins, A.; Queiroz, M.J.R.P.; Ferreira, I.C.F.R. Bioactivity of phenolic acids: Metabolites versus parent compounds: A review. *Food Chem.* **2015**, *173*, 501–513. [CrossRef] [PubMed]
18. Oluwole, O.; Fernando, W.M.A.D.B.; Lumanlan, J.; Ademuyiwa, O.; Jayasena, V. Role of phenolic acid, tannins, stilbenes, lignans and flavonoids in human health—A review. *Int. J. Food Sci. Technol.* **2022**, *57*, 6326–6335. [CrossRef]
19. Valanciene, E.; Jonuskiene, I.; Syrpas, M.; Augustiniene, E.; Matulis, P.; Simonavicius, A.; Malys, N. Advances and Prospects of Phenolic Acids Production, Biorefinery and Analysis. *Biomolecules* **2020**, *10*, 874. [CrossRef]
20. Eom, T.-K.; Senevirathne, M.; Kim, S.-K. Synthesis of phenolic acid conjugated chitooligosaccharides and evaluation of their antioxidant activity. *Environ. Toxicol. Pharmacol.* **2012**, *34*, 519–527. [CrossRef]
21. Vo, T.-S.; Ngo, D.-H.; Kim, S.-K. Gallic acid-grafted chitooligosaccharides suppress antigen-induced allergic reactions in RBL-2H3 mast cells. *Eur. J. Pharm. Sci.* **2012**, *47*, 527–533. [CrossRef]
22. Chen, D.; Bai, R.; Yong, H.; Zong, S.; Jin, C.; Liu, J. Improving the digestive stability and prebiotic effect of carboxymethyl chitosan by grafting with gallic acid: In vitro gastrointestinal digestion and colonic fermentation evaluation. *Int. J. Biol. Macromol.* **2022**, *214*, 685–696. [CrossRef] [PubMed]
23. Sun, Y.; Ji, X.; Cui, J.; Mi, Y.; Zhang, J.; Guo, Z. Synthesis, Characterization, and the Antioxidant Activity of Phenolic Acid Chitooligosaccharide Derivatives. *Mar. Drugs* **2022**, *20*, 489. [CrossRef]
24. Dai-Nghiep, N.; Kim, M.-M.; Kim, S.-K. Protective effects of aminoethyl-chitooligosaccharides against oxidative stress in mouse macrophage RAW 264.7 cells. *Int. J. Biol. Macromol.* **2012**, *50*, 624–631.
25. Mi, Y.; Tan, W.; Zhang, J.; Guo, Z. Modification of Hydroxypropyltrimethyl Ammonium Chitosan with Organic Acid: Synthesis, Characterization, and Antioxidant Activity. *Polymers* **2020**, *12*, 2460. [CrossRef]
26. Xing, R.; Xu, C.; Gao, K.; Yang, H.; Liu, Y.; Fan, Z.; Liu, S.; Qin, Y.; Yu, H.; Li, P. Characterization of Different Salt Forms of Chitooligosaccharides and Their Effects on Nitric Oxide Secretion by Macrophages. *Molecules* **2021**, *26*, 2563. [CrossRef]
27. Belalia, R.; Grelier, S.; Benaissa, M.; Coma, V. New bioactive biomaterials based on quaternized chitosan. *J. Agric. Food Chem.* **2008**, *56*, 1582–1588. [CrossRef]
28. Zhang, J.; Tan, W.; Luan, F.; Yin, X.; Dong, F.; Li, Q.; Guo, Z. Synthesis of Quaternary Ammonium Salts of Chitosan Bearing Halogenated Acetate for Antifungal and Antibacterial Activities. *Polymers* **2018**, *10*, 530. [CrossRef]
29. Chikkulapalli, A.; Aavula, S.K.; Mona, R.N.P.; Karthikeyan, C.; Kumar, V.C.H.; Sulur, M.G.; Sumathi, S. Convenient N-acetylation of amines in N,N-dimethylacetamide with N,N-carbonyldiimidazole. *Tetrahedron Lett.* **2015**, *56*, 3799–3803. [CrossRef]
30. Engstrom, K.M. Practical Considerations for the Formation of Acyl Imidazolides from Carboxylic Acids and N,N′-Carbonyldiimidazole: The Role of Acid Catalysis. *Org. Process Res. Dev.* **2018**, *22*, 1294–1297. [CrossRef]
31. Liu, Y.; Liu, Z.; Gao, Y.; Gao, W.; Hou, Z.; Zhu, Y. Facile Method for Surface-Grafted Chitooligosaccharide on Medical Segmented Poly(ester-urethane) Film to Improve Surface Biocompatibility. *Membranes* **2021**, *11*, 37. [CrossRef]
32. Zhang, J.; Tan, W.; Wang, G.; Yin, X.; Li, Q.; Dong, F.; Guo, Z. Synthesis, characterization, and the antioxidant activity of N,N,N-trimethyl chitosan salts. *Int. J. Biol. Macromol.* **2018**, *118*, 9–14. [CrossRef]
33. Witt, J.D.; Gabriel, M.K.; Julian, R.L. Gc-Ft-Ir Analysis Of Commercial Divinyl Benzene. *J. Chromatogr. Sci.* **1979**, *17*, 445–448. [CrossRef]
34. Sedman, J.; Butler, I.S. Polarized Ft-Ir Spectra of Benzene and Anthracene Oriented in A Nematic Liquid-Crystal Solvent. *Appl. Spectrosc.* **1985**, *39*, 621–625. [CrossRef]
35. Li, Q.; Wei, L.; Zhang, J.; Gu, G.; Guo, Z. Significantly enhanced antioxidant activity of chitosan through chemical modification with coumarins. *Polym. Chem.* **2019**, *10*, 1480–1488. [CrossRef]

36. Wang, Y.; Cen, C.; Chen, J.; Fu, L. MgO/carboxymethyl chitosan nanocomposite improves thermal stability, waterproof and antibacterial performance for food packaging. *Carbohydr. Polym.* **2020**, *236*, 116078. [CrossRef]
37. Cui, J.; Sun, Y.; Wang, L.; Miao, Q.; Tan, W.; Guo, Z. Preparation of l-Arginine Schiff Bases Modified Chitosan Derivatives and Their Antimicrobial and Antioxidant Properties. *Mar. Drugs* **2022**, *20*, 688. [CrossRef]
38. Ak, T.; Gulcin, I. Antioxidant and radical scavenging properties of curcumin. *Chem. -Biol. Interact.* **2008**, *174*, 27–37. [CrossRef] [PubMed]
39. Sekine, T.; Masumizu, T.; Maitani, Y.; Nagai, T. Evaluation of superoxide anion radical scavenging activity of shikonin by electron spin resonance. *Int. J. Pharm.* **1998**, *174*, 133–139. [CrossRef]
40. Gill, S.S.; Tuteja, N. Reactive oxygen species and antioxidant machinery in abiotic stress tolerance in crop plants. *Plant Physiol. Biochem.* **2010**, *48*, 909–930. [CrossRef] [PubMed]
41. Sun, T.; Yao, Q.; Zhou, D.; Mao, F. Antioxidant activity of N-carboxymethyl chitosan oligosaccharides. *Bioorganic Med. Chem. Lett.* **2008**, *18*, 5774–5776. [CrossRef]
42. Singhal, M.; Paul, A.; Singh, H.P. Synthesis and reducing power assay of methyl semicarbazone derivatives. *J. Saudi Chem. Soc.* **2014**, *18*, 121–127. [CrossRef]
43. Yang, X.; Lan, W.; Sun, X. Antibacterial and antioxidant properties of phenolic acid grafted chitosan and its application in food preservation: A review. *Food Chem.* **2023**, *428*, 136788. [CrossRef] [PubMed]
44. Mu, K.; Yao, Y.; Wang, D.; Kitts, D.D. Prooxidant capacity of phenolic acids defines antioxidant potential. *Biochim. Et Biophys. Acta-Gen. Subj.* **2023**, *1867*, 130371. [CrossRef]
45. Mansouri, M.; Mobarez, A.M.; Nojoomi, F. Comprehensive study of common Enterogenic E. coli in Iran during 2010–2020: A systematic review. *Gene Rep.* **2021**, *25*, 101316. [CrossRef]
46. Zhang, J.; Wang, J.; Jin, J.; Li, X.; Zhang, H.; Shi, X.; Zhao, C. Prevalence, antibiotic resistance, and enterotoxin genes of Staphylococcus aureus isolated from milk and dairy products worldwide: A systematic review and meta-analysis. *Food Res. Int.* **2022**, *162*, 111969. [CrossRef] [PubMed]
47. Munhuweyi, K.; Lennox, C.L.; Meitz-Hopkins, J.C.; Caleb, O.J.; Opara, U.L. Major diseases of pomegranate (*Punica granatum* L.), their causes and management-A review. *Sci. Hortic.* **2016**, *211*, 126–139. [CrossRef]
48. Dean, R.; Van Kan, J.A.L.; Pretorius, Z.A.; Hammond-Kosack, K.E.; Di Pietro, A.; Spanu, P.D.; Rudd, J.J.; Dickman, M.; Kahmann, R.; Ellis, J.; et al. The Top 10 fungal pathogens in molecular plant pathology. *Mol. Plant Pathol.* **2012**, *13*, 414–430. [CrossRef]
49. Zhang, J.; Tan, W.; Wei, L.; Chen, Y.; Mi, Y.; Sun, X.; Li, Q.; Dong, F.; Guo, Z. Synthesis of urea-functionalized chitosan derivatives for potential antifungal and antioxidant applications. *Carbohydr. Polym.* **2019**, *215*, 108–118. [CrossRef] [PubMed]
50. Li, Q.; Zhang, C.; Tan, W.; Gu, G.; Guo, Z. Novel Amino-Pyridine Functionalized Chitosan Quaternary Ammonium Derivatives: Design, Synthesis, and Antioxidant Activity. *Molecules* **2017**, *22*, 156. [CrossRef] [PubMed]
51. Wei, L.; Li, Q.; Tan, W.; Dong, F.; Luan, F.; Guo, Z. Synthesis, Characterization, and the Antioxidant Activity of Double Quaternized Chitosan Derivatives. *Molecules* **2017**, *22*, 501. [CrossRef] [PubMed]
52. Sun, X.; Zhang, J.; Mi, Y.; Miao, Q.; Tan, W.; Li, Q.; Guo, Z. Synthesis, characterization, and antioxidant activity of carboxymethyl chitosan derivatives containing sulfonium salt. *J. Oceanol. Limnol.* **2022**, *40*, 284–295. [CrossRef]
53. Tan, W.; Li, Q.; Li, W.; Dong, F.; Guo, Z. Synthesis and antioxidant property of novel 1,2,3-triazole-linked starch derivatives via 'click chemistry'. *Int. J. Biol. Macromol.* **2016**, *82*, 404–410. [CrossRef] [PubMed]
54. Sahariah, P.; Masson, M.; Meyer, R.L. Quaternary Ammoniumyl Chitosan Derivatives for Eradication of Staphylococcus aureus Biofilms. *Biomacromolecules* **2018**, *19*, 3649–3658. [CrossRef]
55. Mi, Y.; Li, Q.; Miao, Q.; Tan, W.; Zhang, J.; Guo, Z. Enhanced antifungal and antioxidant activities of new chitosan derivatives modified with Schiff base bearing benzenoid/heterocyclic moieties. *Int. J. Biol. Macromol.* **2022**, *208*, 586–595. [CrossRef]

MDPI AG
Grosspeteranlage 5
4052 Basel
Switzerland
Tel.: +41 61 683 77 34

*Marine Drugs* Editorial Office
E-mail: marinedrugs@mdpi.com
www.mdpi.com/journal/marinedrugs

MDPI

Academic Open
Access Publishing

mdpi.com

ISBN 978-3-7258-5374-8